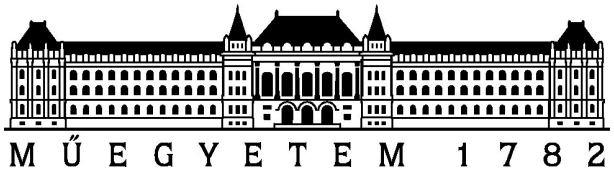

PhD Thesis

Development and investigation of ultra-small on-chip resistive switching memory devices

Tímea Nóra Török

Supervisor: **Prof. András Halbritter**
Department of Physics
Institute of Physics
Budapest University of Technology and Economics

Industrial advisor: **Dr. János Volk**
Nanosensors Laboratory
Institute of Technical Physics and Materials Science
HUN-REN Centre for Energy Research

BME
2024

Contents

Chapter 1

Introduction

The development of information technologies has reached the level where classical computers built in von Neumann architecture are no longer sufficient in many cases to process the rapidly growing amounts of information. The main limitation of the speed of data processing is the limited speed of data transfer between physically separate units performing computing and memory functions. The urge for efficient information processing has led to the spread of novel software solutions, biologically inspired algorithms, and neural networks along with the development of data science. However, the operation of these approaches is extremely energy- and time-consuming, so completely new hardware architectures are also required for the effective application of novel software solutions and algorithms. For this reason, the development of new building blocks providing logic and/or memory functions has become a dynamically developing, increasingly diversified field of science in recent years based on the annual reports of the International Roadmap for Devices and Systems (IRDS)[1–3].

A group of these emerging devices are resistive switching memory devices (RRAMs or memristors), which are generally metal-insulator-metal nanostructures whose conductance can be changed by electrical signals applied to the electrodes of the device [4]. The change of conductance in a resistive switching device can either be volatile, or non-volatile. In the latter case, thanks to the special voltage- and time-dependent dynamics of the resistive switching phenomenon, multi-level (analog) programming can be realized with switching voltage signals of appropriately chosen time and amplitude, while the conductance remains constant at low signal levels. Thus, non-volatile resistive switching memories have analog memory, providing a promising platform for e.g. hardware-level encoding of large weight matrices of neural networks [5]. With such a network of memristors, vector-matrix multiplication operations, which otherwise require a lot of computation steps on a transistor-based architecture, can be performed in a single step. In this way, the use of resistive switching memories promises orders of magnitude faster and more energy-efficient

operation in the case of artificial neural networks (ANNs) compared to the most modern GPU-based realizations [5–8].

Another interesting and well-applicable trait of memristors are their neuromorphic properties. For example, by building simple circuits from devices with volatile memory, various types of artificial neurons and neuromorphic hardware elements can be realized [9, 10]. Utilizing their capability to generate neural spiking waveforms similarly to the nervous system, these circuits can be utilized as hardware components for oscillatory or spiking neural networks (ONN/SNN) [11]. Another interesting feature of these neuromorphic circuits is that they can be directly used for edge computing, i.e. information processing tasks at the edge of a network, close to the point where data originates [12] (as opposed to centralised processing, e.g. cloud computing). These edge networks can play a significant role in specialized systems where energy-efficient operation and small size of the processing unit are important. In such an application, raw signal from a sensor can be directly converted into a series of electrical spikes, encoding information in the frequency of these spikes, providing input data for a SNN [13, 14].

The cause for resistive switching phenomena in memristive devices is a reversible variation of the structure of the inner, active material of the device. For many memristors, the self-organized formation of a well-conducting path, a *filament* is the reason for the increase in conductance. The physical nature of filaments forming during resistive switching, and the microscopic – or even nanoscale – processes which account for switching dynamics are interesting topics with many open questions due to the diverse mechanisms present in different types of memristors. Elucidating specific details of these mechanisms are highly important for the development of devices. Without a thorough understanding of the physical mechanisms that shape memristive properties in different material systems, it is impossible to develop reliable devices that fulfill all strict requirements needed for commercializing this technology.

The aim of the studies presented in my dissertation is twofold: one goal is the development of new memristive devices from a wide array of materials, and an equally important aim is to provide insights into their switching mechanisms to build accurate physical models verified by experiments. Relying on these studies, I also show some circuit-level applications I worked on related to these self-made memristive elements. References numbered as [O1–O6] are distinguished in the beginning of the bibliography, to mark my own publications which support thesis points in the last Chapter (see Summary).

Since I investigated various resistive switching (RS) material systems in several contexts in my thesis, I provide a literature overview in Chapter 2 which focuses on describing diverse RS phenomena observable in different material systems, to provide background for my own studies. I also show some examples from the broad research area of RS materials and their applications in Chapter 2.

I present my work on the development of on-chip resistive switching memory devices in Chapter 3. This work ranged from producing samples with standard nanofabrication techniques to their characterisation by various methods. As the foundation of my studies, I learned the basics of electron beam lithography and thin film preparation from László Pósa. Chapter 3 is also divided into sections based on the switching mechanism of the devices. I show applications of on-chip devices I developed within our research group [O1–O4], including my own measurements and measurements carried out by my colleagues.

Investigation of the stochastic nature of SiO_x memristors is presented in Chapter 4, focusing on the experimental study and modelling of the set process. I performed this analysis applying nucleation theory, yielding that nucleation of the SiO_x active region governs switching dynamics [O5].

In Chapter 5 the results of superconducting spectroscopy performed on Nb_2O_5 [O6] and Ta_2O_5 [O2] STM point-contact devices are presented. This approach provides a non-destructive diagnostic tool for the in-situ, experimental study of nanofilaments present in the active region of the devices. Beyond the directly extracted information on filament width, it is possible to obtain the individual transmission eigenvalues or the transmission density function of the nanofilament. The former has great importance from the viewpoint of device scalability, whereas the latter quantities reveal fine details on the atomic structure of filaments, providing possibilities to validate atomic-scale memristor models (e.g. models based on density functional theory).

Finally, in Chapter 6, I investigate the application possibility of a VO_2 memristor-based relaxation oscillator circuit in an auditory sensing unit. In this project, I coupled the oscillator to a MEMS cantilever, and demonstrated several bio-realistic traits of the circuit, which fulfill some prerequisites to a possible application in cochlear implants.

Chapter 2

Overview of the research field

Resistive switching phenomena and their mechanisms in different material systems always depend on the specific composition and geometry of the materials utilized. One of the earliest observation of reversible resistance switching in a material dates to the 1960s when S. Ovshinsky discovered that two contacting metallic leads covered by a thin film of an amorphous material exhibits reversible resistive switching effect [20, 21], as shown in Figure 2.1. He studied chalcogenide switches based on tellurium alloyed with arsenic, silicon and germanium, predecessors of today's phase change memory devices [22].

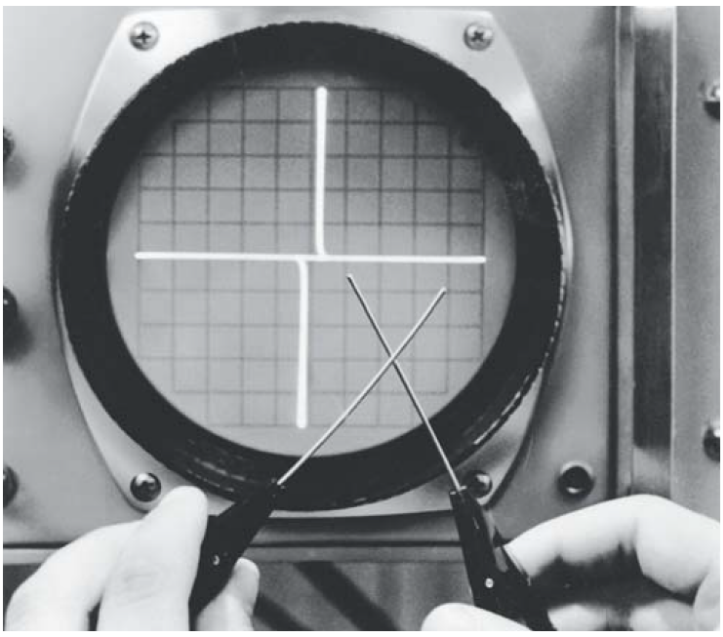

Figure 2.1: *Phase change effect demonstrated in an amorphous material. Horizontal axis on the oscilloscope shows the voltage, and the current is shown along the vertical axis during AC voltage sweeps. Comparing the two lines with very different slopes for each voltage polarity, a large difference of resistance states is observed. [20]*

Another kind of resistive switching effect was discovered also around the 1960s. In thin films of a dielectric material, namely Nb_2O_5, bistable $I(V)$ characteristics was observed due to voltage sweeps [23]. Around that time, similar reversible resistance change effects were reported in other types of dielectric thin films as well, e.g. TiO_2 [24] and NiO [25]. With these discoveries, the potential application possibility as a memory device in computers also arised, but faded immediately, since the reliability of those early devices was very limited. Research on resistive switching devices halted for a long time after the first discoveries. The research field started to grow rapidly after the scientists of Hewlett-Packard Company called their TiO_2 based resistive switching device *memristor* for the first time in 2008 [26], and presented an approach for modelling hysteretic $I(V)$ characteristics based on the work of L. Chua [27].

In the following, I am going to show examples of resistive switching phenomena in material structures relevant for the context and background of my own studies. The structure of this Chapter follows the classification of resistive switching devices based on their mechanisms. In the end, I also provide an overview of present state-of-the-art memristor applications and architectures from a technological point of view.

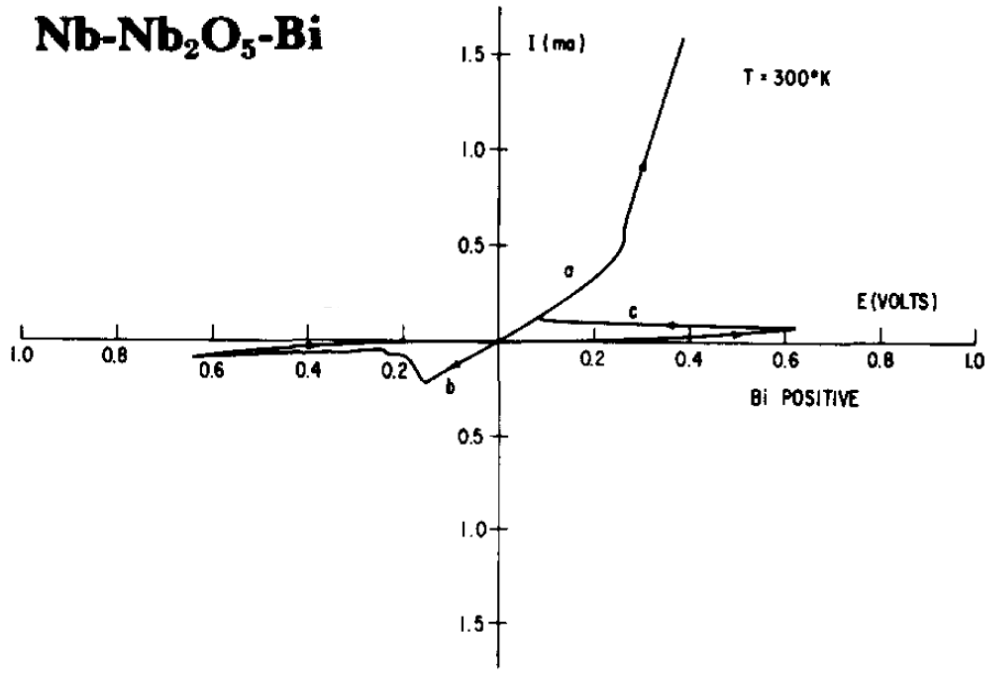

Figure 2.2: *Resistance switching effect observed in $Nb/Nb_2O_5/Bi$ structures. The direction of circumnavigation is indicated with small arrows on the lines. The sign of voltage is defined as positive for a positive voltage applied to the Bi electrode. [23]*

2.1 Classification of resistive switching phenomena

The above discussed early observations of resistive switching phenomena yield very different $I(V)$ characteristics. The switching effect shown in Figure 2.1 is a *unipolar* phenomenon, which means that the transition from the high resistance state (HRS or OFF state) to the low resistance state (LRS or ON state) happens at the same driving electrical polarity as the opposite process. In contrast, the switching effect depicted in Figure 2.2 is of *bipolar* nature, referring to the opposite polarity electrical signals needed for the *set* (OFF→ON) and *reset* (ON→OFF) processes. General $I(V)$ characteristics of bipolar and unipolar switching phenomena are displayed in Figure 2.3.

Bipolar characteristics are usually displayed as it is shown in Figure 2.3.a, showing the set process at positive polarity, and the reset at negative. I follow the same convention during the analysis of my own measurements involving bipolar RS phenomena. An illustration of unipolar $I(V)$ characteristics is shown in Figure 2.3.b. It his hard to give an accurate scheme for such phenomena since the magnitude of the absolute value of set and reset voltages (V_{set} and V_{reset}) determine the general appearance of the $I(V)$ curve. We can see examples for all three possibilities of $V_{\text{set}} > V_{\text{reset}}$, $V_{\text{set}} < V_{\text{reset}}$ and $V_{\text{set}} \approx V_{\text{reset}}$ in different RS devices. Furthermore, the traits of $I(V)$ curves can be affected by the characteristic timescales governing switching dynamics (e.g. leading to the appearence of bipolar characteristics in a principally unipolar device). Therefore classification based solely on the topology of $I(V)$ characteristics should be taken with caution. In the following, I am going to take another approach to introduce different RS devices, based on their switching mechanisms.

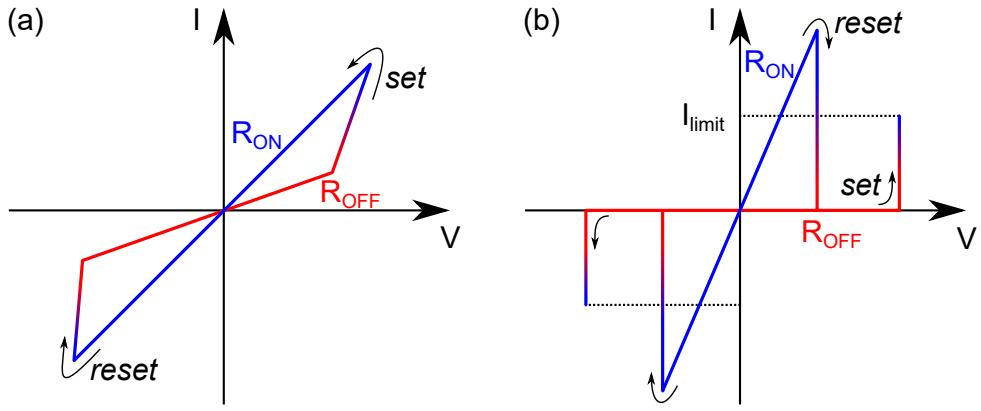

Figure 2.3: *Illustration of RS phenomena with different $I(V)$ characteristics, showing examples for (a) bipolar and (b) unipolar resistive switching. In certain cases, an external current limit is applied during the set programming process, to prevent damage to the device due to high currents, as illustrated with I_{limit} marked in panel (b).*

2.1.1 Phase change memristors

The operation of PCM devices (referring to phase change mechanism) relies on changes in local temperature, driven by Joule heating and passive thermal dissipation which results in the amorphisation/crystallization of the active volume [12, 22, 28, 29]. Typical layout and programming of a PCM device made of GST (a chalcogenide compound of Ge, Sb and Te) is illustrated in Figure 2.4.a. The crystalline phase of the active material usually yields low resistance, whereas the amorphous phase has high resistance. Crystallization of the material is governed by Joule heating, holding the temperature above the crystallization temperature (usually $T_{\text{cryst}} \approx 400°\text{C}$). Crystallization can be carried out in small steps using electrical pulses with well-defined amplitudes, as illustrated in Figure 2.4.a. This procedure can lead to multiple programmable resistance states in a device, realizing analog (multilevel) programming in a single cell (write or set process) [29]. The process of amorphisation (erase or reset process) is usually carried out with higher amplitude electrical pulses causing a melt-quench process, where the material is heated above its T_{melt} melting point ($T_{\text{cryst}} < T_{\text{melt}} \approx 600°\text{C}$), and rapidly quenched to an amorphous state.

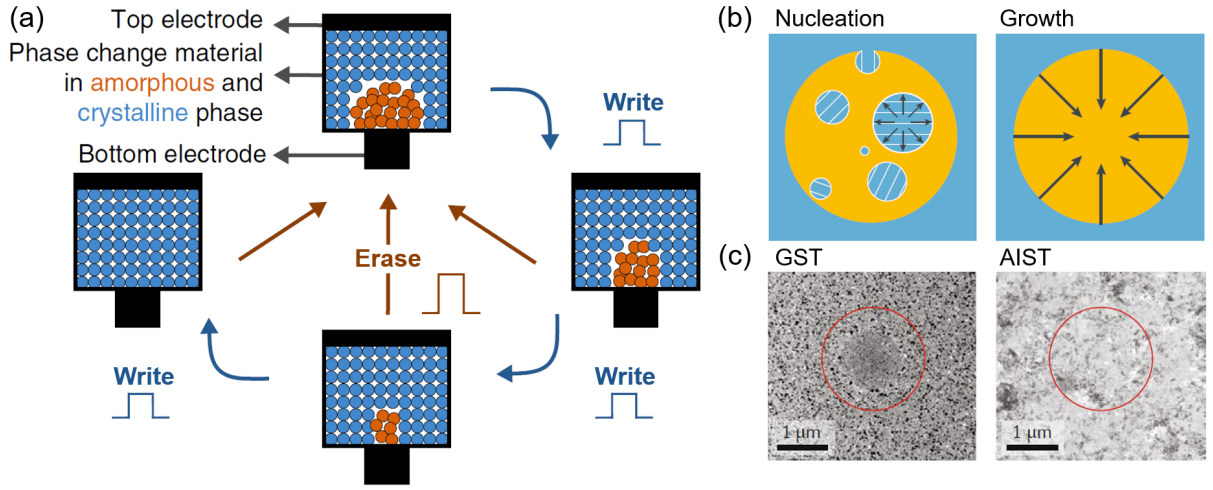

Figure 2.4: *Operation of PCM devices. (a) General layout and programming of a PCM device. Operation relies on the reversible amorphisation/crystallization of the active volume. Writing (set) can be performed in multiple steps, enabling analog programming of the device (indicated by blue arrows). Erasing (reset) can be performed in a single step (orange arrows). [29] (b) Illustration of nucleation and growth driven phenomena, which shape switching dynamics in a PCM device. [28] (c) TEM micrographs of recrystallized region (indicated by a red circle) in GST/AIST reveal a distinguishable/indistinguishable region compared to the surrounding crystalline matrix, indicative of a nucleation driven/growth driven process (see left/right images, respectively). [28, 30]*

There are two physical processes which can account for the dynamics of crystallization in a PCM device. Crystallization can occur as a nucleation driven, or a growth driven phenomenon, as illustrated in Figure 2.4.b [12, 28]. These processes arise from the thermodynamic conditions at play during the crystallization process. In devices operating via a nucleation driven process, switching dynamics is determined mainly by the incubation time needed for the creation of crystalline nuclei. In contrast, a growth driven process yields a rapidly growing crystalline volume along the crystalline–amorphous interface, shrinking the amorphous region (without the formation of robust crystalline seeds). These processes can result in crystalline structures with different morphology, which can be imaged via electron microscopy. TEM (transmission electron microscopy) images of different materials, $Ge_2Sb_2Te_5$ (GST) and $Ag_4In_3Sb_{67}Te_{26}$ (AIST) are shown in Figure 2.4.c, showing recrystallized regions inside a crystalline matrix. Both materials were investigated via a laser-based technique designed for studying the crystallization/melt-quench processes in materials used in common PCM devices [30]. In the case of GST, the structure of the recrystallized region with small crystallites inside clearly differs from the surrounding crystalline matrix, indicating the role of nucleation. As for AIST, the recrystallized region is indistinguishable from the surrounding matrix, indicative of a growth driven process (see red circled areas in the TEM images shown in Figure 2.4.c for the two materials). It is important to note that nucleation/growth driven behavior is not solely dependent on the active material, as device structure, geometry and size of the active volume can have profound effects on thermodynamic conditions.

Similarly, the resistive switching phenomenon observable in SiO_x nanogap devices is the result of a change between different phases of a material. However, in SiO_x-based devices, phase change phenomenon is only one of the possible processes which can play significant roles in RS phenomena [32]. In an amorphous carbon/SiO_x/amorphous carbon (α-C) planar nanogap-type device illustrated in Figure 2.5.a [31] (which is similar to graphene/SiO_x/graphene nanogap devices I studied [O5]), in-situ high-resolution transmission electron microscopy (HRTEM) studies indicate the presence of a semi-metallic crystalline Si-III phase in the ON state, while the OFF state rather contains an amorphous, poorly conducting phase in the nanosized active region (see the pristine state of the device in Figure 2.5.b, and the ON/OFF states in Figure 2.5.c/Figure 2.5.d, respectively). Resistive switching characteristics of reset/set processes recorded between imaging of the ON and OFF states are displayed in Figure 2.5.e/Figure 2.5.f. The device exhibit $V_{\text{reset}} \approx 10$ V and $V_{\text{set}} \approx 5$ V switching voltages, similarly to our graphene/SiO_x/graphene nanogap devices. The observation of such distinct Si nanocrystals (confirmed also by Refs. 33, 34) suggest that nucleation might play an important role in the set process of SiO_x-based devices, which motivated my own studies (reported in Chapter 4). Scaling down the active region of phase change memories, along with better understanding of

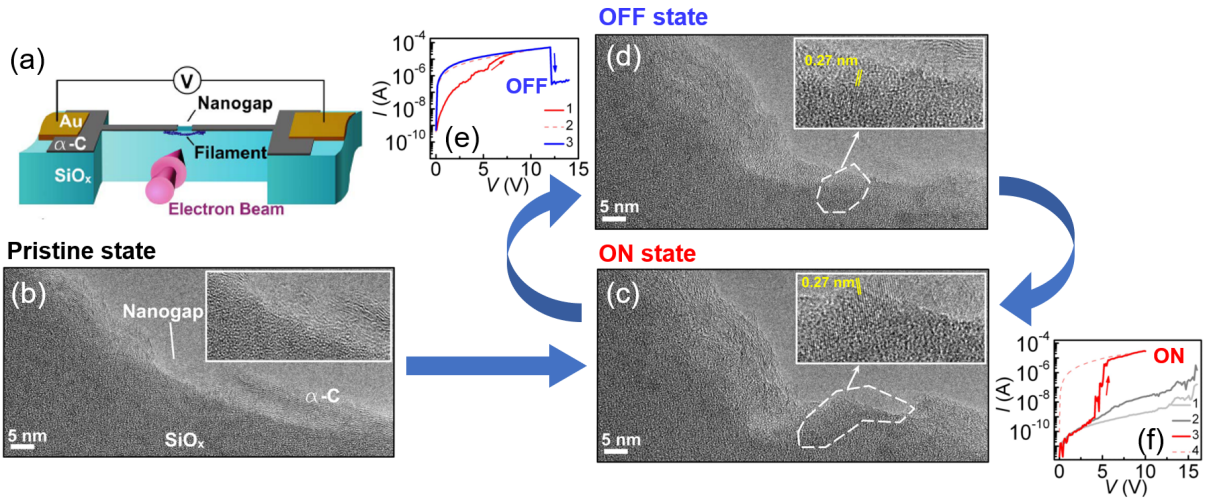

Figure 2.5: *In-situ TEM studies of a SiO_x nanogap device. (a) Illustration of the thin-walled α-C/SiO_x/α-C structure prepared for TEM imaging. In-situ TEM images of the device in its (b) pristine state (c) ON state and (d) OFF state. Insets show magnified images of the active region in each state, revealing amorphous structure in the pristine nanogap region, and different magnitudes of crystalline Si in the ON and OFF states, respectively (also marked by white dashed regions in panels (c) and (d)). Reset and set switching are realized with electrical signals according to the $I(V)$ characteristics depicted in panels (e) and (f), respectively. [31]*

nucleation/growth driven phenomena governing switching dynamics at such confined volumes can lead to improvements in device performance, via using knowledge from the field of material science to control nucleation and growth [35].

Formation procedure of nanogap graphene/SiO_x/graphene devices is illustrated in Figure 2.6.a, developed by my colleague László Pósa [32, 36]. Via a controlled electrobreakdown process of graphene nanostripes on top of a SiO_2 layer, a 2–3 nm wide gap separating graphene electrodes can be established. The electrobreakdown process consists of increasing amplitude voltage pulses, where the amplitude of subsequent pulses are ramped up in a stepwise manner. One can depict such an electrobreakdown process by displaying the current measured in each cycle as a function of the applied pulse amplitude, as shown in the $I_{\text{high}} - V_{\text{high}}$ traces in Figure 2.6.b. The first cycle of the process marked with red color is terminated when a relative decrease in the current is detected (signaling partial electrical breakdown of the graphene), and the cycle is started over again. The described feedback to the current is maintained along subsequent breakdown cycles (see black lines) to ensure control over the process. As the process progresses, current of each cycle decreases, until the complete breakdown of the graphene.

Afterwards, resistive switching can be initiated, which is usually carried out by applying slowly ramped triangular voltage signals with < 10 V amplitude to the nanogap. After

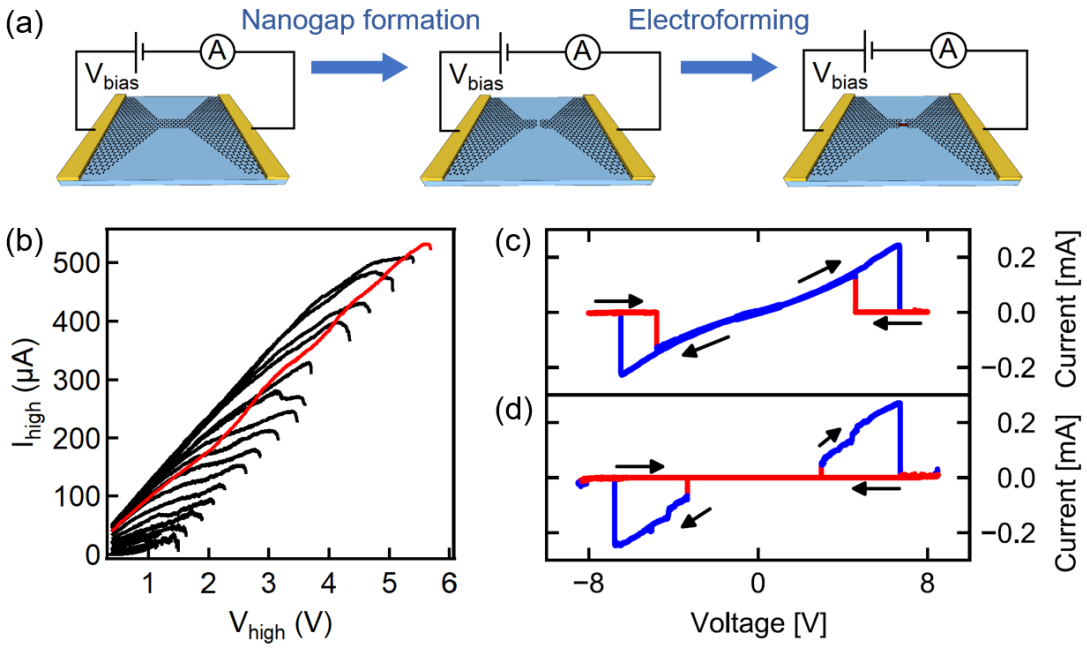

Figure 2.6: *Nanogap formation, electroforming and resistive switching in graphene/SiO_x/graphene devices, developed and studied by our group. (a) Illustration of nanogap formation and electroforming procedures. [32] (b) Controlled electrobreakdown procedure depicted as the evolution of current – voltage traces, measured during each voltage pulse of the process. First cycle is marked with red color. Amplitude of voltage pulses is increased in small steps, until a decrease in current is detected, which restarts the cycle (ensuring control over the breakdown). Continuous decrease in the current is observed in subsequent cycles (marked with black lines), until a complete breakdown of the graphene occurs. [32] (c,d) Typical I(V) characteristics of graphene/SiO_x/graphene devices. Different I(V) curves appear when the period of the triangular driving voltage signal is tuned compared to the dead time, τ_{dead}. The latter quantity describes the timespan for which the set process remains prohibited after a successful reset event. For the curve above, (c) the driving signal has a $T = 6$ s period ($T > \tau_{\mathrm{dead}}$), and for the bottom curve (d) $T = 1$ s ($T \approx \tau_{\mathrm{dead}}$). [O5]*

~ 50 unstable $I(V)$ characteristics (an electroforming process), RS stabilizes between well-defined ON and OFF states. However, there are different types of $I(V)$ characteristics observable at this stage due to the three characteristic timescales – set time (τ_{set}), reset time (τ_{reset}) and dead time (τ_{dead}) – characteristic of these devices. The τ_{set} and τ_{reset} parameters characterize the typical timescales of set and reset processes, while τ_{dead} is a special parameter defining the timescale of a device to remain in its OFF state after a reset event, irrespective of the driving conditions [36] (see studies of the three timescales later in Figure 2.7).

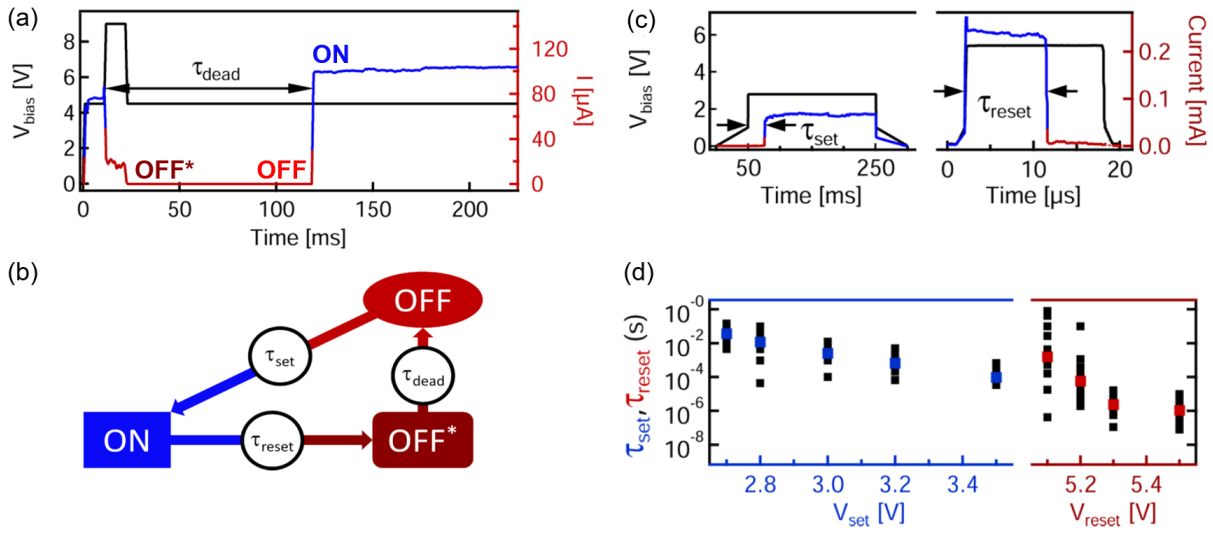

Figure 2.7: *Studies of characteristic timescales in graphene/SiO_x/graphene devices. (a) Typical scheme for a dead time measurement showing the applied pulse in black and the current response in red/blue (referring to OFF/ON states). (b) Illustration of the observed dead time rule: after a successful reset event, the device arrives at an OFF* state, in which the ON state cannot be programmed as long as the dead time has not passed. After τ_{dead} time, the OFF state is restored and the OFF→ON process becomes enabled. This effect enables programming either the ON and OFF states at zero bias by properly tuning the period of the driving voltage signal (see Figure 2.6.c,d previously). (c) Typical schemes for set time and dead time measurements. The effect of the black programming signal is delayed at both cases, by the characteristic τ_{set} and τ_{set} timescales of the device. (d) Both set and reset times are decreased upon increasing the amplitude of programming pulses, spanning many orders of magnitude. [36]*

Driving graphene/SiO_x/graphene devices with symmetric triangular voltage signals of different period (T) results in distinct $I(V)$ characteristics (see Figure 2.6.c-d.). When the driving period is large enough compared to the dead time ($T \gg \tau_{\mathrm{dead}}$) and the device is initialized in the ON state, the $I(V)$ curve is symmetric (as shown in Fig. 2.6.c). In this case, the initial ON state transitions to the OFF state at V_{reset}, but during the backward sweep, the device switches back to the ON state at a lower voltage (V_{set}). Consequently, the OFF state cannot be achieved at zero bias. If T is selected such that it is comparable to the dead time (more precisely, $\tau_{\mathrm{dead}} \lesssim T/2$), the set process can remain forbidden until the completion of the first half period, the device becomes stuck in the OFF state as the voltage is decreased, as shown in Figure 4.1.b. Therefore, through appropriate driving conditions, both the ON and OFF states can be programmed and maintained at zero bias.

For studying the τ_{set}, τ_{reset} and τ_{dead} characteristic timescales of graphene/SiO_x/graphene devices, the schemes shown in Figure 2.7 were employed in Ref. 36. To study the statistics of the dead time, pulses in the scheme of Figure 2.7.a were applied to a device (initialized in its ON state) in cycled measurements. First, the device was switched OFF with a larger pulse of 9 V amplitude (see black line), and then a smaller, constant voltage was applied, above the set threshold of the device. After τ_{dead} time passes, the set process is enabled, therefore the device switches ON (see the red/blue current response of the device colored according to /OFF/ON states). The observed dead time-rule is illustrated in Figure 2.7.b.

To study the timescale of the set and reset processes, similar pulse schemes were used, as shown in Figure 2.7.c (see black lines). Upon varying the amplitude of these set/reset pulses, τ_{set} and τ_{reset} can be tuned in a broad range, as the experimental data indicates in Figure 2.7.d. This observation served as a starting point for my studies of the set time distribution in SiO_x devices reported in Chapter 4.

2.1.2 OxRAM devices

Metal oxide-based resistive switching memrory devices operating via the migration of anions or cations of the inner nanoscale insulator layer, accompanied by redox reactions involving the electrode material or the insulator are often referred to as *OxRAM devices*. Some typical examples for the material of the active region are dielectrics such as tantalum oxide [41–44], niobium oxide [45–47], hafnium oxide [48], nickel oxide [49], titanium oxide [26, 50] or yttrium oxide [51]. The characteristics and physical mechanisms of resistive switching are especially sensitive to the stoichiometric composition of the inner material and the type of electrode materials as well, since these factors have direct influence on the possible redox reactions and the mobility of different ions. In most of OxRAM devices, the motion of oxygen ions (or positively charged vacancies) is thought of as the primary reason for resistive switching [4]. The formation of oxygen deficient regions causes a valence change of the metal cations, resulting in resistance change. Due to that aspect, the mechanism is also called *valence change mechanism (VCM)*. This mechanism can lead to either filamentary-type or interface-type resistive switching [52] as illustrated in Figure 2.8.a,b. The key difference between these types is that the interface-type mechanism leads to device area-dependent resistive switching (observable e.g. in the current), whereas the formation of filaments can confine the active region of the device to a much smaller volume, independent of the size of overlapping electrode area.

Exemplary filamentary/interface-type material systems and their resistive switching $I(V)$ characteristics are shown in Figure 2.8.c,d. Typical, bipolar RS characteristics of a filamentary Pt/TaO_x/Ta device are shown in Figure 2.8.c, which resemble the $I(V)$ characteristics of my own crosspoint Ta_2O_5 devices (see later in Section 3.2). The filamentary

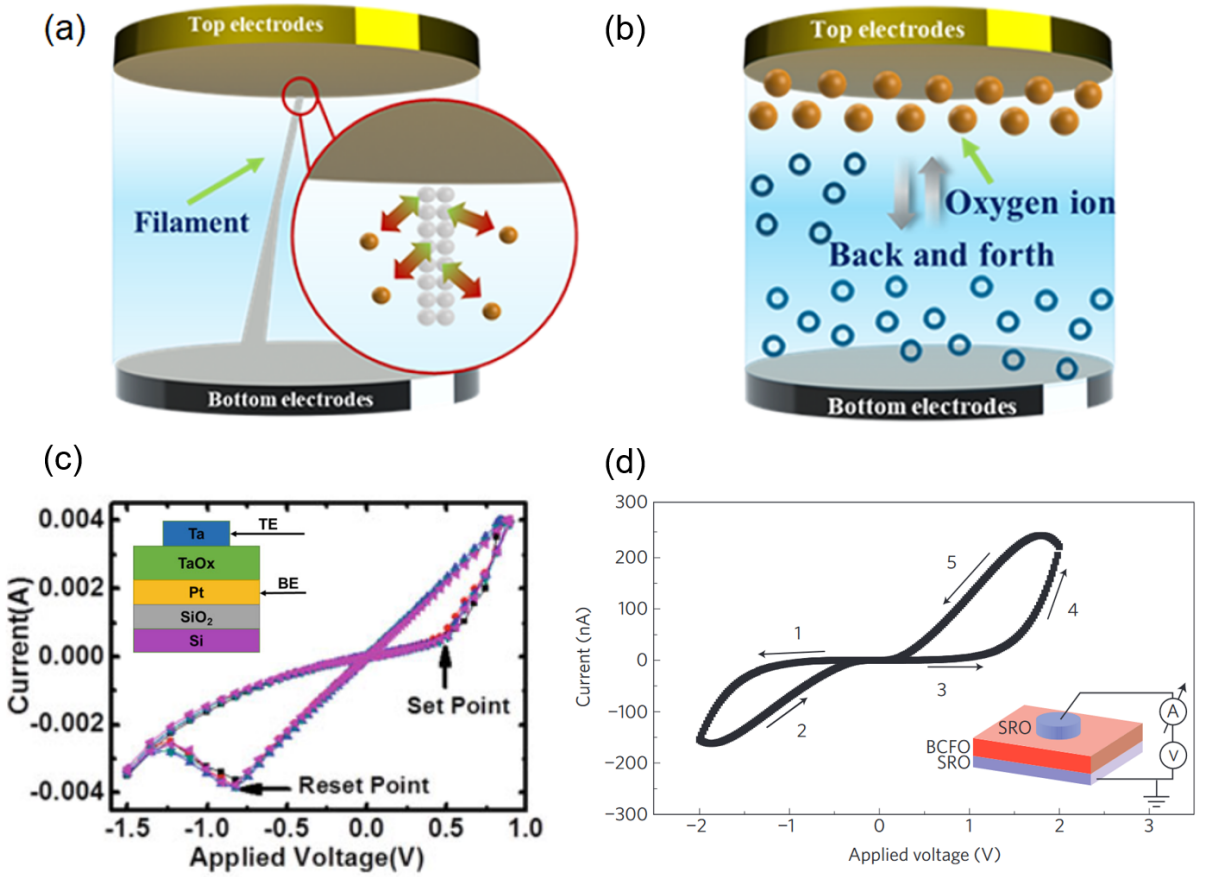

Figure 2.8: *Realization of resistive switching in VCM devices, illustrating (a) filamentary resistive switching, and (b) interface-type switching. [37] (c) Typical resistive switching $I(V)$ characteristics of a filamentary-type $Pt/TaO_x/Ta$ device (material stack shown in inset). [38] (d) RS $I(V)$ characteristics of an interface-type device made of $SrRuO_3/BiFeO_3/SrRuO_3$ (structure shown in inset). RS effect originates from the accumulation of oxygen vacancies at interfaces due to voltage sweeping. Note, that arrows indicate volatile, unipolar characteristics. [39, 40]*

nature of resistive switching in VCM devices is often studied by indirect measurements, e.g. studying the typical ON state current values among devices with different area. However, the formation of multiple filaments could lead to similar area scaling as interface-type RS mechanism. Direct imaging of nanoscale conductive filaments is possible with measurement techniques relying on transmission electron microscopy, scanning probe microscopy methods or X-ray-based spectromicroscopy [53, 54]. For example, TEM images taken in the ON state of TiO_2-based devices showed the appearance of a Magnéli phase (Ti_4O_7), and ∼10 nm scale filament widths. However, special sample preparation techniques (fabrication of 20 – 100 nm thin lamellae) needed for TEM imaging can influence device operation in such experiments [55].

Interface-type valence change mechanism is governed by the accumulation of oxygen vacancies near electrode surfaces [40]. These can either be mobile species in the active region or localized along the interface; the latter is usually facilitated by an additional layer serving as a buffer/reservoir for oxygen vacancies. The role of vacancies is the trapping/de-trapping of electron charges in the RS process. Figure 2.8.d shows an example for interface-type switching, the operation of a $SrRuO_3/BiFeO_3/SrRuO_3$ device. In this case, the reversible redistribution of oxygen vacancies along interfaces shape RS characteristics, yielding unipolar and volatile operation – at the timescale of the $I(V)$ measurement. This example system encompasses some typical traits characteristic of filament-free devices [56]: limited retention time (the timescale at which constant resistance is preserved when voltage is released), slow switching speed and low operating current. The latter is advantageous, while the former two general traits hinder applications of interface-type devices in analog crossbar arrays. However, retention time can be improved, as reported for multilayer $Pt/Ta_2O_5/Nb_2O_{5-x}/Al_2O_{3-y}/Ti$ charge trap devices in a recent study [57].

Time and voltage-dependent, rich resistive switching dynamical properties of OxRAM devices offer prospects to carry out elaborate signal processing tasks at the analog domain, using only one or a small number of devices. Besides, these unique dynamical properties are observable up to the picosecond timescale, as shown by Miklós Csontos in a recent study [44] using a high bandwidth measurement setup. Dynamical properties of $Pt/Ta_2O_5/Ta/Pt$ devices developed for high time-resolution electrical studies are shown in Figure 2.9.a-c. Devices exhibit the usual $I(V)$ curve, characteristic of filamentary Ta_2O_5 OxRAM devices, as exemplified by measurements at low drive voltage signal frequency of 1 Hz and 2 V amplitude (see Fig. 2.9.a). Increasing the drive amplitude to 3 V in an ultra-fast pulsed measurement with 20 ps FWHM (full width at half maximum) pulse length (see black curve in Figure 2.9.b), set process is observed and completed approximately during the rising time of the pulse. The observation relies on the analysis of the transmitted voltage signal during the set process (see blue curve in Figure 2.9.b), compared to reference measurements in the high resistance state (see red curve in Figure 2.9.b) and low resistance state of the device.

Switching dynamics of OxRAM devices can be characterized by the drive voltage amplitude and pulse length needed for achieving resistance change with a targeted $R_{\mathrm{OFF}}/R_{\mathrm{ON}}$ ratio. For the discussed Ta_2O_5 devices, ultra-fast measurements yielded the tendency shown in Figure 2.9.c, where datapoints show the pulse width dependence of the lowest set voltage amplitude which induces resistive switching. The tendency indicated by this measurement is rather general for memristive material systems extending many orders of magnitude in time, and it is not exclusively limited to OxRAM devices operating via VCM. Different classes of memristors, where operation is governed by cation motion

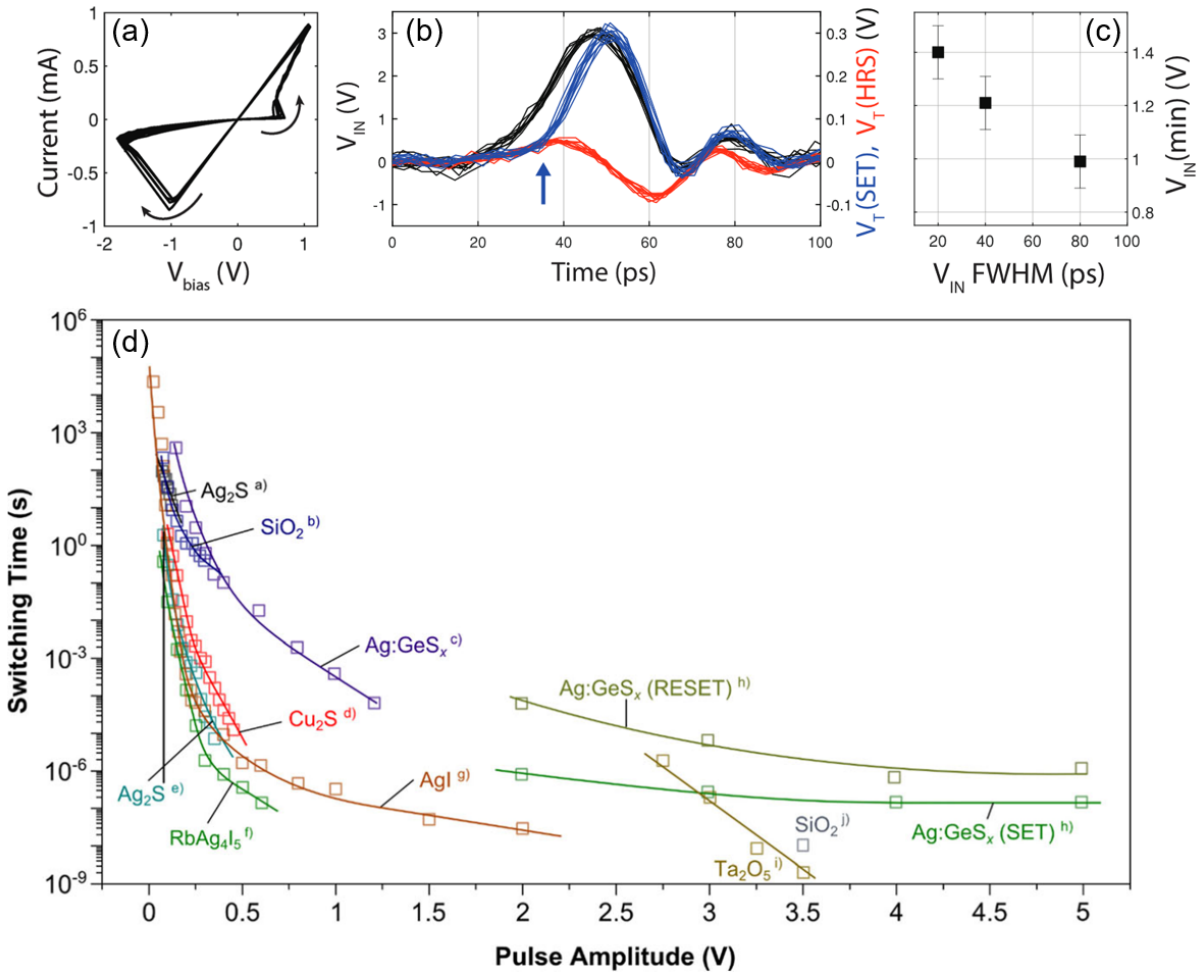

Figure 2.9: *Studies of switching dynamics of filamentary memristors up to the picosecond timescale. (a-c) High time-resolution electrical studies of $Pt/Ta_2O_5/Ta/Pt$ devices, ahowing (a) DC $I(V)$ characteristics at 1 Hz drive frequency and 2 V drive amplitude, (b) ultra-fast set process observed at the 20 ps timescale, and (c) pulse width dependence of the minimum set voltage amplitude needed for inducing resistive switching. [44] (d) Overview of switching dynamics of cation-based CBRAM devices, where different colors and legends indicate the material of the surrounding matrix in which metallic filaments are formed as a result of cation motion. [58]*

and electrochemical processes instead of oxygen vacancy migration – often referred to as CBRAM (conductive bridging random access memory) devices or ECM (electrochemical metallization) cells – also exhibit similar scaling [58, 59]. An overview of dynamical properties of various CBRAM systems (see Figure 2.9.d) illustrate a strong non-linar scaling, e.g., the time needed for resistive switching decrease by many orders of magnitude when driving pulse amplitude is increased in the ~ 1 V regime at a linear scale.

In principle, filament diameters in OxRAM devices can be much smaller than the $\sim$10 – 100 nm scale often indicated by TEM studies [53, 55]. Confining resistive switch-

ing at the ultimate smallest, single-atom dimensions, and the in-situ imaging of such atomic-scale filaments in a non-destructive manner would be a rather challenging objective. An indication of atomic switching was reported for silver-based filamentary devices earlier [60], however, the lack of reliable experimental tools for the direct observation of atomic-scale processes/filaments motivated my efforts to work out a method for investigating these phenomena in OxRAM devices. Results of these studies are reported in Chapter 5.

2.1.3 Mott memories

Mott transition (insulator-metal/metal-insulator transition, IMT/MIT) is a versatile phenomenon arising from a change in localized/delocalized nature of valence electrons in a material (a Mott insulator), resulting in a change of the band structure of the material [61–64]. The pristine, insulating state of a Mott material is unexpected from the viewpoint of classical band theory (see first panel of Figure 2.10.e). In this approach, Mott materials would yield a narrow, half-filled band around the Fermi energy (e.g. certain transition metal oxides with partially filled $3d$, $4d$, or $4f$ orbitals). Taking into account electron correlations, a bandgap is introduced, leading to an insulating state. The electron-electron interaction in question is the Coulomb repulsion between electrons (U), which competes with the kinetic energy of electrons (t), shaping the band structure of Mott insulators. For $t < U$, delocalization is inhibited (see Figure 2.10.a), which yields one empty and one filled band in the band picture (see second panel of Figure 2.10.e).

Principally, a transition to the metallic state can be induced in two ways, by the variation of t or via changing the effective U between electrons. Compressing the lattice decreases the lattice constant and increases the W bandwidth, resulting in bandwidth-controlled IMT (see Figure 2.10.b). The other way is to reduce energy cost for electron hopping via electron/hole doping which leads to a decreased effective U, called as filling-controlled IMT (see Figure 2.10.c,d). In some cases both mechanisms may be involved, e.g. in certain temperature-induced transitions. Right panels of Figure 2.10.e illustrate the development of band structure during bandwidth-controlled IMT and filling-controlled IMT.

Mott transition can be induced with thermal, electrical, optical and even mechanical excitations (see Figure 2.10.f). Generally, the system (initially in its insulating state) undergoes a sharp phase transition when the external excitation surpasses a specific threshold, resulting in a significant drop in resistivity by several orders of magnitude. Upon removal of the external excitation, the system returns to the insulating phase in a hysteretic process. The intermediate state between insulator and metallic phases involves the coexistence of both phases, typically indicated by a smooth change in resistivity in response to the external excitation. Abrupt transitions without phase coexistence may

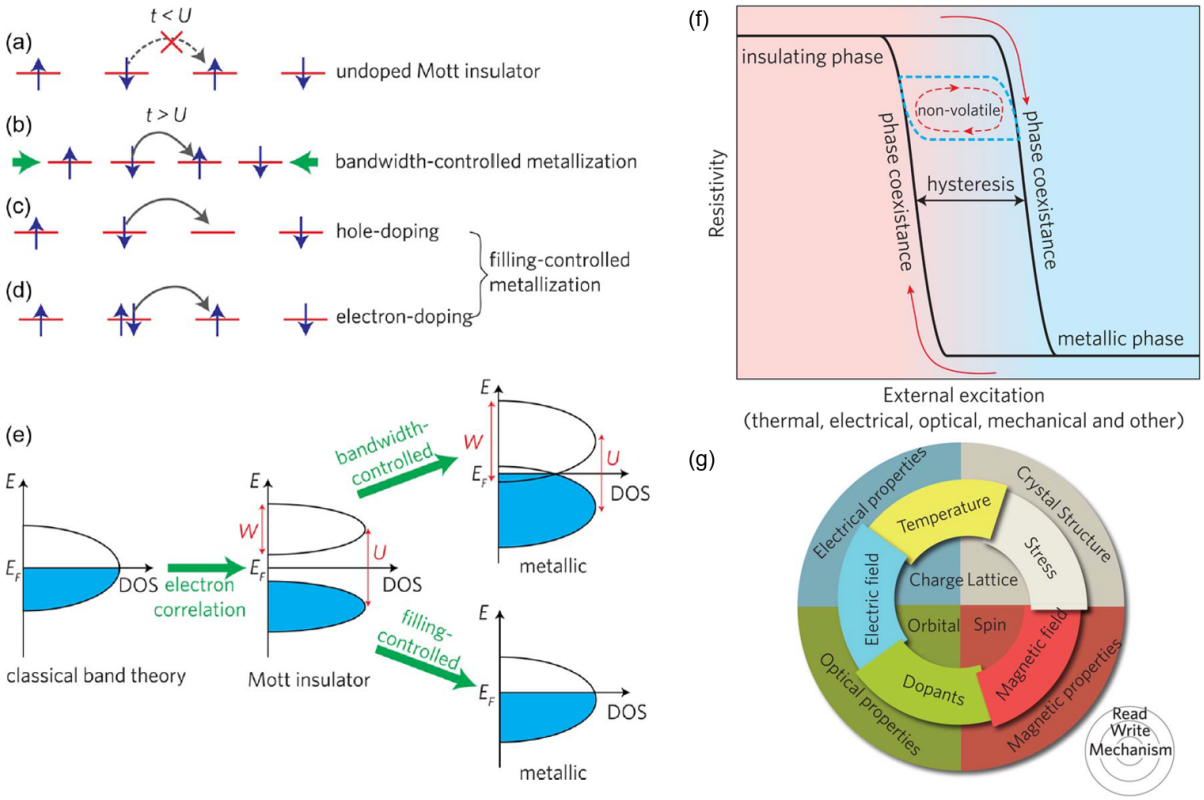

Figure 2.10: *Illustration of versatile mechanisms and traits of Mott transition, showing (a-d) inhibited/possible electron hopping processes and the (e) corresponding schemes of band structures in the insulating phase and metallic phases of the material. (f) Generalized hysteresis curve of resistivity in Mott insulators. (g) An illustration referring to various physical mechanisms (inner circle) and physical properties (outer circle) coupled to each other in a Mott insulator. The middle ring shows different ways to trigger IMT. [62]*

be observable in cases where the size of the system is smaller than the size of domains during phase transition. Not only the external excitations to trigger Mott transition are diverse; the transition can lead to changes in many physical properties, such as the crystal structure, electrical, magnetic or optical properties of the material, through coupling between inner mechanisms. This versatility pictured in Figure 2.10.g can introduce new functionalities to devices utilizing Mott materials.

The aspects off Mott transition in VO_2 are widely studied, motivated by the material's relatively low, $T_c^{\text{Mott}} \approx 340$ K transition temperature (facilitating applications), and also by the fact that IMT can be triggered via temperature, strain, pressure, chemical doping, intense optical or electrostatic fields in this material [63]. Usually, IMT in these devices is accompanied by a structural transition from an insulating monoclinic phase to the metallic tetragonal rutile phase.

One interesting aspect of the IMT in VO_2 involves experimental studies of the speed of transition [64]. For example, in experiments with optically triggered IMT, a change in reflectivity [65] or electron diffraction patterns [66] are observable at the ∼100 fs timescale. Electrically triggered transitions were observed at a slower, ∼2 ns timescale in another study involving VO_2 switches [67]. The limitations for the speed of electrically triggered IMT in Mott memristors are less understood [66], so I recently started the development of VO_2 devices suitable for electrical studies in the RF domain (radio frequency domain, ≈ 20 kHz – 300 GHz), placed in a co-planar waveguide patterned with electron beam lithography. Development steps of these samples are reported in the end of Chapter 3.

The properties of Mott memristor devices can be affected by the structure and thickness of the VO_2 thin layer used for creating the device, and even by the material or crystal structure of the substrate. Figure 2.11 illustrates these effects through some examples from the literature [68], where the resistivity – temperature ($\rho - T$) dependencies of VO_2 layers with different thicknesses and/or substrates were studied. In Figure 2.11.a, $\rho - T$ dependencies of sputtered VO_2 layers on top of different substrates are compared. Films 1, 2 and 3 correspond to Si(nat.ox.)/VO_2(70 nm), Si(nat.ox.)/VO_2(130 nm) and Al_2O_3/VO_2(120 nm) structures (shown with purple, black and green lines, respectively). The films also have similar granular structures visible in their SEM images in Figure 2.11.b. Film 3 exhibits the largest resistivity change during the temperature sweep, possibly caused by a smaller lattice mismatch at the Al_2O_3/VO_2 interface.

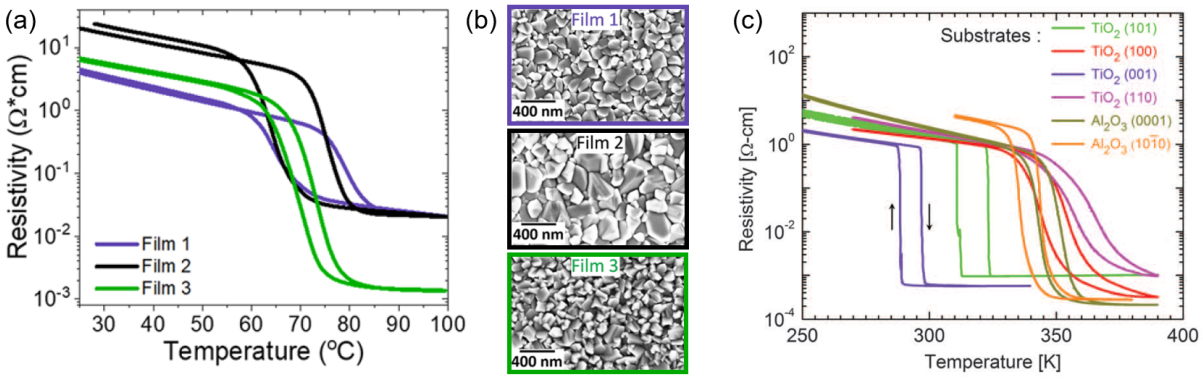

Figure 2.11: *Effects of structure, thickness and the type of substrate material on temperature-triggered Mott transition in VO_2 thin films. (a) Temperature dependent resistivity curves of sputtered VO_2 layers. Films 1, 2 and 3 correspond to Si(nat.ox.)/VO_2(70 nm), Si(nat.ox.)/VO_2(130 nm) and Al_2O_3/VO_2(120 nm) thin film structures. (b) SEM images of the films studied in panel (a). [68] (c) $\rho - T$ curves of VO_2 films deposited on different facets of TiO_2 and Al_2O_3 single crystal substrates (see color-coded legend) via pulsed laser deposition technique. [69]*

Figure 2.11.c displays resistivity – temperature curves for VO_2 films deposited via pulsed laser deposition technique on different facets of TiO_2 and Al_2O_3 single crystal substrates (with varying thicknesses of 7–20 nm). These layers exhibit markedly different transition temperatures as the result of different strains in VO_2 thin films. For example, the 10 nm thick VO_2 layer on TiO_2 (001) is strained by –1.2%, with a critical temperature of $T_c^{\mathrm{Mott}} \sim 290$ K for Mott transition (see purple trace in Figure 2.11.c). In contrast, the 20 nm thick VO_2 film on Al_2O_3 (1010) is completely relaxed, $T_c^{\mathrm{Mott}} \sim 340$ K (see orange trace in Figure 2.11.c).

Fabrication steps of the VO_2 nanogap memristive devices developed by our group are illustrated in Figure 2.12.a [O3]. First, a 100 nm thick vanadium is deposited on a $Si/SiO_2(1\ \mu m)$ substrate. Then, thermal oxidation of the vanadium layer (carried out in a tube furnace at 400 °C for 4.5 h under 0.1 mbar sparse air) results in a V_2O_5/VO_2 structure. Finally, Au electrodes are deposited in patterns created with electron beam lithography, resulting in a planar-type device, as shown in Figure 2.12.b (also illustrating local temperature in the nanogap region during switching, as captured with finite element simulations). These nanogap devices yield temperature-dependent resistivity curves with pronounced phase transition and hysteresis displayed in Figure 2.12.c, similarly to VO_2 thin films (see previously in Figure 2.11). The phase transition closely accompanied by a drastic change in resistance can be induced by electrical signals also, which is observable in driving voltage-dependent characteristics of a VO_2 nanogap device shown in Figure 2.12.d. In this case, Joule heating of the junction facilitates the set process, but also the effect of the electric field has to be considered for a full explanation of RS characteristics. Temperature-dependent resistivity curves of the device recorded before and after electrical studies (see black and blue curves in Figure 2.12.c, respectively) show a small difference, with the transition becoming more abrupt after electrical studies. The observed steepness can arise from the small size of the device [62], with its ≈ 30 nm-sized gap region.

The structure of vanadium oxide layer is V_2O_5(170–190 nm)/VO_2(30–50 nm). The chemical composition of layers and their thicknesses were analyzed with transmission electron microscopy and electron energy loss spectroscopy (EELS). TEM image of the oxide film is shown in the inset of Figure 2.12.e, whereas EELS spectra corresponding to the top and bottom layers are shown in Figure 2.12.e, indicating chemical compositions of VO_2 (red spectrum) and V_2O_5 (blue spectrum).

Temperature dependent electrical transport measurements were carried out by my colleagues on these nanogap VO_2 devices. $R(V)$ curves computed from these measurements are well fitted with a combined electronic and thermal simulation, constructed in a finite element simulation software (COMSOL Multiphysics), employing realistic composition, physical parameters and geometry of the studied devices. Moreover, a purely thermal or

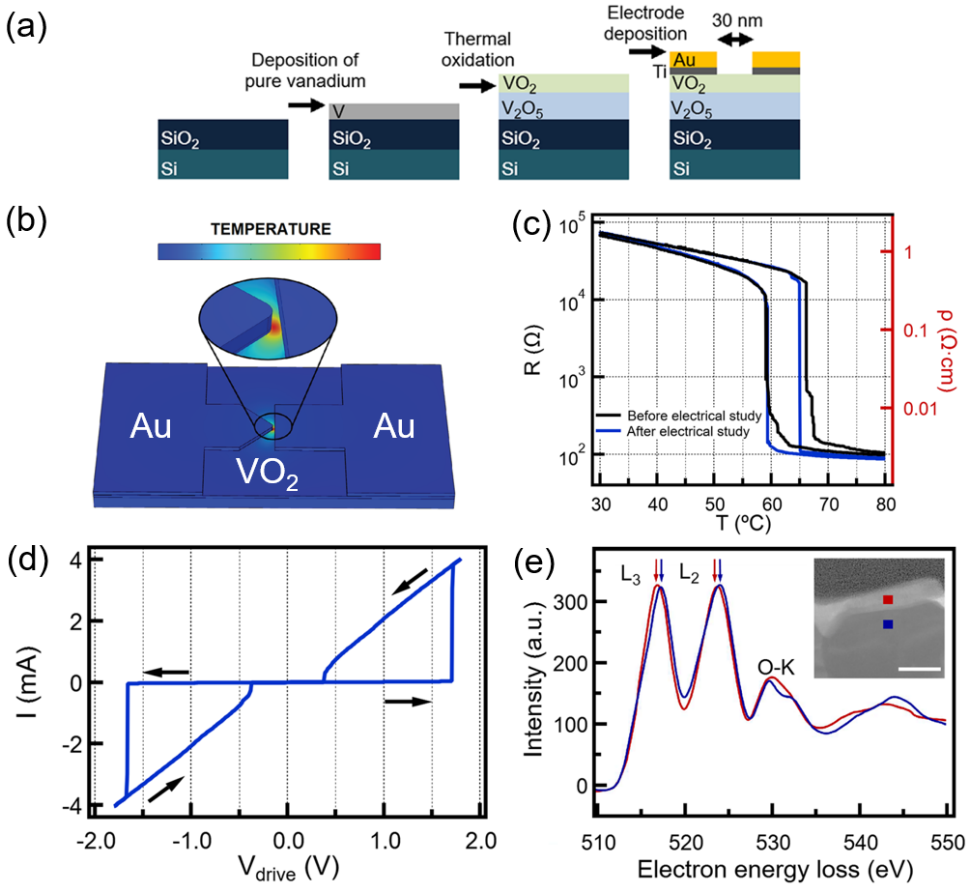

Figure 2.12: *General characteristics of VO_2 nanogap memristors developed by our group. (a) Deposition steps of the devices illustrated schematically. (b) Structure of the planar-type device, also illustrating the local temperature in the device, as captured with finite element simulations. (c) Resistance – temperature dependence of a device before (black lines) and after (blue lines) electrical studies, exhibiting drastic resistance change with hysteresis, indicative of Mott phase transition. Right axis shows the resistivity calculated from the device geometry, using finite element simulations for determining the scaling factor between the resistance and resistivity. (d) Typical driving voltage-dependent RS $I(V)$ characteristics of VO_2 nanogap devices. Joule heating of the junction facilitates the set process, but high electric field in the nanoscale junction area also affects the resistance change process. (e) EELS spectra recorded at the top (red line) and bottom (blue line) layers identified by cross-sectional TEM imaging (shown in the inset, with corresponding colors). [O3]*

purely electronic model fails to describe these characteristics, which indicate an interplay of thermal and electronic effects shaping the operation of VO_2 nanogap devices.

Motivated by the above studies, I varied different fabrication methods to further optimize VO_2 nanogap devices for different purposes, relying on different kinds of measure-

ment techniques ($R(T)$ and $I(V)$ characterisation, noise spectroscopy measurements). I also fabricated devices with different gap sizes, and studied the effect of the gap size on the RS characteristics [O3]. I have also been involved in the development of vanadium oxide-based devices optimized for high frequency operation, using a co-planar waveguide geometry design, inspired by the work of Miklós Csontos (see Figure 2.9.a-c earlier) [44]. My contributions to the development of VO_2 devices are discussed in Section 3.3.

2.2 Applications and architectures

Emerging computing paradigms and applications (e.g. artificial intelligence, neuromorphic computing, autonomous systems, smart sensing or edge computing) introduce increasingly higher demands for performance and energy-efficiency on hardware architectures [1]. As an alternative for conventional CMOS-based technologies, architectures based on resistive switching devices are presented in this Section.

Artificial neural networks in a nutshell To introduce these topics, I provide a brief overview for the terminology and basic concepts of artificial neural networks. Note, that the following description is rather general and might not accurately describe some specific types of networks.

A neural network can be thought of as a graph where nodes are connected to each other as depicted in Figure 2.13.a, where a single *layer* is emphasized. During standard operation, the incoming information at each node travels along the edges. At full connectivity, these edges can be thought of nonzero matrix elements (see illustration and color coding of 2.13.b). A single layer performs a vector-matrix product of the incoming vector.

Larger networks usually consist of multiple layers, where the propagation of information during computing is called *inference*. Usually, input data is presented at the first layer in some form, whereas the last layer yields the result of e.g. a classification task. Layers in the middle are referred to as *hidden layers*. To perform some kind of operation, *training* is also required, which means the proper setting of the matrix elements (the *synaptic weights*) of the network. This training can be performed before the computation or *in-situ*.

The above concept is rather general, applicable to many problems, where vector-matrix operations are the essence of computation, such as classification tasks with large networks, image recognition (where filters can be encoded as matrices), convolution or certain optimization tasks, where the problem can be encoded in the elements of a matrix

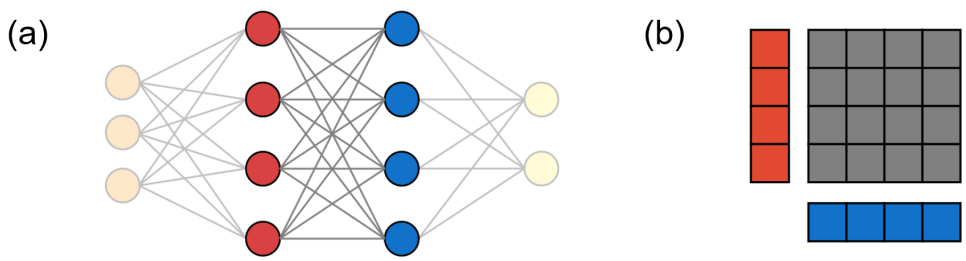

Figure 2.13: *Illustration of general concepts behind artificial neural network operation. (a) Generalized topology of a network. (b) Illustration of a vector-matrix operation performed by a single layer.*

(e.g. Hopfield neural networks). A key aspect which connects several types of artificial neural networks is that they can be used to process information in the *analog domain*, rather than utilizing digital encoding of the information.

2.2.1 Neural network on an analog crossbar chip

Analog memory arrays have the capability to execute parallel vector-matrix operations by directly processing analog data at each memory element. In contrast, digital systems require individual access to each memory cell and the transfer of data to a separate computation unit, resulting in higher energy consumption and longer latencies in general.

Such analog in-memory computing can be realized with memristive elements in a crossbar architecture, as demonstrated in Ref. 70. In this work, a 12 × 12 crossbar array of Al_2O_3/TiO_{2-x} memristors (see Figure 2.14.a) was developed for the demonstration of a classification task with memristive hardware. Typical RS characteristics of these devices are shown in Figure 2.14.b.

The constructed memristive crossbar was utilized to create a simple single-layer neural network (perceptron) with ten inputs and three outputs, establishing full connectivity with a total of 30 synaptic weights (see Figure 2.15.a). The vector-matrix products are calculated in a single step, encoding synaptic weights in the $G^+_{i,j}$ and $G^-_{i,j}$ conductance values of differential pairs of memristors (see Figure 2.15.b):

$$I_i = \sum_{j=1}^{10} W_{i,j} \cdot V_j = (G^+_{i,j} - G^-_{i,j}) \cdot V_j.$$

Here, V_j for $j = 1, ..., 9$ are the input signals, V_{10} is a constant bias, $W_{i,j}$ are the (trainable) synaptic weights and $I_i = I^+_i - I^-_i$ is the product vector. This approach using differential

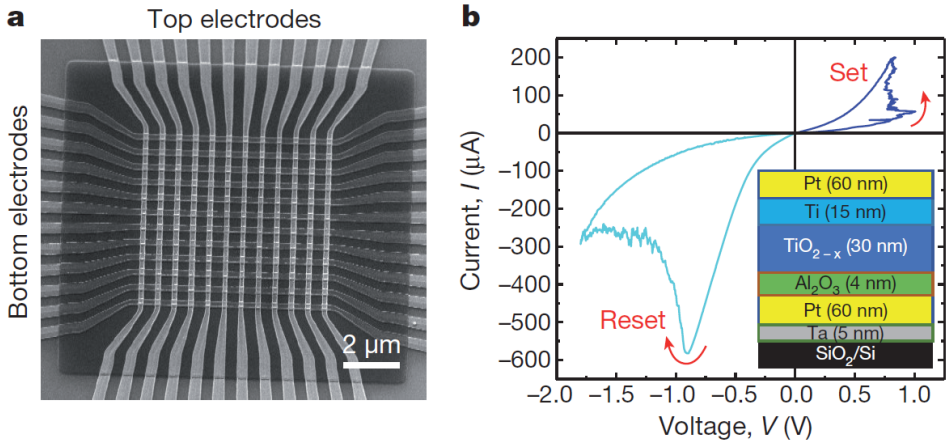

Figure 2.14: *Integrated, 12 × 12 crossbar of OxRAM devices. (a) SEM image of the crossbar unit with Al_2O_3/TiO_{2-x} memristors at each crosspoint. (b) Typical RS $I(V)$ curve of a memristor, with the inset showing material stack of the device. [70]*

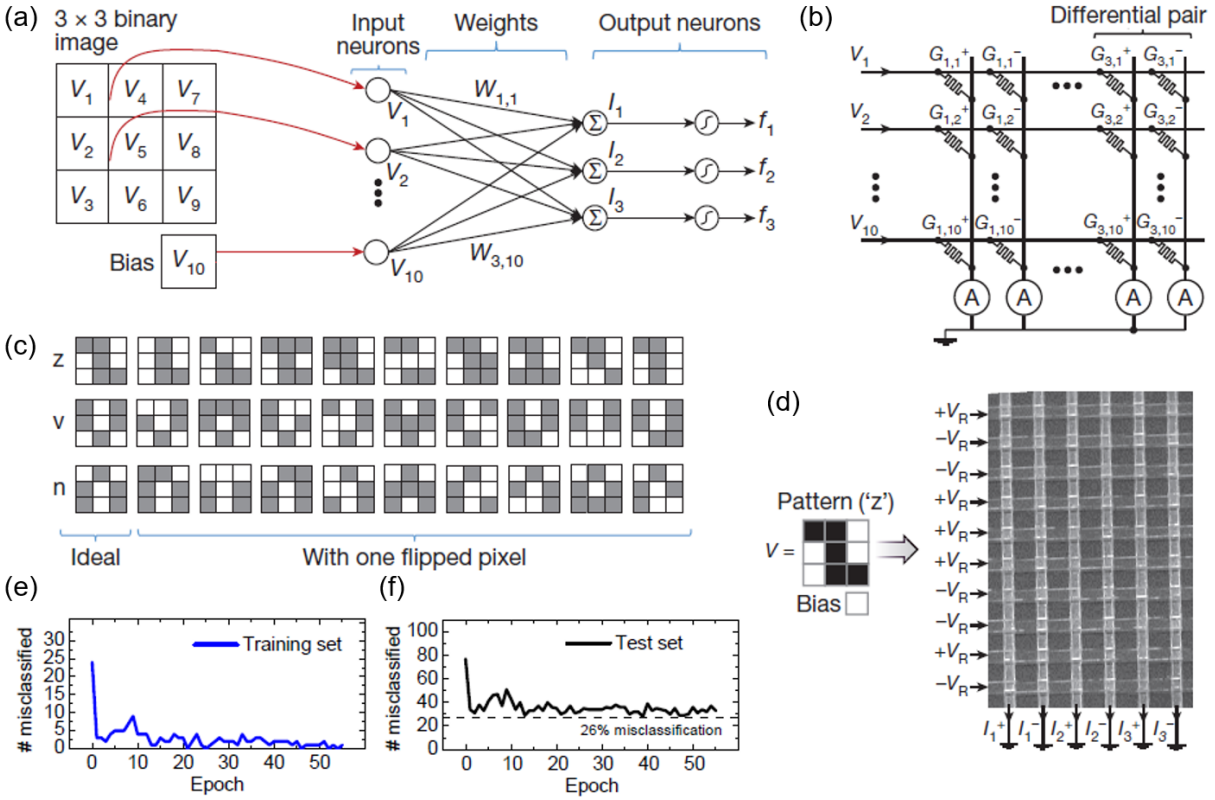

Figure 2.15: *Perceptron on an analog crossbar chip. (a) Illustration of the operation of the fully connected single-layer neural network. (b) Circuit schematic showing differential pairs of memristors in a matrix. (c) Training dataset of 3 × 3 images of three classes, 'z', 'v', and 'n'. (d) Network inference illustrated (using a segment of the crossbar). Classification convergence (e) for the training set shown in panel (c), and (f) for a test set generated via flipping 2 random pixels of the original images. [70]*

pairs of memristors with positive $G^+_{i,j}$ and $G^-_{i,j}$ conductance values is necessary for the device-level encoding of negative $W_{i,j}$ synaptic weights, which are common in artificial neural networks. Note, that the above equation yields the essence for hardware-level analog crossbar accelerators for neural network operation, since the vector-matrix product is calculated in the analog domain, in a single step. In contrast to that, a digital, transistor-based architecture computes the same product broken down into elementary sums and multiplications using logical gates, which can be a computationally intensive operation for large matrices.

The perceptron's outputs (f_i, with $i = 1, 2, 3$) are calculated as the following (nonlinear activation function):

$$f_i = \tanh(\beta I_i),$$

where β is a parameter controlling nonlinearity of the function.

The operation of memristive crossbars is usually affected by the sneak path current problem, referring to electrical currents that may flow through unintended pathways during the read operation of individual devices (necessary e.g. to validate the programming of synaptic weights to the array). These sneak currents occur at alternative paths between the addressed electrode line pair of a device, leading to inaccurate readout of the resistance of the addressed device. This effect is usually resolved via using a selector device (e.g. a transistor) next to each memristive element, but sneak currents can be reduced via using memristors with nonlinear $I(V)$ characteristics as well, similarly to the Al_2O_3/TiO_{2-x} devices used in the discussed study (see Figure 2.14.b).

This network is capable of classifying 3×3 black-and-white (binary) images into three classes, where the nine network inputs $(V_1, ..., V_9)$ represent pixel values. The network was evaluated on a dataset of 30 patterns, comprising stylized letters ('z', 'v', and 'n'), along with three sets of nine noisy variations for each letter created by flipping one pixel in the original image (see Figure 2.15.c). The network was trained *in-situ*, in a supervised fashion, using the Manhattan rule [71]. Except for vector-matrix operations and weight updates which were performed at the hardware level, all the other steps during network inference (e.g. the activation function) were carried out using external electronics (software level).

Figure 2.15.d shows an example for the operation of the network, using a 10×6 segment of the crossbar array for the realization of synaptic weights. Using the training set shown in Figure 2.15.c, the number of misclassified patterns decreases to 0 after $\sim$20 epochs (see Figure 2.15.e). In comparison, for a test set generated by randomly flipping 2 pixels of the original image, the number of misclassified patterns saturates at 26% rate (see Figure 2.15.f). It is to be noted, however, that this test set includes so distorted images that even a human would hardly classify.

The above example from 2015 was one of the first proof-of-concept demonstrations of the capability of a memristive crossbar array for pattern classification via analog computing. In the following, I present some more recent examples of the applications of large-scale memristive arrays as hardware accelerators for neural networks.

2.2.2 Large-scale integrated networks for accelerating AI

Wafer-level production of large-scale integrated memristors was reported in Ref. 72 in 2018 (Figure 2.16.a–e shows the scaling of the integrated memristor array from wafer scale down to the nanometer scale). In this study, a multilayer neural network was implemented in a 128×64 memristor array, consisting of $Ta/HfO_2/Pt$ devices. On-chip series transistors were used to address each memristors individually during training (resolving sneak path problem mentioned in the previous Subsection). A dedicated conductance programming scheme was also utilized to achieve linear and symmetric conductance tuning.

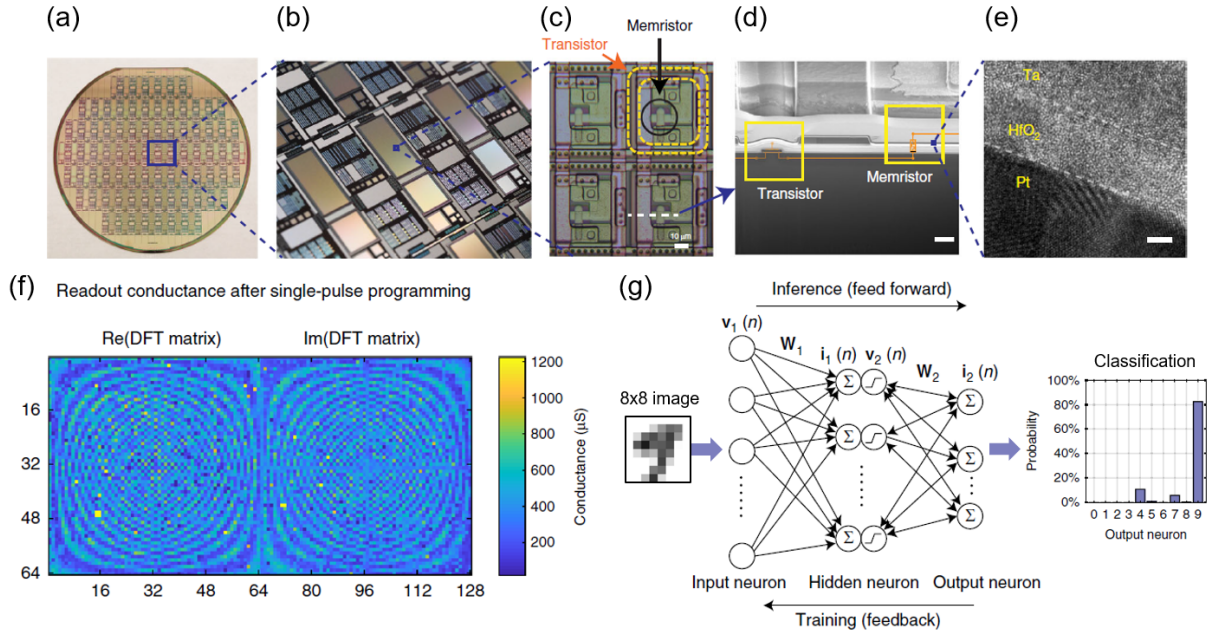

Figure 2.16: *Memristive platform for handwritten number recognition. (a) Photo of a 6-inch wafer with transistor arrays. (b) Zoomed-in image showing arrays of different sizes. (c) One transistor–one memristor (1T1R) structure of a unit. Microscope image, scalebar: 10 μm. (d) Cross-sectional SEM image of a 1T1R cell, cut by a focused ion beam along the dashed line in (c), scalebar: 2 μm. (e) Cross-sectional TEM image of the Ta/HfO_2/Pt memristor. Scalebar: 2 nm. (f) Conductance of a 128 × 64 array after the analog programming of the matrix of a DFT filter (several devices are stuck, shown in yellow). (g) Structure and operation illustrated for the hardware-encoded two-layer neural network used for handwritten digit classification. [72]*

This was carried out by voltage pulses applied to the memristor, and to the gate electrode of the its transistor simultaneously, providing a convenient way to set a current limit during conductance programming. Figure 2.16.f illustrates the efficiency of the approach, showing the matrix of a DFT (discrete Fourier transformation) filter programmed to the 128 × 64 memristor array, using only two electrical pulses to program each memristor. Only a few stuck devices are visible (see yellow pixels in the image plot of Figure 2.16.f).

A two-layer neural network (shown in Figure 2.16.g) was implemented using the memristor crossbar array. The network consisted of 64 input neurons, 54 hidden neurons, and 10 output neurons, using 7992 memristors altogether (differential pairs were employed to encode negative weights as in the previous Subsection). The classification of handwritten numbers from the Modified National Institute of Standards and Technology (MNIST) [73] database was carried out. Input images were rescaled to 8x8 pixel size to match the size of the network (see Figure 2.16.g), resulting in 64-dimensional input vectors with analog elements encoding intensities of each pixel of the grayscale images. A backpropagation

algorithm was utilized for training, and the desired weight updates were calculated at the software level. Similarly to the previous study reported in Subsection 2.2.1, the vector-matrix operations and the weight updates were performed at the hardware level (which are key aspects for the targeted acceleration of neural networks). For training of the network, 80000 images of the database were used. Afterwards, the network correctly classified 91.71% of the 10000 images from a separate test dataset.

In the past years, large-scale hardware architectures were introduced targeting versatile artificial neural network applications via in-memory computing with memristor-based integrated chips [74–78]. These chips utilize either OxRAM or PCM devices to encode millions of synapic weights and accelerate different neural network operations in the analog domain. An example for such an architecture from Ref. 76 is illustrated in Figure 2.17. The chip called *NeuRRAM* consists of 48 individual cores, reconfigurable for specific AI tasks, and also enabling parallel computations (different mapping of neural network models to the cores are indicated by colors in Figure 2.17.a). Each core contains a TNSA (transposable neurosynaptic array) made up of 256 × 256 RRAM devices and 256 CMOS neuron circuits (see Figure 2.17.b), which implement analog-to-digital converters (ADCs) and activation functions. Peripheral circuits along the edge are also included, which provide the control for network inference and also manage programming of RRAM devices. A cross-sectional TEM image showing the integration of memristors and access transistors is shown in Figure 2.17.c. Memristors are fabricated between M4 and M5 metallic layers, consisting of TiN/HfO_x/TaO_x/TiN stacks. These devices operate via a filamentary mechanism originating from the HfO_x switching layer, while the role of the TaO_x layer is to enable linear conductance tuning during set and reset processes, via an electro-thermal coupling method [79].

An important advantage of the NeuRRAM chip compared to other approaches is a close integration of ADCs with RRAM devices in the corelets of the TNSA array, as shown in Figure 2.17.e,f. These 16 × 16 units of RRAM devices and CMOS neuron circuits are connected along the length of both rows and columns. In this manner, bidirectional pass gates are realized, allowing for reconfigurable dataflow in both directions. This approach yields higher energy-efficiency compared to other in-memory computing chips employing memristors [78].

The performance of the NeuRRAM chip was tested on various AI benchmark tasks. Classification accuracies of 99.0% and 85.7% were reported (for classifying images of handwritten numbers) for the MNIST dataset [73] and the CIFAR-10 dataset [80], respectively. A 84.7% accuracy was demonstrated for Google speech command recognition [81], and a 70% reduction in image-reconstruction error was also reported on an image-recovery task. The 159 mm^2 area chip can be operated with 2, 4 or 8-bit precision, and shows comparable energy efficiency to some state-of-the-art digital CMOS AI inference accelerators

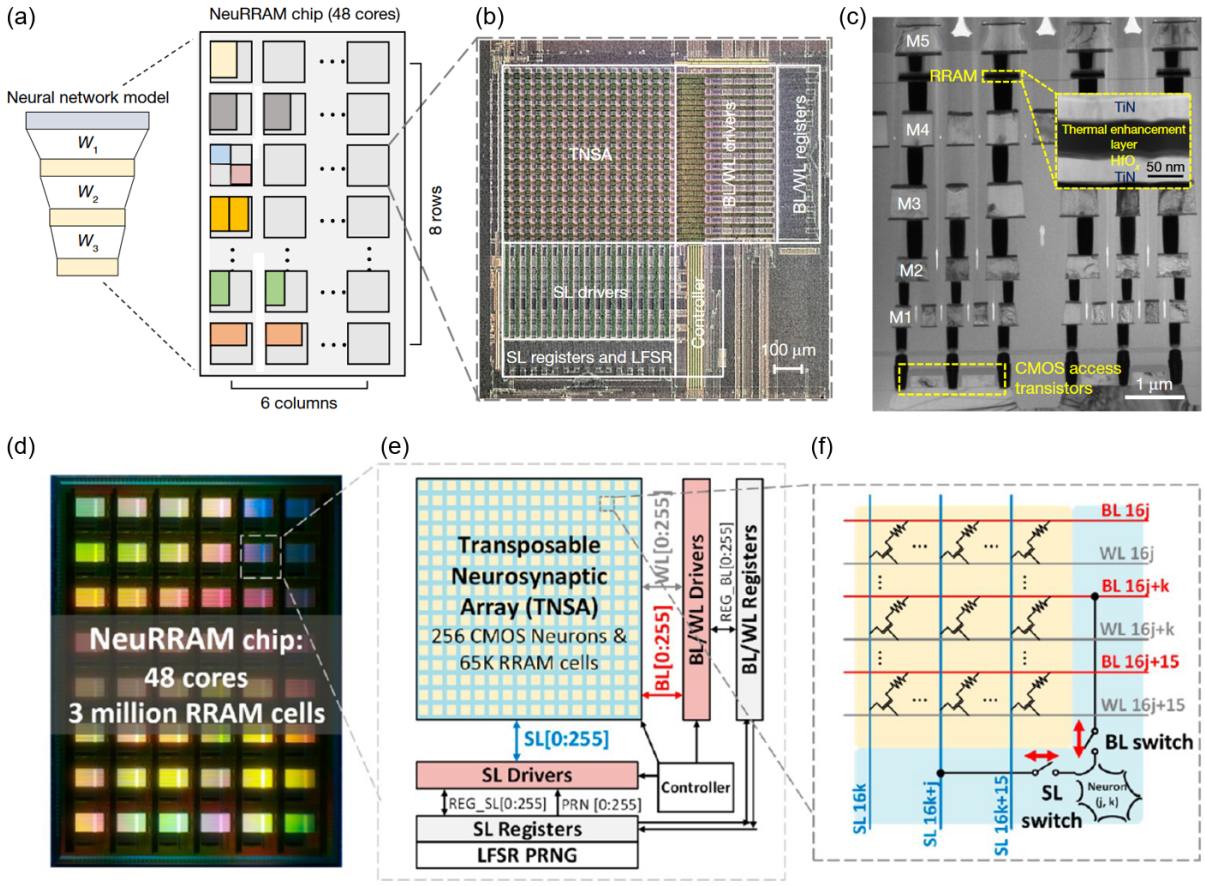

Figure 2.17: *NeuRRAM chip architecture with 48 cores and 3 million memristors. (a) Graphical illustration of possibilities for mapping a neural network to the cores of NeuRRAM. (b) Zoomed-in micrograph of a core, showing its main components. (c) Cross-sectional TEM image showing the integration of $TiN/HfO_x/TaO_x/TiN$ memristors with foundry-made CMOS access transistors. (d) NeuRRAM chip micrograph; chip area: 159 mm^2. Illustration of the structure of the (e) transposable neurosynaptic array (TNSA) and its (f) corelets including 16 × 16 memristors and a CMOS neuron circuit. [76, 78]*

(see Extended Data Table 2 in Ref. 76). It is to be noted, that NeuRRAM was realized with an older 130 nm node CMOS technology, and projecting its performance to 7 nm technology yields much higher energy efficiency than similarly projected performance of digital CMOS AI inference accelerators.

2.2.3 Noise of memristive systems: limitation or resource?

Artificial neural networks realized with memristive hardware benefit from the analog programming of RRAM devices. The 8-bit resolution (corresponding to 256 analog states) demonstrated in the previous example is far from the limits of memristive devices. Recently, a method for achieving 11-bit resolution in $Pt/HfO_2/Al_2O_3{:}TiO_x/Ta$ devices was

presented in Ref. 82. Arrays of 256 × 256 memristors were fabricated and integrated with CMOS circuits on a wafer, as illustrated in Figure 2.18.a-c. An operation procedure was introduced for these devices, to overcome limitations concerning the number of possible

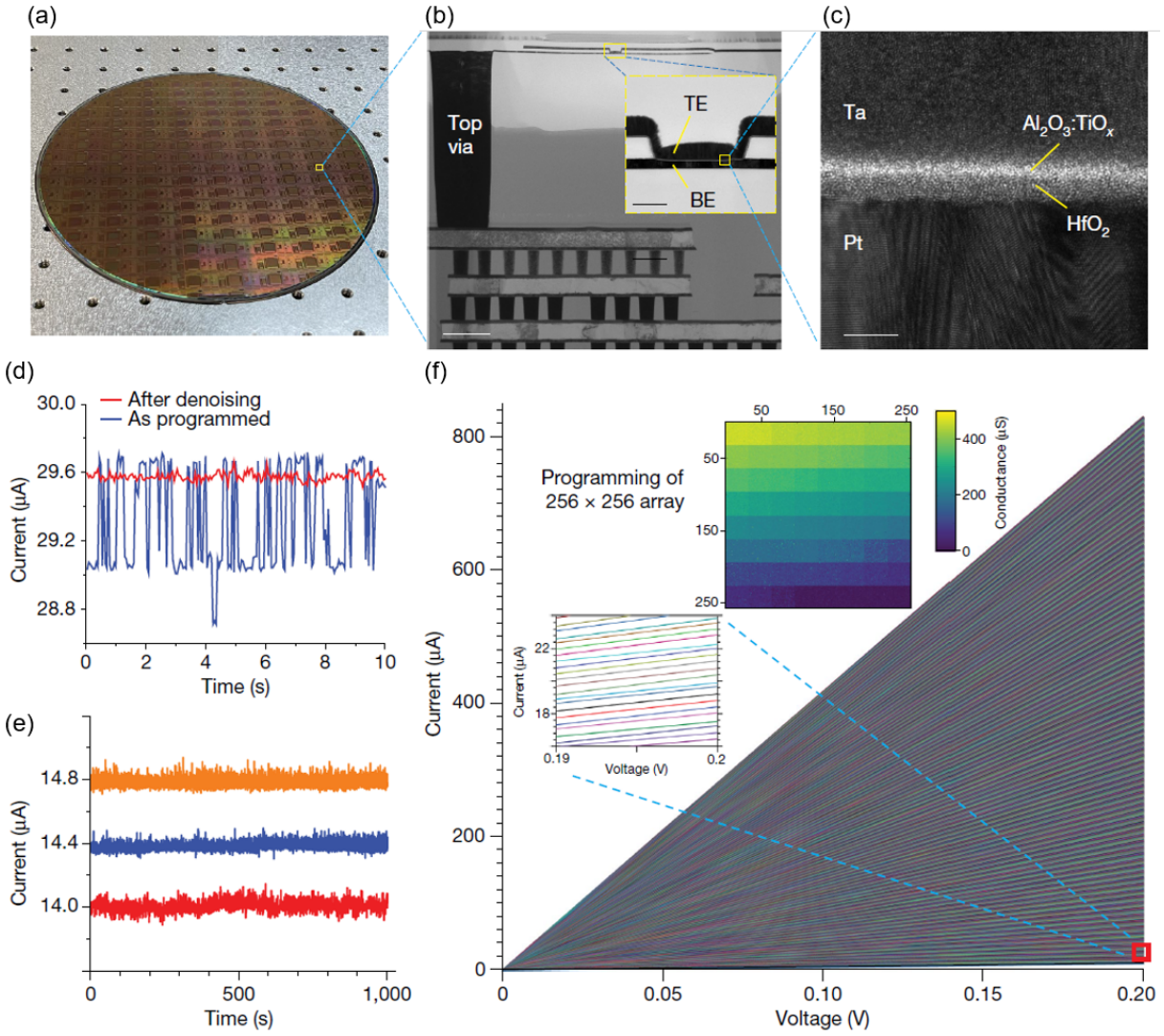

Figure 2.18: *11-bit precision programming of 256 × 256 integrated memristor arrays. (a) Photo of the 8-inch wafer carrying memristor arrays, fabricated by a commercial semiconductor manufacturer. (b) Cross-sectional TEM image of a memristor, scalebars: 1 μm and 100 nm (inset). (c) Cross-sectional TEM image of the memristor stack, scalebar: 5 nm. (d) Current signals measured in the as-programmed (blue) and denoised (red) states of a memristor (read by a constant 0.2 V voltage). (e) Current signals of three neighboring states after denoising (read by 0.2 V voltage). (f) 2048 individual states programmed to a single device. Bottom inset shows a zoomed-in part of the linear I(V) characteristics. Top inset shows an array-level programming of the 256 × 256 memristors to 64 states, in 32 × 32 blocks. [82]*

conductance levels achievable in a single device, thus creating high-precision memristors for various applications.

In principle, an arbitrary number of states would be possible in a device where the conductance can be set to the desired value. This is not the case in reality, because fluctuations of the conductance – originating from inner physical processes, and perceived as the inner noise of the device – limit each state to a given conductance range. The blue curve in Figure 2.18.d shows an as-programmed state of a $Pt/HfO_2/Al_2O_3{:}TiO_x/Ta$ device, where current fluctuations are clearly observable. After a denoising process carried out by applying electrical pulses to the device below its set/reset thresholds, the red curve in Figure 2.18.d shows a state with greatly reduced fluctuations. As a result, neighboring states after the denoising process are well distinguishable from each other, as shown in Figure 2.18.e. Results of tuning an individual memristor to 2048 resistance states (ranging from 50 μS to 4144 μS with a 2 μS interval) is presented in Figure 2.18.f. It is to be noted, that the high precision programming algorithm presented involves verifying the denoising step, requiring for instrumentation for the precise measurement of fluctuations and also precise ADC circuitry. The feasibility of the denoising process for the whole 256 $\times$ 256 array was also demonstrated, via programming 64 different states to 32 $\times$ 32 blocks of the array (see top inset of Figure 2.18.f).

The inner noise of memristive systems is often presented as an obstacle which hinders precise hardware-level neural network operations. This is not always the case, since there are certain networks and algorithms which could benefit from the noise of memristors, such as probabilistic computing or stochasticity-aided optimization. An example for the latter approach is reported in Ref. 83. In this study, a Hopfield neural network (HNN) was realized using a crossbar array of TaO_x-based memristors (and access transistors), as shown in Figure 2.19.a-d. The scheme of a Hopfield network is shown in Figure 2.19.e, which is a single layer fully connected network with constant, binary synaptic weights (shown with blue/yellow lines). The memristor crossbar array is an ideal platform for encoding such a fully connected network, as shown in Figure 2.19.f.

Hopfield networks can be used for solving optimization tasks, and the optimization problem can be encoded in the synaptic weights. These weights assign an energy function to the optimization problem, such that the minimum of the global energy function represents the solution to the problem. In a recurrent operation, the values of binary neurons (shown with orange/green nodes in Figure 2.19.e) are updated in each step. It can be shown that during each iteration the state of the neurons change so that the energy function decreases (similarly to a gradient descent method). However, the optimization process is likely to get stuck in local minima for complex problems with complicated energy landscapes.

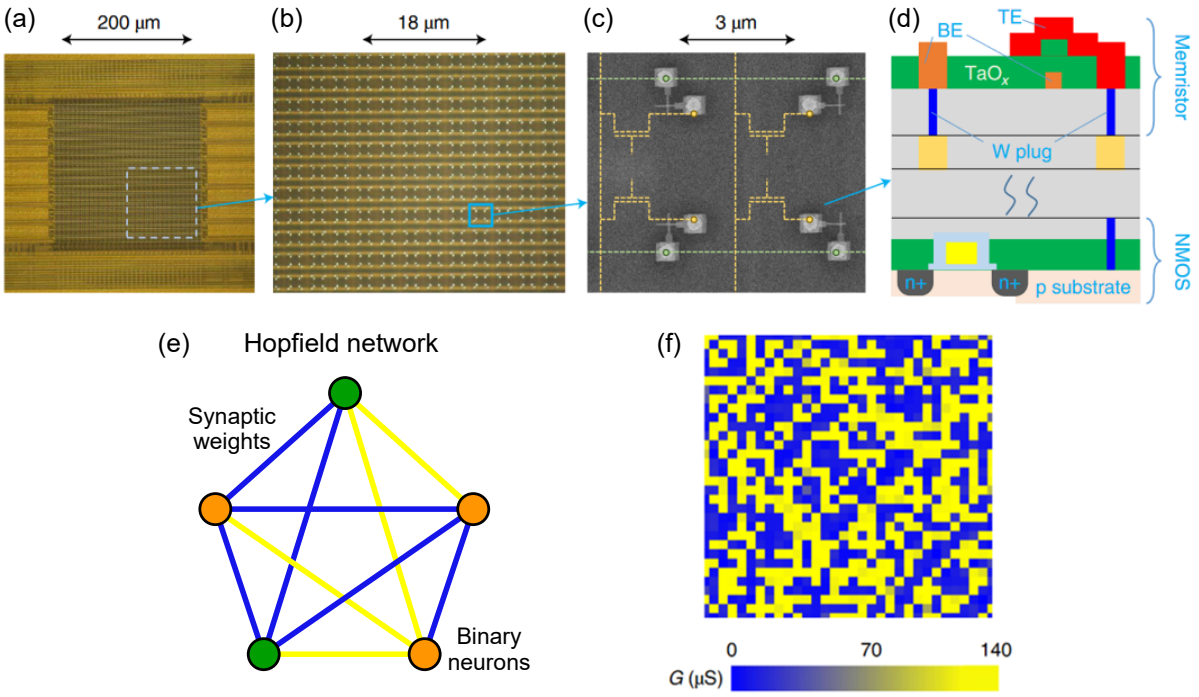

Figure 2.19: *Hardware implementation of a Hopfield neural network with a crossbar array of memristors. (a) Micrograph of the memristor crossbar chip, and (b) magnified view. (c) SEM image of four TaO_x memristors in the array. Dashed lines indicate interconnects and access transistors beneath the surface. (d) Cross-sectional schematics showing the integration of a memristor and its buried access transistor. (e) Abstract illustration of a Hopfield neural network, indicating binary synaptic weights (blue/yellow edges) and binary neurons (orange/green nodes). (f) Synaptic weights encoded as the conductances of memristor matrix (representing the max-cut problem of a 32-node graph). [83]*

The operation of the network can be improved via introducing a stochasticity (e.g. noise), which keeps the energy function out from local minima. However, the noise has to be tuned down as the global minimum is approached, to ensure proper convergence to the solution, e.g. in a simulated annealing scheme (see the illustration of Figure 2.20.a). In case of the memristive HNN, the whole optimization process was realized according to the scheme in Figure 2.20.b. The synaptic weights of the memristor array were used for encoding max-cut problem of a graph with 60 nodes, aiming to find the maximum number of edges to cut to attain two separate graphs (as illustrated in Figure 2.20.c). Binary neuron states were represented by state vectors applied to lines of the crossbar array in each recurrent step. The tunable stochasticity vital for convergence of the network was implemented via a separate, hysteretic threshold circuit (and also, additional circuitry was utilized to ensure recurrent operation, as shown in Figure 2.20.b).

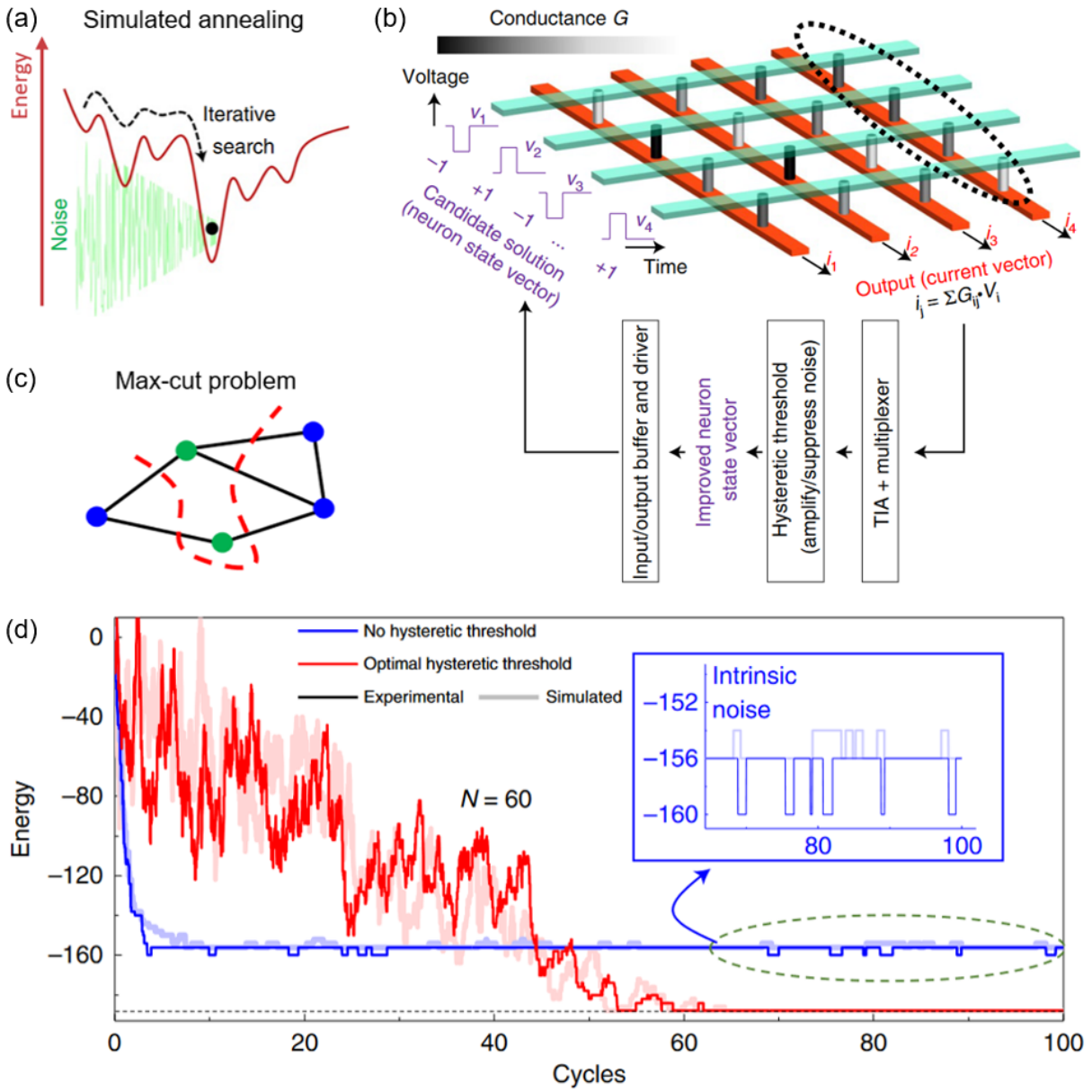

Figure 2.20: *Stochastic optimization with a memristive Hopfield network. (a) Scheme for simulated annealing. (b) Illustration of the experimental realization of the memristive HNN, also showing the steps of recurrent optimization and functions realized with additional circuitry outside the crossbar array. (c) Illustration of the max-cut problem (finding the maximal cut of a graph, involving the most edges). (d) Energy descent during finding the maximal cut of a 60-node graph. The red/blue curve represents the energy with/without additional stochasticity (realized via simulated annealing), while the black dashed line shows the global energy minimum for the problem. The inset shows a magnified view of energy fluctuations for the case where no external noise was injected, which is an effect of intrinsic noise of the memristive crossbar array. [83]*

Energy descent during solving the max-cut problem of a 60-node graph with a 60×60 memristor array is shown in Figure 2.20.d. Via gradually decreasing the noise (realizing simulated annealing), the network converges to the solution, as shown with the red curve. However, without any noise injection the network is stuck in a local minimum (see blue curve). Still, there are some small fluctuations in the energy observable in this case also, which are shown in the magnified view of the inset. These fluctuations originate from the intrinsic noise of the network, mainly from the sources of (i) the non-idealities of the crossbar array, (ii) the inner noise of memristors.

Noise tailoring of memristive devices for stochastic optimization Inspired by the above work, the possibilities of utilizing inner noise of memristive devices for stochasticity-aided optimization with Hopfield neural networks was studied by our group in Ref. 84. The study was carried out by my former student János Gergő Fehérvári. He started to investigate operation of stochastic Hopfield neural networks as part of his BSc project, in which I helped him as supervisor [85].

The work reported in Ref. 84 relies on prior experimental studies of $1/f$ noise characteristics of various memristive material systems [86–88] [O1]. Experimental noise data

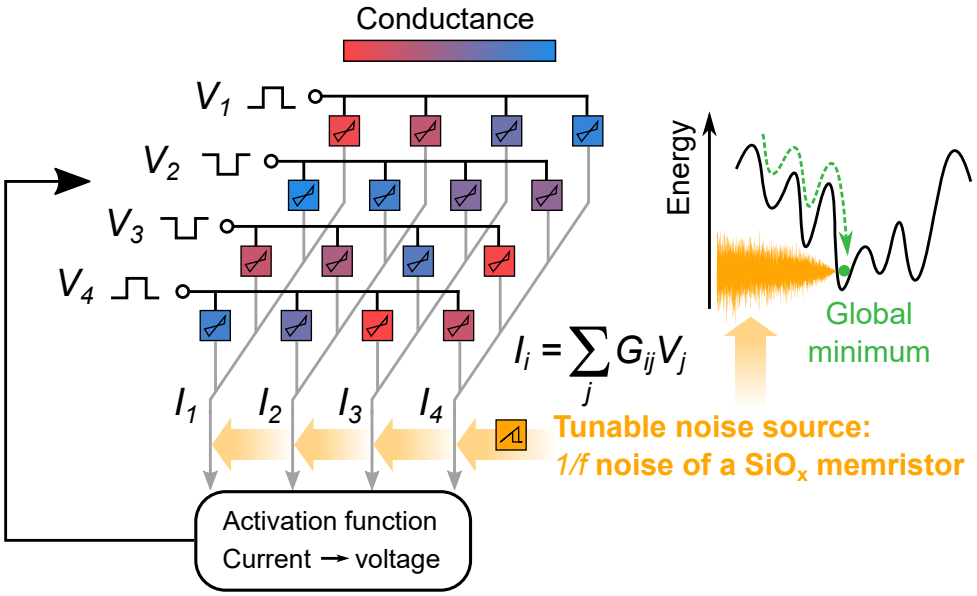

Figure 2.21: *Illustration of concepts reported in Ref. 84 for enhancing stochastic optimization in memristive Hopfield networks using the inner noise of memristive devices as a source for stochasticity. The conductance of devices in a crossbar array can be utilized to control noise levels, or additional noise can be injected using a SiO_x memristor as a tunable noise source. Annealing schemes can be realized via tuning device noise through the conductance, to find the global minimum in the complex energy landscape of an optimization problem.*

were utilized to simulate and analyze the operation of memristive Hopfield neural networks with different noise characteristics while solving the max-cut problem (the same benchmark task as in Ref. 83). According to these simulations, the efficiency of optimization can be enhanced by properly tuning the inner noise of memristive devices in the crossbar array or injecting the noise of a SiO_x device as a tunable noise source to the network (see graphical illustration of these concepts in Figure 2.21). These concepts employ the fact that device noise scales with the conductance, which can be used as a control parameter for realizing noise annealing strategies.

In later parts of my thesis, $1/f$ noise spectroscopy studies of several memristive devices are reported. Noise characteristics of on-chip devices I developed and/or produced were measured by my colleagues Botond Sánta, György Lázár and Sebastian Werner Schmid. Results of these experiments are presented in Subesections 3.2.3 and 3.3.3, and are discussed focusing on the material-specific aspects of each investigated memristive system.

2.2.4 Biologically inspired systems

Neuromorphic computing holds great promise as a computational framework to address the von Neumann bottleneck, mainly in applications which involve learning, recognition, optimization, and classification [89]. On the hardware front, the central idea is to construct a computing system that can mimic certain functions and mechanisms observable in the nervous system. Such biologically inspired systems include artificial synaptic and neuronal devices with dynamics that closely resemble biological processes. In this way, certain physical mechanisms associated with perception and learning can be accurately replicated at the hardware level.

In contrast to the examples presented in the previous Subsection involving large numbers of memristors, now I focus on discussing a fundamentally different approach, where the inner resistive switching dynamics are utilized as a computational resource, enabling complex signal processing operations in the analog domain with only a few devices. This approach can enhance efficiency of operations carried out by artificial synapses or even larger analog crossbar arrays, via realizing neuronal functions (e.g. accumulation of input signals or activation functions) at the hardware level. Central components to these neurodynamic circuits can be resistive switching devices with volatile characteristics, e.g. TaO_x [90], NbO_x [91, 92] or VO_2 [9] devices or PCM devices [93, 94].

Relevant to understanding the context of my own studies presented in Subsection 3.3.5 and Chapter 6, I show some examples of creating artificial neuronal circuits out of VO_2 Mott memristors, according to Ref. 9, which inspired my own work also. After that, I show another example from the literature, an application of a volatile memristor-based oscillator circuit for processing the raw signal of a sensor [13]. Both studies rely on the concept and possibility to construct a relaxation oscillator out of a volatile memristor and

an RC circuit, also known as memristor-based relaxation oscillator [95]. I introduce the operation of such an oscillator in the following.

Figure 2.22 shows the operation of a relaxation oscillator built from a volatile VO_2 memristor (taken from the Supplementary Information of Ref. 9). Typical $V(I)$ characteristics of the memristor (plus a serial resistor) is depicted in Figure 2.22.a, where the direction of hysteresis is indicated by the blue arrows. The set and reset processes, along with the ON and OFF states of the memristor are also labeled. The oscillator circuit shown in Figure 2.22.d exhibits oscillations under a constant DC bias. This is due to the fact that the ON and OFF state resistances of the memristor differ considerably and also the abrupt nature of set and reset processes (with respect to the characteristic timescales

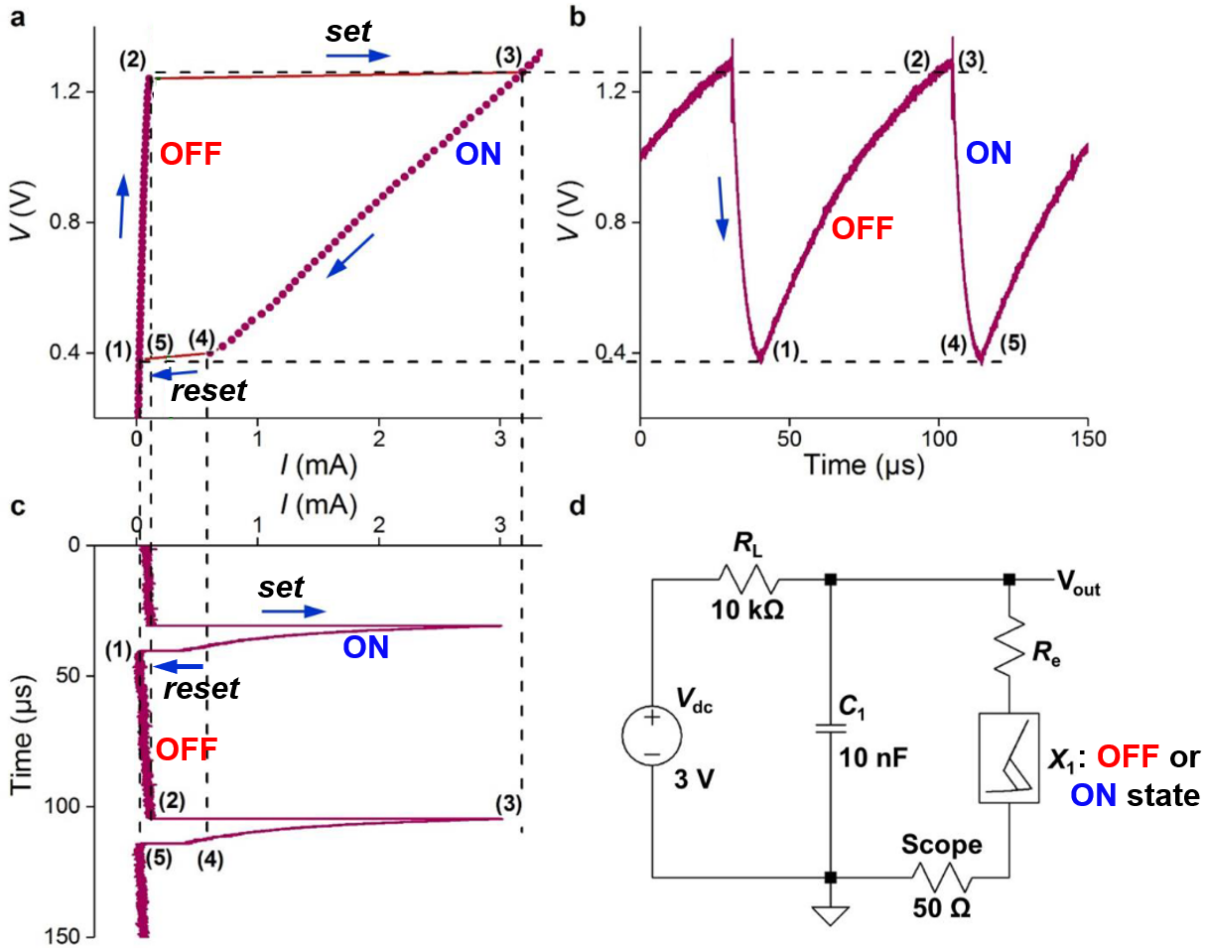

Figure 2.22: *Characteristics of a relaxation oscillator using a VO_2 memristor. (a) Volatile resistive switching $V(I)$ characteristics of a circuit component consisting of a VO_2 memristor (X_1) and a serial resistor R_e shown in panel (d). Time-dependent traces of the (b) voltage drop V_{out} on the X_1 memristor plus R_e serial resistor branch and (c) current flowing through the memristor, during the operation of the oscillator circuit depicted in (d). Panel (d) shows the circuit schematics of the oscillator circuit. [9]*

of the circuit). The voltage drop on the X_1 memristor plus R_e serial resistor as a function of time is shown in Figure 2.22. The observable, two characteristic timescales of the circuit are determined by the markedly different ON and OFF state resistances of the memristor. The circuit always relaxes towards its equilibrium state where the division of the input DC voltage between load resistor (R_L) and the memristor plus serial resistor branch ($R_e + X_1$) is determined by the ratio of their resistances ($R_L : (R_e + X_1)$, where X_1 can be either the ON state or OFF state resistance of the memristor). Note that these equilibrium voltage values are never reached, as the set and reset thresholds of the memristor are reached beforehand, maintaining the oscillation. Current through the memristor also exhibit oscillations in the process, manifesting as a spiking waveform shown in Figure 2.22.c. The current remains low while the memristor is in its high resistance OFF state. A sudden jump appears as a result of the set process, followed by a rapid decrease. When the reset threshold of the memristor is reached, the memristor retains its OFF state and the current drops. It is important to note, that the C_1 capacitor (parallel to the memristor branch) affects both characteristic timescales of the circuit. The observed current spikes in the ON state of the memristor are effectively the result of the rapid discharge events of C_1, while charging of the capacitor begins repeatedly when the memristor recovers its OFF state.

Artificial neuron from volatile memristors In the following, I show an example for an artificial neuron circuit, which is effectively two oscillators connected in series (omitting serial resistances from the memristor branches), where memristors are biased oppositely to each other (see Figure 2.23.c).

Figure 2.23.a-b illustrate the schematic structure and mechanism for generation and propagation of action potentials in a biological neuron. Generally, the precisely timed opening and closing of many ion channels at a location result in a potential change between the inside and outside of the cell – the membrane potential. This rapid change of membrane potential ($\sim$100 mV in $\sim$ 1 ms) is called the action potential, which is a voltage spike with a specific waveform [96]. Action potential generation is governed by biochemical processes, and can arise from ion channels sensitive to external inputs (light, acoustic or mechanical stimuli) or internal conditions (hormones, neurotransmitters). The propagation of action potentials along neurons (as illustrated in Figure 2.23.a) can be pictured as a coupled change of the local membrane potential and ion concentration which travels in a direction along the axons, the speed of propagation is roughly 1 cm under 1 ms. The Na^+ and K^+ ion channels (illustrated in Figure 2.23.b) have key roles in propagation of the action potential along the axon.

In Figure 2.23.c, the circuit topology of an artificial neuron based on VO_2 Mott memristors is presented. Vertically stacked crosspoint memristor devices used in the study

are shown in Figure 2.23.d (see SEM image and schematics). The circuit comprises two memristors (X_1 and X_2) biased to $-E_{\mathrm{Na}}$ and $+E_{\mathrm{K}}$ DC voltage levels, and four passive elements (R_{L1}, R_{L2} load resistors and C_1, C_2 parallel capacitors). The memristors X_1 and X_2 are biased at opposite levels, to achieve similar dynamical behavior as the operation of Na^+ and K^+ ion channels located along the membrane of biological neurons. The mutual operation of the memristors, along with the proper choice of passive circuit elements and $-E_{\mathrm{Na}}$, $+E_{\mathrm{K}}$ DC biases result in the generation of a waveform (see Figure 2.23.e) similar to true action potentials in the nervous system. Furthermore, the study presented in Ref. 9 demonstrates experimental realizations of 23 independent neuronal behaviors using properly coupled VO_2 memristors. The 20 spiking patterns of the neuron model of

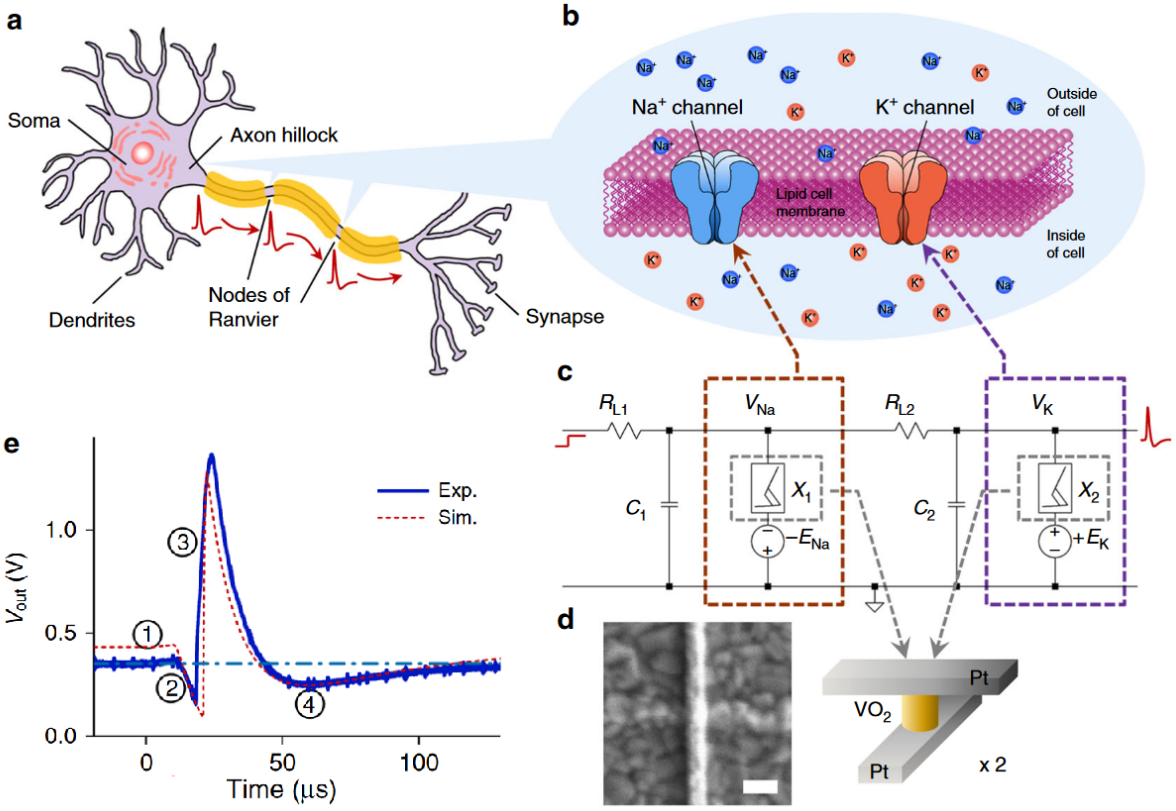

Figure 2.23: *Artificial neuron from VO_2 memristors. (a) Illustration of a biological neuron, showing the firing of an action potential near the axon hillock, which travels along the axon towards output synapses. (b) Illustration of Na^+ and K^+ ion channels across the cell membrane. (c) Basic circuit schematics of the memristor-based artificial neuron. (d) Scanning electron micrograph (scalebar: 100 nm) and schematic illustration of vertically stacked crosspoint VO_2 memristors used in the study. (e) Waveform generated by the circuit shown in panel (c), resembling the shape of true action potentials. [9]*

Izhikevich [97] are realized, with three additional spiking behaviors characteristic of the nervous system.

Artificial sensing with a memristor-based relaxation oscillator In the next example from Ref. 13, the spiking behavior of a NbO_x Mott memristor-based oscillator circuit was utilized for directly processing the analog signal from a sensor. The underlying biological inspiration is the behavior of afferent nerves, illustrated in Figure 2.24.a. In general, these nerves encode information in the frequency of output spikes which depends on the intensity of the stimulus. However, they also realize protective inhibition, via decreasing firing rates when stimuli are too high, to prevent damage to the nervous system. The NbO_x Mott memristor-based circuit which emulates this behavior is shown in Figure 2.24.b. This circuit framed with blue dashed lines produces a tonic output oscillation pattern due to an input bias, as described in the beginning of present Subsection. Upon increasing the input signal, oscillations at the output appear (after surpassing a threshold input level). The frequency of oscillations increases with increasing input voltage (provided by the sensor). Then, the output frequency saturates and decreases, resembling protective inhibition in a biological system. The resulting spiking pattern can be carried to a spiking neural network for further processing.

A piezoresistive sensor's output voltage level is sufficient to the drive the NbO_x oscillator circuit, as shown in Figure 2.24.c. When pressure is applied to the sensor, positive voltage is generated, which decreases when the pressure is lifted. In this manner, an artificial mechanoreceptor unit is realized as exemplified by its voltage traces during sensing, shown in Figure 2.24.d. The voltage of the sensor (blue trace, upper panel) increases with increasing pressure (intensity and duration of the pressure signal are indicated via dark/light blue backgrounds in the graph for stronger/weaker stimuli, respectively). First, the frequency of oscillations increases (see raw output signal of the NbO_x oscillator circuit with red lines), and when pressure is to strong, the frequency falls abruptly (protective inhibition). Upon decreasing pressure, the usual excitatory operation is retained. An important advantage of this approach is that there is no need for external power source for the operation, which could facilitate applications in neurorobotics.

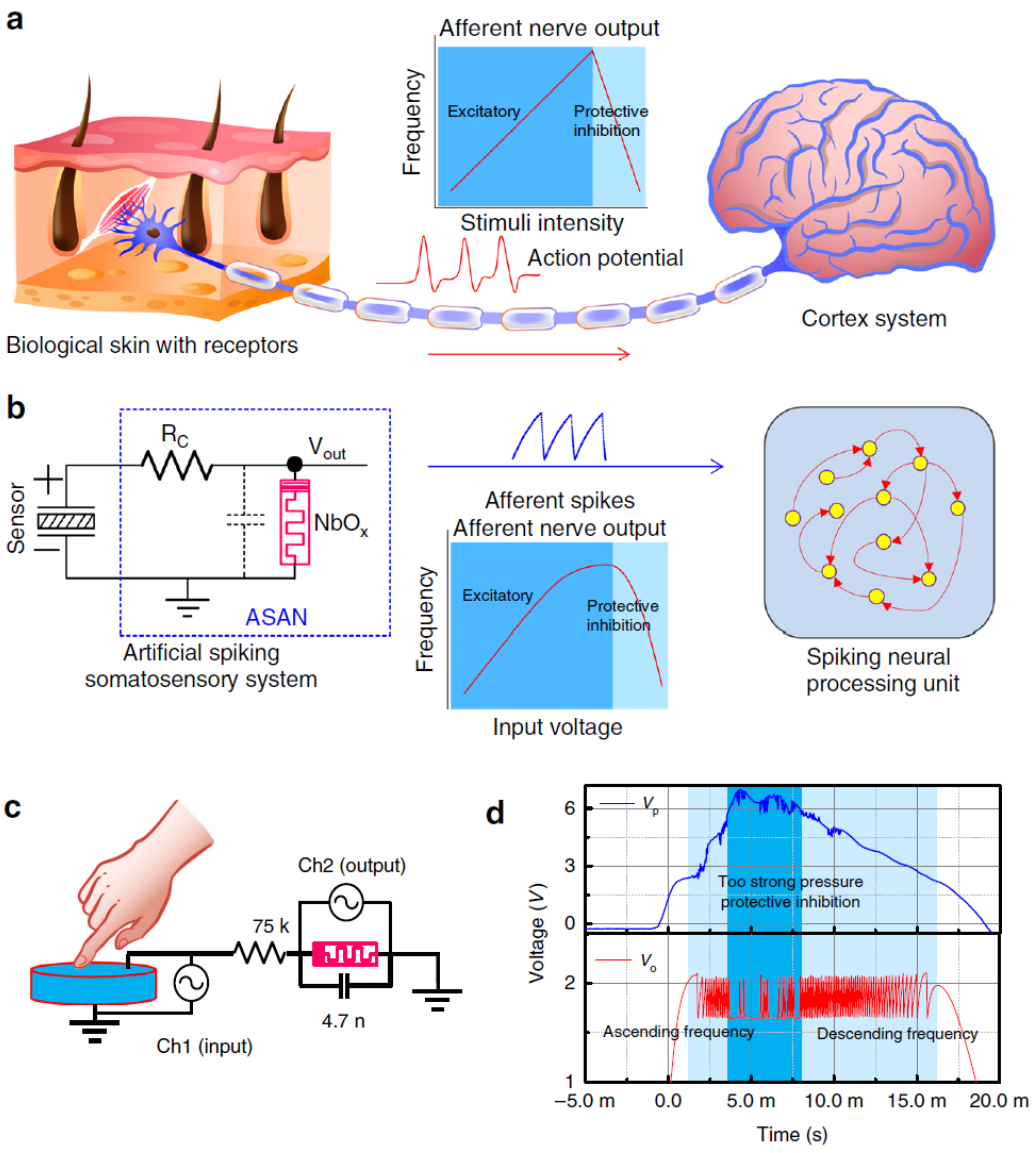

Figure 2.24: *Artificial sensing with neurodynamic NbO_x oscillators. (a) Illustration for the mechanism of afferent sensing in biology. (b) The realization of artificial sensing with NbO_x relaxation oscillators realize characteristics similar to protective inhibition. (c) Circuit schematics showing the connection of the NbO_x oscillator to a piezoresistive sensor. (d) The voltage of the sensor (blue trace, upper panel), and the raw output signal of the NbO_x oscillator circuit (red trace, bottom panel) displayed as a function of time. The intensity and duration of the pressure signal are indicated via dark/light blue backgrounds in the graph (for stronger/weaker stimuli, respectively). Excitatory/protective inhibition characteristics are retained for weak/strong stimuli. [13]*

Chapter 3

Development of on-chip memristors

The foundation of the development process of integrated memristive networks is the fabrication, characterisation and optimization of single on-chip devices, through providing proper feedback for the production process based on device characterization measurements. When I started my PhD studies, our research group primarily studied STM point-contact memristive devices [59, 86, 98–102]. Reliable device fabrication process within our group existed only for planar graphene/SiO_x/graphene devices (see general layout for planar geometry in Figure 3.1.a), developed by László Pósa and Cornelia Nef at the University of Basel [32, 36]. I started to learn the methodology of nanofabrication processes from László already during the end of my MSc studies, and we worked on creating vertically stacked Nb_2O_5 crosspoint memristive devices (see general layout for vertical geometry in Figure 3.1.b). As a parallel project, László created planar SiO_x memristors with metallic electrodes which I characterized. After I had these first experiences with on-chip device fabrication and characterization processes, I started my own development project with the fabrication and characterization of Ta_2O_5 crosspoint devices, motivated

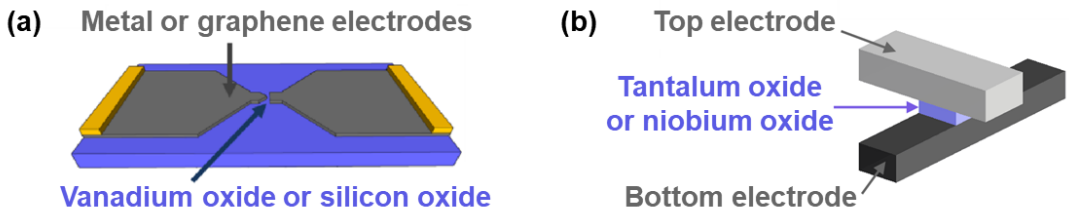

Figure 3.1: *Graphical illustration of devices I developed during my PhD studies, showing RS materials of the active regions. Schematics show (a) planar-type and (b) vertical crosspoint device geometries. Different devices are discussed in the following Sections of the thesis: planar SiO_x devices with metallic electrodes in Section 3.1, vertical crosspoint OxRAM devices with Nb_2O_5 and Ta_2O_5 active layers in Section 3.2 and planar VO_2 memristors in Section 3.3.*

by this material's high technological relevance [41–44, 103–105] and also by my own low temperature measurements on Ta_2O_5 STM point-contacts. In the meantime, I worked to establish a reliable electroforming process for our Nb_2O_5 and Ta_2O_5 devices, and also studied set time statistics of SiO_x-based devices (including graphene and metal electrode devices). As these projects progressed, László started to work on finding a reliable fabrication method of VO_2 thin layers [106], as this material exhibits Mott transition slightly above room temperature, offering promising possibilities to realize VO_2-based memristive devices [9, 107, 108]. I joined László in the development process of planar VO_2 nanogap-type devices (also illustrated in Figure 3.1.a), investigating the effect of different electrode materials, the role of the gap size and studying VO_2 layers made with different deposition techniques. Recently, I carried on this project to create VO_2 devices in a co-planar waveguide geometry, designed for radio frequency (RF) measurements, relying on the idea of Miklós Csontos [44].

As part of my PhD studies, I had the opportunity to participate in all stages of the development process of various memristive material systems. In this Chapter, I am going to present results of multiple development projects I participated in during my work. In Section 3.1, focusing on the development of SiO_x phase change memristors with metallic electrodes, I mainly took part in applying the electrobreakdown procedure [32] for metallic electrodes, basic electrical characterisation and studying switching dynamics. As for vertical OxRAM devices (Section 3.2) and planar VO_2 memristors (Section 3.3) I engaged in the fabrication of the on-chip samples carried out by electron beam lithography, thin layer deposition and etching techniques. Within these projects, I aimed at the elaboration of a reliable electroforming process for OxRAM devices, and also participated in basic electric and temperature-dependent characterisation of VO_2 devices. In these Sections, I include results of further studies targeting some applications (e.g. utilizing the switching dynamics of OxRAM devices and $1/f$ noise spectroscopy studies of on-chip devices), which were carried out by my colleagues. Results of my own projects aiming at the investigation and application of RS material systems are reported later in Chapters 4, 5 and 6. A brief summary of the developed and investigated devices and also the proper Sections describing the various devices is provided in the caption of Fig. 3.1.

General circuit schematics for $I(V)$ characterisation The scheme of the circuit shown in Figure 3.2 is routinely applied for $I(V)$ characterisation of various memristors in my studies. Memristors are connected to an R_s serial resistor, and triangular drive voltage signals are applied (V_{drive}), while the current (I) is measured using an amplifier for most of the cases. The voltage drop on the memristor is denoted as V_{bias}, and it is computed as $V_{\mathrm{bias}} = V_{\mathrm{drive}} - R_s \cdot I$. Note, that $I(V)$ characteristics are either plotted as a

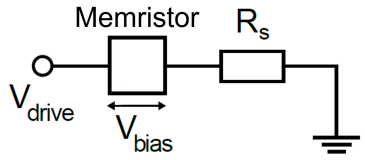

Figure 3.2: *General scheme of the circuit used for $I(V)$ characterisation of memristors in my thesis.*

function of the applied V_{drive} drive voltage or the computed V_{bias} bias voltage, indicated by the label of the x axis.

I use the terms volatile and non-volatile referring to the nature of the induced resistance change in a memristive device in a certain measurement. Therefore, volatility of the resistance change can be considered with respect to the timescale of measurements. It is to be noted though, that volatile/non-volatile can also indicate a general trait of a memristor, referring to its behavior in relatively slowly recorded $I(V)$ measurements (at ~ 1 Hz).

3.1 SiO_x phase change devices with metal electrodes

The first development project I participated in focused on the development process of on-chip SiO_x based devices prepared with metallic electrodes. This project was motivated by the successful studies of previous graphene/SiO_x/graphene nanogap devices, exploring the three timescales characteristic of silicon oxide phase change memristors: the set time, the reset time and the dead time (see Subsection 2.1.1) [32, 36]. One advantage of using metallic electrodes instead of graphene is the ease of production via a single electron beam lithography step (there is no need for the transfer of graphene to the chip). Devices with platinum and niobium electrodes were fabricated by László Pósa, with the aim to compare characteristics of the new devices with previous ones with graphene electrodes. For this purpose, planar samples were prepared in three different kinds of geometries: asymmetric gap-type, line and bowtie electrodes (as shown in Figure 3.3). Devices in the latter two geometries need to go under an electrobreakdown process to create a gap between the electrodes (similarly to graphene/SiO_2/graphene devices), however the first, asymmetric geometry does not need electrobreakdown, since a nanogap is already patterned during lithography.

My task was to carry out electrical characterisation of these samples, including the optimization of the electrobreakdown process [32] for metals, aiming for stable switching characteristics (with or without electrobreakdown), and exploring the characteristic timescales of these devices, using data from the graphene/SiOx/graphene system as a comparison basis.

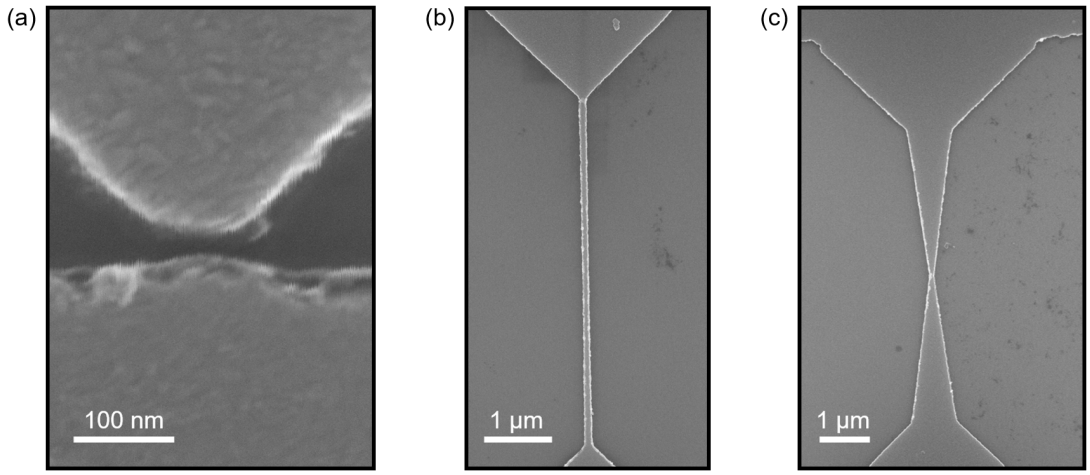

Figure 3.3: *Representative SiO_x devices with metallic electrodes, prepared by László Pósa. SEM images taken by László show (a) asymmetric gap-type, (b) line and (c) bowtie geometries. The latter two types need to undergo an electrobreakdown process to establish a gap.*

3.1.1 Platinum electrode devices

Upon studying 24 different SiO_x samples with metallic electrodes (12 devices with Pt and 12 devices with Nb electrodes), I obtained the most reliable RS characteristics in line-type Pt electrode devices, where I optimized the electrobreakdown process to establish a gap in a metallic nanostripe (see the description of the process for graphene electrode devices in Subsection 2.1.1).

A typical example of an electrobreakdown process for a line-type Pt electrode device is shown in Figure 3.4.a, which I carried out using 100 μs pulse length, 2 mV step size, 100 kΩ threshold for the resistance and a constant $V_{\text{low}} = 100$ mV amplitude of triangular readout signals applied between pulses. A feedback was applied to the resistance (instead of the current, as usual for the breakdown of graphene, see Subsection 2.1.1), restarting each breakdown cycle when a pre-defined increase in the resistance is detected within the last 100 steps.

After the electrobreakdown process, >MΩ resistance was measured. In this state, irregular RS $I(V)$ characteristics were observable, as shown in Figure 3.4.b. Afterwards, the device was studied in pulsed measurements, e.g. an endurance measurement with >2500 successful set-reset cycles was performed, as shown in Figure 3.4.c. After > 10000 set-reset cycles stable RS $I(V)$ characteristics was observed (see Figure 3.4.d), where well-defined set/reset threshold values, and > 2-times higher ON state currents are observable, compared to initial irregular RS characteristics.

In the following, I investigated the τ_{dead} dead time statistics of a device, in which stable RS was initialized according to the described procedure, an electrobreakdown followed by

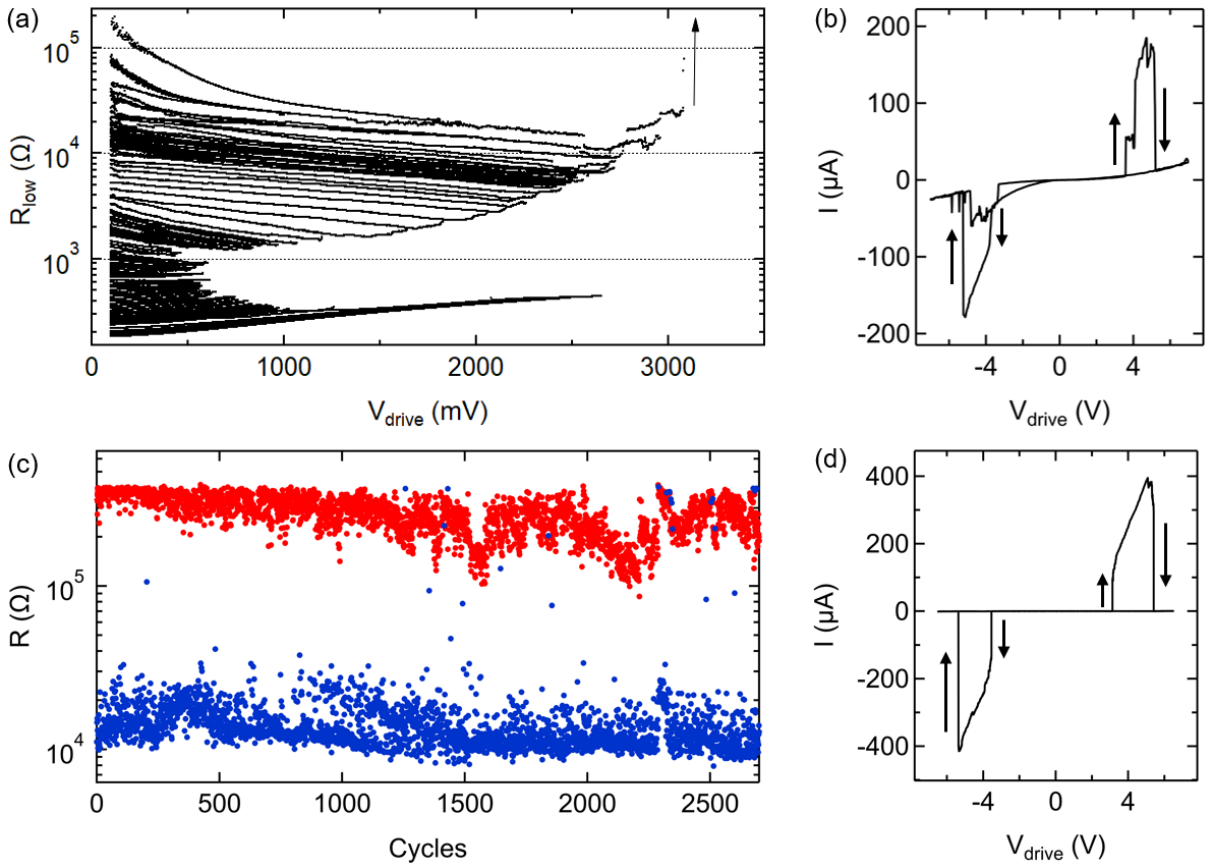

Figure 3.4: *Initializing RS in a line-type Pt/SiO_x/Pt device. (a) Electrobreakdown procedure shown as the evolution of resistance – voltage traces, measured between each voltage pulses of the process, with small amplitude triangular readout signals. The amplitude of voltage pulses (V_{drive} on the horizontal axis) is increased in small steps ($V_{\mathrm{step}} = 2$ mV), until a pre-defined increase of resistance is detected relative to the resistance values measured in the last 100 steps (defined as a percentage). This feedback event restarts a cycle, usually at a slightly elevated resistance. The process is maintained until a complete breakdown of the metallic stripe occurs, resulting in >MΩ resistance. (b) Irregular RS $I(V)$ curve recorded directly after the electrobreakdown process. (c) Endurance measurement of the device yields >2500 set-reset cycles, carried out with applying 1 s long, 3.7 V amplitude, and 20 ms long 6.8 V amplitude set/reset pulses in a cycled measurement. ON and OFF state resistances (see blue and red dots, respectively) were evaluated at the end of programming pulses, at high voltage levels. The device remained operational after the measurement. (d) Stable RS $I(V)$ characteristics after $>$ 10000 set-reset cycling of the device, exhibiting $>$ 2-times higher ON-state currents than the initial, irregular $I(V)$ curves.*

5000 set/reset cycles in pulsed measurements. The dead time is a characteristic timescale for which the set process is blocked after a successful reset event. To study this effect, the device was initialized in its ON state, and then a similar waveform was applied to it, as

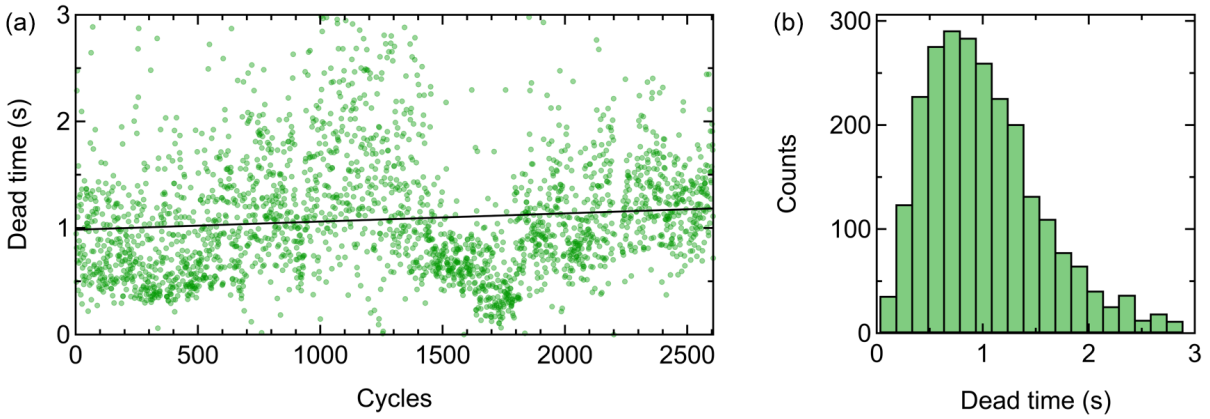

Figure 3.5: *Studying the dead time over* ≈ 2500 *set/reset cycles in a Pt/SiO$_x$ device. (a) Evolution of the dead time over the cycled measurement. The black line fitted to the green datapoints reveal only a minimal change in* τ_{dead} *over cycling. (b) Histogram of* τ_{dead} *data in (a).*

shown earlier in Figure 2.7.a of Subsection 2.1.1. The waveform consisted of a 20 ms reset pulse with 7 V amplitude followed by a 3 s long segment of 3.25 V voltage level (above the $\approx$ 2.9 V set threshold voltage, determined from prior $I(V)$ measurements). Dead time values observed over $\approx$ 2500 cycles are plotted in Figure 3.5.a, and their histogram is shown in Figure 3.5.b. It is to be noted that in a few cases, no set event occurred during the 3 s long period of the signal, yielding some points at $\tau_{\text{dead}} = 3$ s as an evaluation artifact, which were removed.

The line fitted to the green datapoints in Figure 3.5.a reveal only a minimal change in τ_{dead}, in contrast to graphene/SiO$_x$ devices, where this *aging effect* can lead to an increase in τ_{dead} by a factor of 3 over prolonged cycling [106]. The dead time values have a broad distribution, falling to the typical range of 100 ms – 1 s of graphene/SiO$_x$ devices.

3.1.2 Niobium electrode devices

Similarly to Pt/SiO$_x$ devices, the electrobreakdown of Nb electrode line-type samples were carried out, using the parameters described earlier. The procedure resulted various resistances in the 15 kΩ – 10 MΩ range, for multiple samples. Larger resistance values could only be reached when feedback to the resistance was switched off in the last cycle, releasing the control over the process. Keeping the feedback on could not yield any increase in the resistance after ∼15 – 20 kΩ zero-bias resistance was reached. Note, that 15 kΩ zero bias resistance would be rather unusual for a well-established, pure SiO$_x$ nanogap, so it is a first indication for some other effects.

Upon a slow triangular voltage sweep of a 10 MΩ Nb/SiO$_x$ sample, a one-time resistance change to 1 MΩ was observed, resembling the usual electroforming of OxRAM

devices. Afterwards, some transient $I(V)$ characteristics of bipolar nature were observed, as shown in Figure 3.6.a (for only a few cycles, with $R_{\mathrm{OFF}}/R_{\mathrm{ON}} = 1$ MΩ/10 kΩ = 100 switching ratio). Besides bipolar character, a strong nonlinearity dominates the characteristics. The overall shape of these $I(V)$ curves are very similar to certain types of $I(V)$ characteristics of Nb_2O_5 STM point-contact devices which I investigated during my BSc studies [101], indicating the presence of Nb in the active region which affects operation.

In case of another device with 15 kΩ zero-bias resistance, I begun $I(V)$ characterisation without going any higher in resistance, which revealed the characteristics plotted in Figure 3.6.b. A pronounced nonlinearity is observed, along with a small hysteresis of 0.1 V width, as indicated by the arrows. These characteristics were stable on the scale of $\sim$ 10 cycles, but I did not investigate the effect any further due to the lack of my experience with Mott-type devices with volatile characteristics at that point. However, the NbO_x device in Ref. 92 exhibits very similar $I(V)$ characteristics as the one shown here (for comparison with Fig. 3. of Ref. 92, current is plotted at the logarithmic scale and inset shows the same data at linear scale).

I moved on to testing gap-type devices with asymmetric electrodes with $\sim$ 30 nm gap (determined from SEM imaging, see Fig. 3.3.a). Pristine state of these samples was > 1 GΩ, and RS was initialized with ±10 V amplitude triangular signals, which resulted in similar irregular $I(V)$ curves as the initial $I(V)$ characteristics of Pt/SiO_x devices. Upon prolonged $I(V)$ cycling characteristics somewhat improved, some clearer curves

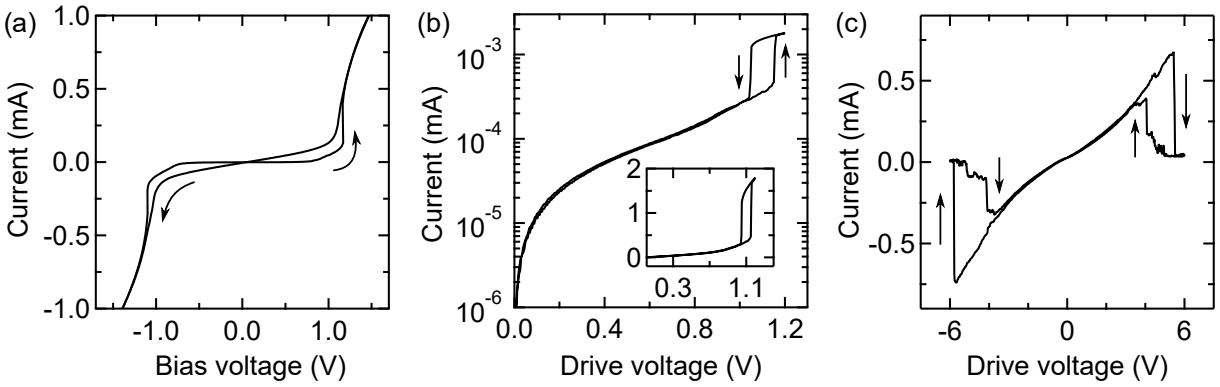

Figure 3.6: *Different kinds of hysteretic $I(V)$ characteristics in various Nb/SiO_x samples. (a) Transient bipolar, and (b) unipolar characteristics with pronounced nonlinearity, indicating the presence of Nb in the active region. Note, that in (b) the current is plotted at a logarithmic scale, while inset shows the same data at a linear scale. (c) Usual RS $I(V)$ characteristics of the SiO_x phase change process appear in gap-type devices. Resistive switching is maintained for thousands of cycles, but remained irregular, as the pristine $I(V)$ characteristics in a Pt/SiO_x device after electrobreakdown.*

were observable by chance (as the one plotted in Fig. 3.6.c), but RS was not uniformly clear; irregularities were still present.

Summary To summarize my experiences, Nb can indeed be present in the active region of line-type Nb/SiO_x samples, irrespective of the value of resistance after electrobreakdown. I have observed both bipolar and unipolar characteristics typical for Nb_2O_5 and NbO_x systems. Gap-type Nb/SiO_x samples also proved to be functional and exhibited the phase change-type characteristics of SiO_x, but were less reliable than graphene/SiO_x devices. In case of Pt/SiO_x devices, line-type samples yielded reliable operation after electrobreakdown and prolonged set-reset switching of a few thousand cycles. An advantage of gr/SiO_x devices is the possibility of integration to 2D electronics, however, the fabrication of Pt/SiO_x devices is much easier using a a single lithography/deposition step of metallic electrodes, without the need for transferring graphene to the chip and its selective etching. I discuss further comparison of the Pt/SiO_x system to gr/SiO_x devices in the end of Section 4.2, where the variation of set time statistics of a Pt/SiO_x device is analyzed with the same experimental approach used also for the detailed analysis of the stochastic nucleation process in gr/SiO_x memristors [O5].

3.2 Vertical OxRAM devices

STM point-contact technique is a versatile approach for studying RS materials, especially suitable for performing fast experiments on a thin layer sample, since there is no need for patterning electrodes via nanofabrication processes. However, STM point-contact systems have very limited mechanical stability and integration of these devices is impossible, limiting their applications. Motivated by these aspects, I started to work on the development of on-chip OxRAM devices with László Pósa. As a first step towards this goal, László experimented with creating Nb_2O_5 thin layers with reactive sputtering. On top of a SiO_2 substrate he produced a $SiO_2/Nb/Nb_2O_5$ thin layer sample, which I received for testing in an STM point-contact setup I routinely used around that time for room temperature [101] and low temperature [O6] measurements on Nb_2O_5 layers created with anodic oxidation. In these STM point-contact measurements a sharpened metallic tip is approached and touched to the surface of the sample while the tip is electrically biased, until a pre-defined setpoint resistance is reached. Using this method, the tip is indented to the surface of the layer which can result a nanometer-sized active region thickness. This was confirmed by my later studies comparing RS characteristics of memristive STM point-contacts and a crosspoint Ta_2O_5 device with active layer thickness of 3.5 nm [O2].

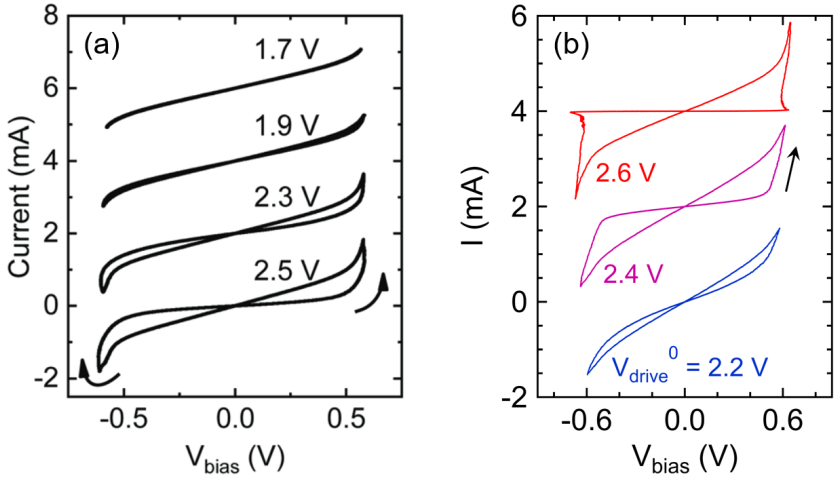

Figure 3.7: *Test measurements of Nb_2O_5 thin layers deposited with reactive sputtering, using STM point-contact technique. Comparison of typical, driving voltage amplitude (V^0_{drive})-dependent RS characteristics of (a) Nb/Nb_2O_5(an.)/PtIr(tip) and (b) Nb/Nb_2O_5(sp.)/PtIr(tip) junctions, at room temperature conditions. Abbreviations refer to the deposition method of the niobium oxide layer; 'an.' = anodic oxidation and 'sp.' = reactive sputtering.*

Figure 3.7 shows a comparison of typical, driving voltage amplitude-dependent RS characteristics recorded on a 20 nm Nb_2O_5 thin layer sample made with anodic oxidation (shown in panel (a)) and the 55 nm sputtered Nb_2O_5 thin layer sample (shown in panel (b)) I received from László Pósa. RS characteristics show similar traits for both layers, operating in the same current- and voltage regime and exhibiting similar nonlinearity in the resistance states (close to switching).

Resistive switching properties of vertically stacked structures are highly dependent on their fabrication technique, since variations in the composition of the active layer or the electrode materials can lead to very different device characteristics [109]. I had the opportunity to experiment with different compositions, and also to perform RS characterisation measurements in the same time, thus fine-tuning fabrication parameters in an iterative manner. In the following, I show some examples of the best-performing Ta_2O_5 and Nb_2O_5-based crosspoint resistive switching devices which I developed in such an iterative development process. The general lithography layout of these structures is shown in Figure 3.8.

A usual sample fabrication cycle starts with cutting a SiO_2 substrate to ~1 cm x 1 cm pieces, which I am going to refer to as *chips* from now on. On top of these chips, usually 10 x 10 individual devices are formed in a matrix with 500 μm spacing between the devices. Each device has a pair of 150 μm x 150 μm rectangular bonding pads (see Figure 3.8.a) leading to the electrodes whose width is varied between 500 nm – 2 μm. Near the crossing, the bottom layer contains 4 x 2 small rectangles used as markers (see dark blue regions

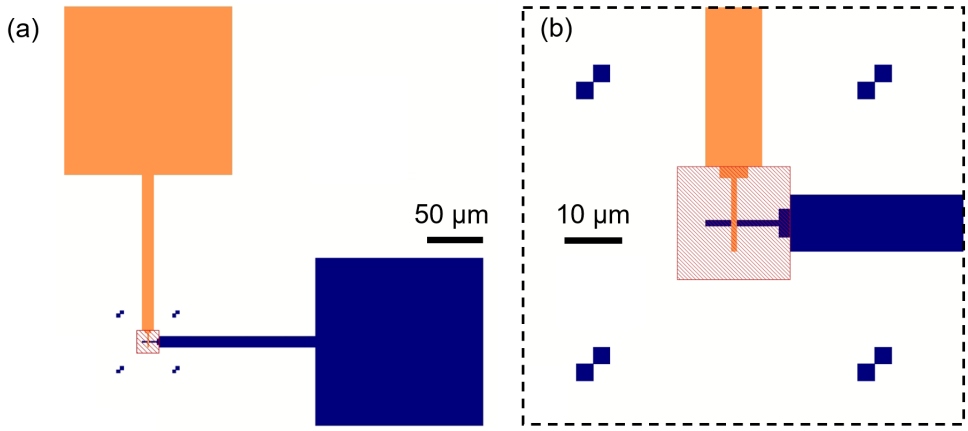

Figure 3.8: *Typical design of vertical crosspoint memristors shown (a) at a full scale and (b) magnifying around the crossing of electrodes. The width of electrodes near the crossing point is usually varied between 500 nm – 2 µm, the image shows a sample with 1 µm electrode width. The lithography/deposition of layers is performed in the following order: 1. dark blue regions (metallic bottom electrode), 2. red striped area (metal oxide active layer), 3. orange regions (metallic top electrode).*

in Figure 3.8.b) for the correct positioning of subsequent layers. The production of each layer consists of (i) patterning via a standard electron beam lithography process using a single layer of PMMA as resist, and (ii) a thin layer deposition step with electron beam evaporation or sputter deposition (either reactive or not).

The parameters of six chips containing Ta_2O_5 and Nb_2O_5 based devices with different layer structures are listed in Table 3.1 (from bottom to top layers, including nominal layer thickness values and optional layer treatment in brackets). The proper choice of electrode material is crucial for the operation of these on-chip devices. For stable and reproducible RS characteristics, a sort of asymmetry is vital, to ensure bipolar operation with a well-defined switching direction. The application of different electrode materials is the only possibility to introduce asymmetry in the design of crosspoint devices, since establishing a geometric asymmetry similar to STM point-contact devices (sharp tip - flat counter electrode) would be challenging in a vertically stacked on-chip memristor. Therefore, I applied Pt bottom electrodes for all devices as an inert layer (with respect to possible redox reactions), and Ti, Al, or Ta top electrodes which are metals with stable oxides, commonly used in OxRAM devices (see material structure of the 11-bit precision memeristor shown earlier in Figure 2.18 [82]). Under the Pt bottom electrodes, thin Ti layers were deposited in all cases, to ensure proper adhesion to the substrate.

The choice of electrode materials and layer thicknesses for Nb-chips were motivated by examples from the literature [45, 110–113]. The thickness of the oxide layer was fixed to 17 nm for all chips. Chip Nb#1 was designed and fabricated relying on my prior experiences and also inspired by examples from the literature as a base structure. For chip Nb#2, Ar^+ plasma treatment of the active layer was carried out with the mask of the top layer, directly before the deposition of the top electrode. Chip Nb#3 was another experimental design, with the replacement of the aluminum top electrode material to titanium.

Chip name	Layer structure
Nb#1	Ti(5 nm)/Pt(50 nm)/Nb_2O_5(17 nm)/Al(60 nm)
Nb#2	Ti(5 nm)/Pt(50 nm)/Nb_2O_5(17 nm, Ar^+)/Al(60 nm)
Nb#3	Ti(5 nm)/Pt(50 nm)/Nb_2O_5(17 nm)/Ti(60 nm)
Ta#1	Ti(5 nm)/Pt(50 nm)/Ta_2O_5(5 nm)/Ta(100 nm)
Ta#2	Ti(5 nm)/Pt(50 nm)/Ta_2O_5(3.5 nm)/Ta(100 nm)
Ta#3	Ti(5 nm)/Ta(100 nm)/Pt(3.5 nm)/Ta_2O_5(3.5 nm)/Ta(100 nm)

Table 3.1: *Layer structures of the developed Nb_2O_5 and Ta_2O_5 crosspoint devices.*

As for the Ta_2O_5 devices, I determined electrode materials and the thicknesses of the active layers based on examples from the literature [42, 43, 104, 114–116], aiming the smallest oxide layer thickness possible. One important goal of these series of chips (Ta#1, Ta#2 and Ta#3 listed in Table 3.1) was to fabricate ultra-small on-chip devices suitable for superconducting spectroscopy measurements. Chips Ta#1 and Ta#2 were developed for general purposes, while chip Ta#3 was designed specifically for superconducting subgap measurements (see later in the end of Chapter 5). A device for subgap studies should fulfill two basic properties: (i) bulk electrode materials should be superconductors (e.g. tantalum) and (ii) the thickness of the active region should be as small as possible, since the presence of intrinsically non-superconducting regions can limit the resolution of subgap spectroscopy, and the applicability of our model (superconductor – constriction – superconductor physical system). The first point conflicts with resistive switching, since the stability of switching is heavily affected by the asymmetry of the system [100]. I attempted to resolve this problem by creating devices with both electrodes made of tantalum and introducing a compositional asymmetry with a thin Pt layer on top of the bottom electrode to facilitate RS (chip Ta#3).

3.2.1 Experiments with electroforming

During the electroforming process of memristive devices, a conductive filament in the oxide layer is formed for the first time, therefore electroforming of filamentary devices is crucial for later operation [117]. Usually, a slow voltage sweep is carried out employing a current limit in the 10μA – 1mA range. As a first approach, I attempted to carry out electroforming in a similar manner, applying driving voltage sweeps up to 10 V, experimenting with different serial resistances providing different current limits. In my experience, an irreversible dielectric breakdown occurred in nearly all of the 30 devices I tested, arriving at (a typically permanent) resistance state falling in the 100–200 Ω range, irrespective of the applied serial resistance. It is worth noting that only 3 out of 30 devices remained operational, via applying a similar, slowly ramped reset voltage with the opposite polarity, which could restore device resistance to the $\sim$10 kΩ range.

As a next attempt, I tried a slightly different approach to "slow down" the electro-breakdown process via applying constant driving voltages to the devices (keeping the serial resistance in the circuit). One of the first successful attempts is seen in Figure 3.9. I applied constant voltage to the device for a longer time period (in the $\sim$s range), while monitoring the resistance. When no change was observed in the resistance, I increased driving voltage in a stepwise manner, and when I observed a considerable decrease in the resistance, I decreased driving voltage. First, I applied 100 kΩ serial resistance limiting the current at $\sim$25 μA, and when the resistance of the memristor reached the $\sim$100 kΩ

range, I decreased the serial resistance to 20 kΩ limiting the current at ∼125 μA (at 2.5 V driving voltage level).

The above described slow, manual process has some disadvantages, since (i) it employs a feedback to the resistance which could be implemented via a software trigger event, however defining a proper trigger condition is not trivial; (ii) a change of the serial resistance is needed which is also not an easy task to carry out in a fully automatized forming process, and (iii) the whole electroforming process took ∼600 s time, which is too long if there are many devices to characterize. Again, I turned to try another approach, inspired by the work of László Pósa. Electrobreakdown process for establishing nanosized gaps in SiO_x/graphene devices was worked out and optimized by László [32, 36] (see more details on applying this process for metal/SiO_x samples in Section 3.1). This controlled electrobreakdown process results in truly nanometer-sized gaps which cannot be created with standard lithography techniques. The core element of the procedure is to facilitate thinning and an eventual breakdown of a graphene nanostripe via short driving voltage pulses, increasing in amplitude in a stepwise manner, while employing a feedback to the resistance (stopping and restarting the voltage amplitude-increasing cycle when the resistance increases with a pre-defined percentage). The whole process is terminated when a given setpoint resistance is reached.

To avoid irreversible dielectric breakdown during electroforming of OxRAM devices, and inspired by the above described electrobreakdown procedure capable of creating nanosized devices from graphene stripes, I eventually took the following approach: I decreased

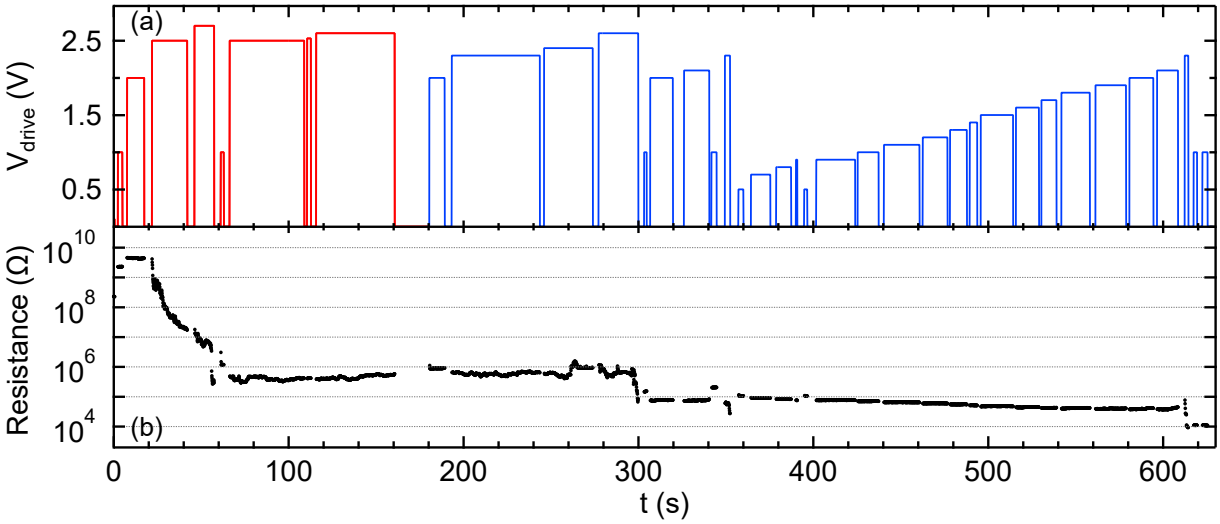

Figure 3.9: *Slow, manual electroforming performed on an Nb_2O_5 crosspoint device. Panel (a) shows the applied driving voltage signal, and panel (b) shows device resistance over time. Color code of panel (a) marks different serial resistance values of 100 kΩ (red) and 22.9 kΩ (blue).*

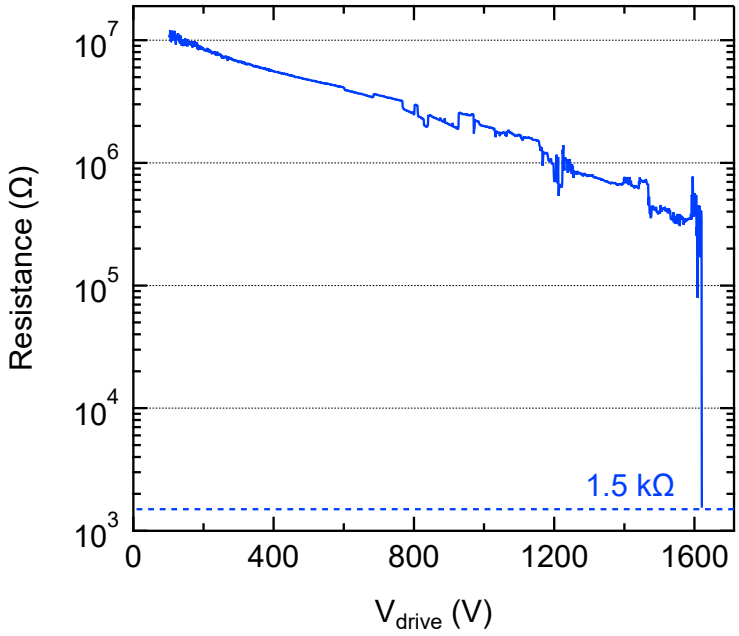

Figure 3.10: *Example for a fast, pulsed electroforming process of a Ta_2O_5 crosspoint device, displaying the device resistance measured during each pulse versus the amplitude of the driving voltage pulse. Parameters of electroforming were $R_s = 100$ $k\Omega$, $R_{\text{setpoint}} = 100$ $k\Omega$, 1 mV stepsize and $t_{\text{pulse}} = 100$ μs pulse length.*

the applied driving pulse width to $t_{\text{pulse}} = 500$ μs to speed up the electroforming process, I increased the number of voltage steps with a fine stepsize of 1 mV, I applied a constant 100 kΩ serial resistance to limit the current, and I completely omitted any feedback to the resistance to simplify the process. I applied only a single condition: the process stops when the resistance decreases below a certain value (setpoint resistance, R_{setpoint}). Decreasing the pulse width and decreasing the voltage stepsize can both contribute to a "soft" dielectric breakdown process. An exemplary resistance – driving voltage pulse amplitude trace is shown in Figure 3.10. Omitting feedback to the resistance is the single factor which hinders "soft" electroforming, however it considerably speeds up the forming process.

The above described fast, pulsed electroforming process was routinely employed for my own Nb_2O_5 and Ta_2O_5 devices, and also for Ta_2O_5 devices received from Miklós Csontos (used in the neural detector circuit discussed later in Subsection 3.3.6). My Nb_2O_5 and Ta_2O_5 devices electroformed with this method were the subject of noise spectroscopy measurements of Botond Sánta [O1] and my own low temperature measurements [O2].

3.2.2 Characterisation of resistive switching

Endurance of a resistive switching memory device is usually defined as the number of cycles it can be switched between two states, maintaining high enough $R_{\mathrm{OFF}}/R_{\mathrm{ON}}$ ratio [118]. The results of typical endurance measurements of Nb_2O_5 and Ta_2O_5 devices are displayed in Figures 3.11 and 3.12. Measurements were carried out using driving triangular voltage signals at ∼1 Hz frequency. Both devices required an asymmetric

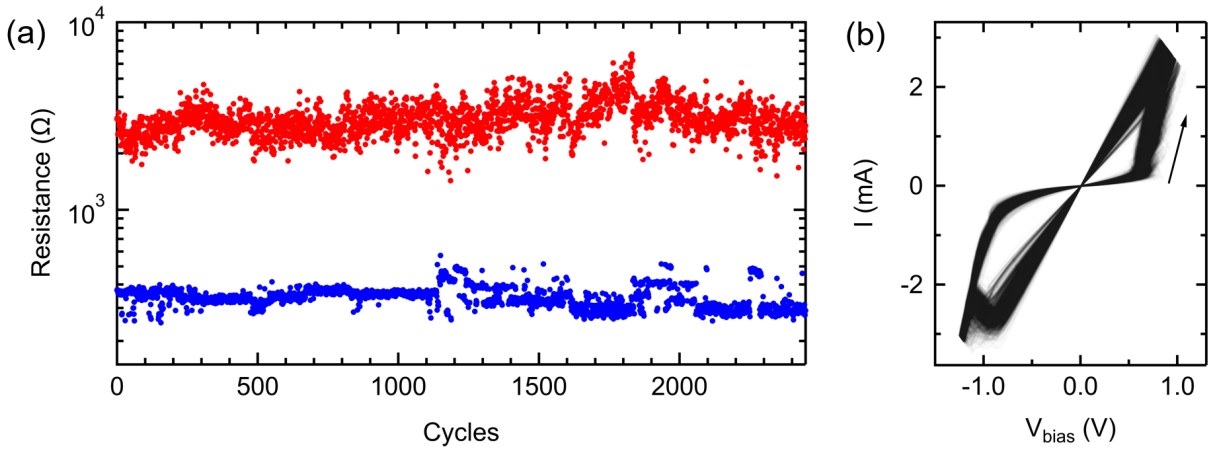

Figure 3.11: *Endurance measurment performed on $Pt/Nb_2O_5/Al$ crosspoint devices via cycling triangular voltage signals at ∼1 Hz frequency. (a) Resistances of ON and OFF states as a function of the cycle number, extracted from fitting of the 0–100 mV range of $I(V)$characteristics. (b) 2450 consecutive $I(V)$ traces (source of panel (a)) displayed on top of each other using semitransparent black lines (with $\alpha = 0.02$ transparency).*

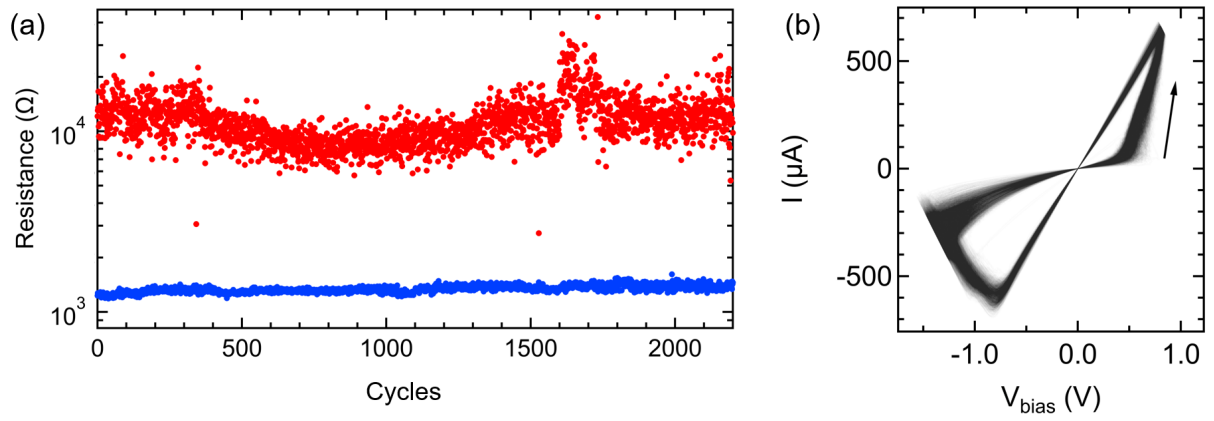

Figure 3.12: *Endurance measurment performed on $Pt/Ta_2O_5/Ta$ crosspoint devices via cycling triangular voltage signals at ∼1 Hz frequency. (a) Resistances of ON and OFF states as a function of the cycle number, extracted from fitting of the 0–100 mV range of $I(V)$characteristics. (b) 2200 consecutive $I(V)$ traces (source of panel (a)) displayed on top of each other using semitransparent black lines (with $\alpha = 0.05$ transparency).*

driving voltage for maintaining a given $R_{\mathrm{OFF}}/R_{\mathrm{ON}}$ ratio. For both devices, the positive and negative amplitudes of asymmetric driving signals could be tuned such that RS remains stable with $R_{\mathrm{OFF}}/R_{\mathrm{ON}} > 10$ ratio, for more than 2000 cycles. In general, when devices are programmed with short voltage pulses, the $R_{\mathrm{OFF}}/R_{\mathrm{ON}}$ ratio can be maintained for more cycles than for $I(V)$ sweeps carried out at relatively slow $\sim$1 Hz frequency, meaning that the endurance of devices in measurements where they are programmed with voltage pulses can be much higher than the 2000 cycles reported here. The latter observation is consistent with examples from the literature [118]. Furthermore, the $I(V)$ sweep approach does not replicate the stresses experienced by devices in realistic application scenarios. Consequently, the data obtained through this method may not accurately reflect the endurance of the same resistive switching (RS) cell during actual operational conditions. However, performing endurance measurements using slow $I(V)$ sweeps has the advantage of seeing the whole $I(V)$ trace during cycle to cycle (see $>$ 2000 consecutive measurements plotted on top of each other in Figure 3.11.b and Figure 3.12.b), which carries valuable information on the stability of operation.

3.2.3 Measurements towards applications

In the following I am going to present results of measurements targeting some applications the OxRAM devices I have developed. Some of these measurements were carried out by my colleagues; neural signal detection measurements were performed by Dániel Molnár and noise spectroscopy measurements were done by Botond Sánta and György Lázár.

Neural spike detection with OxRAM devices Many resistive switching structures exhibit a peculiar time- and voltage dependent characteristic, often referred to as time-voltage dilemma [58]. The essence of this phenomenon is that memristive devices programmed by high driving voltage signals "speed up" on an exponential scale (roughly speaking), i.e. the time required for switching to a certain state decreases drastically upon a slight increase of the driving voltage amplitude [59]. In measurements performed via triangular driving signals (see $I(V)$ curves for Nb_2O_5 and Ta_2O_5 devices in Figure 3.13.a,b, respectively), the $R_{\mathrm{OFF}}/R_{\mathrm{ON}}$ switching ratio can be calculated as a function of the V^0_{drive} driving voltage amplitude and f frequency. Figure 3.13.c shows such a dependence measured on a $Pt/Nb_2O_5/Al$ device. It is apparent that slowly ramped triangular signals ($f_{\mathrm{drive}} = 215$ Hz) at the highest applied drive amplitude ($V^0_{\mathrm{drive}} = 2.3$ V) lead to $R_{\mathrm{OFF}}/R_{\mathrm{ON}} \approx 2$ switching ratio (see orange point in the top left corner of the image plot), whereas faster signals ($f_{\mathrm{drive}} = 10$ kHz) with the same amplitude result in a decreased switching ratio, $R_{\mathrm{OFF}}/R_{\mathrm{ON}} = 1.36$ (top right corner, dark green datapoint). Maintaining $f_{\mathrm{drive}} = 10$ kHz) frequency and decreasing the drive amplitude to $V^0_{\mathrm{drive}} = 1.5$ V leads to

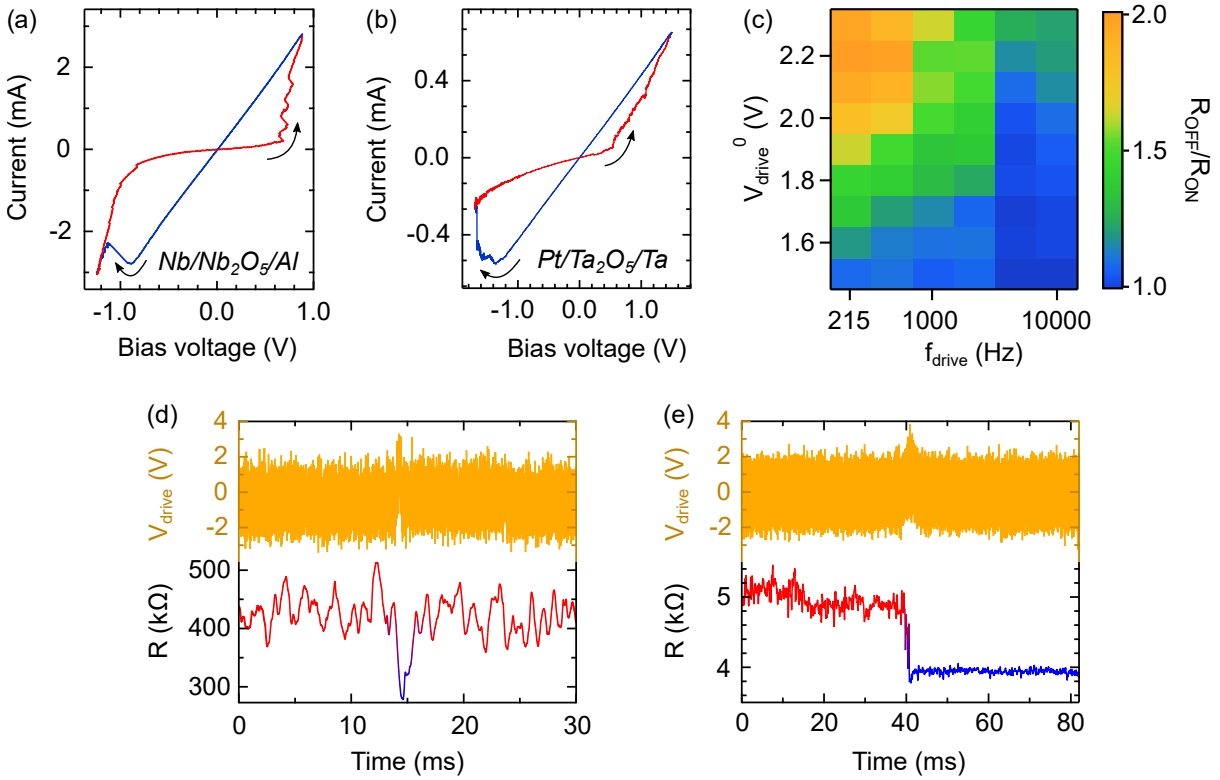

Figure 3.13: *First steps towards neural spike detection using OxRAM devices. Typical RS characteristics of (a) $Pt/Nb_2O_5/Al$ devices and (b) $Pt/Ta_2O_5/Ta$ devices. (c) Time-voltage dilemma of $Pt/Nb_2O_5/Al$ devices, displaying the driving amplitude- and frequency-dependent switching ratio. Neural spike detection performed with (d) $Pt/Nb_2O_5/Al$ and (e) $Pt/Ta_2O_5/Ta$ devices, where orange traces show the drive voltage and red/blue colored curves are the computed resistance values. Noted that the resistance traces are evaluated from the drive voltage and the current, and are not compensated with the serial resistance values, which were 50 Ω and 3350 Ω in the two cases, respectively. Panels (c-e) show measurements of Dániel Molnár [119].*

closing of the hysteresis in the RS $I(V)$ curves, yielding $R_{\mathrm{OFF}}/R_{\mathrm{ON}} \approx 1$ (see dark blue datapoint in the bottom right corner).

This dynamical property of OxRAM devices can be utilized for recognizing specific patterns hidden in a noisy background, where the amplitude of noise spikes is comparable to the targeted pattern, while their typical timescales differ. In a detection measurement using memristors, the driving voltage signal consists of a Gaussian pulse added to a noisy background with Gaussian distribution and a small DC bias voltage. This setting resembles the conditions where true neural spikes are measured in neuroscience [96], therefore I am going to address the Gaussian pulse to be detected as *neural spike*.

The result of a neural spike detection experiment using a $Pt/Nb_2O_5/Al$ device is displayed in Figure 3.13.d. The incoming neural spike with $\mathrm{FWHM}^{\mathrm{Nb}}$ =0.27 ms and

$V_{\text{peak}}^{\text{Nb}} = 2.52$ V height is hidden in a Gaussian background with $\sigma^{\text{Nb}} = 0.76$ V standard deviation and offset to the mean $\mu^{\text{Nb}} = -0.57$ V level. Fluctuations originating from this noisy background do not change the resistance, whereas the neural spike induces a slight decrease in the device resistance which seems to be volatile, as it relaxes back to its initial state in $t_{\text{relax.}}^{\text{Nb}} \approx 1$ ms time. The intrinsic non-linearity of each resistance state in Nb_2O_5 devices, which appears independently of RS [101] hinders neural spike detection experiments, since resistive switching – especially a volatile one relaxing to its original state on the timescale of the neural spike – can be hard to distinguish from the effect of non-linearity.

This disadvantageous effect can be alleviated by using a memristor with more linear characteristics, such as a Ta_2O_5-based device. A similar spike detection experiment with a $Pt/Ta_2O_5/Ta$ device is shown in Figure 3.13.e. The neural spike has $\text{FWHM}^{\text{Ta}} = 2.86$ ms width and $V_{\text{peak}}^{\text{Ta}} = 1.05$ V height, while the noise has $\sigma^{\text{Ta}} = 0.65$ V standard deviation and it is offset to the mean $\mu^{\text{Ta}} = -0.12$ V level for readout. In contrast to the Nb_2O_5 device, the Ta_2O_5 memristor remains in a stable state on the timescale of the measurement, showing a clear detection event. This resistance change, however, is a challenging task to detect e.g. in a targeted edge computing application. By passing a similar signal to the input of a volatile VO_2 memristor-based oscillator circuit, an autonomous neural spike detector unit can be established [O4] (see more details on this detector unit in Section 3.3.6).

Noise tailoring of OxRAM devices Noise measurements enable to determine the maximum bit resolution which the internal device noise allows for, a highly important parameter of analog crossbar arrays. Comparative noise spectroscopy studies of different memristive systems contribute to the proper material choice to achieve high bit resolution with low-noise devices. Drive voltage-dependent noise spectroscopy measurements targeting the voltage domain just before the onset of switching events is particularly useful for seeking special procedures to influence noise characteristics in a given resistance state (similarly to the denoising procedure presented in Subsection 2.2.3 [82]). Tunable noise characteristics can also aid hardware-level operation of stochastic optimization algorithms, as shown previously in the last paragraph of Subsection 2.2.3 and in Ref. 84. For such applications, studying noise characteristics and finding ways to control these in on-chip devices are essential.

Our research group has extensive experience with noise spectroscopy studies of atomic junctions, single-molecule junctions, graphene nanogaps and memristive systems [86–88, 120, 121]. Fluctuations can be perceived as current noise, which is defined as the difference from its mean value, $\Delta I(t) = I(t) - \langle I(t) \rangle$. The mean squared deviation of this quantity, calculated within a frequency band Δf centered around an f_0 central frequency and

normalized to Δf, provides the spectral density of the current noise:

$$S_I = \frac{\langle (\Delta I(t|f_0, \Delta f))^2 \rangle}{\Delta f}.$$

The origin of fluctuations in an electronic device can be attributed to processes at the scale of electrons and atoms, e.g. trapping/de-trapping of electrons in vacancies or the scattering of electrons on atomic fluctuators [88]. These phenomena can have their individual characteristic timescale in a broad domain, which yields fundamental consequences on $S_I(f)$ noise spectra, leading to a universal, $1/f$-type dependence for a large ensemble of fluctuators distributed evenly in the system. Studying individual characteristics of these $1/f$-type noise spectra (e.g. deviations from $1/f$ character) or mapping the scaling of $1/f$ noise on the resistance of the system can reveal fundamental information on physical processes behind the transport and the source of fluctuations.

In a usual noise spectroscopy measurement on a memristor, the device is initialized in a state via driving triangular signals or voltage pulses higher than the switching threshold, and then the current is recorded for long time periods with a high bandwidth measurement setup at constant, subthreshold bias levels. Then, raw noise spectra are computed via FFT (fast Fourier transform) of the $I(t)$ signal, and the zero bias noise floor is subtracted. The numerical integration of these spectra yield the $\Delta I/I$ relative current fluctuation. This quantity is the subject of the studies shown in Figure 3.14, carried out by my colleagues Botond Sánta and György Lázár, investigating Nb_2O_5 and Ta_2O_5 crosspoint devices I have developed.

Figure 3.14.a shows a comparative study of $\Delta I/I$, measured in various resistance states of $Pt/Nb_2O_5/Al$ crosspoint devices (see gray datapoints), and in the ON and OFF states of $Nb/Nb_2O_5/PtIr$ STM point-contact junctions (dark blue and dark red points) [O1]. The measurements reported here were the first noise spectroscopy studies of on-chip samples in our research group. From an applications perspective, it is important to investigate if prior measurements on STM point-contact devices correspond to results on on-chip devices or not. Devices made of the same active material – in this case Nb_2O_5 – could yield markedly different noise characteristics, due to the presence of different species (Al instead of Nb) at the active electrode site. In the case of STM devices, more than 20 independent point-contact junctions were studied with varying ON and OFF state resistances. As for the crosspoint device, multilevel programming was accomplished via applying voltage pulses. A well-defined resistance scaling of $\Delta I/I$ is observable, irrespective of the type of device or ON/OFF states, similarly to prior measurements on Ag-based filaments in Ag_2S and AgI memristive devices [86]. However, an important difference to Ag-based systems is the overall decreased magnitude of $\Delta I/I$ current fluctuations, which promote employing oxygen migration-based Nb_2O_5 devices instead of Ag^+ cation migration-based memristors in certain hardware applications, where low noise levels are favorable.

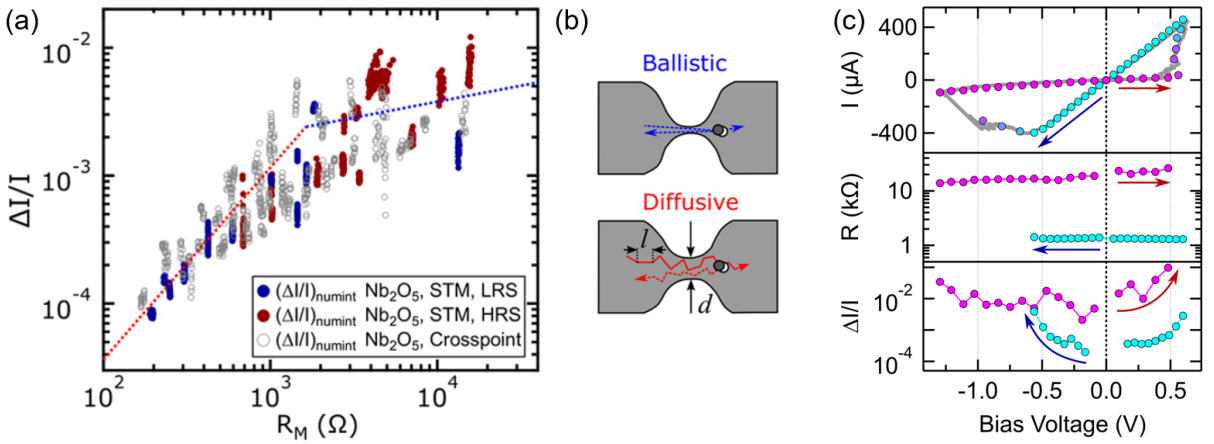

Figure 3.14: *Noise spectroscopy studies of OxRAM devices. (a) Scaling of $\Delta I/I$ relative current fluctuation on device resistance, measured in a $Pt/Nb_2O_5/Al$ crosspoint device (gray points) and $>$ 20 independent $Nb/Nb_2O_5/PtIr$ STM point contact junctions (dark red/blue points, referring to OFF/ON states of each device). (b) Illustration of the models considering the effects of a dynamical defect near a ballistic ($l > d$, top panel), and a diffusive ($l < d$, bottom panel) [O1] junction, where d denotes the junction diameter and l is the mean free path of electrons. (c) Studies of non-linear noise characteristics of $Pt/Ta_2O_5/Ta$ devices, showing the $I(V)$ curve of the device (top panel) during triangular voltage sweeps (gray curve) and noise spectroscopy measurements at discrete DC bias levels (see pink/cyan datapoints for the OFF/ON states). Panels in the middle and at the bottom show the resistance of the device and the relative current fluctuation evaluated from noise spectra. Dark blue/dark red arrows indicate those datapoints, where the ON/OFF state yields constant resistance. Note, that the relative current fluctuation undergoes a drastic increase already before the onset of resistive switching (see curved arrows at the bottom panel). [122] Panel (a) show measurements of Botond Sánta and data in panel (c) was measured by György Lázár.*

The datapoints in Figure 3.14.a follow two distinct tendencies as a function of the resistance, scattering around lines with different slopes for different resistance regions. To reveal the origin of this difference, a point-contact model is considered which relies on electron scattering processes on dynamical defects (TLSs). The noise contribution of a single TLS near the junction depends on the ratio of the electron mean free path l and the diameter of the junction d, in other words, the ballistic ($l > d$) or diffusive ($l < d$) nature of the contact in terms of electron transport (as illustrated in Figure 3.14.b). Taking into account the proper geometric coefficients and the Maxwell/Sharvin formulae for the diffusive/ballistic regime, the data in Figure 3.14 are well fitted with the formulas obtained, as illustrated by the red/blue dashed lines.

A similar scaling of the relative current fluctuations on device resistance and also a correspondence of on-chip and STM point-contact devices were observed by my colleague György Lázár, who studied noise characteristics of $Pt/Ta_2O_5/Ta$ crosspoint devices I have produced [122]. As compared to Nb_2O_5 memristors, Ta_2O_5 devices have more linear resistance states (see Figure 3.14.c, top panel), which enable studying the noise characteristics near the switching events, where the $I(V)$ curve is still linear. The dark blue/dark red arrows in the top and middle panels of Figure 3.14.c mark regions where the resistance is still constant in the ON/OFF states, before the onset of resistance change. In these linear states, $\Delta I/I = const.$ is expected, when fluctuators are not excited. On the contrary, a considerable increase of $\Delta I/I$ is observed experimentally for both ON and OFF states (see curved arrows in the bottom panel of Figure 3.14.c), yielding roughly a factor of 10 noise increment when bias voltage levels are near the switching thresholds. A possible explanation for this effect can be the presence of mobilized oxygen vacancies just before the switching event, which can introduce excess noise to the system. The redistribution of vacancies can enhance electron scattering, practically meaning the excitation of atomic fluctuators, which directly influences noise spectra. In applications where low-noise operation and/or high accuracy bit resolution are expected, the above identified voltage region where fluctuators are excited should be avoided.

Low temperature measurements of Ta_2O_5 on-chip devices Memristors are usually studied at room temperature conditions. In my works reported in Refs. [O6] and [O2] (see also Chapter 5), I have shown that important details on quantum transport properties of STM point-contact devices can be obtained by superconducting subgap measurements, performed at cryogenic temperatures. Questions arise whether this analysis can also be applied to on-chip devices, or whether on-chip samples are functional at all in low temperature environment. Finding the answer to the latter question is important not only for subgap spectroscopy measurements, but also because of the potential to use memristors for information processing in quantum electronic circuits. With a slight modification of the low temperature STM point-contact sample holder, I performed measurements to test low temperature operation of crosspoint Ta_2O_5 samples. A scanning electron micrograph of a representative crosspoint Ta_2O_5 sample is shown in Figure 3.15.a. The samples I developed for low temperature measurements exhibited very similar RS characteristics as STM point-contacts. Also, the room temperature and low temperature RS $I(V)$ characteristics of these samples show good agreement (see Figures 3.15.b-d). Furthermore, gradual tuning of the resistance states in the vicinity of the quantum conductance unit ($G_0 = 2e^2/h$, where e is the electron charge and h is Planck's constant) is possible in the set and reset directions as well, as shown in Figure 3.15.c. The inset depicts the evolution of the normal conductance of the device in these gradual

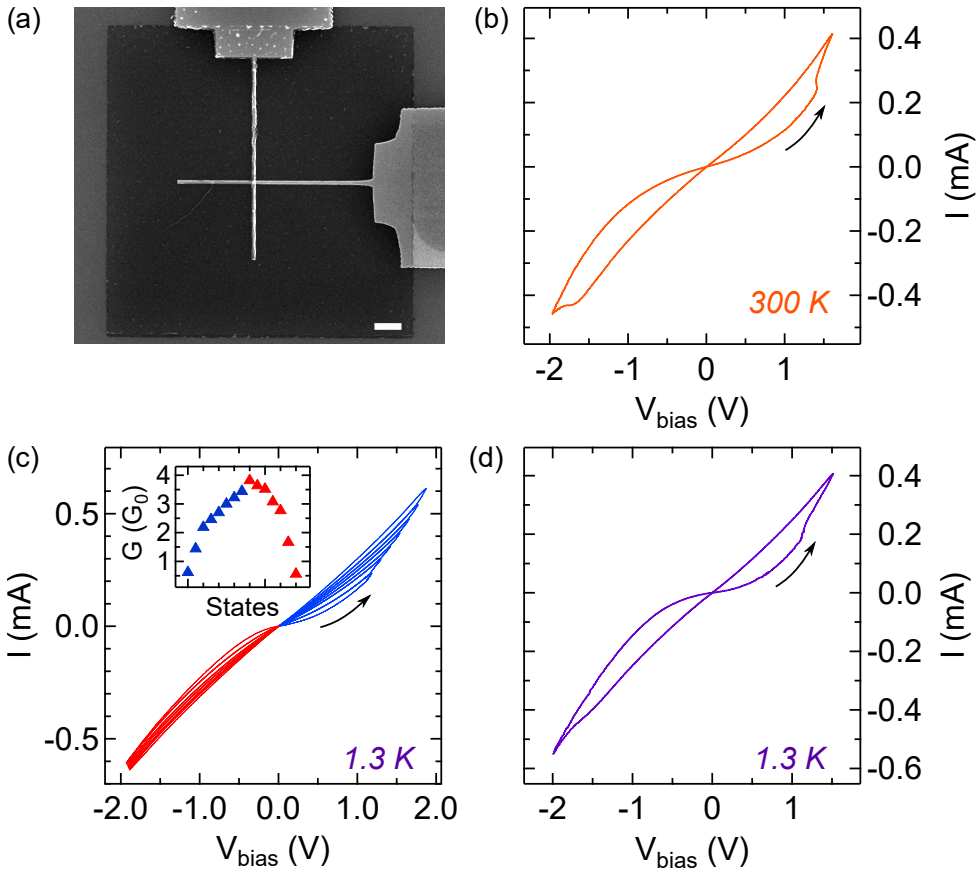

Figure 3.15: *Comparison of low temperature operation and room temperature $I(V)$ characteristics, for on-chip Ta_2O_5 crosspoint devices. (a) Scanning electron micrograph of a representative Ta_2O_5 device. Typical $I(V)$ curves of another device are shown at (b) $T = 300$ K and (c-d) $T = 1.3$ K temperature environment. Panel (c) depicts gradual set and reset characteristics, where tuning of the conductance is possible in small steps, slightly increasing the drive voltage amplitude in each step. Inset shows the normal conductance of each consecutive state of the device, evaluated from small bias voltage amplitude $I(V)$ sweeps in the ± 10 mV range. In panels (b-d), arrows show the set processes, indicating switching direction.*

states, determined from small bias voltage amplitude $I(V)$ sweeps in the ± 10 mV range (outside the voltage range of the superconducting energy gap, the $\pm 2\Delta_{\mathrm{Ta}}/e \approx \pm 1.33$ mV range). My measurements showed that switching is possible at ultra-low temperatures, yielding similar characteristics as room temperature device operation. Furthermore, I also demonstrated multilevel programming in the vicinity of the quantum conductance unit. I discuss the results of superconducting subgap measurements performed on Ta_2O_5 devices in the end of Chapter 5, Subsection 5.4.4. These experiments indicate that subgap characteristics of on-chip devices indeed reveal information on quantum transport properties, but further optimization would be needed for better resolution to fit subgap characteristics.

3.3 Planar VO_2 Mott memristors

For studying VO_2 Mott memristors, I created different devices in a planar geometry according to the lithography layout shown in Figure 3.16. The design of the smallest parts of the electrodes in the middle (marked with blue, a triangle facing a flat line) was optimized by László Pósa. During my work, I used this geometry for the fabrication of all devices. I kept the electrode separation always at a constant 30 nm value in the design, and the size of the resulting nanogaps were fine-tuned with the variation of the dose during lithography. The size of the nanogaps was measured via taking SEM images after the deposition of the electrode material.

I varied the electrode materials and also the type of VO_2 active layers to explore possibilities towards further optimization of device materials, relying on different kinds of measurement techniques ($R(T)$, $I(V)$ characterisation, pulsed endurance measurements, SEM imaging and noise spectroscopy measurements). I have also fabricated devices with different gap sizes, and studied the effect of the gap size on the RS characteristics. Different kinds of vanadium oxide devices subject to my studies are summarized in Table 3.2.

My work also involved the development of vanadium oxide-based devices optimized for studying the RS phenomena and resistance relaxation effects falling to the < 1 ns timescale. The design of these devices was based on the electrode layout of tantalum pentoxide devices made by Miklós Csontos, which currently hold the world record for time-resolved, electrically induced resistive switching, operable with 20 ps signals (see a brief summary of these ultra-fast measurements earlier in Section 2.1.2) [44]. For these devices,

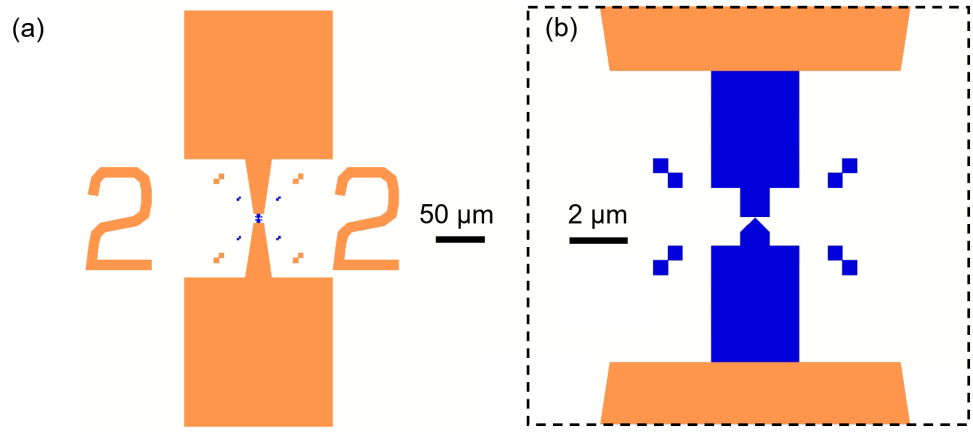

Figure 3.16: *Typical design of planar VO_2 memristors shown (a) at a full scale and (b) magnifying around the nanogap region. The numbers in panel (a) denote the row and column indices of the sample. Samples were prepared in a single step, the colors only mark small (blue) and large (orange) structures scanned with different settings during lithography (aperture, writefield, stepsize etc.).*

Fixed	Au electrodes	Thermal VO_2 layer	Au electrodes, thermal VO_2
Varied	VO_2 layer:	Electrode:	Gap size:
	Thermal, PLD, ALD	Au, Pt, Cr	10 ... 80 nm range

Table 3.2: *Summary of different types of vanadium oxide devices subject to my studies.*

establishing a coplanar waveguide geometry was vital for real-time radio frequency (RF) electric measurements. Fabricating the waveguide required the selective removal of the VO_2 layer in order to avoid conduction between the ground lines and the inner electrode line. For this purpose, I applied chemical and physical etching techniques for two types of VO_2 layers, thermal and epitaxial oxides (see Subsection 3.3.7). These RF vanadium oxide devices were tested by Sebastian Werner Schmid and Miklós Csontos using a high bandwidth measurement system at the laboratories of ETH Zurich.

3.3.1 Role of the VO_2 layer's deposition techinque

To study the effect of the deposition techinque of the VO_2 layer (see first column of Table 3.2), the resistance – temperature dependence of nanogap devices are compared in Figure 3.17.a. For these studies, I analyzed VO_2 films created via thermal oxidation [O3], PLD (pulsed laser deposition) [123], and ALD (atomic layer deposition) [124] methods. The latter, PLD and ALD VO_2 films were deposited onto Al_2O_3 substrates, while the thermal VO_2 film was created on a $Si/SiO_2(1\ \mu m)$ layer. The deposition techniques and the resulting layer structures are summarized as follows:

- Th-VO_2: A 100 ± 4 nm vanadium layer on top of a $Si/SiO_2(1\ \mu m)$ is oxidized in a tube furnace at 400°C for 4.5 hours at 0.1 mbar sparse air. The thermal annealing procedure results in the expansion of the vanadium film, yielding a V_2O_5(170–190 nm)/VO_2(30–50 nm) bilayer structure with varying thicknesses and granular morphology. [O3] The layers were prepared by György Molnár.

- ALD VO_2: On top of a sapphire substrate, amorphous vanadium oxide layers are prepared via atomic layer deposition, which is a self-limiting layer-by-layer growth technique. During the process, TEMAV (tetrakis ethylmethyl-amino vanadium) precursor gas and H_2O oxidant were used, and a post-deposition annealing was carried out at 500°C and 3 hours. The resulting VO_2 layer is uniform and crystalline. An important difference to Th-VO_2 layer is that TEM images revealed a compact, dense layer, without any cavities. Layer thickness is $\approx$ 65 nm. The layers were prepared by Zsófia Baji, and the detailed procedure is reported in Ref. 124.

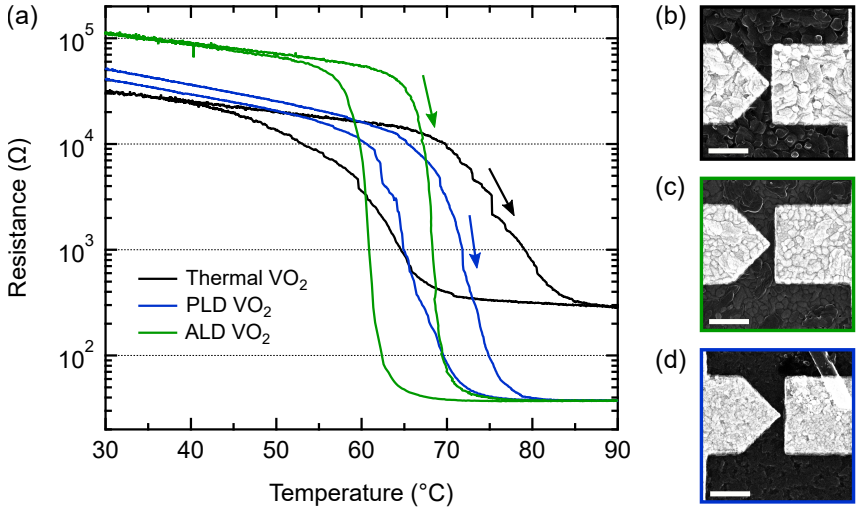

Figure 3.17: *Effect of the VO_2 layer's deposition techinque on the insulator-metal transition. (a) Resistance – temperature characteristics of nanogap devices fabricated on Th-VO_2, ALD VO_2 and PLD VO_2 layers (see color code in legend). (b-d) SEM images of different devices, scalebars are 500 nm in all images. Coloring of the frames correspond to the color coding in panel (a).*

- PLD VO_2: On top of a sapphire substrate, epitaxial vanadium dioxide layers are prepared via pulsed laser deposition, resulting in a Al_2O_3/VO_2(50 nm) structure. Layers were prepared at the Naval Research Laboratory in USA, according to the procedure reported in Ref. 123, without any buffer layers between the single crystal Al_2O_3 substrate and the VO_2. Epitaxial growth of vanadium oxide was confirmed by X-ray diffraction (XRD) measurements.

For this purpose, similar devices were fabricated on top of each layer using the same electrode material, gold. Representative SEM images are shown in Figure 3.17.b-d, for devices on Th-VO_2, PLD VO_2 and ALD VO_2 layers, respectively. The Th-VO_2 layer exhibits the usual granularity [O3], along with the ALD VO_2 film [124]. In contrast, the surface of the PLD VO_2 layer looks more smooth. Note, that a rod-like structure is observable in the top right corner of the image (Figure 3.17.d), which is typical for the PLD VO_2 layers received, according to my experience. VO_2 is known to form various morphologies at the micro- and nanoscale, including rod-like structures [125, 126]. However, they are only sparsely found on the surface, so there is only a small chance to accidentally create a nanogap exactly at the same position as a rod.

Resistance – temperature dependencies of nanogap devices fabricated on Th-VO_2, ALD VO_2 and PLD VO_2 layers (see black, green, blue traces in Figure 3.17.a, respectively, with the same color as the frame of corresponding SEM images) reveal that the insulator-metal transition temperatures are similar for the three cases. The Th-VO_2 device exhibits

wide hysteresis and small resistance ratio of insulator and metallic phases, $R_{\text{ins}}^{\text{Th}}/R_{\text{met}}^{\text{Th}} = 106$ (evaluated at 30°C and 90°C). For PLD and ALD devices, the observed ratios are $R_{\text{ins}}^{\text{PLD}}/R_{\text{met}}^{\text{PLD}} = 1385$ and $R_{\text{ins}}^{\text{ALD}}/R_{\text{met}}^{\text{ALD}} = 3020$, respectively. Multiple factors can account for the deviation of the Th-VO_2 device from the other two devices. The known bilayer structure with inhomogeneous thicknesses of the top VO_2 and the underlying V_2O_5 layers can explain reduced resistance ratio, as the substrate material and the layer thickness can have profound effect on $R-T$ characteristics (see Section 2.1.3). Grain size can also affect $R-T$ curves, larger grain size can lead to higher resistivity ratio and decreased hysteresis width in general [63], however, it is hard to decouple all the effects of grain size and thickness experimentally. In addition, the Th-VO_2 layer expands during annealing, which can also affect the phase transition.

3.3.2 Device endurance measurement

I tested the endurance of a VO_2 device according to the pulsed measurement scheme shown in Figure 3.18.a. Driving voltage pulses with $V_{\text{set}}^0 = 3.5$ V amplitude were applied to the device to set the ON state, followed by smaller pulses with 1.7 V amplitude to measure the resistance in the OFF state (see black lines). This scheme was repeated $> 200\ 000$ times in a cycled manner and the current response was recorded, as shown with the pink line on an example trace of three cycles. Rise times of the set pulses were tuned sufficiently long to ensure the accurate determination of the V_{th} threshold level of the set process, as indicated by the black and green dashed lines in Figure 3.18.a. As long as $V_{\text{th}} < V_{\text{set}}^0$ and the device is operational, switching is maintained.

The evolution of the set threshold level and also the R_{ON} (R_{OFF}) resistance along cycling are shown in Figure 3.18.b, evaluated during every set (read) pulse. The top green trace showing V_{th} exhibits a continuously increasing trend through cycling. There is also a stepwise increase observable around the 100 000th cycle. Shortly after this event, a similar stepwise decrease and increase are observable in the otherwise uniform R_{OFF} (see red trace). The R_{ON} value (blue trace) preserves its uniformity during the whole endurance measurement.

The observed irregular step-like changes in the set threshold and the OFF state resistance might arise from interplay of the known granularity of the thermal VO_2 layer and the ultra-small, 12 ± 4 nm size of the gap region (see the SEM image of the device in Figure 3.18.c).

The endurance measurement is terminated shortly after the 220 000th cycle, due to the increased V_{th} threshold for the set process, since in the end $V_{\text{th}} < V_{\text{set}}^0$ condition is not satisfied, the threshold drifts to a higher value than the amplitude of the set voltage. It is to be noted, that that the device remained operational after the measurement, only at a slightly elevated set switching threshold. The resistance – temperature characteristics recorded

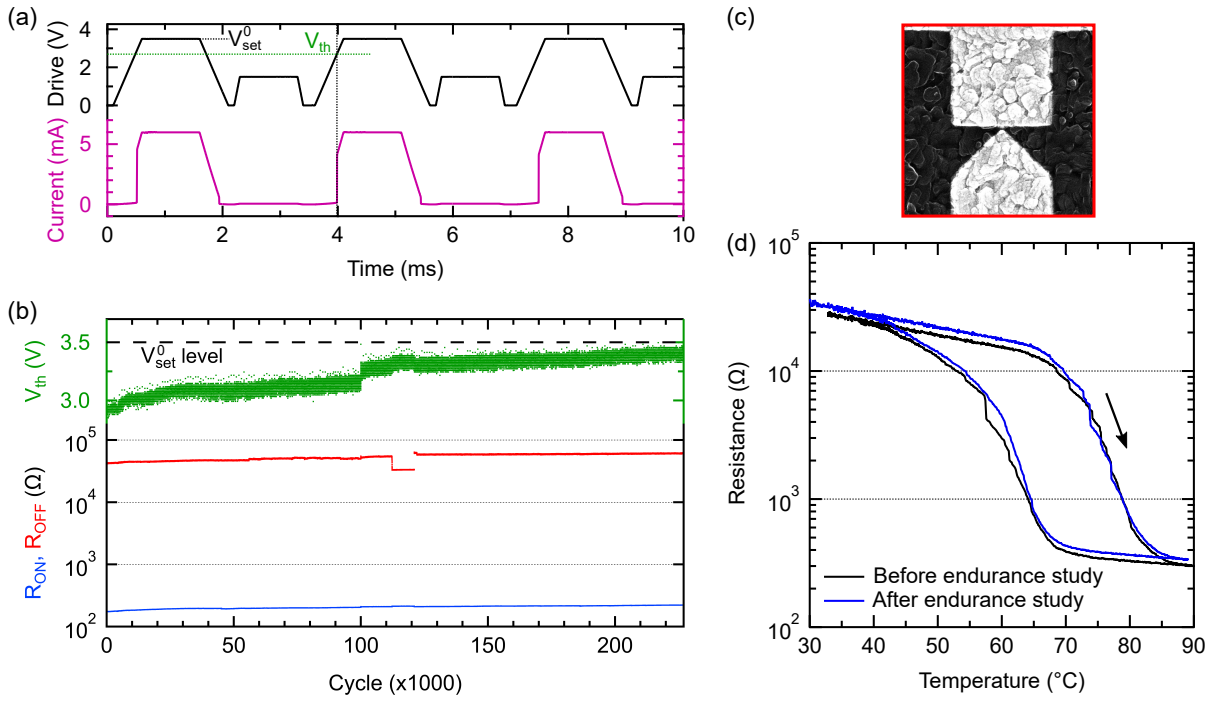

Figure 3.18: *Device endurance measurement of a planar VO_2 nanogap memristor. (a) Pulsed measurement scheme showing the drive voltage (black line) and the recorded current response of the device (pink line) for three cycles. (b) Evolution of the set threshold level and also the R_{ON} and R_{OFF} resistances along the endurance measurement. (c) SEM image of the device showing a 12 ± 4 nm gap region, scalebar: 200 nm. (d) Resistance – temperature dependencies of the device, recorded before (black trace) and after (blue trace) endurance measurement, showing minimal changes.*

before and after the endurance measurement (see black and blue traces in Figure 3.18.d) indicate that the device retained its original characteristics for temperature-driven Mott transition.

3.3.3 Effect of the electrode metal on $1/f$ noise spectra

The VO_2 samples I produced with different electrode materials (see second column of Table 3.2) were studied by my colleague Sebastian Werner Schmid. All of the samples were deposited onto the same piece of VO_2 carrier deposited via the usual recipe onto SiO_2 substrate. The lithography was done in one step, and then the piece containing devices in 6×7 matrices was cut to smaller pieces before the deposition of Au, Cr and Pt electrode materials in three separate steps. SEM images of the gap region of pristine samples with different electrode materials are shown in Figure 3.19.a-c for Au, Cr and Pt electrode samples. Gap sizes were determined as 26 ± 6 nm, 15 ± 6 nm and 20 ± 6 nm from the images (respectively for the Au, Cr and Pt electrode devices).

Bias voltage-dependent $1/f$ noise spectra of these devices was recorded, as function of the base temperature, and the evaluated nonlinear OFF state resistance values ($R-V$ curves) and the $\Delta I/I$ relative current fluctuations ratios are displayed in Figure 3.19.d-f (for the Au, Cr and Pt electrode devices, respectively). The targeted base temperatures shown with different shades of red/gray markers (according to the legend of panel (f)) were set within a ± 3 K margin of error. The resistance shows the expected smooth, nonlinear trend for the Au and Pt samples, whereas the $R-V$ curve of Cr device exhibits irregularities nearing the switching for 300 K and 310 K temperatures (see the two darkest red traces in Figure 3.19.e). Upon comparing the $\Delta I/I - V$ noise characteristics of the devices (see bottom parts of Figure 3.19.d-f, set to display the same range according to the labels of panel (d)), the overall magnitude of the relative current fluctuations and the large fluctuations in case of the Cr device are apparent (while Au and Pt devices exhibit more smooth trends). The affinity of Cr atoms to dope vanadium oxide can affect Mott

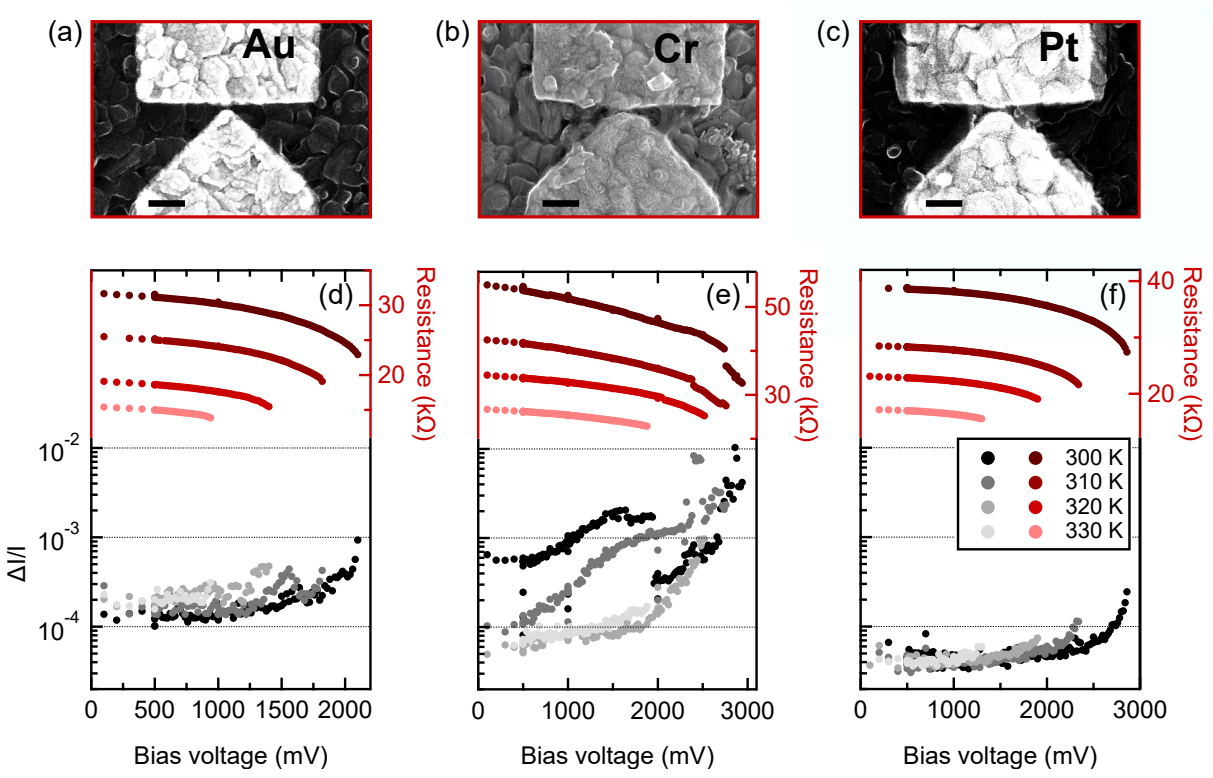

Figure 3.19: *Noise characteristics of VO_2 devices with different electrodes. (a-c) SEM images of devices with Au, Cr and Pt electrodes, with 26 ± 6 nm, 15 ± 6 nm and 20 ± 6 nm gap sizes. Scalebars are 200 nm in all images. (d-f) Nonlinear OFF state resistance values ($R-V$ curves), and $\Delta I/I$ relative current fluctuations, evaluated from $1/f$ noise spectra, as function of the base temperature. Different shades of red and black markers denote the base temperature, as shown according to the legend of panel (f). Panels (d-f) show measurements of Sebastian Werner Schmid [127].*

transition [128, 129]. Doping can also lead to an increased number of fluctuators, which can account for such irregular variation and large magnitude of $\Delta I/I$ (affecting even the $R-V$ curve of the device). Platinum electrode devices yield the least relative current fluctuations, an order of magnitude smaller than gold electrode devices. This experience corresponds to the observation of higher stability of platinum nanogaps compared to nanogaps made of gold, reported in Ref. 130. Therefore, the increased magnitude of relative current fluctuations for Au/VO_2 devices might originate from the instability of the gold electrodes.

3.3.4 Role of the gap size

For studying the effect of gap size on RS characteristics, I fabricated devices with varying electrode separation, and compared their RS $I(V)$ characteristics. The size of the nanogap affects the threshold voltage of the set process (V_{set}), as shown in Figure 3.20 [O3]. According to the usual approach described in the introductory part of present Section, I varied the dose during lithography to attain devices with different gap size. I determined the size of the nanogaps from SEM imaging after the deposition of Au electrodes, for which some examples are shown in Fig. 3.20.b-c (showing devices with 75 nm and 35 nm gaps, respectively). Then, I carried out electrical characterisation of 8 devices using a probe station, concentrating on the first few $I(V)$ characteristics of the devices (see corresponding data with black markers in Figure 3.20.a). All of them exhibited stable RS characteristics, however in some cases, a higher amplitude driving voltage signal (6 –

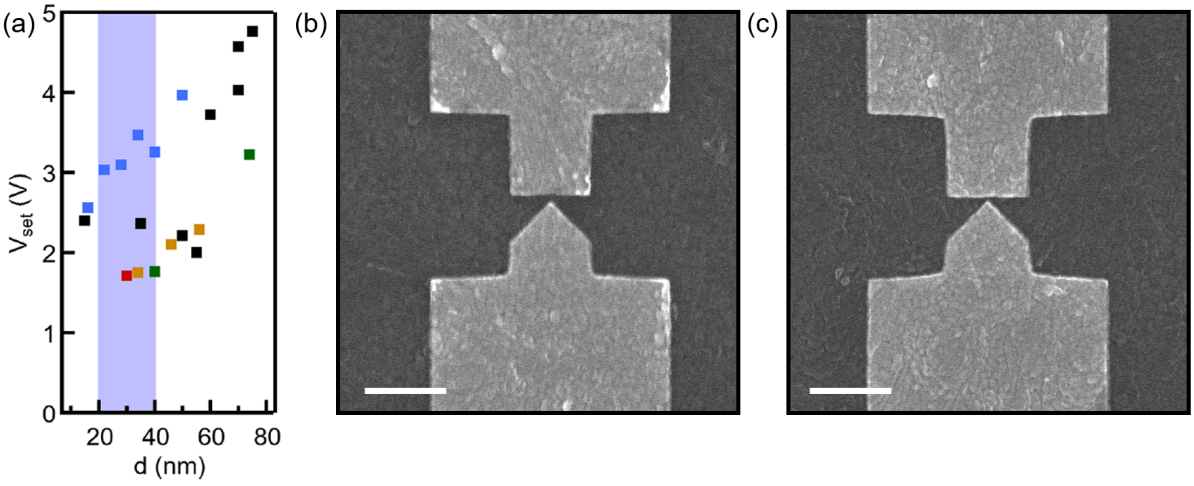

Figure 3.20: *The effect of gap size on VO_2 device operation. (a) Set voltage thresholds determined from the first few $I(V)$ characteristics measured at each device, as the function of their gap size (evaluated from SEM images). Electron micrographs of VO_2 devices with (b) 75 nm and (c) 35 nm gap size. Scalebars are 1 μm.*

9 V) was needed to initiate the first switching. After that, the threshold voltage of the set process decreased considerably to a well-defined, stable level, and this threshold is considered as the V_{set} value in Figure 3.20.a. After the first, initiating signal, the drive amplitude was reduced to prevent high currents flowing through the sample (which might lead to degradation of the devices). Measurements performed by my colleagues on other devices from different chips (see colored datapoints in Figure 3.20.a) align with my observations that devices with smaller gaps have generally lower V_{set} value.

3.3.5 Neurodynamic behavior of VO_2 memristor-based circuits

I started to build small neurodynamic circuits, artificial neurons from volatile VO_2 memristors inspired by Ref. 9. I aimed to reproduce behaviors of a tonic and a phasic neuronal circuit (namely the 'Tonic bursting' and 'Rebound spike' waveforms shown in Fig. 4. of Ref. 9), and to study the tunability of the output waveform with the variation of circuit parameters. For this purpose, I used two VO_2 devices (see their SEM images in Figure 3.21.a-b), which had similar current-voltage characteristics seen in Figure 3.21.c-d.

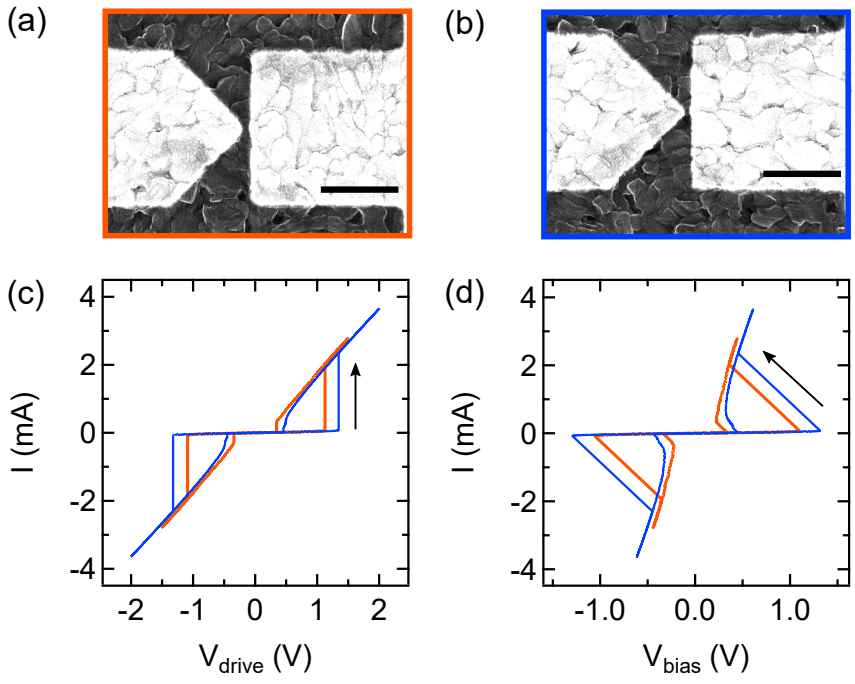

Figure 3.21: *Two Pt/VO_2/Pt devices with similar characteristics for building artificial neuron circuits. (a-b) SEM images of the devices, scalebar: 500 nm. Coloring of the frames refer to the devices' $I(V)$ characteristics in panels (c,d). (c) Drive voltage dependent, and (d) bias voltage dependent $I(V)$ characteristics. Set and reset voltages, and ON/OFF state resistances are similar for the two devices.*

A tonic neuron was assembled from the two devices, with four additional passive elements according to the schematics of the circuit shown in Figure 3.22.a ($R_1 = R_2 = 4.7$ kΩ, $C_1 = 4.7$ nF, $C_2 = 2.2$ nF). In these experiments the two memristors were biased with constant voltages of $-V_1$ and $+V_2$ with opposite polarities, and a 200 μs long pulse was applied to the input with V_{in} amplitude.

In the first experiment, the biasing voltages were kept at constant $-V_1 = -1$ V and $V_2 = 1$ V levels, and input voltage amplitude was varied, as shown in Figure 3.22.b. For an input pulse of $V_{in} = 1$ V amplitude, a bursting waveform was observed in the V_{out} output voltage (see blue lines). When the input level was increased to $V_{in} = 1.7$ V (see

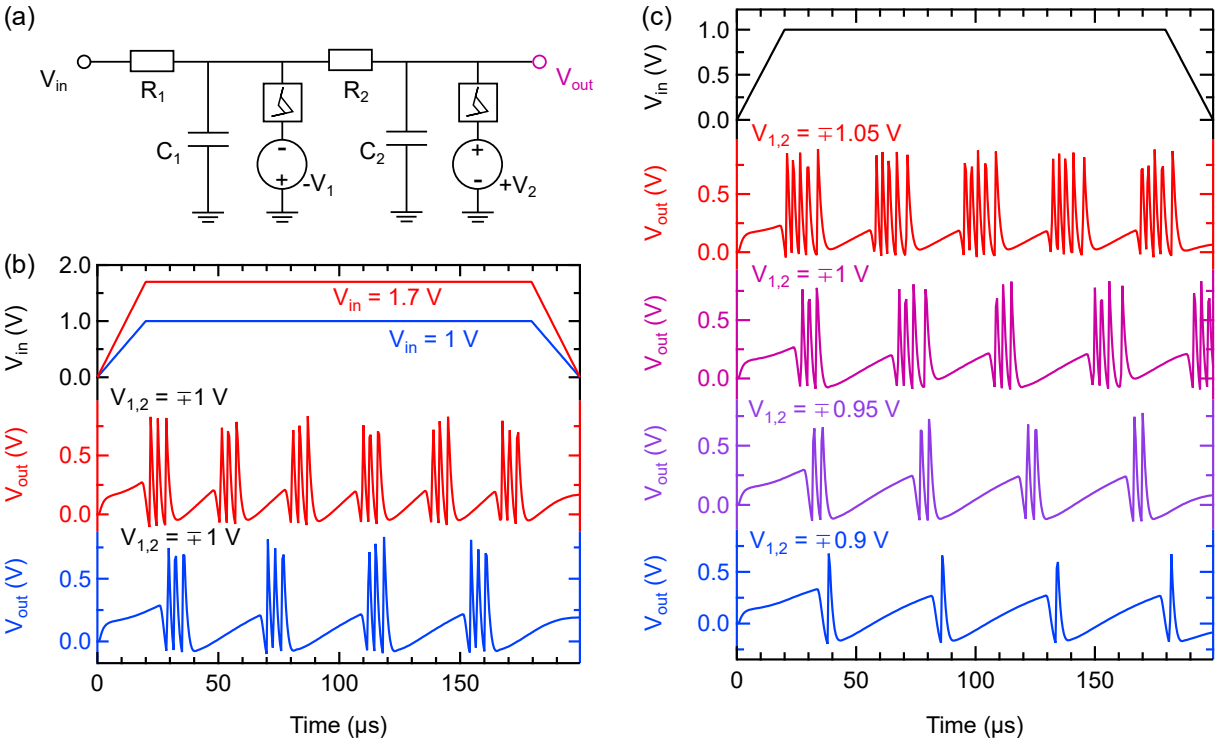

Figure 3.22: *Tunability of an artificial neuron built from VO_2 memristors with tonic behavior ('Tonic bursting'). (a) Circuit schematic of the artificial neuron, where the values of passive elements were set to $R_1 = R_2 = 4.7$ kΩ, $C_1 = 4.7$ nF, $C_2 = 2.2$ nF. (b) Tuning the frequency of output bursting events via the variation of the input voltage amplitude (marked with blue and red colors for $V_{in} = 1$ V and $V_{in} = 1.7$ V, respectively), keeping constant $-V_1 = -1$ V and $V_2 = 1$ V biasing levels. The number of spikes in a burst remains constant ($N_{burst} = 3$). (c) Results of the variation of biasing voltage levels from ∓ 0.9 to ∓ 1.05 V in 0.05 V steps, different output waveforms are marked with different colors. Input voltage pulse with a constant $V_{in} = 1$ V amplitude is marked with black lines. Stepwise increase of the burst count (from $N_{burst} = 1$ to $N_{burst} = 5$), and a slight increase in the frequency of bursts are observed.*

red lines), I observed that the frequency of bursting events increased, while burst count (the number of voltage spikes in a burst) remained constant, $N_{\text{burst}} = 3$.

I also studied the effect of varying bias voltages of the memristors, keeping the input pulse amplitude at a constant, $V_{\text{in}} = 1$ V level (see the results of these experiments in Figure 3.22.c). As the voltages of $-V_1$ and $+V_2$ were varied from ∓ 0.9 to ∓ 1.05 V in 0.05 V steps, the burst count increased from $N_{\text{burst}} = 1$ to $N_{\text{burst}} = 5$, in a similar stepwise manner (see color coded output voltage waveforms in Figure 3.22.c). Along with that, a slight increase in the frequency of bursts was also observed.

In a similar approach, an artificial neuron with phasic behavior was also realized according to the circuit schematic shown in Figure 3.23.a ($R = 4.7$ kΩ, $C_1 = 1$ nF, $C_2 = 4.7$ nF). The circuit emits a spike whenever a fast increase of voltage happens at its input, being insensitive for fast decreases of the signal in the same time (rebound spike behavior, according to the terminology in Ref. 9). When symmetric, ∓ 1.2 V biasing voltage is applied to both memristors, a positive voltage is measured at the output (at zero input level), as seen in the baseline of the light blue curve shown in Figure 3.23.b.

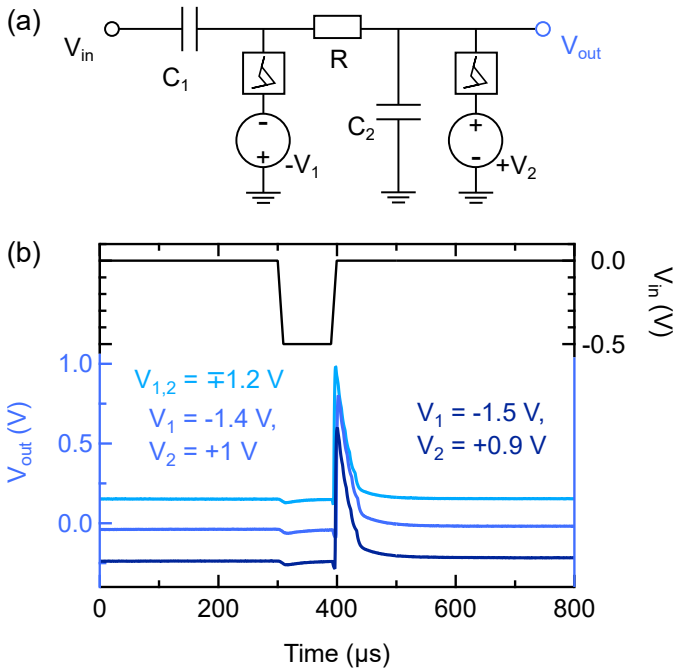

Figure 3.23: *Tunability of an artificial neuron built from VO_2 memristors with phasic behavior ('Rebound spike'). (a) Circuit schematic of the artificial neuron, where the values of passive elements were set to $R = 4.7$ kΩ, $C_1 = 1$ nF, $C_1 = 4.7$ nF. (b) Tuning baseline voltage of the output waveform via the variation of biasing voltages. Different V_1, V_2 pairs and corresponding waveforms are denoted with different shades of blue. The input waveform is identical in the three cases, as shown with black line in the upper part of the graph.*

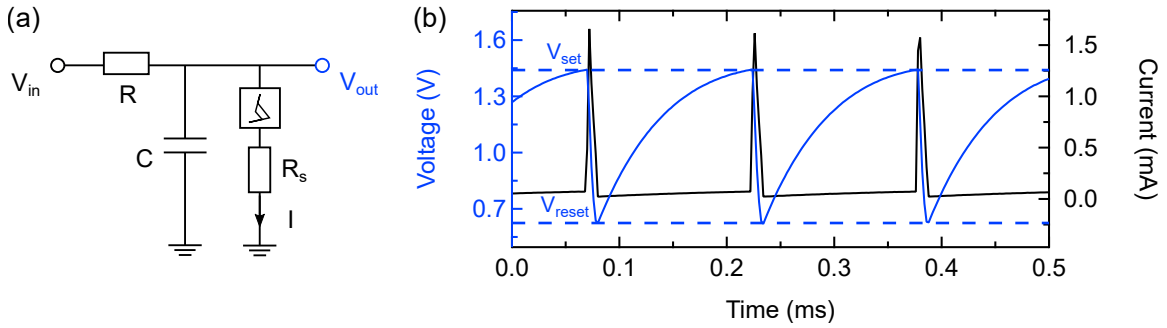

Figure 3.24: *Typical operation of a VO_2 oscillator circuit. (a) Circuit schematics of the oscillator, with $R = 30$ kΩ, $C = 4.7$ nF, $R_s = 380$ Ω and $V_{in} = 3.2$ V. (b) Output voltage (blue line) and current (black line) signal of the oscillator circuit. Voltage level oscillates between V_{set} and V_{reset} values of the memristor plus R_s series resistor component, and a current spike is observed in each period of oscillations.*

This baseline can be varied with the variation of biasing voltages, since it is formed as the result of a voltage division in the DC equivalent circuit of the two memristors (in their OFF states), the R resistor and the two biasing voltages, $-V_1$ and V_2. Tuning the latter levels to $-V_1 = -1.4$ V and $V_2 = 1$ V, the baseline can be brought close to zero level (blue line). In a further step, negative basline can be set with applying $-V_1 = -1.5$ V and $V_2 = 0.9$ V (dark blue curve). Spiking behavior is preserved in all cases, irrespective of the biasing voltages.

Spiking behavior can be achieved with only a single VO_2 memristor, utilizing its volatility. To demonstrate it, I assembled an oscillator circuit according to Figure 3.24.a, by simply placing an RC circuit (with $R = 30$ kΩ and $C = 4.7$ nF) next to the usual memristor–series resistance ($R_s = 380$ Ω) connection. Note, that the driving voltage dependent $I(V_{drive})$ characteristic of the second part is known from previous measurements, see the blue curve in Figure 3.21.c. The operation of the oscillator circuit can be pictured as follows:

- Initially, resistance R and the memristor in its OFF state (plus R_s) form a voltage divider circuit together, which result in an equilibrium voltage drop of $V_{OFF}^{eq.} = V_{in} \cdot (R_{OFF} + R_s)/(R + R_{OFF} + R_s)$ (calculated for the memristor and the serial resistance together).

- When V_{in} is applied, charging of the parallel capacitor begins, which sets the timescale for the increase of the output voltage, as it is seen in the V_{out} signal displayed in Figure 3.24.b with blue color.

- If the $V_{OFF}^{eq.} > V_{set}$ condition is satisfied, the memristor switches to its ON state before reaching the equilibrium value. At this moment, the conditions for voltage

division change, and a new equilibrium voltage becomes valid for the circuit, $V_{\mathrm{ON}}^{\mathrm{eq.}} = V_{\mathrm{in}} \cdot (R_{\mathrm{ON}} + R_s)/(R + R_{\mathrm{ON}} + R_s)$. Hence, output voltage suddenly drops, and a current spike appears after the memristor (see black curve in Figure 3.24.b), as a result of the discharge of the capacitor.

- If the new equilibrium voltage meets the $V_{\mathrm{ON}}^{\mathrm{eq.}} < V_{\mathrm{reset}}$ condition, the memristor switches back to its OFF state eventually, as the output voltage decreases. Then the cycle starts over again, with charging of the capacitor.

In some of my later studies involving oscillators, the R_s serial resistor was omitted from the circuit for the sake of simplicity. In the above example, however, the V_{set} and V_{reset} voltages experienced during oscillations (see dashed blue lines in Figure 3.24.b) are characteristic not only of the memristor, but the memristor and the R_s serial resistor component together. Therefore, these values are in good agreement with switching voltages visible in the driving voltage dependent $I(V_{\mathrm{drive}})$ characteristic of the device (see blue curve in Figure 3.21.c).

3.3.6 VO_2 oscillator in an autonomous neural transceiver unit

Conceptually, combining the tunable synaptic functionality of a non-volatile Ta_2O_5 memristor and the neuronal dynamics provided by a volatile VO_2 memristor can offer a powerful unit for complex computations like real-time signal processing tasks. To leverage the dynamical properties of both devices, finding the proper parameters for their coupling are essential. The realization of such a concept starts with careful characterisation of both components.

Ta_2O_5 devices are sufficient for realizing pattern recognition in a noisy environment with a single device, as shown in the circuit schematics of Figure 3.25. The first steps towards this application were the neural spike detection measurements with OxRAM devices, performed by my colleague Dániel Molnár using Nb_2O_5 and Ta_2O_5 samples I developed (see Subsection 3.2.3 earlier). The studies reported here utilized $Pt/Ta_2O_5/Ta/Pt$ devices prepared by Miklós Csontos, fabricated in the same crosspoint geometry and similar layer thicknesses as my own Ta_2O_5 devices (see optical microscopy image of a representative sample of Miklós in Figure 3.25 with red frame). A key difference is the deposition technique of the Ta_2O_5 layer, as Miklós used high-power impulse magnetron sputtering method for this purpose (whereas the oxide layers of my devices are made with RF sputtering).

The resistance change of Ta_2O_5 caused by a successful neural spike detection event is a challenging task to process, as only the raw current or voltage signals can be used for further information processing in an analog circuit. Therefore, the approach shown in the circuit schematics of Figure 3.25 is applied, to sense the resistance change through

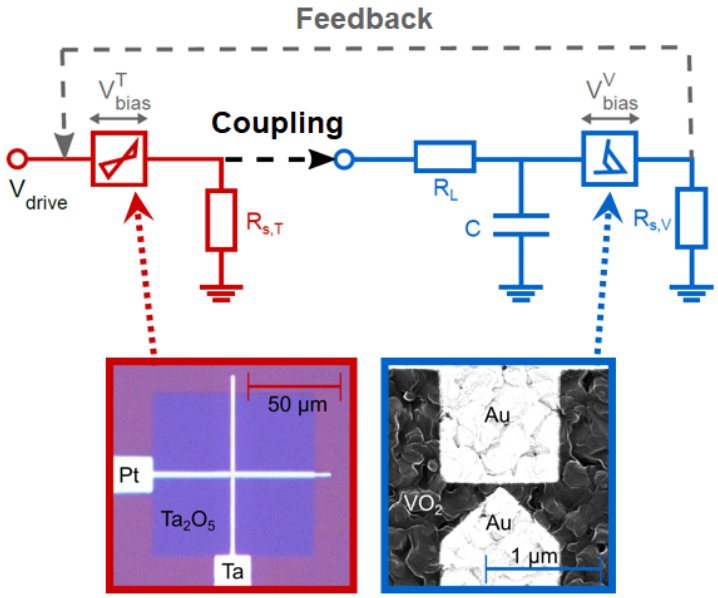

Figure 3.25: *Simplified circuit schematics of the neural transceiver unit, also showing the optical microscopy and SEM images of the utilized Ta_2O_5 and VO_2 devices. [O4]*

a voltage divider composed of the Ta_2O_5 memristor and an $R_{s,T}$ resistor. In this way, switching of the Ta_2O_5 memristor appears as a change in the output voltage level of this first part of the circuit, which can be carried on to a VO_2 oscillator circuit. In this manner, voltage oscillations or current spikes appear at the output of the circuit when the Ta_2O_5 memristor detects a signal. This output is already sufficient for further processing, and also can be used for the reset of the Ta_2O_5 memristor, realizing autonomous operation (as illustrated with a gray dashed arrow indicating a feedback in Figure 3.25). This way, the circuit is ready for processing the next incoming spike after the autonomous reset of the Ta_2O_5 memristor.

The operation of the circuit without feedback is shown in Figure 3.26. The Ta_2O_5 memristor is not sensitive to the noise, while a Gaussian pulse superimposed to the noise (see driving voltage, black signal) induces a switching of $R_{\mathrm{OFF}}/R_{\mathrm{ON}} \approx 10$ ratio (see the evaluated resistance, red signal). Shortly after, spiking of the oscillator part is initiated (see the output current, blue signal). Due to the properly chosen negative offset of the drive voltage, the initial high resistance state of the Ta_2O_5 device is slowly recovered. Therefore, oscillation is terminated when the Ta_2O_5 memristor retains its initial value. By employing a feedback circuit branch (illustrated with gray dashed line in Figure 3.25), the initiated spiking of the VO2 oscillator unit can immediately reset the Ta_2O_5 device. This can be realized with additional circuitry. Further details on this operation mode are found in Ref. [O4].

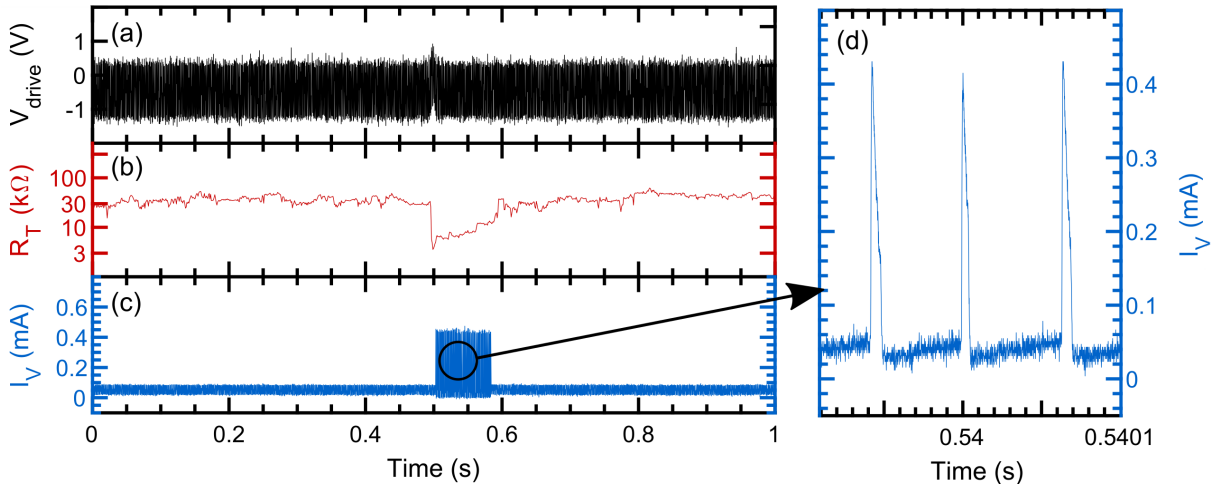

Figure 3.26: *Operation of the neural transceiver unit. (a) Drive voltage – time trace, showing a single Gaussian spike hidden in a noisy background, with a negative offset. (b) The evaluated resistance of the Ta_2O_5 memristor shows sharp resistance change upon detection, and reset of the Ta_2O_5 memristor is achieved by proper tuning of the negative offset of the drive voltage. (c) Current response of the vanadium oscillator part reveals that oscillation starts when the resistance of the Ta_2O_5 device is decreased and oscillation is terminated when the initial resistance of the Ta_2O_5 memristor is recovered. (d) Zoomed-in plot of the current oscillations at the output of the VO_2 oscillator part. [O4]*

In this project, the major work was done by Dániel Molnár, my contribution focused on the development and optimization of VO_2 oscillator circuits from self-produced VO_2 memristors. This development activity delivered VO_2 oscillator circuits with well-understood and tailored characteristics, which were suitably applied as spike generators in the demonstrated neural signal processor circuit. Related to this project Dániel and I were co-supervising the student research work (TDK) of Roland Kövecs [18].

3.3.7 VO_2 devices for RF measurements

For studying the speed of RS phenomena in VO_2 nanogap devices, I prepared samples according to the lithography layout shown in Figure 3.27. The nanogap samples (dark blue regions) were embedded in a co-planar waveguide (orange parts), deposited in the same step, made of 50 nm thick gold layer (as usual). The waveguide has identical design as the one reported in Ref. 44, used for studying and monitoring ~20 ps RS phenomena in Ta_2O_5 samples via real-time electrical measurements. Compared to those devices, an important, additional step was vital to realize the waveguide. The ground lines (top and bottom orange islands according to the top-view orientation of Figure 3.27) must be at a different potential, as the electrode pair leading to the sample (left and right orange islands). This

condition is not fulfilled, if VO_2 is present between the ground and signal lines, since it is not a good insulator in its pristine state (despite the fact that it is usually referred to as insulator phase – sometimes the phase is referred to as semiconductor phase, and in this case the Mott transition is called SMT instead of IMT). To eliminate conduction between the ground and signal lines, a selective etching step have to be carried out after the deposition of metallic electrodes. For this purpose, an etching mask was created along the light blue lines shown in Figure 3.27, with the exact same electron beam lithography method as the electrodes.

Two types of samples on different VO_2 films were created with the above described layout:

- Th-VO_2 layers were created on sapphire substrate following the same steps for thermal oxidation as described in Section 3.3.1. After depositing the electrodes a wet chemical etching technique was used: the sample was immersed to an acidic solution (H_2O_2:H_3PO_4:CH_3COOH:HNO_3 (2:16:1:1)) heated to 50°C, for ∼5 seconds, in two rounds. I optimized this procedure to yield appropriate results.

- PLD VO_2 films (from the same source as described in Section 3.3.1) were used to create nanogap samples. After the deposition of electrodes reactive ion etching (RIE) was carried out in a single step, using CF_4 gas, applying 0.64 mbar pressure

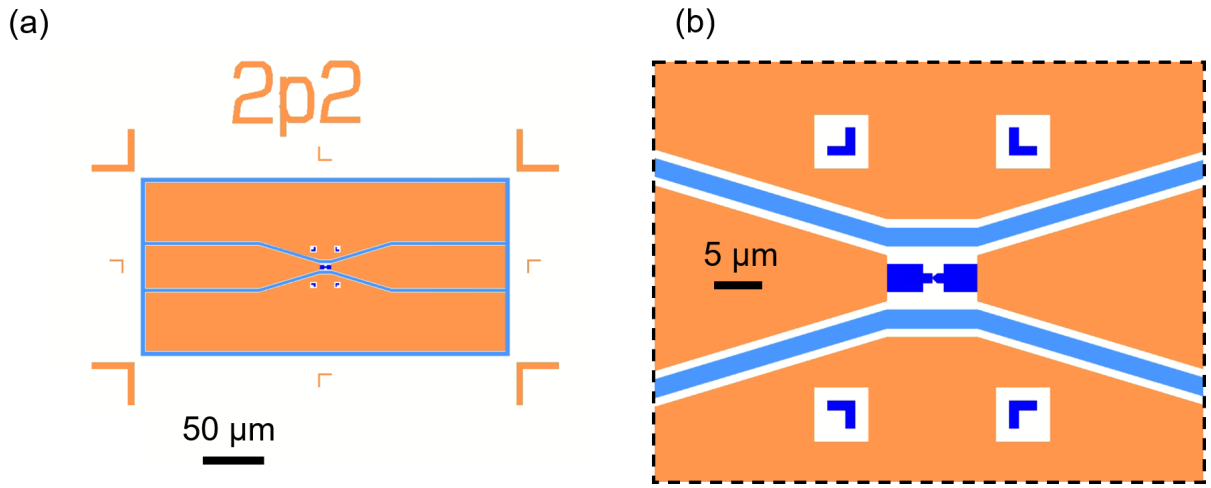

Figure 3.27: *Design of VO_2 nanogap devices for RF measurements shown (a) at a full scale and (b) magnifying around the nanogap region. Numbers in panel (a) denote the row and column indices of the sample. Small (dark blue) and large (orange) structures were formed in the first lithography cycle, followed by the deposition of Au electrodes. Afterwards, light blue lines indicating the etching mask were scanned in a second lithography step.*

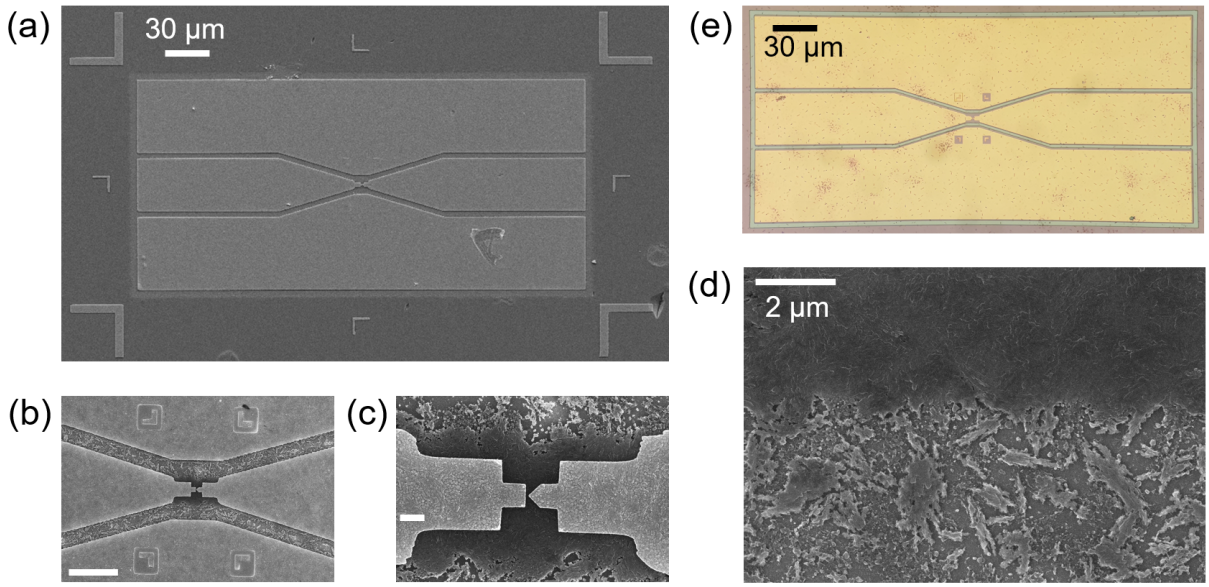

Figure 3.28: *Scanning electron and optical micrographs of RF VO_2 devices. (a-c) SEM images of a sample on Th-VO_2(sapphire) substrate after the second round of wet etching, at different magnifications. The $\sim$ 10 µm-sized damage of the bottom ground line in panel (a) is caused by the tip of the probe station used for prior electrical testing of the device. Scalebars for (b) and (c) are 10 µm and 1 µm. (d) The contrast between damaged/undamaged Th-VO_2 is apparent along the edge of a spot where no device was deposited, but a 150 µm × 150 µm 'window' was created in the etching mask. (e) Optical microscopy image of a device on a PLD VO_2 layer after RIE process. No signs of under-etching are visible.*

and 240 W plasma power for 30 s time, in a single step. The parameters of the RIE process were optimized by my colleague Áron Vándorffy.

At optimized parameters, both etching processes yielded the removal of VO_2 along the lines between electrodes while the VO_2 layer around the gap region remained undamaged.

Optimizing the wet etching technique was challenging due to the under-etching phenomenon in case of the first attempts with 15 s etching times. Although insulation between the electrodes was sufficient, SEM images revealed severe damage to the VO_2 near the nanogap region. Therefore I reduced etching time to 5 s, and also started to test samples with electric measurements using a probe station, instead of time-consuming SEM imaging. According to my measurements, the resistance between ground lines was still in the 10–100 kΩ range after the first round of etching, so I repeated the process. After the second round, the ground-ground resistance increased considerably, to the 1-10 MΩ domain. After I confirmed successful etching along the lines, I also tested some samples for RS characteristics, which were indeed observable, with the usual $I(V)$ characteristics. As a last qualifying measure, I took SEM images of the samples, which confirmed that etching

was successful along the desired lines, leaving the region of the nanogap unaffected. The SEM images with different magnifications shown in Figure 3.28.a-c show brighter regions along the lines of etching, while the areas of unaffected VO_2 regions are darker. The gap region shown in Figure 3.28.d is preserved, and the dark/light contrast originates from the remanent, damaged vanadium oxide, which is also observable in Figure 3.28.d, taken at a spot where no device was deposited, but a rectangular area was defined in the lithography design of the etching mask for testing purposes.

The RIE process did not yield under-etching, as shown in the optical microscopy image (Figure 3.28.e). Upon electrical measurements, ground-ground resistance was > 1 GΩ (not resolved with the measurement setup), and usual RS characteristics were also confirmed, similarly to the Th-VO_2(sapphire) devices.

My colleague, Sebastian Werner Schmid carried the as-prepared RF VO_2 samples to Miklós Csontos at ETH Zurich, where similar time-resolved measurements were performed as in Ref. 44. Preliminary results indicate set processes at the $\approx$20 ps timescale, much faster than e.g. the 2 ns switching times reported for VO_2 devices in Ref. 67.

This is the end of the final Section where my contributions to on-chip memristor development were presented. In the next Chapters, I describe results of my own experimental works aiming the investigation (Chapters 4, 5) and application (Chapter 6) of resistive switching memory devices.

Chapter 4

Tunable stochasticity in SiO_x memristors

In this Chapter, I discuss the results of my studies to reveal the crystallization process governing resistive switching dynamics in SiO_x based phase change memory devices [O5]. Related to this project, I supervised the student research work (TDK) of Gergő Fehérvári [15].

Silicon oxide is a well-known dielectric material that shows potential for resistive switching and is highly compatible with CMOS technologies [131]. It also has desirable properties for use in flexible and transparent electronic devices [132]. In addition, the stochastic behavior of silicon oxide resistive switching devices could be exploited as a resource for solving certain NP-hard optimization problems at the hardware level, such as graph segmentation [83, 133] or prime factorization [134].

The graphene/SiO_x/graphene devices subject to present study contain an active volume that is restricted to nanogaps between graphene electrodes. Prior research conducted on similar device geometries using transmission electron microscopy (TEM) revealed that the formation and degradation of distinct Si nanocrystals plays a vital role in the switching process [33, 34]. In-situ high-resolution transmission electron microscopy (HRTEM) analysis further indicated that the low resistance state (LRS, ON state) contains a semimetallic crystalline Si-III phase [31], while the high resistance state (HRS, OFF state) is characterized by an amorphous and poorly conducting active region. Our research group previously introduced a controlled electrobreakdown technique for creating ultra-small nanogap devices from graphene nanostripes on top of a SiO_2 layer, capable of addressing a single or a few Si nanocrystals in a confined active volume. Apart from their small size, these devices also yield peculiar switching dynamics via their three characteristic timescales governing resistive switching phenomena. For further details on the basic properties of graphene/SiO_x/graphene devices see Subsection 2.1.1 and Ref. 36.

Here, the formation dynamics of such nanocrystals is investigated by analyzing the set time values, which refer to the timespan between the programming pulse edge and the set transition from the high resistance state (HRS) to the low resistance state (LRS). To gain fundamental insights into the nanocrystal formation mechanism, the present study goes beyond investigating the average set time characteristics and analyzes the entire statistical distribution of the stochastic set time of the graphene/SiO_x/graphene devices using nucleation theory [135–137]. The variability of the set time statistics is also examined by modifying the reset voltage amplitude during sequential pulsed measurements. This phenomenon has the potential to be utilized for managing stochasticity in memristor-based probabilistic computing applications via controlling the structural arrangement of the active volume.

4.1 Exploring set time dynamics

The resistive switching phenomenon occurring in the graphene/SiO_x/graphene nanogap devices (see Figure 4.1.a-b) results in a wide spectrum of analog states, which cover a range of resistance states spanning multiple orders of magnitude [132, 138, 139] ($\approx 10^4$ Ω to 10^{11} Ω). It is necessary to utilize pulsed measurement schemes for applications where interconnected memristive elements are programmed [7, 29], or to examine

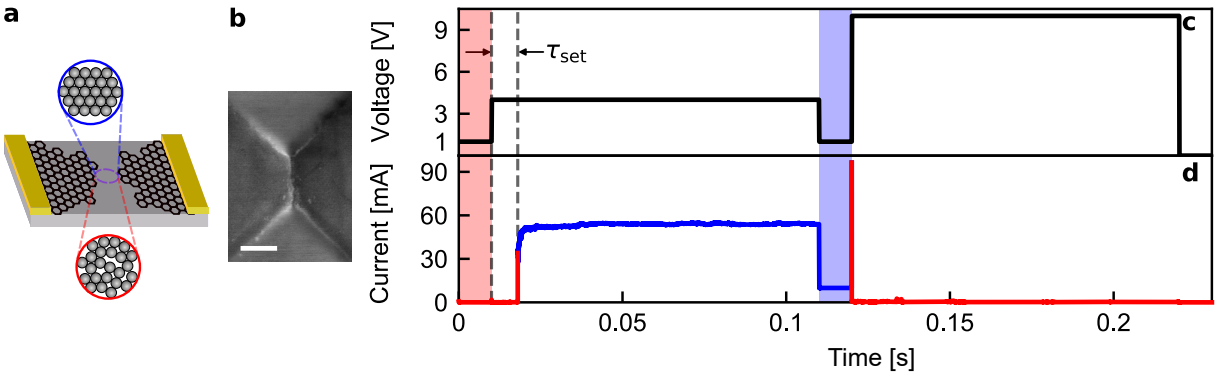

Figure 4.1: *Pulsed measurement scheme for studying the set time in graphene/SiO_x/graphene nanogap devices. (a) Illustration of a planar graphene/SiO_x/graphene nanogap device with gold electrodes. The crystalline structure of the ON state and the amorphous structure of the OFF state are depicted. (b) Scanning electron microscopy image of a graphene/SiO_x/graphene nanogap device with a scalebar of 200 nm. (c) Rectangular switching pulse scheme for studying set time dynamics and (d) typical current response of the device. Red/blue colors of the current trace correspond to OFF/ON states of the memristor, and red/blue shaded areas denote the plateaus where the OFF/ON resistances are evaluated at 1 V signal level. [O5]*

device properties and study switching times. The basic pulsed programming scheme used in this study is shown in Figure 4.1.c, and a typical current response is displayed in Figure 4.1.d. The device is initially prepared in the OFF state (red line in Fig. 4.1.d). A set pulse with $V_{\text{set}} = 4$,V is applied to switch the device to the ON state (blue line in Fig. 4.1.d). The set transition occurs with a time delay compared to the rising edge of the set pulse, which determines the τ_{set} set time. The device remains in the ON state until the subsequent reset pulse is applied ($V_{\text{reset}} > 5$ V). A time delay of τ_{reset} also appears after the rising edge, however it is not resolved with the measurement setup used in this study. The τ_{set} and τ_{reset} time intervals can be adjusted in the range of $10^0 - 10^{-8}$ s range by varying the amplitude of the corresponding set and reset voltage pulses used for programming [36]. It is worth noting that the falling edge of the reset pulse is much shorter than $\tau_{\text{dead}} \approx 0.1 - 1$ s (see the effect of the dead time on $I(V)$ characteristics of the device earlier in Figure 2.6.c-d of Section 2.1.1). As a result, the device remains in the OFF state until the pulse scheme is repeated. A lower readout voltage of 1 V is applied prior to the programming pulses, thus the OFF and ON state resistances of the device are measured during these time intervals denoted with red and blue backgrounds in Figure 4.1.c-d. The current response of the device is measured using a custom-built multiple output current to voltage converter [140]. This converter allows for the real-time measurement of the ON and OFF state resistances differing by more than four orders of magnitude in a simultaneous manner. The current is amplified through parallel output channels with different amplification factors. Therefore, there is no need for slow gain switching. To determine the OFF and ON state resistances, the current response is measured simultaneously through a high and a low gain output of the converter. The measured current values are then averaged along the red and blue readout regions in Fig. 4.1.d.

Set time statistics were recorded through continuously cycled measurements following the pulsed scheme depicted in Figure 4.1.c, where the cycling period was usually set to 6–10 s, which is much larger than τ_{dead}. To perform a statistical analysis of R_{OFF}, R_{ON} resistances of both states and τ_{set} set time, multiple samples were measured, and several switching cycles were recorded. During this analysis, the set time statistics were examined under homogeneous driving conditions at a well-defined set and reset pulse amplitude and length. The obtained results were compared to the expectations of nucleation theory under the following considerations. The formation dynamics of Si nanocrystals can either be dominated by a stochastic nucleation process or a deterministic growth process [22, 28]. Even though in-situ TEM measurements showed a transition between crystalline and amorphous Si phases, the involvement of oxygen migration in the switching processes cannot be ruled out [31]. In contrast to common nanoscale $Ge_2Sb_2Te_5$ (GST) phase change memory devices where the growth from the embedding crystalline matrix is crucial

for the set transition (see earlier Figure 2.4.a in Section 2.1.1), SiO_x devices have an amorphous embedding matrix, and the small active volume of the devices reduces the likelihood of crystalline seeds in the as-quenched OFF state. Consequently, the emergence of nucleation seeds is essential for the set transition. Once a nucleation seed forms, growth time is expected to be minimal due to the nanometer-scale volume. This suggests that the nucleation time is the primary factor that dominates the set process. This is supported by the observed nature of set process in the SiO_x nanogap devices: after the rising edge of the set pulse, an abrupt transition occurs, which is significantly delayed from the pulse edge, as shown in Fig. 4.1.c-d, and also in Ref. 36. A nucleation-driven process exhibits such a time-delayed abrupt transition, while a growth-driven process typically results in a gradual resistance decrease, as it is observed in GST devices [141].

I attempted to verify these hints of a possible nucleation driven process in SiO_x nanogap devices by the quantitative analysis of the set time distributions. I present this analysis in the next Section.

4.2 Studying the stochastic nucleation process

In a nucleation-driven process, the nucleation time is a good approximation to the set time. The former is a stochastic variable that follows an exponential probability density function with an expectation value of $\bar{\tau}_{\text{nucleation}} \sim \exp(W/k_BT)$ [135, 136], where W represents the effective nucleation barrier [137]. According to the field-induced nucleation model, the nucleation barrier breaks down during the set process due to the driving voltage, and as a result, the set process speeds up exponentially while the set voltage is increased linearly. This is consistent with the measured set voltage dependence of the average set time [36]. A theoretical estimation suggests that the electric field required to start the set transition from amorphous to crystalline state is around 300 MV/m [142], which is a feasible value in SiO_x nanogap devices, as they have an active volume of less than 10 nm.

To confirm the accuracy of the nucleation model, multiple switching cycles were measured and the set time histograms were analyzed using the exponential probability density function predicted by nucleation theory. This probability density function has a unique characteristic where the $\log_{10}(\tau_{\text{set}})$ values should display a standard deviation of $\sigma^{\text{exponential}}_{\log(\tau)} = \pi/(\ln(10)\cdot\sqrt{6}) \approx 0.56$, irrespective of the mean set time. This means that the standard deviation of $\log_{10}(\tau_{\text{set}})$ should always cover about half an order of magnitude on the time axis. If the standard deviation is significantly smaller, it would contradict the nucleation model. Conversely, if it is larger, it would indicate the existence of additional stochasticity, such as the cycle-to-cycle variation of the nucleation barrier, W.

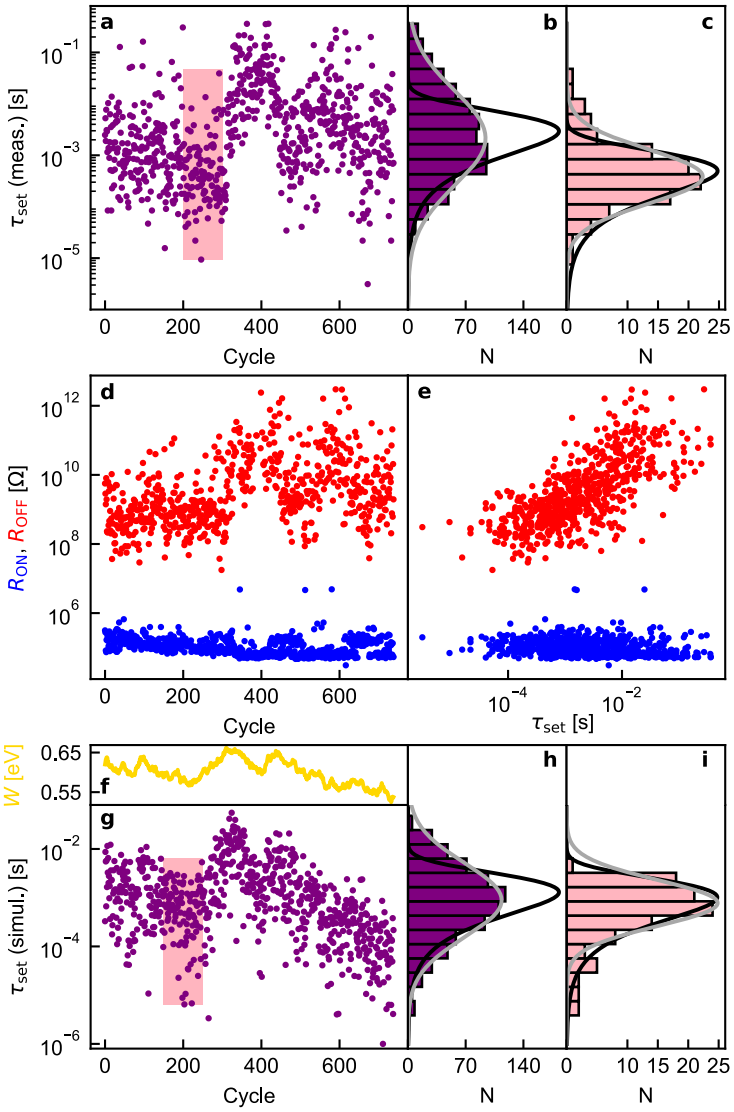

Figure 4.2: *Set time and ON/OFF state resistance statistics of graphene/SiO_x/graphene devices. (a) Set time during 700 repeated switching cycles, and (b) the whole set time histogram (purple) displayed with its best fitting exponential (black) and lognormal (grey) probability density functions. (c) Set time histogram for a shorter, temporally homogeneous part of the data (marked with a pink background in panel (a)), which is equally well fitted with the exponential (black) and lognormal (grey) probability density functions. (d) Cycle-to-cycle evolution of R_{OFF} and R_{ON} resistances during the same 700 cycles. (e) ON and OFF resistances vs. the set time in the same cycle. (f-i) Results of the simulation where the set process is viewed as a nucleation process with a ΔW variaton of the nucleation barrier around its $\overline{W}$ mean value, resulting in a specific correlation cycle number (n_{corr}). Simulated (f) ΔW and (g) τ_{set} results for 700 cycles. Set time histograms (h) for the whole, and (i) for the restricted (see pink shading in panel (g)) parts. Both histograms are fitted with exponential (black) and lognormal (grey) probability density functions. [O5]*

A set of measurements consisting of 700 consecutive switching cycles is shown in Fig. 4.2.a-e. The histogram of the measured set time values is presented in Fig. 4.2.b on a logarithmic axis, along with the best fitting exponential probability density function represented by the black line. It is apparent that the measured set time distribution is broader than the best fitting exponential probability density function, with a standard deviation value of $\sigma_{\log(\tau)}^{\text{measured}} \approx 0.87$, which is considerably larger than the universal value of $\sigma_{\log(\tau)}^{\text{exponential}} \approx 0.56$. This indicates that the system has multiple characteristic time-scales, and a lognormal distribution (grey line in Fig. 4.2.b) more accurately describes the data. It should be noted that the standard deviation of $\log_{10}(\tau_{\text{set}})$ for the best fitting lognormal density function, $\sigma_{\log(\tau)}^{\text{lognormal}} \approx 0.91$, appropriately describes a similarly broad distribution as the experimental result. For fitting of such histogram data with equidistant binning on a logarithmic axis, the appropriate transformation of exponential and lognormal functions were performed to obtain the fitting formulae, according to Ref. 143.

Figure 4.2.a depicts the cycle-to-cycle variation of the set time, revealing that the broad distribution of set times does not stem from a temporally homogeneous dataset. Instead, a significant drifting of the average set time is observed on the time scale of approximately $100 - 200$ cycles. In this context, it is worthwhile to explore the set time distribution for a more statistically homogeneous portion of the data, such as the 100 datapoints with pink background. For this restricted dataset, both the exponential and lognormal probability density functions provide similarly good fitting results to the measured set time distribution (see Fig. 4.2.c). The measured standard deviation for this subset is $\sigma_{\log(\tau)}^{\text{measured}} \approx 0.61$, which is slightly greater than the universal $\sigma_{\log(\tau)}^{\text{exponential}} \approx 0.56$ value. However, the latter happens to be the same as the standard deviation of the best fitting lognormal distribution, $\sigma_{\log(\tau)}^{\text{lognormal}} \approx 0.56$. For temporally homogeneous parts of the data, the $\sigma_{\log(\tau)}^{\text{measured}}$ values are no more than 20% greater than the universal $\sigma_{\log(\tau)}^{\text{exponential}}$ value, which implies that the exponential distribution describes well the experimental set time histograms.

Taken together, the above discussed observations suggest that the set time distribution can be suitably described by the nucleation theory over a shorter time scale, where the nucleation barrier $W(V_{\text{set}})$ remains constant at a given set voltage. However, the nucleation barrier of the OFF state shows random drifting after approximately 100-200 cycles. Since the set time is exponentially dependent on W, even a small cycle-to-cycle variation ΔW in the nucleation barrier can result in significant broadening of the set time distribution.

It is also interesting to analyze how the ON and OFF state resistances vary along the same 700 switching cycles of Fig. 4.2.a, and to what extent these resistances are correlated with the actual set time values. Fig. 4.2.d demonstrates that R_{ON} (blue curve) exhibits minor temporal inhomogeneities, whereas R_{OFF} displays significant temporal variations

with similar pattern to τ_{set} (Fig. 4.2.a). Fig. 4.2.e shows the ON and OFF state resistances as a function of the set time in the same cycle, demonstrating the lack of correlation between R_{ON} and τ_{set} and very significant correlation between R_{OFF} and the set time. This finding indicates, that the OFF state resistance and the related detailed nanostructure of the active volume in the HRS is not stable in time, rather exhibits temporal variations on the time-scale of $100 - 200$ cycles. Such variation can be caused by e.g. the random structure of atomic configurations of the amorphous region after each reset event [22], or the variation of the effective active volume's size, which perturbs the length-scale at which the voltage drops in the OFF state. This variation is mirrored in the temporal inhomogeneity of the set time via the variation of the nucleation barrier according to the actual nanostructure of the OFF state. Similar findings were observed along several switching cycles recorded on various samples.

Numerical simulations can mimic the temporal inhomogeneity of the set time by using an exponential probability density function for the set time and a nucleation barrier (W) with a random temporal variation. The variation of the nucleation barrier (ΔW) and the resulting correlation time (n_{corr}) are such that the correlation function $\langle W(n) \cdot W(n + \Delta n)\rangle$ decays on the scale of $\Delta n \approx n_{\text{corr}}$ switching cycles. Figures 4.2.f-i. demonstrate an example of such a simulation with an average nucleation barrier of $\overline{W} = 0.62$ eV, a standard deviation of $\Delta W = 0.04$ eV, and a correlation time of $n_{\text{corr}} = 200$ cycles. In the numerical simulations, the correlated evolution of W is computed as a low-pass filtered white noise, or the so-called Ornstein-Uhlenbeck process [144]. In this manner, the nucleation barrier in the $n + 1$. cycle is calculated as:

$$W_{n+1} = W_n - \frac{1}{n_{\text{corr}}}(W_n - \overline{W}) + \xi(\sigma_{\Delta W}, n),$$

where $\overline{W} = 0.62$ eV is the average nucleation barrier and $n_{\text{corr}} = 200$ is the correlation cycle number. $\xi(\sigma_{\Delta W}, n) = \mathcal{N}(0, \sigma_{\Delta W})$ is a Gaussian random variable with zero expectation value and $\sigma_{\Delta W} = 0.004$ eV standard deviation. $\overline{W}$ and $\sigma_{\Delta W}$ are chosen such that the average set time values according to the formula $\overline{\tau}_{\text{set}} = \overline{\tau}_{\text{nucleation}} \approx \tau_0 \cdot \exp(W/k_B T)$ should result in similar set time statistics, as the experimental data presented in Fig. 4.2.a. (The τ_0 attempt frequency is approximated as a typical phonon frequency, $\tau_0 \sim 10^{-13}$ s [135, 136].) After obtaining a $\overline{\tau}_{\text{set}}$ in the above described process, τ_{set} values are drawn from an exponential distribution characterized by the $\overline{\tau}_{\text{set}}$ expectation value.

The simulation closely resembles the experimental results shown in Figures 4.2.a-e., with a small cycle-to-cycle variation of the W nucleation barrier ($\Delta W/\overline{W} = 6.5\%$, see Fig. 4.2.f.) resulting in orders of magnitude variation of the set time (Fig. 4.2.g.), and a broadened lognormal set time distribution for cycle numbers greater than $n_{\text{corr}} = 200$ (Fig. 4.2.h.). The set time histogram for the entire simulated dataset in Fig. 4.2.g. is shown in Fig. 4.2.h., where both of the best fitting lognormal (grey, $\sigma^{\text{simulated}}_{\log(\tau)} \approx 0.77$) and

exponential (black) probability density functions are displayed. However, for a shorter segment, the set time variation is more homogeneous (see e.g. 100 switching cycles highlighted with pink coloring in Fig. 4.2.g.), where the set time distribution is accurately described by one exact W nucleation barrier and a resulting exponential probability density function. The histogram for this restricted dataset with $\sigma_{\log(\tau)}^{\text{simulated}} \approx 0.62$ is shown in Fig. 4.2.i, where the best fitting exponential and lognormal probability density functions ($\sigma_{\log(\tau)}^{\text{lognormal}} \approx 0.48$) are also displayed.

The measurements and simulations presented here stand in stark contrast to the behavior of mushroom-type GST-based memory devices, in which the measured set time distribution is narrower than the universal exponential distribution. The data in Fig. 11.b of Ref. 22 suggest $\sigma_{\log(\tau)}^{\text{measured}}$ values that are $3-10$ times smaller than the universal $\sigma_{\log(\tau)}^{\text{exponential}}$ value. In the latter GST devices, the set time is governed by a deterministic growth driven process, while in the graphene/SiO_x/graphene devices, the set time distribution is determined by a stochastic nucleation driven process with considerable variation in the nucleation barrier over the course of $100-200$ switching cycles.

Set time analysis of Pt/SiO_x/Pt devices Motivated by the above discussed results, I also performed set time analysis of Pt/SiO_x/Pt devices in a similar approach (see electric characterisation of these devices previously in Subsection 3.1.1). The pulsed scheme of the measurement was alike to the one depicted in Figure 4.1.c. The set and reset voltage amplitudes were adjusted to accommodate lower switching voltage levels of

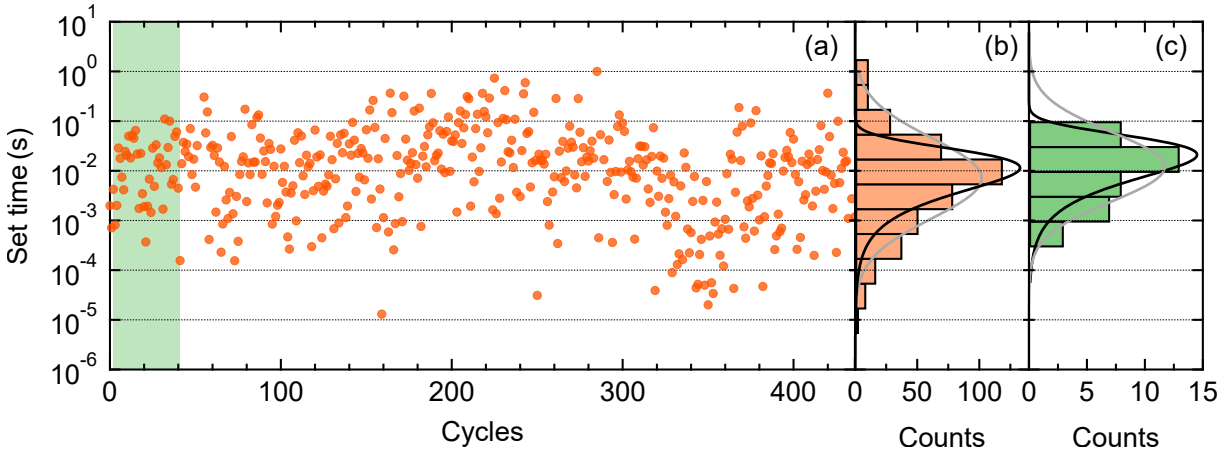

Figure 4.3: *Set time analysis of Pt/SiO_x/Pt devices. (a) Evolution of the set time in a pulsed measurement, recorded with 3.5 V and 7 V set and reset voltage amplitudes and 1 s set pulse length. Panels (b) and (c) show logarithmically binned histograms of the whole set time data (orange) and the restricted data (green) marked with green background in panel (a). Black and gray lines represent the best fitting exponential and lognormal probability density functions.*

the device (compared to graphene electrode devices), to the values of 3.5 V and 7 V. The length of the set pulse was increased to 1 s, to capture the whole statistics and minimize the possibility of events where no set transition occurs in a cycle. Figure 4.3.a shows the evolution of the set time in a pulsed measurement, for ≈ 400 consecutive cycles. The logarithmically binned histogram of these set time values is shown in Fig. 4.3.b for the whole dataset (with orange color), along with the best fitting exponential and lognormal probability density functions (represented by the black and gray lines). A similar trend can be observed as for the graphene electrode devices, since the measured histogram is much broader than the best fitting exponential probability density function, with a standard deviation value of $\sigma_{\log(\tau)}^{\text{measured}} \approx 0.93$. In contrast, the best fitting lognormal function retrieves the width of the histogram accurately, as an indication for multiple characteristic timescales.

As comparison, a restricted, homogeneous part of the whole set time data is also analyzed. The first 40 points marked with green background in Figure 4.3.a yield a standard deviation of $\sigma_{\log(\tau)}^{\text{measured}} \approx 0.64$, close to the universal $\sigma_{\log(\tau)}^{\text{exponential}} \approx 0.56$ value. Histogram of the restricted data shown in Figure 4.3.c (with green color) yield similarly good fits for exponential and lognormal probability density functions (see black and gray lines).

4.3 Tuning the set time statistics

The observed correlation between R_{OFF} and τ_{set} (see Fig. 4.2.e) suggests an opportunity for tuning the τ_{set} statistics by varying the amplitude of V_{reset}. A higher amplitude reset signal could lead to increased R_{OFF} in principle, thus controlling the τ_{set} set times through their correlation.

To test this hypothesis, the effects of varying the reset voltage amplitude were studied (while keeping other parameters of the driving voltage signal constant). To mitigate drift phenomena (depicted in Fig. 4.2.a), changes in τ_{set} were studied within the correlation cycle number (200 cycles), as depicted in Fig. 4.4.a,b. Both the mean values of τ_{set} and $\log(R_{\text{OFF}})$ (indicated by lines in Fig. 4.4.a,b) increased upon ramping V_{reset} from 8.5 V to 10 V (in 0.5 V steps). These values also recovered their initial states while decreasing V_{reset}. Note, that the expectation value of R_{ON} remained constant throughout the cycles.

These trends are further illustrated by plotting the mean values of τ_{set} and $\log(R_{\text{OFF}})$ versus V_{reset} (see Figs. 4.4.c-d). The observed dependencies result in a correlation plot shown in Figure 4.4.e, which is similar to Fig. 4.2.e. However, in this case (Figure 4.4.e), the correlated variation of the set time and OFF state resistance is not due to a random drift but it is deliberately induced via tuning the reset voltage. These findings verify the initial hypothesis that (i) the OFF state resistance is tunable (unlike in GST phase change

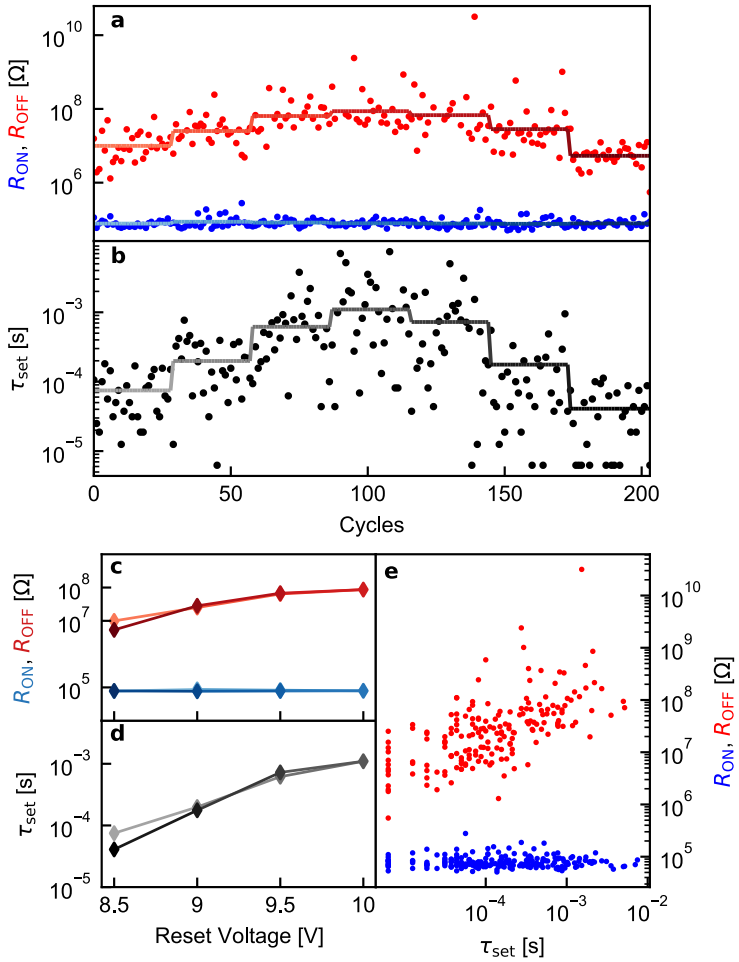

Figure 4.4: *With varying the reset voltage amplitude, the distributions of the set time and the OFF state resistance are tunable. (a-b) OFF, ON state resistances (red, blue dots) and set time values (black dots) during a cycled measurement. Set pulses are kept at a constant duration and signal level ($V_{set} = 4$ V) during the cycles, and reset amplitude is changed in every 10 cycles in 0.5 V steps, starting from 8.5 V up to 10 V and back to 8.5 V again. Solid lines mark the logarithmically averaged values for the resistances for and the mean set time values of the 10-cycle units with constant V_{reset}. (c-d) Logarithmically averaged R_{ON}, R_{OFF} values, and mean set time values as a function of the reset voltage, where coloring from lighter to darker markers/lines denotes the order of the measurements similarly to the lines in panels (a,b). (e) OFF/ON state resistances vs. the set time. [O5]*

devices [29]), and (ii) the set time statistics are also tunable (through its correlation with R_{OFF}), which can achieved by adjusting the amplitude of the reset pulse.

4.4 Conclusions

In conclusion, studying the set time statistics of SiOx resistive switching devices yielded the following results: (i) Measured set time distributions of short segments of pulsed cycling measurements are well fitted with an exponential probability density function, indicative of a nucleation process with a constant nucleation barrier. (ii) Over longer segments of switching cycles, measurements show broader set time distribution, which is attributed to the cycle-to-cycle variation of the nucleation barrier height W with a typical correlation parameter of $n_{\mathrm{corr}} \approx 200$ switching cycles for graphene/SiOx/graphene devices. (iii) A similar study of the set time statistics was carried out on Pt/SiOx/Pt devices, where short 40 cycle segments of set time data are well fitted with an exponential function. This finding further confirms that the observed traits of set time statistics originate from nucleation in the SiO_x active region. (iv) A strong correlation between τ_{set} and R_{OFF} was observed, which implies that the temporal variation of the nucleation barrier is linked to the cycle-to-cycle variation of the nanostructure of the OFF state. (v) Relying on this observation, we confirmed that both τ_{set} and R_{OFF} are tunable by adjusting the amplitude of the reset voltage pulse.

The analysis performed here offers a method to distinguish between nucleation driven and crystal growth driven processes governing the dynamics of the set process in phase change memristors. The above results also facilitate fundamental understanding of the stochastic set process in planar-type SiO_x RS devices. The realization of neuronal activation functions [16], stochastically firing neurons, or energy-efficient true random number generation [17] could benefit from tunable stochastic properties of SiO_x devices.

Chapter 5

Quantum transport diagnostics of atomic scale filaments

The continuous miniaturization of electronic devices has entered a regime, where the characteristic size of the active volume is comparable to the Fermi wavelength of the electrons, and therefore the the conduction properties are described by quantum transport approach. In semiconductor devices the conduction electrons are provided by the doping atoms, and the related relatively low electron density ($10^{-4} - 10^{-2}$ electron/lattice atom [145]) yields a typical Fermi wavelength of $\lambda_F^{\text{semi.}} \approx 10 - 100$ nm and Fermi energy of $E_F^{\text{semi.}} \approx 10$ meV. The latter is smaller than the $k_BT \approx 25$ meV thermal energy at room temperature, and therefore quantum transport properties are rather manifested in a cryogenic temperature environment. On the other hand, the Fermi wavelength is orders of magnitude larger than the $a \approx 0.2 - 0.3$ nm lattice constant, thus smooth quantum conductance channels with clear conductance quantization features are easily established in a nanofabricated quantum point contact (QPC) geometry [147].

As a sharp contrast, resistive switching memory technology has delivered devices, where the size of the active volume can reach the ultimate atomic dimensions. In these structures, the current is transmitted through *metallic* nanofilaments, which yields a completely different *quantum transport regime* compared to semiconductor heterostructures: (i) The large electron density ($\approx$ 1 electron/lattice atom) results in orders of magnitude larger Fermi energies ($E_F^{\text{metal}} \approx 3 - 10\,\text{eV}$ [146]) than in semiconducting systems. Therefore, quantum transport is realized at room temperature due to the $E_F \gg k_BT$ condition. (ii) Unlike in semiconductor heterostructures, the metallic Fermi wavelength ($\lambda_F^{\text{metal}} \approx 0.3 - 0.6\,\text{nm}$) falls in the regime of the lattice constant. This extremely small metallic Fermi wavelength enables highly conducting metallic wires with diameters as small as a single or a few atoms. On the other hand, at such small λ_F the electrons experience a potential landscape which is rough on the scale of their wavelength. This results in far more complex quantum transport properties than universal conductance

quantization in semiconductor quantum point contacts [147], where a smooth, transparent quantum channel is realized. This complex quantum transport behavior has been widely investigated in pure metallic atomic-sized nanowires, [148–150] but has remained poorly explored in filamentary RS devices.

OxRAM devices commonly used in memristor crossbar arrays typically operate below 1000 μS, with some devices operating close to the $G_0 = 2e^2/h \approx 77.5$ μS universal conductance quantum [6, 70, 72, 151–155]. This makes it tempting to interpret the device state as an atomic-sized filament that represents the smallest possible memory element. However, this assumption cannot be verified by the measurement of solely the conductance value, since the very same $\approx 1G_0$ conductance may arise at fundamentally different junction arrangements with completely different cross-sectional areas. The present Chapter discusses the use of superconducting subgap spectroscopy to study the quantum transport properties of $Nb/Nb_2O_5/Nb$ and $Ta/Ta_2O_5/Ta$ resistive switching memories. This method – being a well-established experimental technique for studying clean atomic junctions in the field of mesoscopic physics [148–150, 156, 157] – is capable of providing more detailed information than overall conductance values by decomposing the conductance to transmission probabilities of individual quantum conductance channels, the so-called quantum PIN code [158].

I present the motivation of my studies in Section 5.1, where counter arguments to conductance quantization in transition metal-based atomic junctions and OxRAM devices are discussed. In Section 5.2, I introduce the theoretical framework of my studies and also the experimental tools and techniques required for performing subgap spectroscopy on RS devices. Then, I present results of subgap spectroscopy studies for Nb_2O_5 and Ta_2O_5 devices (Sections 5.3 and 5.4), relying on Refs. [O6] and [O2]. It is to be noted, that although I investigate similar, transition metal oxide-based RS systems in both studies, the targeted conductance regime differs. In case of Nb_2O_5 devices, the $\sim 1\ G_0$ conductance range is explored, where subgap spectroscopy is highly sensitive to a possible opening of conductance channels. As for Ta_2O_5 devices, I investigate quantum transport properties of device states in a slightly higher, $\approx 3 - 10\,G_0$ conductance regime.

5.1 Counter arguments to conductance quantization in transition metal junctions

Direct microscopic imaging of the active volume of resistive switching devices is challenging at atomic dimensions. Claims about atomic-scale switching usually rely on indirect evidence, such as the statistically pronounced occurrence of quantum conductance in silver-based filamentary RS units [60, 159, 160]. These observations can indeed be an indication of a single atom-wide filament, because silver is a monovalent metal, prone to exhibit quantized conductance at atomic dimensions. However, conductance quantization features are restricted to alkali and noble metal atomic junctions, where the loosely bound s electrons experience a smooth atomic potential landscape. In the rest of the metals, especially in transition metal nanowires, absolutely no conductance quantization features are observable.

A robust and reliable techinque for the statistical analysis of the conductance during the thinning (and eventual rupture) of atomic wires is the mechanically controllable break junction (MCBJ) technique (see more details on this method later in Subsection 5.2.2). Upon increasing displacement of the electrodes, conductance traces are recorded (see exemplary traces for Ta and Nb junctions in Figure 5.1.b and Figure 5.1.d, respectively). Conductance histograms (as the ones displayed in Figure 5.1.a and Figure 5.1.c for pure Ta and Nb junctions, respectively) can be constructed from thousands of individual conductance traces gained from repeatedly pushing together and pulling apart the electrodes in break junction experiments.

Such conductance histograms of single-atom nanowires made of transition metal elements have broad conductance distributions, and the conductance quanta are not distinguished in any sense [148, 161]. These characteristics are also apparent in measurements involving pure Ta and pure Nb atomic wires, shown in Figure 5.1.a,b and Figure 5.1.c,d, respectively. Furthermore, the variable oxygen content of the conducting filaments in transition metal oxide-based OxRAM devices is expected to increase the conductance variety, making it challenging to identify the physical nature of the conducting filaments in these structures.

Typical resistive switching $I(V)$ curves of Ta(thin film)/Ta_2O_5/PtIr(tip) and Nb(thin film)/Nb_2O_5/PtIr(tip) junctions with device states near the quantum conductance unit are shown in Figure 5.1.e-f ($T = 300$ K). As the amplitude of the triangular driving voltage signal (V^0_{drive}) increases, the $G_{\mathrm{ON}}/G_{\mathrm{OFF}}$ switching ratio grows, showing capability of multilevel programming. These curves exhibit a rather smooth variation of the conductance for each V^0_{drive} driving voltage amplitude. Moreover, there are no plateaus appearing in the G_{ON}, G_{OFF} vs. V^0_{drive} traces, as shown in the bottom inset of Fig. 5.1.e-f. Accordingly, the OFF states can be fine-tuned in the $1 - 2.5\ G_0$ interval, for both Ta_2O_5 and

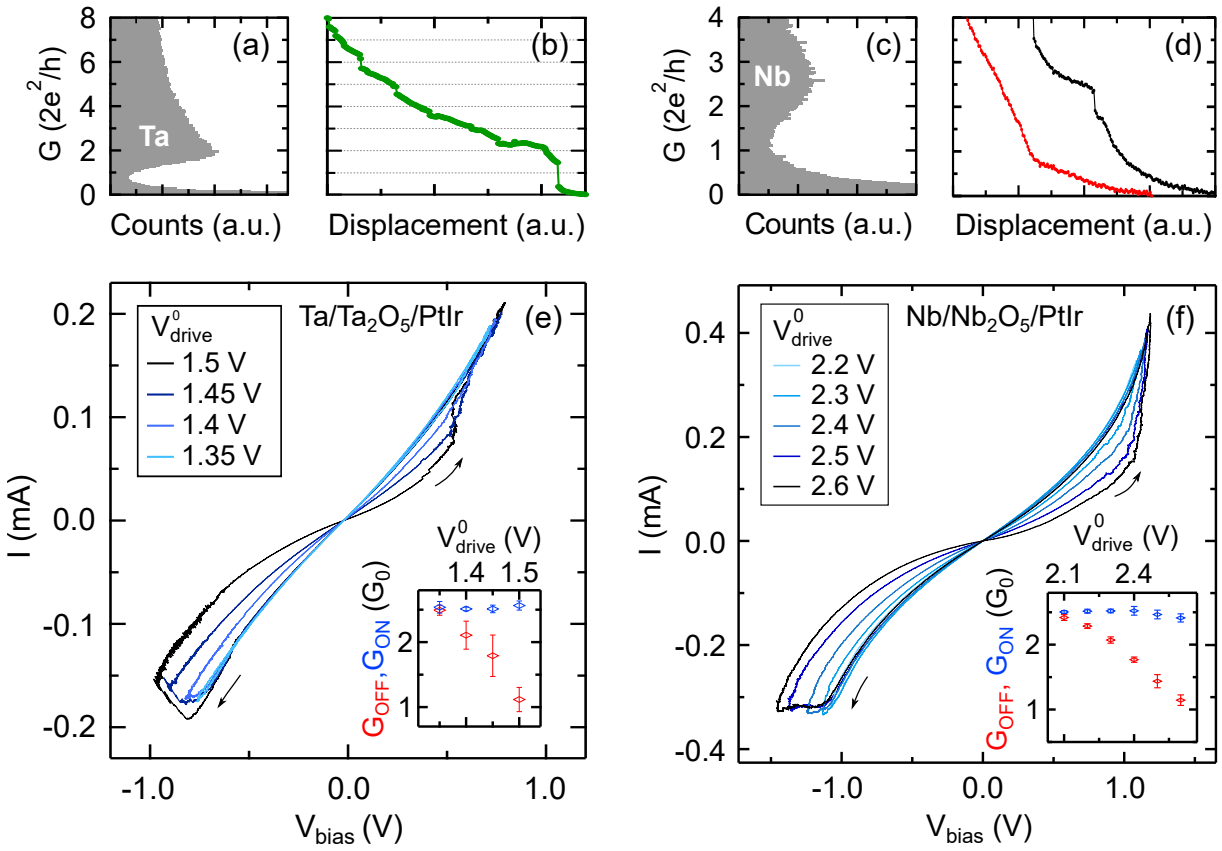

Figure 5.1: *Smooth conductance variation near the quantum conductance unit in transition metal-based junctions. (a-d) Representative conductance histograms of pure Ta (a) and Nb (c) nanowires calculated from thousands of conductance versus electrode separation traces of consecutive breaking cycles, measured with an MCBJ setup. Panels (b) and (d) show typical conductance versus electrode displacement traces for pure Ta and Nb junctions, respectively. Both curves exhibit smooth evolution of the conductance, lacking any quantized conductance features. (e-f) Multilevel programming of Ta(thin film)/Ta_2O_5/PtIr(tip) (e) and Nb(thin film)/Nb_2O_5/PtIr(tip) (f) junctions in the range of the quantum conductance unit. As the driving voltage amplitude is increased, the G_{ON}/G_{OFF} switching ratios grow for both systems. The bottom insets in both panels show G_{ON} and G_{OFF} (the slopes of the $I(V)$ curves in the $\pm 100\,mV$ region) as a function of V^0_{drive} driving voltage amplitude. Error bars mark the standard deviations of the conductance values calculated from $\approx$ 10 consecutive $I(V)$ curves with the same V^0_{drive} amplitude. [O2, O6]*

Nb_2O_5 devices. These voltage-controlled Ta_2O_5 and Nb_2O_5 devices (see Fig. 5.1.e,f) and also the mechanically varied pure Ta and Nb nanowires (see Fig. 5.1.a-d) show similar smooth tunability of the conductance, operated close to 1 G_0, without any conductance quantization features.

The above observations clearly indicate, that extracting conclusive information on atomic-scale processes in transition metal-based junctions is not possible in experiments where only the total conductance is monitored.

5.2 Foundations of superconducting subgap spectroscopy

The Landauer description provides an efficient theoretical framework for describing quantum transport by decomposing the total conductance to the contribution of various quantum conductance channels. This approach models a quantum point contact as a constriction having different τ_i transmission eigenvalues for individual quantum channels. In this manner, each channel carries τ_i fraction of the $\frac{2e^2}{h} = G_0$ conductance quantum. The whole contact is composed of M number of channels, thereby the overall conductance is given as

$$G = \frac{2e^2}{h} \sum_{i=1}^{M} \tau_i.$$

Note, that the above formula clearly states the possibility of a 1 G_0 junction yielding multiple quantum channels ($M > 1$) with non-perfect transmissions ($\tau_i < 1$). The latter τ_i values are the relevant quantities which describe the quantum transport properties of a junction, rather than the sole value of the conductance.

Superconducting subgap spectroscopy was originally developed in the field of atomic and molecular electronics to uncover the M channel number and τ_i transmission eigenvalues of single-atom nanowires [150] and has more recently been applied to identify the different atomic configurations upon reversible current-driven single-atom rearrangements [162].

5.2.1 Theoretical approach

OxRAM devices can operate via a variety of switching mechanisms, which can lead to markedly different active volume arrangements illustrated in Figure 5.2.a-c. Therefore, a memristive junction with a given conductance, can either be an atomic-scale filament (Fig. 5.2.a.), a wider filament with a tunable tunnel barrier in it (Fig. 5.2.b.), or an interface-type switch, where the filling/emptying of oxygen vacancies account for resistive switching involving a larger area (Fig. 5.2.c.) [52]. All these fundamentally different arrangements may yield the very same conductance, close to the quantum conductance unit ($\approx 1G_0$) or even higher ($\gtrsim 1\ G_0$). Due to the presence of oxygen in the system, weak or strong barriers may form in the active region, therefore the conductance value alone is not enough to claim the presence of a truly atomic-sized filament in the active volume.

Analysis close to the quantum conductance unit Let us consider a fictive memristor with the $I(V)$ curve shown in Fig. 5.2.d, where we set the conductance to 1 G_0 value. This conductance state is the result of deliberate programming, and quantum transport properties are not known. Using superconducting electrodes to contact this memristor (see inset in Fig. 5.2.d.), very different $I(V)$ characteristics emerge in the voltage range of the superconducting energy gap (Δ), the *subgap* region. As a direct consequence of the arrangement of atoms in the active region, distinct, fine-structured subgap curves emerge (see Fig. 5.2.e.), which accurately reflect the physical nature of the junction. Furthermore, these subgap curves are especially sensitive to the possible formation of a single-atom junction. Consequently, the possible active region arrangements pictured in Fig. 5.2.a-c. can be identified in this manner.

The appearance of the distinct, fine-structured subgap $I(V)$ characteristics can be explained by multiple Andreev reflection processes [149, 150, 156, 157]. In the Andreev picture, a superconductor - nanoconstriction - superconductor (ScS) junction is considered to analyze single electron transport processes. A single electron can pass the junction with τ probability, but due to the presence of the Δ superconducting gap in the density of states of the left and right superconducting electrodes, this is only possible at $eV > 2\Delta$ energies (first order process). However, the simultaneous transport of n electron charges (with τ^n probability) is enabled at a reduced energy of $eV > 2\Delta/n$ (n^{th} order processes). Some possible cases can be pictured as follows:

- In a tunnel junction ($\tau_i \ll 1$ for all channels), all of the higher order transport processes involving more electrons are negligible. Therefore the current remains zero at the $eV < 2\Delta$ *subgap* region. At higher voltage, a linear $I(V)$ curve is observed which retains the G_N normal state conductance (see the green curve in Fig. 5.2.e).

- In an atomic-sized metallic junction, usually some channels are transparent ($\tau_i \approx 1$ for one or more channels), which allows higher order transport processes in the subgap range. This results in finite subgap current at $eV < 2\Delta$, and also in the appearance of some fine structures at $2\Delta/n$ thresholds (see the red curve as an example and grid lines at $2\Delta/n$ in Fig. 5.2.e).

- At the limiting case of $\tau_i = 1$, all of the higher order processes ($n \gg 1$) are enabled at the subgap region. This results in an infinitely steep, stepwise current rise at zero voltage (see the blue curve in Fig. 5.2.e).

By the numerical fitting of experimental $I(V)$ curves in the subgap region, all τ_i transmission eigenvalues can be determined, so it is possible to distinguish physically different device states (even if they have the same conductance). As in metals, the Fermi wavelength is comparable to the lattice constant, a truly atomic-sized junction yields only

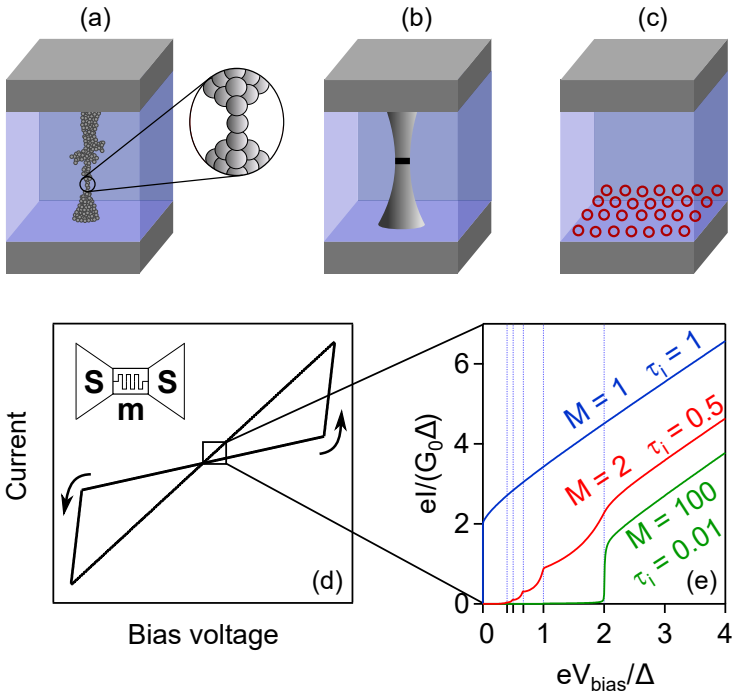

Figure 5.2: *Scheme for the subgap spectroscopy analysis of a memristor state programmed to* 1 G_0 *conductance. Top panels illustrate various possible arrangements of the active region in an OxRAM device [52]: (a) single-atom filament; (b) a wider filament with a tunable tunnel barrier in the middle; (c) oxygen vacancies distributed near the bottom electrode (a naive picture of an interface-type non-filamentary device state). An imagined memristor with the* $I(V)$ *curve shown in panel (d) contacted with superconducting electrodes (see inset) exhibits markedly different* $I(V)$ *characteristics in the subgap domain, as depicted in panel (e). Analyzing these subgap curves provide a unique possibility to distinguish different types of junctions even if they would share a device state with the same,* $\sim$ 1 G_0 *conductance. Panels (a–d) are illustrations, whereas panel (e) demonstrates distinct theoretical subgap* $I(V)$ *curves [157] for junctions with the same* 1 G_0 *conductance but different* τ_i *and* M *values. [O6]*

one or a few open quantum channels. If the filament is continuous (there is no barrier inside which may block channels), these open channels are highly (or even perfectly) transmitting, affecting subgap characteristics considerably (see markedly different curves in Figure 5.2.e), making the subgap spectroscopy method highly sensitive to the presence of transparent channels. Due to the infinitely steep current increment at zero bias voltage for perfect transmission ($\tau_i = 1$, blue curve), even a small barrier can be definitely distinguished ($\tau_i = 0.5$, red curve), being also far from the case of tunneling ($\tau_i = 0.01$, green curve). Therefore, subgap spectroscopy is a powerful method to uncover the τ_i transmission eigenvalues, which lead to the identification of quantum transport properties. The

latter are related very closely to the atomic arrangement of the active region and also the underlying resistive switching mechanism.

Analysis of the higher conductance regime At higher junction conductance, M can be sufficiently large so that the transmission eigenvalues can be described by a probability density function $\rho(\tau)$. For transition metals, even an atomic-scale junction can yield multiple conductance channels with a variety of transmission eigenvalues. Subgap spectroscopy studies of pure Pb, Al, Nb and Au single-atom junctions identified a connection between the number of open channels and the number of valence electrons [150]. In these cases, Au junctions yielded 1 channel (I/B group), Al 3 channels (III/A group), Pb 3-4 channels (III/A group) and Nb yielded 5-6 channels (V/B group). The latter can be explained by the tight-binding model of a single-atom nanowire [149, 163] identifying 1 s-type and 5 d-type channels in a transition metal corresponding to valence orbitals (the closing of one channel is expected based on symmetry reasons). As a result of the above considerations, $\approx 10-15$ non-vanishing conductance channels are realistic for a junction with only $2\ -\ 3$ atoms diameter (in the narrowest cross-section), for transition metals

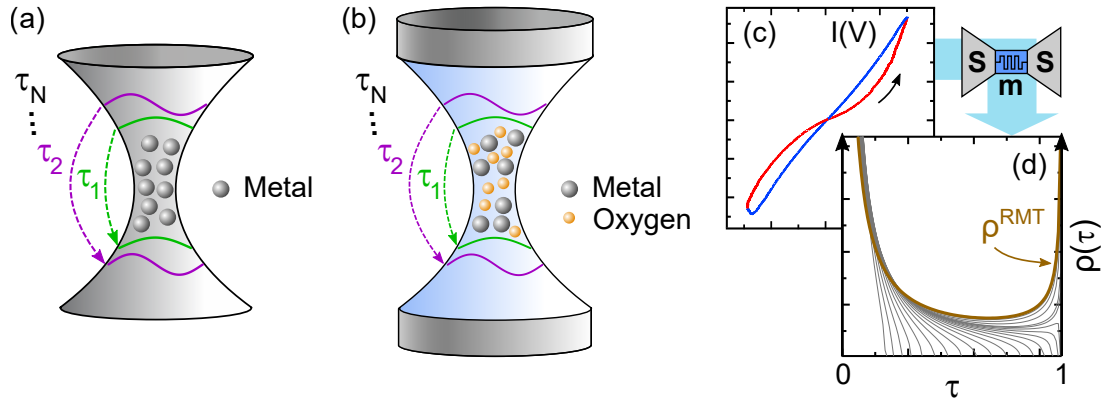

Figure 5.3: *Scheme for the subgap spectroscopy analysis of transition metal oxide based memristor states exceeding* 1 G_0 *conductance. (a) Illustration of the reference system of a pure, transition metal oxide-based single-atom nanowire. (b) Illustration of an oxygen-rich filament in a resistive switching device. Colored labels* ($\tau_1, \tau_2, \ldots \tau_N$) *and arrows in panels (a,b) refer to transmission eigenvalues of individual conductance channels. (c) Schematic RS* $I(V)$ *curve of an OxRAM device. (d) Possible transmission densities of the considered physical systems. The brown curve marks the universal* $\rho^{\mathrm{RMT}}(\tau)$ *density function characteristic of diffusive nanowires, valid for pure transition metal atomic wires. Gray curves correspond to a model where an extended barrier blocks transport in a diffusive nanowire [164]. Black arrows at the sides indicate the limiting case of conductance quantization (only perfect* $\tau_i = 1$ *are possible). [O2]*

like tantalum and niobium. Such a large channel number justifies applying a model based on transmission density functions.

In pure Pb atomic nanowires, $\rho(\tau)$ resembles the following universal probability density function (see brown curve in Figure 5.3.c) in a broad diameter range [157]:

$$\rho^{\mathrm{RMT}}(\tau) \sim \frac{1}{\tau\sqrt{1-\tau}}.$$

The above observation in case of Pb atomic contacts is rather surprising at first sight, since the latter formula was derived for mesoscopic diffusive wires by random matrix theory (RMT) [165]. It can be anticipated, that this universal transmission density is not a specific property of Pb atomic wires. I demonstrate later experimentally, that pure transition metal nanowires (see Fig. 5.3.a), especially Nb and Ta studied in this Chapter also share this same property as Pb junctions.

In a filament formed inside the active region of a transition metal oxide-based resistive switching device (illustrated in Figure 5.3.b,c) oxygen ions can influence transport in multiple ways, either enhancing or blocking the transmission of certain channels, leading to deviations from the $\rho^{\mathrm{RMT}}(\tau)$ universal transmission density function. The latter heavily influences subgap $I(V)$ characteristics, providing an opportunity to experimentally reveal the underlying transmission distribution of a junction by the measurement of subgap $I(V)$ characteristics. This way, the higher, $\gtrsim 1G_0$ conductance states of OxRAM devices can be studied, and the following questions can be answered:

- Do memristive filaments follow the same $\rho^{\mathrm{RMT}}(\tau)$ as pure transition metal nanowires?
- Is transport blocked inside RS filaments? If it is so, in what extent?
- Is transport enhanced by the vicinity of oxygen atoms? (Also a feasible case, as it was observed for oxygen decorated Ni junctions [166].)

Further details on the method I applied for this analysis are found in Subsection 5.4.2.

5.2.2 Experimental techniques

The application of superconducting subgap spectroscopy to STM point-contact resistive switching junctions relies on three important prerequisites:

- Resistive switching should work with a compositionally symmetric electrode arrangement, i.e. using the same electrodes on both sides, replacing PtIr tips routinely used in previous experiments to Ta and Nb tips.
- Device operation should be stable at cryogenic temperatures.

- The presence of the oxide layer should not result in an untolerable reduction of the energy resolution of subgap spectroscopy.

In the following, these requirements are analyzed, along with the experimental techniques I applied for superconducting subgap studies.

Point-contact resistive switching device preparation Studying STM point contacts is a powerful experimental tool to characterize and optimize memristive materials in order to achieve reliable operation of future on-chip RRAM devices. For the study of point-contact devices, Nb_2O_5 and Ta_2O_5 thin film samples were utilized, from the following sources:

- I created Nb/Nb_2O_5(thin film) samples with anodic oxidation of a Nb film in a 1 % aqueous solution of H_3PO_4, maintaining 1 mA/cm^2 current density throughout the process. First, a 300 nm thick Nb thin film was sputtered on the top of a standard Si wafer. X-ray photoelectron spectroscopy (XPS) with subsequent Ar^+ milling steps were performed on Nb/Nb_2O_5(thin film) samples, uncovering the depth profile of the Nb:O stoichiometric composition. The presence of Nb_2O_5 was confirmed at the top of the $\approx 20\,$nm thick oxide layer. For further details on the anodic oxidation and the structural characterization of Nb/Nb_2O_5(thin film) samples see Ref. 101.

- The Ta/Ta_2O_5 layer was prepared by Miklós Csontos, via sputtering of a ∼30 nm thick stoichiometric Ta_2O_5 on top of a 30 nm thick Ta film. Similarly to Nb_2O_5 samples, the thickness and composition of the Ta_2O_5 layer was also confirmed by XPS measurements accompanied by Ar^+ ion milling.

A vital part of creating an STM point-contact sample is the controlled approach of the tip to the surface of the thin layer sample with a given setpoint resistance. According to our past experiences with STM point-contact technique in our research group [59, 86, 98–102] [O1, O6], this process leads to electroforming-free RS junctions, since the tip can be indented to the surface of the RS material. To avoid the bending of the tip during the indentation, I used robust PtIr, Nb and Ta wires with $0.25 - 1\,$mm diameter in my studies. I always paid attention to ensure a short free-standing part af the tips, and also to avoid long and narrow tip apexes by the proper scissor cutting. During the controlled tip-approaching process, the sample was biased with ~ 20 mV, and feedback was applied to the tip-sample resistance. The approach was terminated when $\sim$ nA current was detected, resulting in less than ~ 20 MΩ resistance. Afterwards, the $I(V)$ characteristics with typical voltage driving amplitudes of $V^0_{\rm drive} \approx 1 - 2\,$V readily exhibited resistive switching without a dedicated high voltage electroforming process.

Preconditions to subgap spectroscopy measurements As a prerequisite for subgap spectroscopy measurements, the PtIr tips were replaced by Nb and Ta tips, for establishing point contacts on Ta_2O_5 and Nb_2O_5 thin films. Resistive switching properties were tested first in room temperature and then, at low temperature (1.4 K) conditions. These characterisations revealed that similar RS $I(V)$ curves are observable at both conditions, for both systems (e.g. for Nb_2O_5 devices, see earlier Fig. 5.1.f and later Fig. 5.8.a-b).

Most studies in the field of memristive systems facilitate compositionally asymmetric electrodes, since an asymmetry is needed for defining the direction of resistive switching characteristics. An earlier study of our group (which was carried out on Ag_2S resistive switching junctions) proved, that resistive switching with a well-defined switching direction is possible utilizing compositionally symmetric electrodes while geometrical asymmetry is introduced to the system (e.g. by a tip-sample geometry) [100]. My observations confirm this statement, since based on my studies concerning hundreds of independent Nb(tip)/Nb_2O_5/Nb(thin film) and Ta(tip)/Ta_2O_5/Ta(thin film) junctions, a dominant switching direction occurs for most of the cases (the set transition takes place when the thin film sample is positively biased with respect to the tip). Besides that, low temperature RS operation of both Nb_2O_5 and Ta_2O_5 systems are also confirmed. The reason for this phenomenon is believed to be the high electric fields that exist at the narrowest point of the junction, in addition to the self-heating effect of the active junction area [99].

Preparation of clean metallic nanowires Prior to the study of memristive junctions, reference subgap measurements were carried out by establishing pure atomic Nb and Ta break junctions at cryogenic temperatures. For this purpose, 99.99 % purity Nb wires of 0.25 mm diameter and Ta wires of 0.1 mm diameter were notched with a sharp

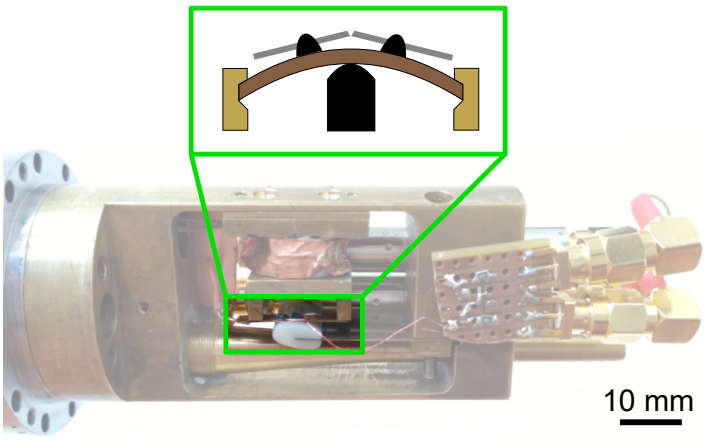

Figure 5.4: *Illustration of the MCBJ arrangement in a three point bending geometry, along with a photo of the low temperature sample holder.*

razor in a preliminary step, followed by the insertion of the wire into a three point bending MCBJ arrangement (see Fig. 5.4). A combined use of a stepper motor and a piezoelectric actuator allows broad range actuation and precise control over breaking the wire, thus various atomic configurations with stable normal conductance can be routinely achieved with this technique. Atomic contacts formed with the MCBJ method are extremely stable, and also of high purity due to the freshly broken surfaces in the cryogenic vacuum environment at liquid helium temperature.

Electric circuitry for resistive switching and subgap measurements I have designed a circuit with various filter stages for the low temperature studies of memristive point-contacts in a customized STM system and also built a duplicate of the circuit for studying pure atomic junctions in an MCBJ arrangement. For this, I used two very similar sample holders (one for STM and one for MCBJ measurements), designed by Attila Geresdi and András Halbritter [167] for low temperature use in a liquid helium dewar or a cryostat. I performed all low temperature measurements at 1.4 K in a *Janis Research SVT200T-5* liquid helium cryostat. The same, general schematics of the STM and MCBJ sample holders used in these measurements are shown in Figure 5.5.a. The image also includes photos of the different measuring heads of these sample holders with blue frames, where the samples are mounted in an MCBJ (left) or STM (right) arrangement.

The STM and the MCBJ setups share the same electromagnetic environment thanks to the same sample holder structure and measurement circuits, including identical filter stages. This is an important aspect, since it enables to perform reference subgap measurements on clean atomic junctions. I optimized the setups to prevent noise pickups, which would induce severe smearing of the spectroscopic information in the subgap $I(V)$ curves. This way, the energy resolution baselines can be determined (for the distinguished cases of Nb and Ta junctions set to the tunneling regime, see upcoming paragraph *Energy resolution of subgap measurements*). Also, subgap spectra of clean junctions with different atomic configurations (see upcoming paragraph *Reference analysis of clean atomic junctions*) can serve as a basis for comparison to later subgap measurements performed on memristive states.

The most important parts of the electrical filtering circuitry used for my measurements are displayed in Figure 5.5.b. Main components of the filtering circuitry are (i) *LakeShore SS-CC-100* cryogenic coaxial cables (operating as RC filters at their full lengths), (ii) *MiniCircuits VLFX-80* low pass filters (145 MHz cutoff frequency and 40 dB insertion loss up to 20 GHz), and (iii) custom-built RC filters from SMD elements ($R = 100\ \Omega$, $C = 2$ nF at $T = 1.4$ K). Another key element of the circuitry is the relay control (marked with red lines), enabling automatized change between recording RS characteristics in the $\sim$1 V regime and measuring subgap $I(V)$ curves in the $\sim$10 mV domain. The filtering

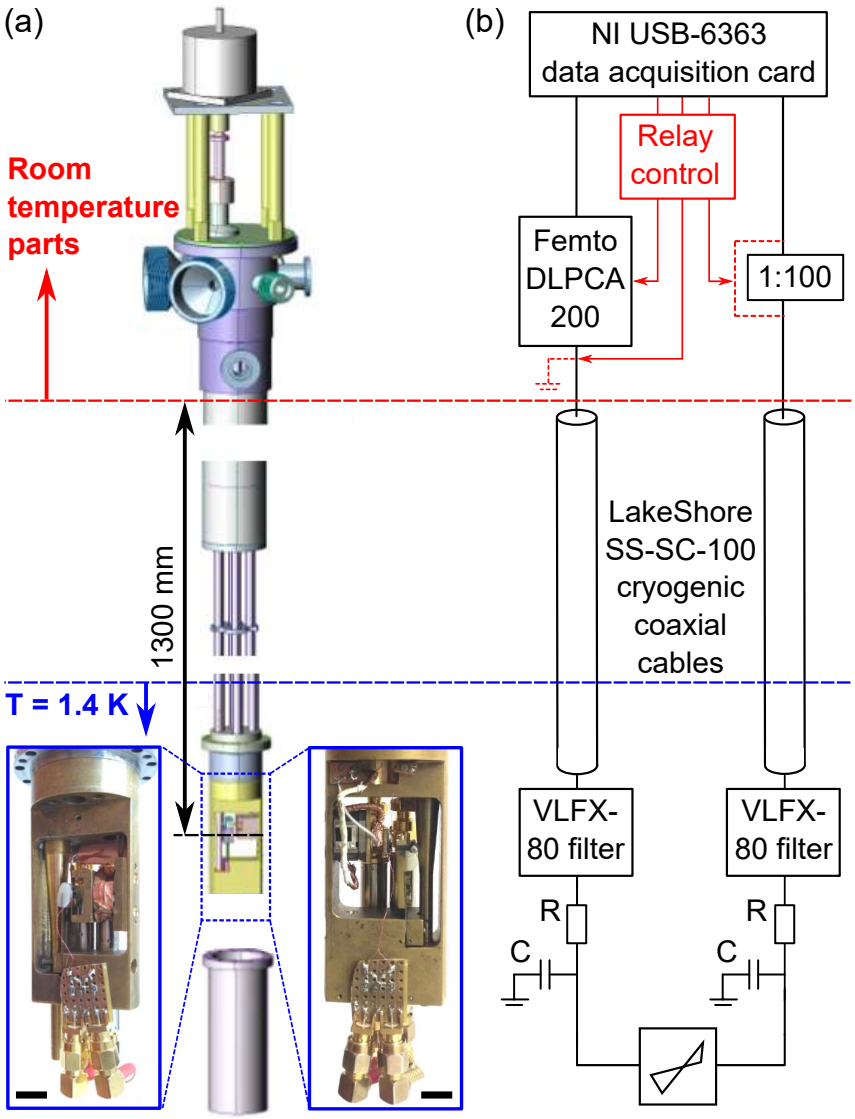

Figure 5.5: *Measurement system for low temperature studies of clean atomic junctions and memristive point-contacts. (a) Technical drawing of the sample holders used for low temperature measurements [167]. The image also includes photos of the different measuring heads of sample holders with blue frames, where the samples are mounted in an MCBJ (left) or STM (right) arrangement. Scalebars of these photos are 10 mm. (b) Circuit diagram showing filtering stages (LakeShore SS-CC-100 cryogenic coaxial cables, MiniCircuits VLFX-80 low pass filters, and custom-built RC filters with* $R = 100\ \Omega$, $C = 2\ nF$ *at* $T = 1.4\ K$*) and relays which grant automatized control for studying different voltage regimes. [O6]*

stages and measurement control realized by relays were essential to record subgap $I(V)$ characteristics with sufficient resolution.

Energy resolution of subgap measurements All the elements listed in the above paragraphs were essential to perform comparative subgap spectroscopy measurements on clean Nb and Ta junctions (see illustration in Figure 5.6.a) and RS point-contact junctions (Figure 5.6.b), established on Nb_2O_5 and Ta_2O_5 thin films. The aim of these measurements were twofold: (i) the validation of sufficient energy resolution of the measurement setup investigated in the $\ll 1\ G_0$ tunneling regime, and (ii) providing subgap $I(V)$ data on clean atomic wires as a comparison basis to subgap characteristics of RS filaments in the investigated $\approx 1\ G_0$ and $\gtrsim 1\ G_0$ conductance regimes (for Nb and Ta-based systems, respectively).

The differential conductance ($\mathrm{d}I/\mathrm{d}V$) curves displayed in Figure 5.6.c,d with green lines (for Ta and Nb atomic junctions respectively) exhibit an appearance of a gap region around zero bias voltage, characteristic of superconductor - tunnel barrier - superconductor junctions. Outside this gap region, normal conductance of the junction is measured, while inside the gap region, the conductance is measured as effectively zero. Another typical trait of these curves are the characteristic peaks separating these two regimes. For a perfect tunnel junction ($\tau_i \to 0$), a very steep jump would appear in the current at the crossover between the two regimes.

The main reasons for finite width of characteristic peaks in experiments, $\Gamma^{\mathrm{Nb}}_{\mathrm{MCBJ}} = 131\ \mu$V and $\Gamma^{\mathrm{Ta}}_{\mathrm{MCBJ}} = 185\ \mu$V are the result of (i) electrical noise and (ii) finite temperature effects. The latter factor is material-dependent, while the former originates from the imperfect noise filtering of the measurement setup. Therefore, these $\Gamma^{\mathrm{Nb}}_{\mathrm{MCBJ}}$ and $\Gamma^{\mathrm{Ta}}_{\mathrm{MCBJ}}$ values are the measures of energy resolution of superconducting subgap spectroscopy for each studied transition metal-based junctions.

The width of the gap region is expected to be 4Δ, where Δ is the energy gap in the superconductor material. Hence, the experimental values extracted from the distance of the measured characteristic peaks, $\Delta^{\mathrm{Nb}}_{\mathrm{MCBJ}} = 1.294$ mV and $\Delta^{\mathrm{Ta}}_{\mathrm{MCBJ}} = 580\ \mu$V is also material-specific. As expected, these measurements performed on pure junctions retain energy gap values known from the literature [168], $\Delta^{\mathrm{literature}}_{\mathrm{Nb}} = 1.38$ mV and $\Delta^{\mathrm{literature}}_{\mathrm{Ta}} = 665\ \mu$V (note, that these latter values are considered at zero temperature).

Compared to that, the differential conductance curves of tunneling subgap $I(V)$ characteristics recorded on pristine STM point-contact junctions (prior to initiating resistive switching) are shown with black lines in Figure 5.6.c,d. The width of superconducting coherence peaks are increased to $\Gamma^{\mathrm{Nb2O5}}_{\mathrm{ox.}} = 565\ \mu$V and $\Gamma^{\mathrm{Ta2O5}}_{\mathrm{ox.}} = 600\ \mu$V, and the superconducting energy gaps of $\Delta^{\mathrm{Nb2O5}}_{\mathrm{ox.}} = 0.866$ mV and $\Delta^{\mathrm{Ta2O5}}_{\mathrm{ox.}} = 454\ \mu$V yield smaller values than in the case of pure Nb and Ta junctions. The Γ-broadening and decreased Δ values are the result of a smearing of subgap traces for STM point-contact junctions containing oxides. This means that the spectroscopic voltage resolution is reduced for memristive junctions. As the electromagnetic environment and the filtering circuits are

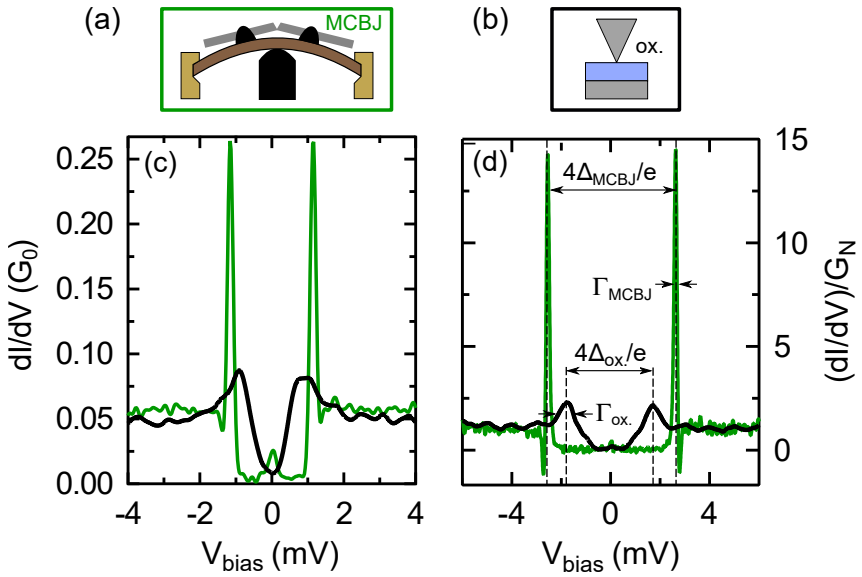

Figure 5.6: *Comparison of oxide-based tunnel junctions to reference measurements on single-atom Nb and Ta junctions in the tunneling regime. Illustration of (a) MCBJ and (b) STM setups for comparison. The coloring of frames in panels (a) and (b) correspond to pure metallic junctions (MCBJ) and pristine metal/thin film oxide/metal junctions (ox.), also yielding the same coloring as corresponding curves in (c) and (d). (c) Raw differential conductance spectra of pure Ta nanowires (green) and $Ta/Ta_2O_5/Ta$ RS devices (black) in the tunneling regime. (d) Differential conductance of pure Nb (green line, G_N =0.016 G_0) and $Nb/Nb_2O_5/Nb$ (black line, G_N =0.0088 G_0) tunnel junctions, normalized to the same conductance level. The width of the characteristic peaks at the gap edges are denoted as* Γ *while their distance is* 4Δ*. The parameters of the four curves in panels (c-d) are the following: In case of tantalum-based junctions (c),* $\Delta^{\mathrm{Ta}}_{\mathrm{MCBJ}} = 580\ \mu V$ *and* $\Delta^{\mathrm{Ta2O5}}_{\mathrm{ox.}} = 454\ \mu V$, $\Gamma^{\mathrm{Ta}}_{\mathrm{MCBJ}} = 185\ \mu V$ *and* $\Gamma^{\mathrm{Ta2O5}}_{\mathrm{ox.}} = 600\ \mu V$*. For niobium-based junctions (d),* $\Delta^{\mathrm{Nb}}_{\mathrm{MCBJ}} = 1.294\ mV$ *and* $\Delta^{\mathrm{Nb2O5}}_{\mathrm{ox.}} = 0.866\ mV$ *for each case, and the width of the characteristic peaks are* $\Gamma^{\mathrm{Nb}}_{\mathrm{MCBJ}} = 131\ \mu V$ *and* $\Gamma^{\mathrm{Nb2O5}}_{\mathrm{ox.}} = 565\ \mu V$*, respectively. [O2, O6]*

exactly the same for the MCBJ and STM measurement setups (see previous paragraph), the Γ-broadening is clearly not related to an increased electronic noise in the STM setup.

The underlying cause to these effects is the phenomenon of proximity superconductivity arising at the regions where suboxides are present in the junctions. These are possibly non-stoichiometric NbO_x and TaO_x regions located at Nb/Nb_2O_5 and Ta/Ta_2O_5 interfaces. These oxygen deficient suboxide layers act as a conducting but intrinsically non-superconducting parts [169, 170] which are susceptible to proximity superconductivity. Such regions are recognized for resulting in a lowered gap value and a smeared superconducting density of states [171–174]. This was proven by subgap spectroscopy conducted on Al/Au/Al atomic contacts [175]. An estimation based on Refs. 175, 176

results in $\Delta^{\mathrm{Nb}}_{\mathrm{ox.}}/\Delta^{\mathrm{Nb}}_{\mathrm{MCBJ}} \approx 0.67$ reduction of the measured gap, if a 10 nm thick proximity superconducting region is introduced to the junction, assuming a 22 nm superconducting coherence length. Such a reduced coherence length is plausible in a highly disordered oxide layer [177] compared to the bulk coherence length of 39 nm in pure niobium [146].

Reference analysis of clean atomic junctions Figure 5.7.a shows some theoretical subgap $I(V)$ characteristics of ScS junctions with a single conductance channel at various transmissions (τ = 0.01, 0.2, 0.4, 0.6, 0.8, 1, respectively). These fine-structured $I(V)$ characteristics exhibit distinct structures at the fractional values of the superconducting gap, $eV_{\mathrm{bias}} = 2\Delta/n$ due to multiple Andreev reflections (as discussed earlier in Section 5.2.1). The sum of such theoretical $I(V)$ curves with different transmission values result in fitting curves with a given quantum PIN code, which can be used for fitting of experimental characteristics. I performed this fitting of $I(V)$ curves using a program written by G. Rubio-Bollinger [157]. It is important to note, that this fitting procedure was only used for later studies of Nb_2O_5 memristive junctions. For fitting Ta_2O_5 curves, I worked out another fitting procedure detailed in Subsection 5.4.1.

Before carrying out subgap spectroscopy measurements on resistive switching junctions, the measurement setup including various filter stages was optimized and tested on

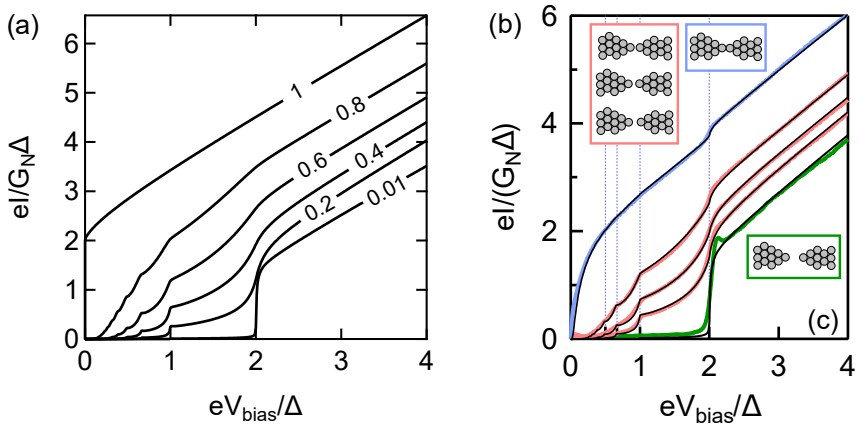

Figure 5.7: *Fitting relying on the theory of multiple Andreev reflections. (a) Theoretical subgap $I(V)$ characteristics of different ScS junctions with various transmission values. (b) Typical subgap $I(V)$ characteristics of pure Nb/Nb atomic junctions. The parameters obtained from the Andreev fits (black curves) corresponding to curves from the top to the bottom are τ_i={0.969, 0.112, 0.022, 0.021, 0.020},{0.686, 0.142, 0.017, 0.014, 0.013}, {0.514, 0.148, 0.024, 0, 0}, {0.344, 0.032, 0.032, 0, 0}, {0.016, 0, 0, 0, 0}; $G_N/G_0 = \sum_i \tau_i$=1.144, 0.872, 0.686, 0.408, 0.016. The insets illustrate possible underlying atomic configurations of these subgap curves (the color of each frame correspond to the curves). [O6]*

the well-studied reference system of pure Nb atomic nanowires [150, 156, 161, 178] created in a MCBJ arrangement. Similar studies were also carried out on pure Ta junctions.

Typical subgap $I(V)$ characteristics measured with different displacements of the Nb electrodes are displayed in Figure 5.7.b. The curves are normalized to a slope of unity so that they are comparable to each other, via the usual normalization factors of $G_N\Delta$ and Δ for the current and the voltage axes, respectively [156].

The subgap curves seen in Figure 5.7.b were well fitted with the theory of multiple Andreev reflections. All curves were fitted using five conductance channels, and the fits result in a single dominant quantum channel for all cases. The transmission of this channel grows as the conductance increases, and further channels start to open up (see τ_i values in the caption of Figure 5.7). The $\tau_1 \ll 1$ value of the green curve represents a tunneling junction, the red curves with $\tau_1 \approx 0.3 - 0.7$ have partially open channels, while the blue curve with $\tau_1 \approx 0.97$ represents a single, nearly perfectly transmitting, dominant channel (similarly to the blue curve in Fig. 5.2.e). This curve has two characteristic features which are typical for subgap curves with $\tau_1 \approx 1$: first, there is a sudden increase in the current near zero, and second, the intersection of the y-axis and the normal conductance slope of the curve, the so-called excess current, which is a positive value greater than zero. (Note, that the analysis of the excess current of subgap curves is also a possible method for extracting information on the transmission eigenvalues [179].)

5.3 Quantum PIN code of Nb_2O_5 memristors

The first physical systems I studied with superconducting subgap spectroscopy were Nb atomic wires and Nb_2O_5 point-contact RS junctions. This choice of materials was motivated by the $T_c^{\mathrm{Nb}} = 9.22$ K superconducting phase transition temperature of niobium which is the highest among elemental superconductors. It is to be noted, that the superconducting energy gap not only depends on the factors discussed earlier (energy resolution of the measurement setup and possible proximity effects in a disordered junction region), but also has a temperature dependence, the gap value has a maximum at zero temperature [180]. Practically, this means, that the further the temperature is from the critical temperature T_c, the larger is the gap value, which is beneficial for resolving subgap features of $I(V)$ characteristics.

Another motivation for choosing niobium pentoxide-based RS devices as the subject of these first studies were the beneficial, yet less explored resistive switching behavior of these devices [113, 181, 182]. Previous studies in our research group investigating ultrafast operation of room temperature point-contact Nb_2O_5 junctions [101] further motivated my pursues of a deeper understanding of the underlying RS mechanisms.

5.3.1 Subgap spectroscopy of the ON and OFF states

In the following, the ON and OFF states of Nb_2O_5 point-contact devices are analyzed in the subgap voltage regime. To this end, junctions were initialized according to the procedures described in Section 5.2.2. First, room temperature characteristics were studied using PtIr and Nb tips, revealing very similar overall traits (typical operation voltage- and current regime, along with a non-linearity of resistance states typical for Nb_2O_5 [101]) of resistive switching $I(V)$ curves, as exemplified by Fig. 5.8.a. Then, low temperature operation was also tested, yielding remarkably similar $I(V)$ characteristics at $T = 1.4$ K ambient temperature (see and compare Fig. 5.8.b to Fig. 5.8.a). After stable, low temperature operation was confirmed, subgap characteristics of ON and OFF states were recorded and analyzed.

Prior to discussing the results of this analysis, the limitations originating from proximity superconductivity should be addressed. The differential conductance of a tunneling Nb(thin film)/Nb_2O_5/Nb(tip) junction deviates from those of pure Nb/Nb tunnel junctions, as seen in Figure 5.6.d previously. These deviations originate from a smearing of tunneling $I(V)$ curves displayed in Figure 5.8.c-d. (see brown traces in both panels). This $I(V)$ curve represents a bottom limit for subgap spectroscopy measurements on memristive junctions, i.e. for the minimum τ_i value which can be detected. All tunneling curves ($\tau_i \ll 1$) are re-scaled to this very same $I(V)$ trace, irrespective of their normal conductance (in the applied normalizations of $eI/(G_N\Delta)$ and $eV_{\mathrm{bias}}/\Delta$). Therefore, the area

below this tunneling $I(V)$ curve is experimentally unreachable in this plane, denoted by a brown shading in Figure 5.8.c-d. Another implication is that any subgap curve which

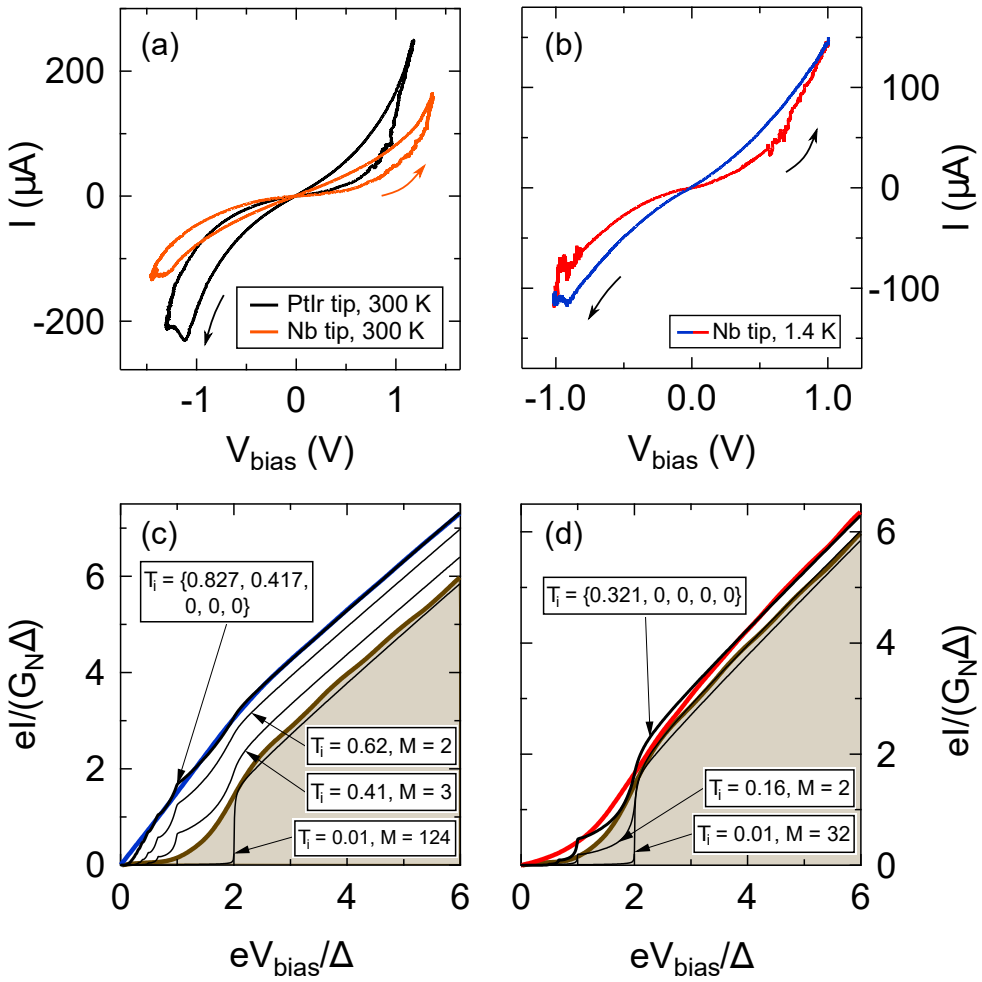

Figure 5.8: *Quantum PIN code of different resistance states in memristive Nb_2O_5 point-contact junctions. (a) Typical resistive switching I(V) curves measured in Nb(thin film)/Nb_2O_5/PtIr(tip) Nb(thin film)/Nb_2O_5/Nb(tip) junctions at room temperature (see legend). (b) Resistive switching measured in a Nb(thin film)/Nb_2O_5/Nb(tip) junction at $T = 1.4\,K$. The red (blue) part marks the OFF (ON) state, the arrows point to the direction of switching. The blue and red traces in panels (c) and (d) show the subgap $I(V)$ characteristics recorded in the ON and OFF states of the resistive switching curve in panel (b). The thick black lines are the theoretical $I(V)$ curves derived from Andreev fits (the transmission eigenvalues are shown in the corresponding boxes). The thin black curves in panel (c) show theoretical subgap curves with total conductances identical to the ON state conductance, which is divided between M channels with equal τ_i transmission eigenvalues. The brown lines show rescaled tunneling subgap curves with $G_N \approx 0.01\,G_0$ conductance recorded on a disconnected junction. [O6]*

grows above this background comes from a contact which is clearly not a tunnel junction, and it has at least one partially open channel.

The red and blue traces displayed in Figure 5.8.c-d. correspond to the OFF and ON states of the resistive switching shown in Figure 5.8.b.

The blue subgap curve of the $\sim 1G_0$ ON state exhibits a steep rise in current already at zero bias, resembling reference subgap curves of (i) a theoretical junction with a perfectly transparent conductance channel (Fig. 5.2.e, blue curve) and (ii) a single-atom Nb junction with one, highly transparent channel (Fig. 5.7.b, blue curve). The fit of this ON state (see the thick black fitting curve) according to the theory of multiple Andreev reflections results in a single dominant channel with a leading transmission close to unity, and a partially open channel with smaller transmission (see corresponding quantum PIN code in label). This observation is a clear indication that the ON state is a filament with high transmission and a single atom at its narrowest cross-section (see the illustration in Figure 5.2.a). If the conductance of the ON state would be shared between several channels equally, completely different subgap $I(V)$ traces would appear (see the thin black lines showing theoretical subgap traces with M equally transmitting channels). On the other hand, a filament made of several atoms at its narrowest cross-section would yield a larger diameter than the $\lambda_F = 0.53$ nm Fermi wavelength, resulting in a larger conductance with several highly transmitting channels [148, 183].

The red subgap curve of the OFF state (Fig. 5.8.d) is best fitted by a single, partially open channel. However, this curve is just slightly above the limiting tunnel curve, which introduces some uncertainty to the interpretation of being truly a single channel. Anyhow, it is likely that during resistive switching, a single-atom ON state resets to a single-atom OFF state, introducing a narrow barrier between the central atoms, induced by voltage.

5.3.2 Statistical analysis of the transmission eigenvalues

The analysis of a greater ensemble of independent Nb(tip)/Nb_2O_5/Nb(thin film) resistive switching junctions is displayed in Figure 5.9. First, the limitations of subgap analysis arising from the smearing of tunneling subgap curves (see brown traces in Figure 5.8.c-d.) are addressed. Since the shape of a tunneling subgap curve is independent of its normal conductance, a validity limit of subgap analysis can be determined by rescaling the brown tunneling curve of Figure 5.8.c-d. to arbitrary conductance values. Fitting these rescaled, fictive tunneling curves define a lower boundary through their τ_1 values, denoted with brown points saturating at $\tau_1 \approx 0.3$ in Figure 5.9.a. Similarly to Figure 5.8.c-d., the brown shaded area in Figure 5.9.a is experimentally inaccessible in memristor junctions due to the smearing of tunneling curves, yet the points falling in the area above contain valid information on the leading transmission, conclusively indicating the opening of the first quantum channel.

For the OFF memristor states (see red circles), the leading transmissions are close to the validity border. However, ON states yield $\tau_1 \approx 0.6-0.9$ around G_0 device conductance, located well above the boundary. This analysis confirms the single-atom filamentary nature (see inset in Figure 5.9.a) of the investigated ON states.

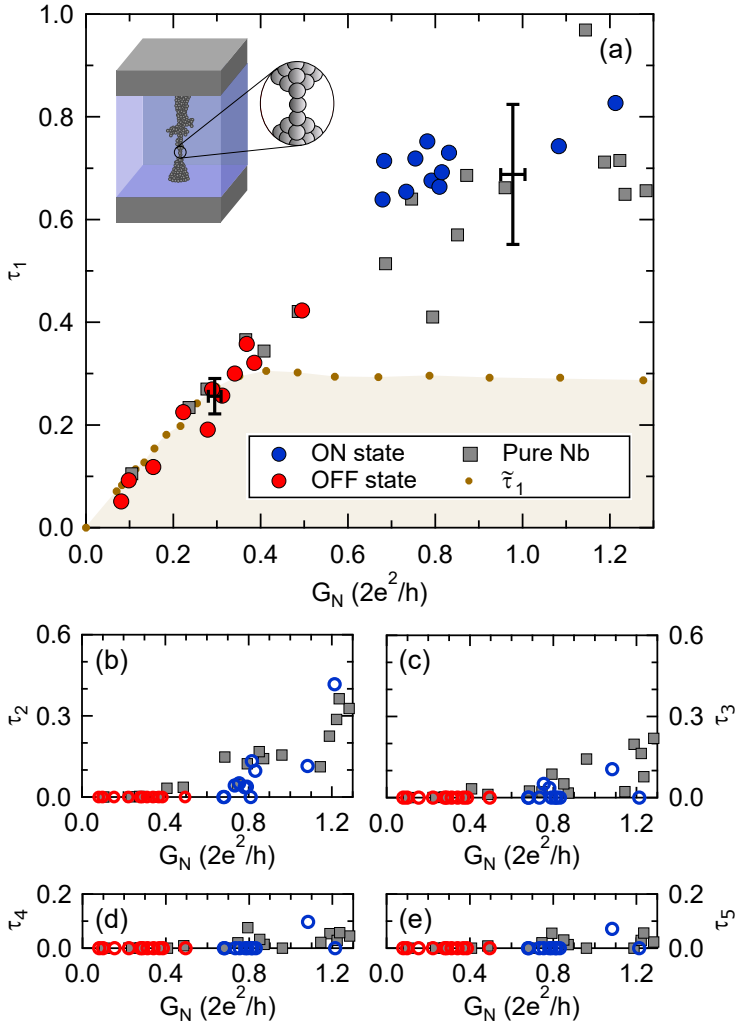

Figure 5.9: *Evolution of transmission eigenvalues near the quantum conductance in pure Nb and memristive Nb_2O_5 systems. (a-e) The distribution of the τ_1–τ_5 transmission eigenvalues calculated in different Nb(tip)/Nb_2O_5/Nb(thin film) resistive switching junctions at $T = 1.4\,K$. The blue (red) circles correspond to the ON (OFF) states, respectively. The grey squares show the τ_i values of pure Nb/Nb atomic junctions. Taken from Ref. 161, the black datapoints and error bars show the mean and standard deviation of transmission values measured on 30+30 different pure Nb/Nb atomic junctions measured around $G \approx 1\,G_0$ and $G \approx 0.3\,G_0$ conductances. The brown shaded area in panel (a) is a region in the $\tau_1 - G_N$ plane where the analysis is not conclusive due to the Γ-broadening. The inset in panel (a) illustrates a single-atom filamentary switch. [O6]*

Finally, the transmission properties of niobium oxide resistive switching filaments and pure niobium atomic wires are compared. A previous study had demonstrated mean transmission probabilities and their variances at 0.3 G_0 and 1 G_0 conductances, for pure single-atom Nb junctions [161] (black data points with error bars in Figure 5.9.a), which was extended (see grey squares) to cover the whole conductance range analyzed for resistive switching. The presence of oxygen in the filament may alter the transmission eigenvalues compared to clean Nb atomic wires. One possible effect is that oxygen induces a barrier at the narrowest cross-section, resulting in reduced τ_i values for the channels with higher transmission. Another possibility is that the oxygen blocks transport through the d orbitals and enhances the role of the s channel, resulting in an increased τ_1 value accompanied by the suppression of the further transmission eigenvalues – similarly to oxygen decorated Ni junctions [166]. However, the analysis presented here shows that the evolution of all transmission probabilities with the total conductance is similar for both resistive switching filaments and pure Nb atomic wires. It implies that the transport in the ~ 1 G_0 ON state of Nb_2O_5 point-contact devices happens in a similar manner as the transport through single-atom Nb nanowires.

5.3.3 Conclusions

The presented analysis of Nb_2O_5 point-contact resistive switching junctions operated near the universal quantum conductance unit demonstrate potential for creating atomic-sized memory devices. Superconducting subgap spectroscopy utilized for this analysis proved to be a powerful tool for the direct experimental study of the transmission properties of resistive switching junctions. This technique is especially useful for investigating the quantum PIN code of the junctions in close proximity to the quantum conductance regime. My measurements on Nb_2O_5 memristor junctions provide the first experimental confirmation that the switching occurs due to the structural reconfiguration of a truly single-atom diameter filament in a transition metal oxide resistive switching system. These studies offer solid basis for further exploration of transmission channel decomposition in other compounds contacted by auxiliary superconducting electrodes.

Relying on my experiences with Nb-based systems, I extended the scope of my studies Ta-based atomic junctions and RS filaments, which I discuss in the next Section.

5.4 Quantum transport properties of Ta_2O_5 memristors

After exploring atomic-sized filaments in Nb_2O_5 memristors, I shifted the focus of my studies to memristors made of another transition metal oxide, Ta_2O_5. This material has great potential as a switching medium for the realization of non-volatile analog memory elements, since multilevel operation with at least 6 bit resolution [105], ∼20 ps switching times [44], endurance of 10^{12} switching cycles [41], and ∼pJ switching energies [42] are feasible with this RS material. All these properties make tantalum oxide resitive switching cells ideal hardware building blocks of large-scale crossbar neural networks [43]. In tantalum oxide based resistive switching cells the transport in each state and resistive switching both can be affected by numerous mechanisms, e.g., the concentration/movement of oxygen vacancies or metal cations, electron trapping, effects of interface defects at electrode sites and temperature or electric field dependent hopping mechanisms [104, 105, 184–188]. Therefore, in-situ, direct experimental studies are needed to facilitate understanding of switching mechanisms in tantalum oxide devices, which become increasingly difficult when nanoscale active regions are involved.

5.4.1 Model approach of the transmission distributions

The modeling approach for fitting the subgap $I(V)$ characteristics of wider RS filaments and pure nanowires (yielding $G_N > 3\ G_0$ normal conductance) is illustrated in Fig. 5.10. In contrast with the approach presented earlier in Section 5.3, the present model aims at the analysis of transmission density functions (instead of determining each individual transmission eigenvalues of all conductance channels). The key element is of this approach is the $\rho^{\mathrm{RMT}}(\tau) \sim \tau^{-1}(1-\tau)^{-1/2}$ universal probability density function (brown curve in Fig. 5.10.b) derived for phase coherent mesoscopic diffusive wires with a large number of open conductance channels ($M \gg 1$). The above expression for the $\rho^{\mathrm{RMT}}(\tau)$ probability density function was calculated using random matrix theory (RMT) [165]. An illustration of the corresponding model system is shown at the second panel of Fig. 5.10.a (brown frame), where the gray background symbolizes the diffusive nature of the transport.

The RMT density function is bimodal: $\rho^{\mathrm{RMT}}(\tau)$ has peaks both at the low-transmission ($\tau \ll 1$) and high-transmission ($\tau \approx 1$) ends, while transmission values in between also exhibit finite weights. The seemingly counter-intuitive presence of highly transparent channels in a diffusive junction can be attributed to the possibility of bypassing point-like defects by certain conductance channels [165]. For example, in Pb atomic-sized wires, transport is affected by an interplay of non-perfect crystalline ordering, non-perfect

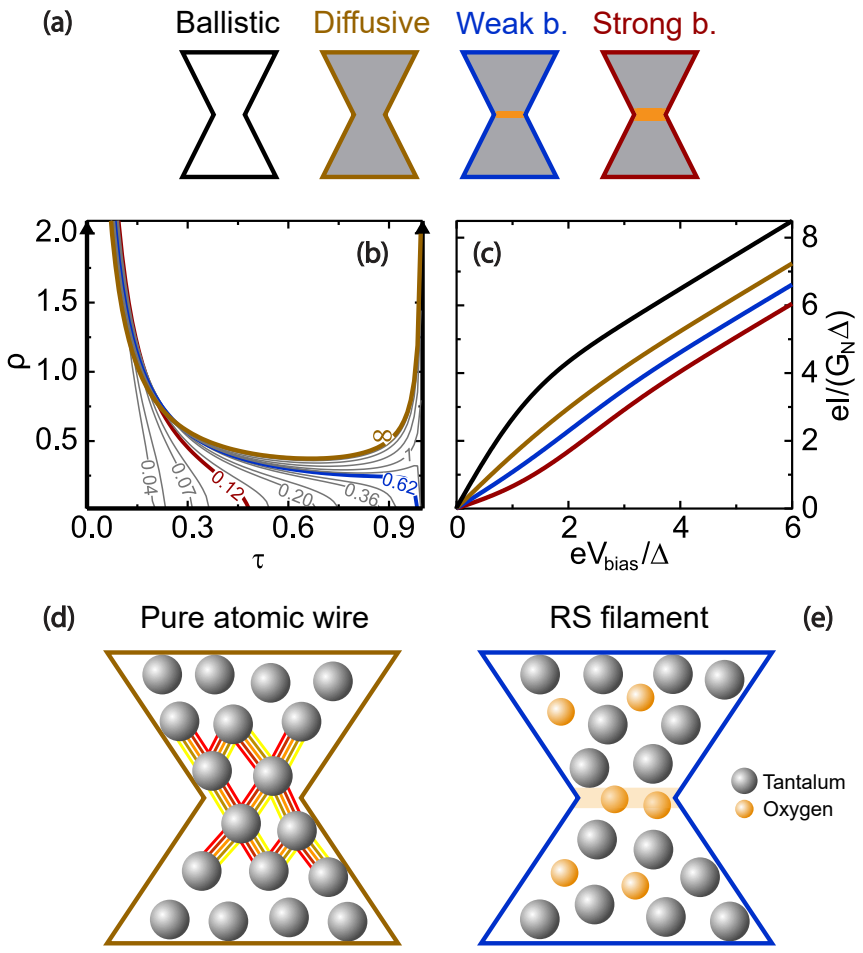

Figure 5.10: *Model approach for the analysis of transmission distributions. Panel (a) shows possible models for transport: a ballistic quantum wire, a diffusive wire without any extended barrier, a diffusive wire with weaker/stronger extended barrier at the bottleneck. The corresponding model transmission density functions are illustrated in panel (b) with the same color-coding as in (a). Black Dirac delta peaks illustrate the case of quantized conductance channels in a ballistic quantum wire. The brown curve shows the* $\rho^{\mathrm{RMT}}(\tau)$ *density function for a diffusive wire. The gray curves including the blue/red example curves represent the density functions in cases of an extended barrier with variable strength, as labeled by the* α *parameters. Panel (c) shows the calculated ScS* $I(V)$ *curves at* $G = 10\,G_0$ *for each modeled case (with the same color-coding as in (a)). Panels (d) and (e) respectively illustrate a pure Ta atomic wire and an oxide-based resistive switching filament, with edge colors corresponding to the color code of the appropriate model. In (d) the five colored lines connecting each neighbor atoms emphasize typical transport through 5 non-vanishing inter-atomic conductance channels in a d-valent metal. As shown in (e), oxygen atoms can form an extended barrier (orange rectangular region), attributed to the voltage-controlled accumulation of oxygen. [O2]*

transmission (especially through highly oriented p orbitals), and surface scattering, which factors result in a bimodal transmission distribution well characterized by the $\rho^{\mathrm{RMT}}(\tau)$ universal density function, apparent even at atomic dimensions [157].

For transition metals, like the investigated pure Ta nanowires, similar behavior is expected. In this case, the electron transmission between two neighbor atoms is shared among ≈ 5 conductance channels, as illustrated by the 5 colored lines between each neighbor atoms in Fig. 5.10.d. This expectation originates from the tight-binding model of a single-atom nanowire [149, 163] identifying 1 s-type and 5 d-type channels in a transition metal (corresponding to valence orbitals), and predicting the closing of one channel based on symmetry reasons. This specific behavior was experimentally verified for Nb and Ta junctions [150, 161]. As a result of the above considerations, $\approx 10-15$ non-vanishing conductance channels are realistic for a junction with only $2-3$ atoms diameter (in the narrowest cross-section), in case of tantalum. Such a large channel number justifies applying a model based on transmission density functions.

The aim of my studies is to experimentally verify the universal transmission density function in pure Ta atomic wires, and to identify and understand possible deviations from this universal behavior in oxide-based RS filaments.

The presence of oxygen near a metallic atomic wire can affect quantum transport properties in multiple ways. Oxygen ions can create either an extended barrier or individual point-like defects, influencing transport. Moreover, they can block transport in d orbitals, thereby amplifying the dominance of the s channel, which was observed experimentally in nickel atomic wires exposed to oxygen [166]. The latter scenario would result in a more transmissive situation compared to $\rho^{\mathrm{RMT}}(\tau)$, while the formation of an extended barrier would lead to a less transmissive situation.

Let us consider possible model transmission density functions with *more transmissive* and *less transmissive* characteristics, compared to the $\rho^{\mathrm{RMT}}(\tau)$ reference universal distribution of a diffusive nanowire (see Figs. 5.10.a,b).

- As an example for a highly transmissive case, the most extreme situation is a fully ballistic junction (see black-framed white junction in Fig. 5.10.a and thick black lines marking Dirac delta functions in Fig. 5.10.b). This scenario corresponds to conductance quantization, where all quantum channels are open with perfect transmission.

- The less transmissive situation (compared to the RMT case) can be considered according to the model of Yu. V. Nazarov described in Ref. 164, where an extended barrier is formed at the bottleneck of a diffusive junction. This results in an enhanced back-scattering in all channels, suppressing the peak at $\tau \approx 1$ in the original bimodal transmission distribution. The model of Nazarov consists of a series connection of

a diffusive wire with R_W resistance and an extended barrier with R_B resistance. The transmission density function derived from these conditions depends on the $\alpha = R_W/R_B$ parameter. Varying this α barrier parameter, distinct transmission distributions can be computed shown by the gray curves in Fig. 5.10b., including also exemplary curves of *strong* and *weak* barrier cases highlighted in red and blue. The associated model systems are illustrated in Fig. 5.10.a (framed by matching colors), where the orange domain marks the extended barrier. Note, that the $\alpha \to \infty$ limit recovers the universal transmission density function $\rho^{\mathrm{RMT}}(\tau)$.

To experimentally investigate relevance of the scenarios above, I compare subgap $I(V)$ traces of pure Ta nanowires and memrisitve Ta_2O_5 point-contact devices to simulated model $I(V)$ characteristics of a given transmission density function as follows.

- The chosen transmission density function $\rho(\tau)$ is normalized to unity, $\int \rho(\tau)\mathrm{d}\tau$=1.
- The corresponding average transmission probability is determined as $\overline{\tau_\rho} = \int \tau\rho(\tau)\mathrm{d}\tau$.
- Relying on this $\overline{\tau_\rho}$ average transmission, the channel number at a given G conductance is estimated as $M_{\rho,G} = \mathrm{round}\,((G/G_0)/\overline{\tau_\rho})$.
- Individual τ_i transmission eigenvalues are computed by generating $M_{\rho,G}$ random numbers according to the chosen $\rho(\tau)$ probability density function.
- These transmission eigenvalues define a particular ScS junction, and the subgap $I(V)$ curve of this hypothetical junction is computed via summing individual theoretical subgap $I(V)$ curves with τ_i transmission eigenvalues (calculated from multiple Andreev reflection theory [157]).
- Last, I calculate 50 hypothetical subgap curves by repeating the above steps, and compute their average.

For tunneling $I(V)$ curves, a similar reduction of Δ and increased Γ-broadening are experienced as in case of Nb_2O_5 junctions (see Figure 5.6.c,d), attributed to proximity superconductivity of TaO_x regions. I model the related smearing of the subgap $I(V)$ curves by smoothing the theoretical subgap $I(V)$ characteristics with a Gaussian kernel according to the actual energy resolution. Furthermore, a bottom cutoff of $\tau_c = 0.03$ is applied in my analysis, i.e., channels with smaller transmission are not considered as open. This bottom cutoff is chosen such that it yields $\overline{\tau}_\rho^{\mathrm{RMT}} = 0.39$ average transmission for $\rho^{\mathrm{RMT}}(\tau)$, reproducing the $\approx 2\ G_0$ conductance attributed to single-atom pure Ta junctions (see the peak of conductance histogram in Figure 5.1.a earlier) with the assumed $M = 5$ open channels. Fulfilling the above relation makes the chosen $\tau_c = 0.03$ bottom cutoff physically realistic.

Figure 5.10.c shows such simulated $I(V)$ characteristics for some hypothetical ScS junctions with the same $G = 10\,G_0$ conductance, calculated from different transmission density functions. The brown subgap curve is computed from the universal $\rho^{\mathrm{RMT}}(\tau)$ density function (shown with brown line in Fig. 5.10.b). The blue and red subgap curves correspond to less transmissive cases, where extended barriers with $\alpha = 0.62$ and $\alpha = 0.12$ parameters are incorporated to their underlying transmission densities (see these $\rho(\tau)$ functions with blue and red lines in Fig. 5.10.b). As a reference, the a more transmissive case is also illustrated by the black curve, corresponding to a junction with conductance quantization, where all open channels yield $\tau_i = 1$ transmission. Note, that this black curve is not infinitely steep at zero voltage due to the incorporated effect of the energy smearing. The resulting ScS $I(V)$ traces are well distinguishable for the above, very different transmission densities, which serves as the foundation of my analysis.

5.4.2 Transmission distribution analysis

The results of subgap studies performed on different systems are exemplified in Figure 5.11. Analysis of the subgap $I(V)$ traces recorded on RS filaments and pure Ta atomic wires are displayed in Fig. 5.11.c and Fig. 5.11.d, respectively. Analysis of the pure Ta atomic system serves as a reference for the memristive states. The black dotted line in Fig. 5.11.d shows an experimental ScS $I(V)$ curve recorded on a pure Ta junction, being very close to the simulated $I(V)$ curve originating from the universal $\rho^{\mathrm{RMT}}(\tau)$ density function (shown with brown dashed line). Applying Nazarov's theory [164] results in a slightly better agreement, as shown with the green dashed $I(V)$ curve computed with the best fitting $\alpha = 1.6$ barrier parameter. The corresponding transmission density functions (green and brown lines in Fig. 5.11.b for the $\alpha = 1.6$ *very weak* barrier and $\alpha \to \infty$ RMT cases) are indeed really close to each other, indicating that this typical ScS curve of a pure Ta atomic wire is well described by the universal transmission density function. The $G = 8.33\,\mathrm{G_0}$ conductance of this particular junction and the $\overline{\tau}_{\rho}^{\mathrm{RMT}} = 0.39$ average transmission yields $M = G/\overline{\tau}_{\rho}^{\mathrm{RMT}} \approx 21$ open channels, indicating a junction with ≈ 4 atoms at the narrowest cross-section (using the 5 channels/one atom estimate).

Figure 5.11.a displays a typical RS $I(V)$ curve at $T \approx 1.3\,\mathrm{K}$, where the ON and OFF memristor states are marked with blue and red colors, respectively. Superconducting features are detected on a much smaller voltage scale than the $\sim 1\,\mathrm{V}$ scale of RS phenomena, near the subgap regime characterized by the superconducting energy gap of tantalum, $V_{\mathrm{bias}} \approx 2\Delta_{\mathrm{Ta}}/e \approx 1.33\,\mathrm{mV}$ [189]. Top and bottom black dotted lines in Figure 5.11.c show the measured subgap $I(V)$ curves of the ON and OFF states, respectively. Blue and red lines represent the best fitting model $I(V)$ curves according to Nazarov's theory, which yield $\alpha = 0.51$ (ON state, blue curve) and $\alpha = 0.12$ barrier parameters (OFF state, red curve). Transmission density functions behind these subgap $I(V)$ traces

are displayed in Fig. 5.11.b with corresponding colors. These density functions are significantly different from the light brown universal transmission density, $\rho^{\mathrm{RMT}}(\tau)$. These

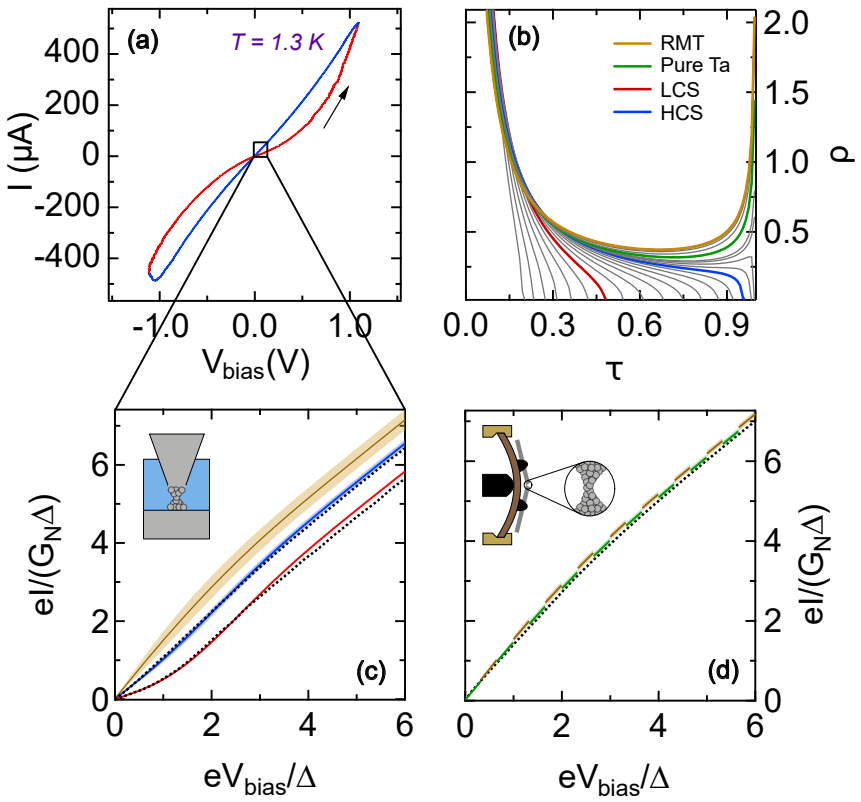

Figure 5.11: *Subgap analysis of a representative RS point-contact junction and a pure Ta atomic wire. (a) Typical resistive switching curve of Ta(tip)/Ta_2O_5/Ta STM junctions at $T = 1.3$ K temperature (arrow indicates the direction of switching). (b) Transmission densities shown with different barrier parameters, as the foundation of the analysis. Red, blue and green lines correspond to the best fitting cases of the LCS (OFF state) and HCS (ON state) of the RS filament in panel (c) and to the pure Ta atomic wire in panel (d), respectively. As a reference, the light brown curve shows $\rho^{\mathrm{RMT}}(\tau)$. (c) Experimental subgap $I(V)$ curves for the HCS (top dotted line, $G = 4.03\ G_0$) and the LCS (bottom dotted line, $G = 2.02\ G_0$), recorded in the different conductance states of the RS $I(V)$ curve in panel (a). The blue and red curves show the best fitting model $I(V)$ curves (yielding $\alpha = 0.62$ and $\alpha = 0.12$ barrier parameters), whereas the light brown curve shows the model $I(V)$ curve for $\rho^{\mathrm{RMT}}(\tau)$ as a reference ($\alpha \to \infty$ case). For all the colored curves the light colored background area marks the standard deviation of the $I(V)$ curves for the same density function, but various random transmission sets. (d) The measured subgap $I(V)$ curve (dotted line, $G = 8.33\ G_0$) and the best fitting model $I(V)$ curve (green dashed line) for the reference pure Ta atomic wire. The measured $I(V)$ curve is very close to the model $I(V)$ curve for $\rho^{\mathrm{RMT}}(\tau)$ (light brown dashed line). [O2]*

significant deviations are also spotted on the plane of subgap $I(V)$ curves in Figure 5.11.c. The brown curve in this same panel (corresponding to $\rho^{\mathrm{RMT}}(\tau)$) is displayed such that the light brown area marks the standard deviation of the averaging over 50 simulated $I(V)$ curves with different sets of random transmissions (generated according to the $\rho^{\mathrm{RMT}}(\tau)$ density function). Similarly, light blue and light red regions near the blue and red model $I(V)$ curves represent standard deviations obtained from the same procedure (though for the red curve these values are so small that it is not visible on the curve). Blue and red $I(V)$ traces are clearly distinguished from the reference brown curve taking in account standard deviations of model $I(V)$ curves, indicating reliability of the above analysis.

Results of a statistical analysis performed in different states of Ta_2O_5-based RS filaments (blue/red circles showing ON/OFF states) and several pure Ta atomic wires (green triangles) are displayed in Figure 5.12.a, in the investigated $\approx 1 - 13\,\mathrm{G}_0$ conductance range. The plotted α barrier parameters are extracted by finding the best fitting model subgap $I(V)$ curves, as discussed above (and illustrated in Figure 5.11). The black line in Figure 5.12.a represents a quantitative boundary for each conductance value, which separate junctions based on their α barrier parameter as follows:

- Large α values describe extremely weak barriers which yield transmission density functions really close to the universal $\rho^{\mathrm{RMT}}(\tau)$ (the $\alpha \to \infty$ limiting case).
- Small α values characterize those barrier strengths for which my analysis is sensitive, meaning that the underlying density functions are clearly distinguishable from $\rho^{\mathrm{RMT}}(\tau)$.

The above conditions can be treated quantitatively, comparing the standard deviation of model $I(V)$ curves of given α parameters at certain G conductance values to reference $I(V)$ curves corresponding to $\rho^{\mathrm{RMT}}(\tau)$. Below the boundary, standard deviation of a model $I(V)$ curve does not overlap with the standard deviation of the model $I(V)$ curve corresponding to $\rho^{\mathrm{RMT}}(\tau)$. This way, the observed clear separation of datapoints to the two sides of the boundary line proves that (i) all measurements on pure Ta atomic wires are well described by the universal transmission density function $\rho^{\mathrm{RMT}}(\tau)$, and (ii) all of oxide-based RS filament states deviate from this model, indicating the presence of a barrier with variable strength for ON and OFF memristor states.

Discussion The above analysis confirms that quantum transport properties of pure Ta atomic-sized nanowires are well characterized by $\rho^{\mathrm{RMT}}(\tau)$. Furthermore, this universal transmission density is valid in the entire investigated conductance range ($\approx 1 - 13\,\mathrm{G}_0$, shown in Fig. 5.12.a). As the Ta wire is mechanically elongated (and thinned also), the number of open channels decreases, while the characteristic distribution of the transmission eigenvalues remains similar, implying a constant $\overline{\tau}_{\rho}^{\mathrm{RMT}} \approx 0.39$ average transmission.

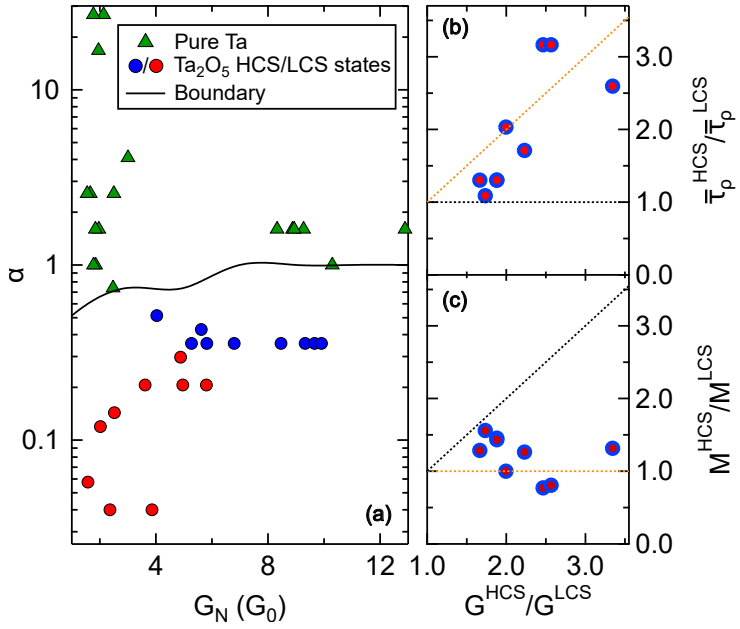

Figure 5.12: *Analysis of the barrier strength for many pure Ta nanowires and RS filament states. (a) The α values gained from fitting of experimental subgap $I(V)$ curves are presented for multiple pure Ta atomic wires (green triangles) as well as HCSs (blue circles) and LCSs (red circles) of various RS filaments. The black line represents a boundary, above/below which the deviation from the $\rho^{\mathrm{RMT}}(\tau)$ universal transmission density function is insignificant/significant. Panels (b) and (c) show the average transmission ratio and channel number ratio as a function of the conductance ratio for all the RS processes behind the blue and red points in panel (a). The orange/black dotted lines illustrate the cases, where solely the transmission/channel number changes during resistive switching. [O2]*

The confirmed $\rho^{\mathrm{RMT}}(\tau)$ density function for atomic-sized Ta junctions indicates a broad variation of transmission eigenvalues, with some highly transparent channels. The reason for this observation lies in the valence electron structure of tantalum. Transparent channels can originate from *s*-type orbitals, whereas *d*-type orbitals contribute to the broad variation of τ_i, most probably. Despite only a few highly transparent channels for pure Ta atomic junctions, $\rho^{\mathrm{RMT}}(\tau)$ does not yield conductance quantization features at all. The validity of $\rho^{\mathrm{RMT}}(\tau)$ in tantalum contrasts the case of noble metals and alkali metals, where a more transmissive density function [190] is realized through highly delocalized *s*-electrons, resulting in conductance quantization [149, 150].

In case of atomic-sized metallic filaments in Ta_2O_5 RS states, average transmission and the number of open channels can be determined, which gives $\overline{\tau_\rho} = 0.25$ and $M = 16$ in the ON state (high conductance state, HCS) and $\overline{\tau_\rho} = 0.12$ and $M = 17$ in the OFF state (low conductance state, LCS). These values are indicative of a markedly different

physical picture compared to pure Ta nanowires. In the RS filament, the reset process leaves the channel number nearly unchanged. Instead, the conductance change manifests as a significant decrease in the average transmission. Such a process can originate from a switching mechanism where electric field-driven redistribution of oxygen ions lead to the formation of a barrier at the filament bottleneck (see the schematic illustration in Fig. 5.11.e), whereas the overall diameter of the filament stays similar. The above analysis yields ≈ 3 Ta atoms in the narrowest cross-section as an estimate on filament size (using the 5 channels/one atom assumption).

A similar analysis is performed in various high conductance and low conductance states of RS junctions, as visible in Figure 5.11.b,c, where the $\overline{\tau}_\rho^{\mathrm{HCS}}/\overline{\tau}_\rho^{\mathrm{LCS}}$ and the $M^{\mathrm{HCS}}/M^{\mathrm{LCS}}$ ratios are plotted as a function of the $G^{\mathrm{HCS}}/G^{\mathrm{LCS}}$ conductance ratio for the RS data of Fig. 5.11a. The orange (black) dotted lines represent the imagined case, where solely the transmission (channel number) changes during RS. It is clear that data follows the trend shown with orange lines, i.e. the junction sizes are similar, but average transmission values are different in related pairs of high/low conductance states of RS. In other words, the reset process yields the formation of an oxygen-based barrier at the filament bottleneck. Relying on the extracted M values from this analysis, RS filaments are composed of $3-8$ Ta atoms in their narrowest cross-section (for the investigated junctions in the $\approx 1-13\,\mathrm{G}_0$ conductance range).

5.4.3 Conclusions

I performed an analysis relying on superconducting subgap spectroscopy to study atomic-sized filaments in Ta_2O_5 point-contact RS devices, in their high and low conductance states. I determined the underlying transmission density functions of the open conduction channels originating from the filamentary active region. I also analyzed and compared my results to the reference system of pure Ta atomic wires. I found that the latter system is well described by the universal $\rho^{\mathrm{RMT}}(\tau)$ density function, known for the description of diffusive junctions. The bimodal $\rho^{\mathrm{RMT}}(\tau)$ density function is found to be valid despite the atomic nature of the studied tantalum junctions in the $\approx 1-13\,\mathrm{G}_0$ conductance range, which is attributed to the valence electron structure of tantalum. The presence of some highly transparent channels is characteristic to the universal transmission distribution, which is sensitively detected by superconducting subgap spectroscopy.

In contrast to pure Ta junctions, the analysis of transmission density functions in Ta_2O_5-based RS filaments yields that transparent conduction channels in the ON state are blocked upon the reset transition. This observation indicates that an extended potential barrier arises at the narrowest cross-section of the filament due to the voltage-induced redistribution of oxygen vacancies or tantalum cations. The number of conductance channels is preserved in the RS process, implying that the filament diameter does not change

in the process. The 5 channels/one atom estimate suggests a configuration of 3 – 8 Ta atoms at the bottleneck of the investigated RS junctions. These findings prove that the resistive switching process in Ta_2O_5 devices result in fundamentally different atomic-sized filaments than the atom-by-atom thinning of metallic nanowires, as indicated by their markedly different quantum transport properties.

5.4.4 Outlook: Subgap characteristics of on-chip devices

The above analysis demonstrates the merits of quantum transport measurements in the microscopic understanding of atomistic processes in filamentary resistive switching devices. This analysis can be extended to the study of atomistic processes in further RS media in the future, even in on-chip devices. These devices must be contacted with two superconducting electrodes for subgap analysis. This technique, however, is restricted for memristive devices with an ultra-small ($\lesssim 10$ nm) thickness of the active volume between the contacting superconducting electrodes, since the thickness of the intrinsically non-superconducting region should not exceed the superconducting coherence length of the electrodes to study the differences in the subgap spectra of various RS states.

The material stack of vertical cross-point samples I prepared for superconducting subgap studies is illustrated in Figure 5.13.a. Tantalum electrodes of 100 nm thickness were applied to contact a 3.5 nm thick Ta_2O_5 active region. Between the bottom electrode

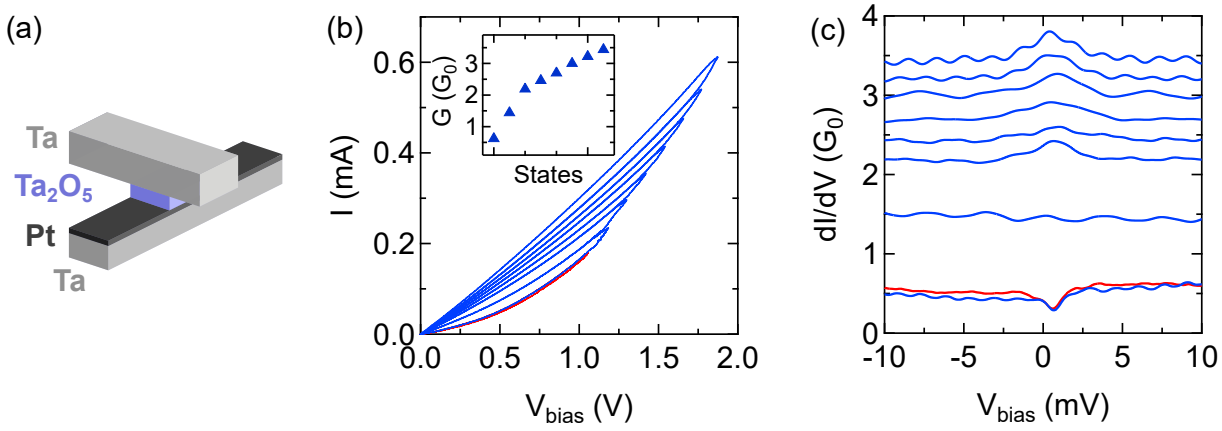

Figure 5.13: *Exploring states in on-chip Ta_2O_5 devices. (a) Illustration of a cross-point device. (b,c) Subgap measurements in multilevel states of a cross-point device, measured at $T = 1.3$ K ambient temperature. Blue curves in panel (b) show gradual set processes, performed by applying positive half-triangle driving voltage signals with increasing amplitude (the red curve is a non-switching curve, recorded at the initial state). Panel (c) shows the differential conductance curves computed from subgap $I(V)$ characteristics recorded in each state shown in (b). Inset in (b) shows the conductance of each state, evaluated from the normal conductance parts of the subgap characteristics.*

and the oxide layer, a 3.5 nm thick platinum layer was introduced (see more details on Ta#3 chip previously in Table 3.1), to ensure an asymmetry, vital for RS with a well-defined switching direction [100]. Even though stable RS characteristics were achieved, the conductance window where I was able to operate the device was very narrow, indicating that the material stack is far from ideal from the viewpoint of resistive switching.

Gradual, multilevel programming of an on-chip device is shown in Figure 5.13.b. The subgap $I(V)$ curves of these states exhibit more smearing and less nonlinear features than those of STM point-contact devices. The reason for this severely reduced energy resolution might arise from proximity superconductivity of the additional platinum layer. Despite this limited resolution, subgap features are still noticeable in the differential conductance curves, such as a dip at zero voltage in case of the smallest conductance state and the appearance of a peak at the same location for the highest conductance state. The crossover around 1 G_0 indicates a change in quantum transport properties. A tunneling $\rightarrow$ atomic filament transition would result in similar features if highly smeared subgap characteristics are considered with greatly reduced effective superconducting energy gap and fairly large Γ-broadening. With further optimization of the device structure, better resolution could be viable, enabling accurate determination of the quantum transport properties in on-chip devices.

Chapter 6

Auditory sensing with VO_2 oscillators

Oscillators made of Mott memristors are compact devices capable of emitting current spikes at a given rate. This spiking behavior can be utilized in spiking neural networks (SNNs), where neural activation can be realized through this property [89]. Another possibility is the application of memristive oscillators in oscillatory neural networks (ONNs), where multiple oscillators are coupled to each other, and computation is realized in the phase space, via synchronization of the oscillators [95]. Furthermore, these devices can also be utilized for edge computing applications [13], e.g. as a transducer for encoding information – originating from a sensor's signal or another memristor – in the frequency space.

The sensation of hearing is the result of a complex biological system in operation, capable of sensing and processing information carried by sound waves. There are a vast amount of biophysical/biochemical mechanisms at play in the human auditory sensing process. These complex mechanisms lead to a perception of loudness and pitch of sounds, enabling the detection of volume in a large dynamic range, up to 120 – 130 dB SPL (sound pressure level, relative to the reference sound pressure of the threshold for human hearing), and also sensing frequencies in a wide, 20 Hz – 20 kHz region. In addition, a healthy individual can recognize a frequency difference of only 1.7% (this sensitivity can be as high as 0.1% for a trained musician) [191, 192].

In this Chapter, the concept and realization of an auditory sensing circuit is presented, using a ScAlN piezoelectric MEMS cantilever and a VO_2 oscillator circuit, aimed at a possible application in a fully implantable cochlear implant. Within this project, I supervised the work of Roland Kövecs [19]. As an introduction, I am going to summarize some processes of human hearing in a nutshell based primarily on Ref. 191. Then, I show some properties of piezoelectric cantilevers used for transducing mechanical vibrations into electrical signals, analyze the properties of VO_2 oscillators in the context of the targeted

application, and present the circuit capable of encoding a biologically realistic stimulus in the frequency of the output spikes.

6.1 Auditory sensing in biology

Key organs of the human auditory sensing process are illustrated in Figure 6.1. Sensing begins at the outer ear, where sound waves enter the external auditory canal, which already performs a frequency selective amplification of propagating mechanical vibrations in the 200 Hz – 10 kHz frequency range, which include key frequencies of the human speech [191]. Then, vibrations are carried through the tympanic membrane to the ossicular bones, the malleus, the incus and the stapes, which are the smallest bones in the body, located in a cavity filled with air. The role of these ossicular bones is to realize impedance matching between the outer air medium and the inner fluids of the body, otherwise 99.9% of the incoming sound energy would be reflected. The stapes is attached to the oval window, transmitting vibrations into the cochlea, a fluid-filled spiral-shaped organ containing auditory sensory cells (hair cells) all along its full length. These cells realize a tonotopic encoding of frequency information of the incoming vibration, meaning that cells located at different locations of the organ are sensitive to different frequen-

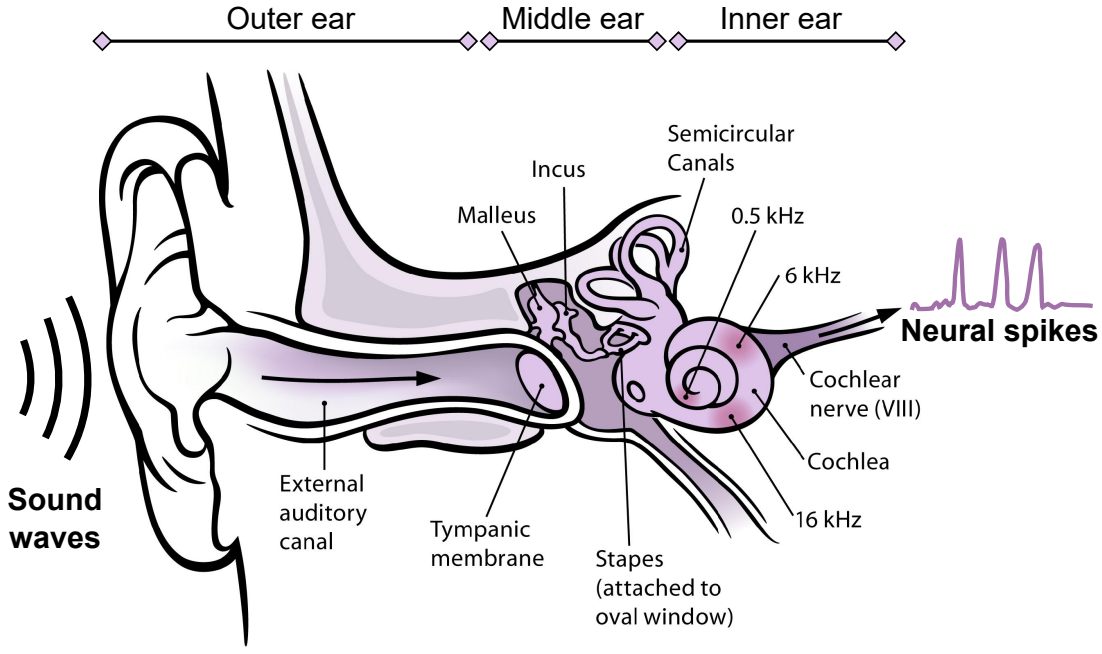

Figure 6.1: *Schematic illustration of the human ear, showing key organs of the auditory sensing process. Incoming sound waves are converted to neural spikes encoding the information carried by mechanical vibrations. These spikes travel through neural pathways to the auditory cortex where they are interpreted as the sensation of hearing. [191]*

cies. Hair cells can sense vibration amplitudes as small as 1 Å, and they generate neural spikes at the hair cell – auditory nerve (cochlear nerve) synapses, as a result of complex biomechanical and biochemical processes. These nerves realize tonic spiking with specific dynamics [193, 194], and the incoming vibration amplitude is encoded in the rate of spiking, via single cells operating according to a sigmoid-shaped amplitude–frequency function [191, 195]. Cochlear nerves transmit neural spikes to the central nervous system through auditory pathways, and decoding information carried by these spikes happens at the auditory cortex.

It is estimated, that 5% of the global population suffer from some kind of hearing loss [198]. Depending on the type of damage to the auditory system, there are hearing aids available for restoring hearing. These usually cannot replicate the sensation of hearing in a healthy body, but these hearing aids can help disabled people overcome difficulties in their everyday lives, e.g. by providing a device to understand speech. Cochlear implants (CIs) can be used to directly activate the auditory nerve, responding to the amplitudes and frequencies of incoming sounds. This process bypasses the need for functioning hair cells.

An illustration of a standard cochlear implant is shown in Figure 6.2.a. These devices usually consist of an external unit containing a microphone and sound processor, and an implanted electrode array carrying electrical signals into the cochlea, where they

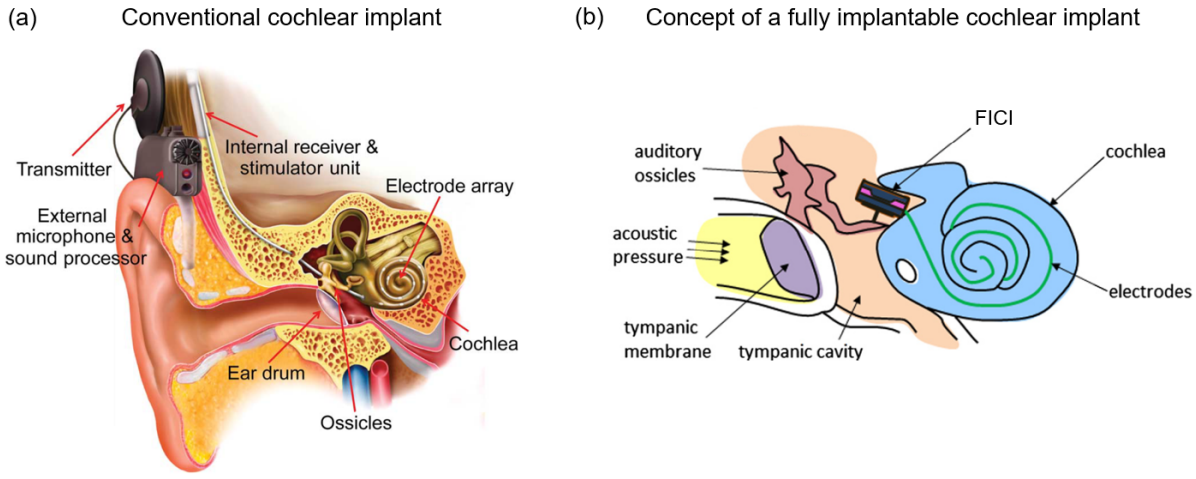

Figure 6.2: *Illustrations of (a) a conventional cochlear implant [196] and (b) a fully implantable cochlear implant [197]. Main components of a conventional CI (shown in (a)) are the external unit containing a microphone, a sound processor, and a transmitter for sending signals to the implanted electrodes via a magnetic inductive link. According to a common concept for a FICI (shown in (b)), the sensory, signal processor/generator parts are mounted to the ossicular bones, transducing their vibration to electric signals suitable for the stimulation of the nervous system.*

can provide sufficient electrical stimuli for the auditory nerve. The concept of a fully implantable cochlear implant (FICI) is shown in Figure 6.2.b. The main benefit of such a fully implantable device is to eliminate the external unit via mounting a small device to one of the ossicular bones capable of sensing and pre-processing vibrations of the bones, which fall into the ∼10 nm range [199]. There are different approaches for realizing a FICI [198], however there are no such device widely available for people, only a small number of clinical experiments were performed using prototypes by a few companies.

Our concept of an auditory sensing circuit is shown in Figure 6.3, which is capable of sensing sound waves with a MEMS cantilever made of a piezoelectric material [200], and also transduces mechnaical vibrations into a spiking output using a VO_2 oscillator circuit. The circuit could be directly used in FICIs, since both components can be produced in an integrated form fulfilling the requirement for small size.

The idea for artificial sensing is to mount the spiral-shaped cantilever directly on one of the ossicles, the incus bone. In this manner the piezoelectric material produces voltage signal due to incoming vibrations at the resonance frequency of the cantilever, which can be fine-tuned by adjusting the material and geometric parameters of the cantilever. In this manner, frequency decomposition of the incoming signal in a FICI device could be realized with an array of cantilevers, each tuned to different resonance frequencies.

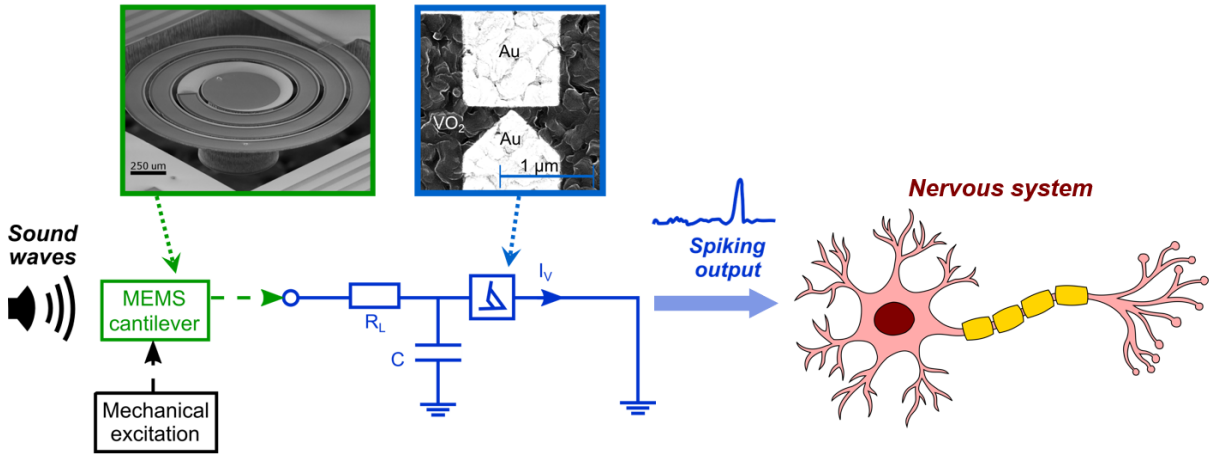

Figure 6.3: *Graphics showing the concept of the auditory sensing circuit, along with SEM images of representative spiral cantilever [200] (green frame) and VO_2 nanogap memristor [O3] (blue frame) devices. Correspondingly, green and blue parts denote the the sensory part and the signal processor/generator part realized by each devices. To demonstrate feasibility of the concept, cantilevers are excited with a biologically realistic, ∼10 nm mechanical excitation provided by a piezoelectric actuator (black box in the circuit schematics) in a custom measurement setup. The main task of the circuit, generation of a spiking output due to incoming sound waves to be carried to the nervous system, is also emphasized graphically.*

The other important component of the auditory sensing circuit is a signal processor/generator circuit capable of producing waveforms with a certain shape suitable for the nervous system. Using VO_2 memristor-based circuits for this purpose have several advantages. Apart from small size and energy-efficiency compared to speech processing units used in conventional CI devices [198], neuromorphic characteristics of these circuits can be useful for mimicking actual neurodynamic behavior of the nerves. After exploring some of these neuromorphic characteristics (as seen previously, in Section 3.3.5), the oscillator was chosen as a processor/spike generator component. Due to the simplicity of the circuit (using only one VO_2 device for oscillations), the energy needed for spike generation is provided at its input, by properly conditioning the output signal of the cantilever.

6.2 Properties of MEMS cantielvers

The MEMS cantilevers used for my experiments were developed at the Nanosensors Laboratory, with the help of Nguyen Quoc Khánh. The piezoelectric material used for the cantilevers was ScAlN, studied extensively by my colleagues [201]. The spiral-shaped design of the cantilevers was optimized to the targeted application previously (see Figure 6.4.a-b) [200]. I applied a slightly different approach (as in Ref. [200]) for characterizing the resonance frequencies of a new set of samples made from ScAlN. To emulate conditions inside the middle ear, the cantilevers were put under ∼1 nm amplitude mechanical excitation, provided by a *PicoScale Vibrometer* instrument, capable of recording the displacement of the cantilever. In this setup, illustrated in Figure 6.4.c, the displacement is measured via laser interferometric principle, and frequency spectra are recorded using lock-in technique. Upon characterizing 16 cantilever samples produced in different geometries, I found that they have resonances usually with $Q > 100$ quality factor (see an exemplary resonance peak in Figure 6.4.d), and the resonance frequencies of the 16 devices cover the desired frequency range of 200 – 700 Hz (see Figure 6.4.e), where fundamental frequencies of human speech are found.

6.3 Properties of VO_2 oscillators

To explore typical dynamics of oscillators, their operation was analyzed using *LTspice* circuit-level simulation software. For this purpose, a circuit-level memristor model was used, published in Ref. [202]. The inner parameters of the model were tuned such that set/reset switching voltages and ON/OFF-state resistances were included, which are characteristic of my nanogap devices based on measurements. My primary goal was to identify fundamental dependencies of the output spiking frequency on other parameters, mainly the value of the parallel capacitance and the input voltage level (see Figure 6.5.a-

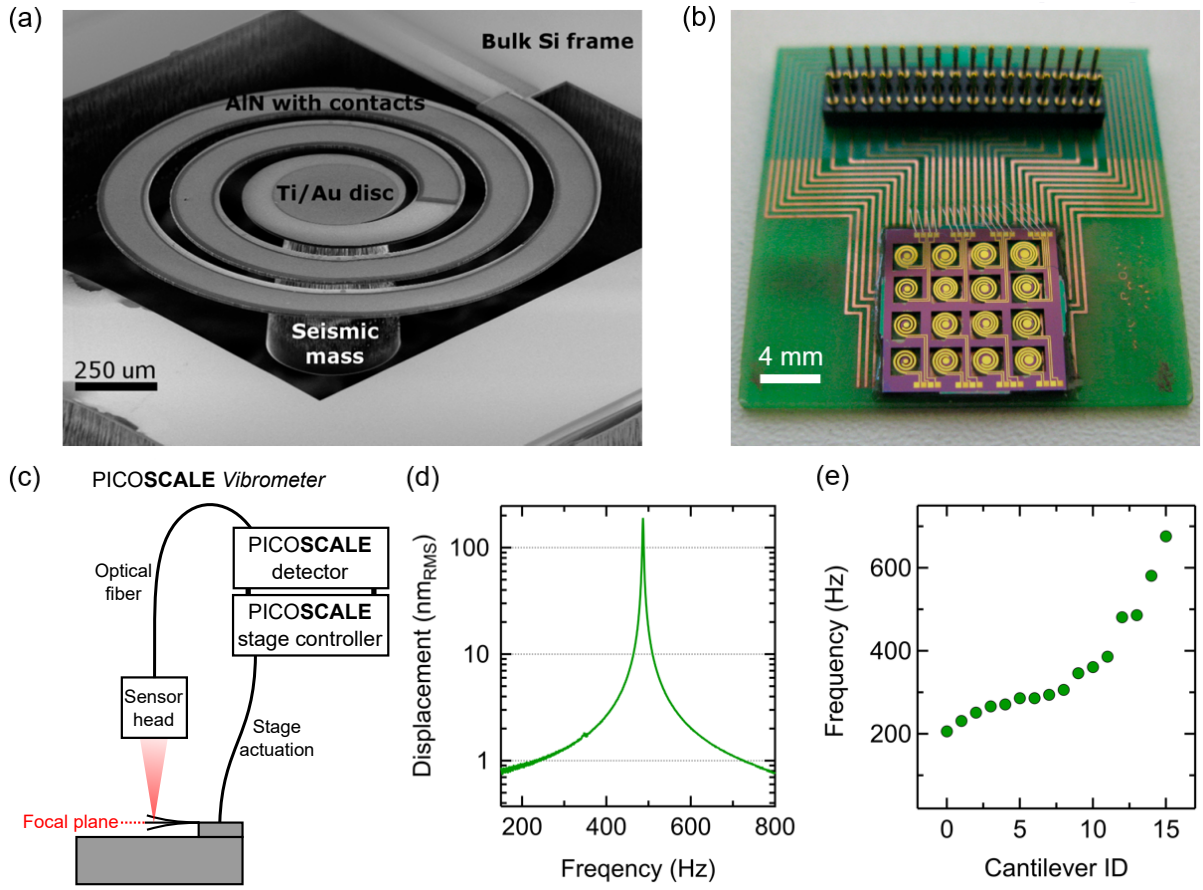

Figure 6.4: *Characterisation of piezoelectric cantilecers. (a) Tilt-view SEM image showing the typical geometry of a cantilever, and (b) 16 cantilevers on a chip, applied to a PCB. Panels (a) and (b) show AlN devices from an earlier study [200]; the ScAlN devices I used for this study were produced in the same spiral-shaped geometry with a seismic mass at the center to set the desired resonance frequency. (c) Illustration of the interferometric measurement setup used for the characterisation of cantilevers. (d) Displacement spectrum of a representative cantilver with $Q \approx 200$ quality factor and $f_r = 486$ Hz resonance frequency. (e) Resonance frequencies of the studied 16 cantilevers covering the 200 – 700 Hz frequency domain.*

b). Scheme of the oscillator circuit is shown in the inset of Figure 6.5.c. The general role of circuit parameters can be summarized as follows:

- The serial resistance R has to be chosen such that it ensures stable oscillation at a desired input voltage range. The resistance and the memristor form a voltage divider circuit together, which result in different equilibrium voltages. The equilibrium voltage drops on the memristor ($V_{\mathrm{OFF}}^{\mathrm{eq.}}$ and $V_{\mathrm{ON}}^{\mathrm{eq.}}$) have to fulfill the following criteria: in the OFF state $V_{\mathrm{set}} < V_{\mathrm{OFF}}^{\mathrm{eq.}}$ and in the ON state $V_{\mathrm{reset}} > V_{\mathrm{ON}}^{\mathrm{eq.}}$. Generally, these

conditions can be fulfilled by choosing R such that $R \gg R_{\mathrm{ON}}$ and $R \lesssim R_{\mathrm{OFF}}$ (not an exact rule, as equilibrium voltages depend on the input voltage as well).

- The parallel capacitance C can be used to tune the overall operation of the circuit to an arbitrary timescale (on a purely circuit-level approach neglecting possible effects of inner dynamics of VO_2 devices). Tuning is carried out using the oscillation frequency–capacitance trend, which is linear with a slope of -1 on the log-log scale according to simulations (see Figure 6.5.a).

- The input voltage level also has an effect on the output oscillation frequency according to my simulations, as seen in Figure 6.5.b. This dependency was later studied

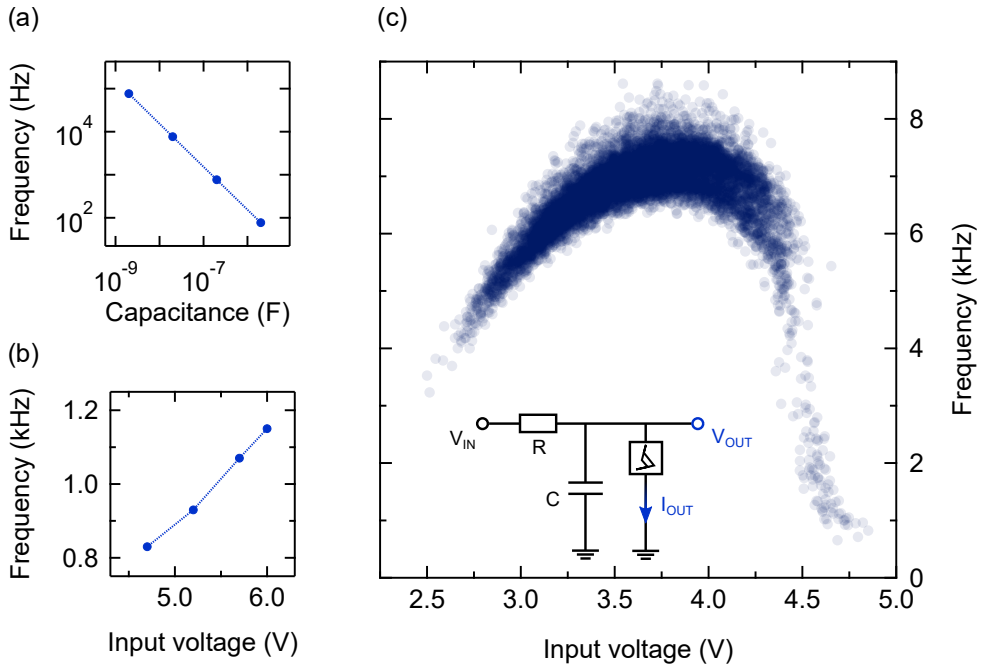

Figure 6.5: *Dependencies of the oscillation frequency on different circuit parameters such as the input voltage level and the value of the parallel capacitence in a VO_2 oscillator circuit explored via (a-b) LTspice circuit-level simulations and (c) experimentally. Simulations were carried out with a realistic memristor model (some typical parameters of $R_{\mathrm{OFF}} = 50$ $k\Omega$, $R_{\mathrm{ON}} = 200$ Ω, $V_{\mathrm{set}} = 2.45$ V, $V_{\mathrm{reset}} = 0.45$ V) modified from the model reported in Ref. 202. Inset of panel (c) shows the circuit schematic used for both simulations and experiments. During parameter sweeps in simulations, other parameters of the circuit were kept constant: for panel (a) $V_{\mathrm{IN}} = 6$ V and $R = 15$ $k\Omega$, for panel (b) $C = 200$ nF and $R = 10$ $k\Omega$. The measured oscillation frequency–input voltage dependence shown in panel (c) was recorded while input voltage was varied in a circuit with $C = 235$ nF and $R = 6.67$ $k\Omega$. This is plotted as a function of the input voltage amplitude evaluated as an average over the timespan between neighboring spikes.*

experimentally, on a circuit brought to an oscillating state, while input voltage was varied. As expected, the frequency of oscillation changed, and the frequency of neighboring spikes (defined as the reciprocal of their time delay) versus the input voltage amplitude is plotted in Figure 6.5.c. This measurement showed that oscillation frequency saturates as expected, and oscillation stops abruptly when the input level is increased further. This observation agrees with our expectations based on an example from Ref. 13 involving NbO_2 oscillators (see Section 2.2.4 previously).

Overall, by properly setting R and C values, the frequency range of possible oscillations can be set to the desired ~1 kHz domain, where typical spiking rates of the auditory nerve are found, based on animal experiments [193, 194]. Furthermore, the experimentally observed input voltage dependency enables the possibility of encoding the amplitude of the incoming signal in the frequency of output spikes. This type of information encoding resembles the natural encoding of sound amplitude in the nervous system, with similar frequency–amplitude characteristic as the sigmoid-shaped functions observable at the cellular level [191, 195]. Moreover, there are also cochlear implants aiming at this type of encoding [197] (as opposed to amplitude-encoding). Whereas the ear has some protective mechanisms against loud sounds (such as muscles which can vary the stiffness

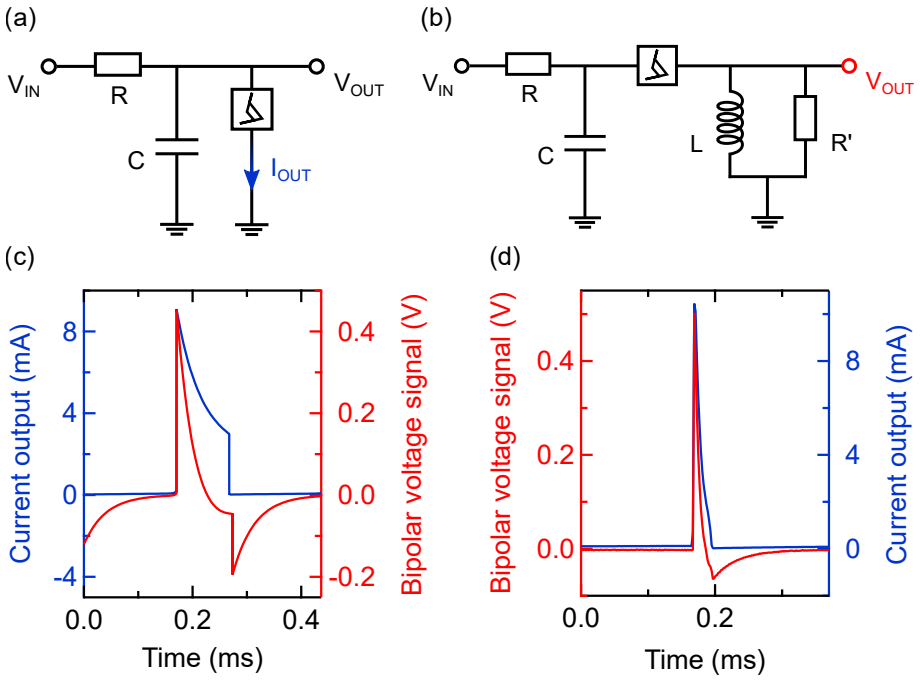

Figure 6.6: *Simulatons and experiments for testing the feasibility of bipolar output signals with an oscillator circuit. Circuit schematics of (a) the original and (b) the modified version of the oscillator. Realizing both circuits with the same memristor and R,C components yield a comparision of output signal characteristics (c) in simulations and (d) in experiments.*

of the ossicular chain), the observed afferent property of the VO_2 oscillator (saturation and abrupt drop of frequency due to increased input voltage level) could also be beneficial in a real setting.

There is one additional, highly important requirement that all CI devices should satisfy. The spiking waveform carried into the nervous system must be bipolar, to exclude the possibility of charge accumulation near the end of the implanted electrodes. Current spikes at the output of an oscillator are unipolar, so additional circuit elements are needed to convert the output into a bipolar signal. The conversion can be realized by adding a parallel LR circuit to the output, as seen in Figure 6.6. In this manner, the appearance of a bipolar voltage signal was confirmed by my simulations and experiments as well (see Fig. 6.6.b-c, respectively). Measurements showed a slight difference in the shape of the waveform as compared to simulations: the negative overshoot of the signal is not as sharp as in a simulation, which can be attributed to the more continuous reset process of real memristors also apparent in real $I(V)$ characteristics. Still, the cumulative effects of the bipolar red signal in Figure 6.6.d are significantly better than the initial, unipolar blue signal.

6.4 Circuit for auditory sensing

One important component of testing the presented concept for auditory sensing is providing biologically realistic, ∼10 nm excitation (in the range of the movement of bones in the middle ear). For this purpose, a custom-built sample holder was designed and assembled by Ferenc Braun, Roland Kövecs and myself, as seen in Figure 6.7. Mechanical excitation is provided by a *PI Ceramic P-142.03* piezoelectric actuator which has a sensitivity of 6 nm/V, and an axial resonant frequency of 120 kHz (far from the 200–700 Hz range under investigation). Nominal mechanical excitation amplitudes (called *stimulus* from now on) are calculated from the drive voltage amplitude of the piezoelectric actuator from the value of its sensitivity. Electric signals of each individual cantilever are lead through ribbon cables to custom PCBs at the two sides where routing of each electrode is possible using two jumpers, leading the signal of a chosen cantilever to a pair of BNC connectors at the sides.

For the connection of the two parts – sensory part with the cantilever and spiking part with the oscillator – proper conditioning of the cantilever's output signal is needed. Provided a sinusoidal mechanical excitation with biologically realistic amplitude in the ∼10 nm range, the electric output of the cantilever is also a sine wave with typical amplitudes of 30–150 μV. These values depend on the mechanical excitation and are estimated from measuring signal amplitudes with an oscilloscope and/or lock-in technique after amplifying the signal with a *Stanford Research SR560* differential amplifier. Black lines in

Figure 6.8.a show the electrical spectrum of a cantilever around its 486 Hz resonance peak (known from laser interferometry measurements), recorded with a *Nanonis OC4 oscillation controller* instrument using lock-in technique. Generally, the frequency of the cantilevers' electric resonances correspond to mechanical resonance frequencies determined by laser interferometry (green line in Figure 6.8.a), within 0.5 Hz.

Since VO_2 oscillators require a DC input in the 1–10 V range, the cantilever's signal needs to be amplified, rectified, and smoothed. These stages were realized by a differential amplifier (the same *SR*560 model used for measuring electric spectra), a diode, and a $C_r = 2$ μF rectifying capacitor, as seen in the circuit diagram in Figure 6.8.b. Filtering of the signal is also important; for this purpose, the *SR*560 amplifier's built-in high-pass filter was used in the 12 dB/oct roll-off setting, and a custom-built low pass filter with 3.3 kHz cutoff frequency was applied directly at the amplifier's output.

The results of an experiment are shown in Figure 6.8.c, where a cantilever is excited at its 486 Hz resonance frequency with 30 nm amplitude stimulus (see black sine wave). After the amplification and filtering stages the green sinusoidal waveform (V_{MEMS}) is measured which is then rectified and smoothed, resulting in a DC signal with ≈6 V amplitude (see

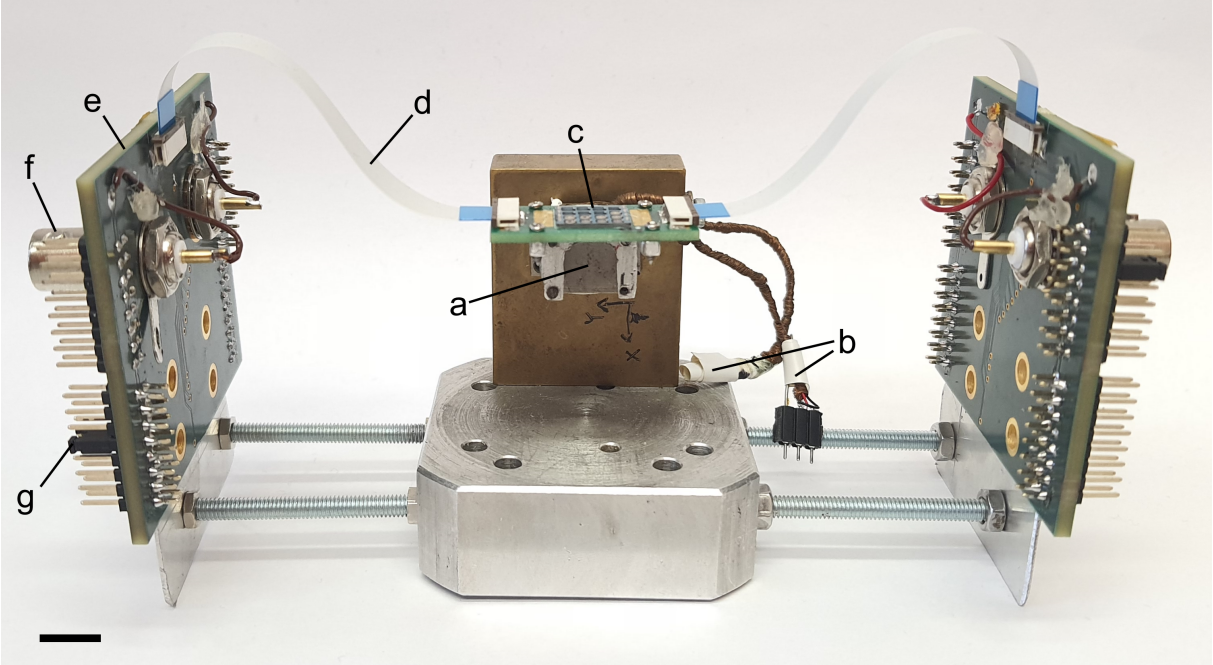

Figure 6.7: *Photo of the custom-built sample holder for auditory sensing experiments. (a) Piezoelectric actuator, (b) shielded electrical connections to the piezoelectric actuator, (c) custom PCB holding the chip with cantilevers, (d) ribbon cables for the measuring the signal of cantilevers, (e) custom PCB for routing the connections to the cantilevers, (f) BNC connector, (g) jumper used for selecting the desired electrode of a cantilever. Scalebar: 1 cm.*

the blue V_{MEMS} signal). This signal is then used as the input of the oscillator circuit, and a spiking current signal appears at the output (see $I_{\mathrm{osc.}}$ with blue).

Another experiment was carried out in a similar setting, where stimulus amplitude was varied [19]. As expected from the oscillator's known dynamics, increased input resulted in faster oscillations, as shown in Figure 6.8.d. This trait is very similar to natural encoding of sound amplitude within the nervous system, observed even at the cellular level [191, 195]. Additionally, there are also cochlear implants designed to specifically employ this encoding approach [197].

These proof-of-concept experiments demonstrate that (i) our auditory sensing unit is capable of emitting a spiking output due to biologically realistic excitation amplitudes, (ii) the spike rate can be tuned to the domain required by the nervous system, (iii)

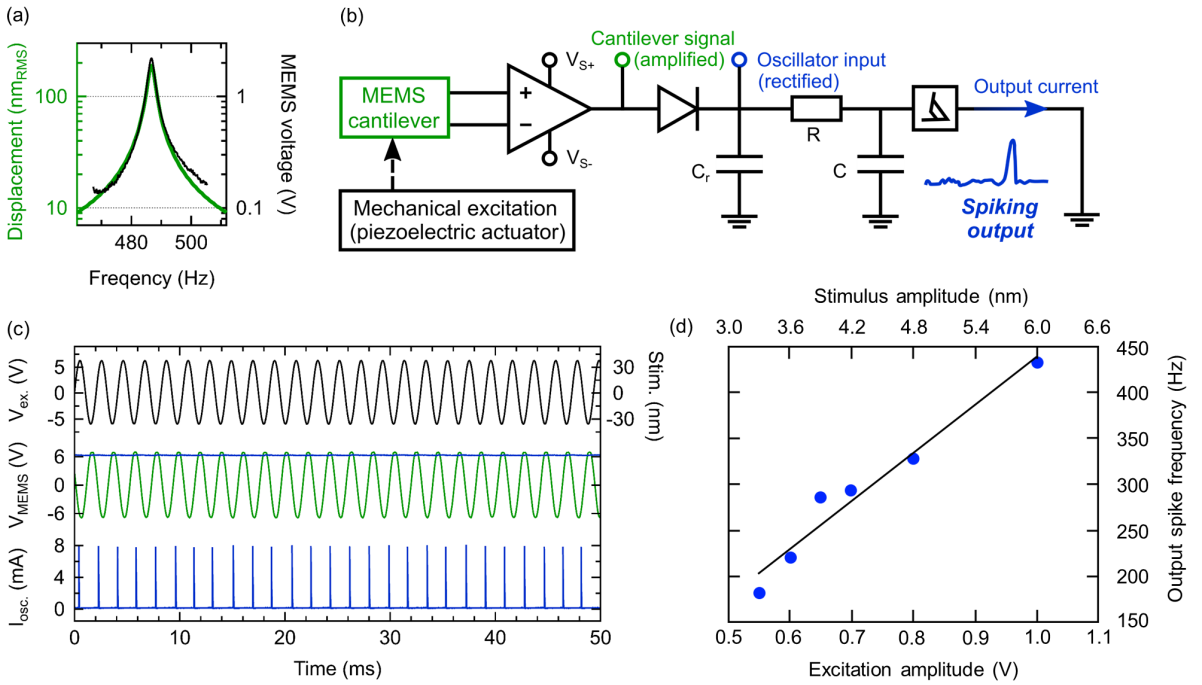

Figure 6.8: *Realization of the auditory sensing circuit. (a) Correspondence of electrical (black) and displacement (green) spectra of a cantilever. (b) Circuit schematics for the connection of a cantilever and a VO_2 oscillator. (c) Results of an auditory sensing experiment, showing the input signal with black, both in units of voltage applied to the piezo actuator (left axis) and mechanical stimulus (right axis). Green signal in the middle panel shows the amplified output signal of the cantilever, and the blue line of the same panel is measured after rectifying/smoothing, also showing the oscillator input. The oscillator output current is displayed in the bottom panel. (d) The excitation amplitude can be encoded in the output spike frequency of the oscillator, as shown by a previous measurement in a similar setting.*

unipolar current spikes can easily be transformed to a bipolar waveform as a prerequisite of application in cochlear implants, and (iv) the stimulus amplitude can be encoded in the frequency of spikes. These results already indicate that it is worth pursuing the demonstration of the circuit in whole, employing bipolar output spikes and showing capabilities for frequency – amplitude encoding. Another goal is to realize the coupling with a custom-built amplifier circuit designed specifically for this task, enabling calculations for energy consumption which are essential to explore the feasibility of the overall concept in a realistic setting.

Summary

Conclusions of my Ph.D. studies are summarized in the following thesis points:

1. I have developed and produced on-chip memristors from a variety of materials, using electron beam lithography and thin layer deposition methods. I developed Nb_2O_5 [O1] and Ta_2O_5 [O2] vertical crosspoint OxRAM devices. I worked out a method for the pulsed electroforming of these devices in a controlled manner. I also performed their $I(V)$ characterization, which revealed stable non-volatile characteristics. I performed room temperature and low temperature ($T = 1.3$ K) studies of my Ta_2O_5 crosspoint devices and compared their operation with Ta_2O_5 STM point-contact devices, revealing similar resistive switching characteristics at both conditions [O2]. I also contributed to the development of VO_2 nanogap devices which yield volatile resistive switching characteristics. I produced and characterized devices with different gap sizes, and I observed a general tendency of decreased set voltage values for devices with smaller gaps [O3]. I demonstrated tunable neurodynamic behavior of circuits built from these VO_2 nanogap devices and I also optimized a VO_2 oscillator circuit to provide a spike generator unit for application in an autonomous neural detector circuit [O4]. These device developments provided versatile on-chip resistive switching building blocks for our research group [O1–O4].

2. Upon studying the set process of graphene/SiO_x/graphene nanogap phase change memristors, I observed that the statistical distribution of the set timescale shows variations as a function of measurement cycles. I found, that within shorter segments of $n_{\mathrm{corr}} \approx 200$ switching cycles (the typical correlation parameter of the data) the set time histograms are well fitted with an exponential probability density function, indicating a nucleation process with constant nucleation barrier. For longer segments, however, the set time histograms follow a lognormal density function with higher standard deviation than the universal logarithmic standard deviation of the exponential density function ($\sigma_{\log(\tau)}^{\mathrm{exponential}} = 0.56$). A similar study of Pt/SiO_x/Pt devices further confirmed that the effect originates from nucleation in the SiO_x active region and excluding a crystal growth driven set process, which would yield fundamentally different set time statistics. I have also observed correlation of τ_{set}

and R_{OFF} quantities, attributed to cycle-to-cycle variations in the nanostructure of the OFF state. Utilizing this effect, I showed that both quantities are tunable within the correlation cycle number ($n_{\mathrm{corr}} \approx 200$) by properly adjusting the reset voltage pulse amplitude. [O5]

3. I performed low temperature ($T = 1.4$ K) experiments on Nb (sample)/Nb_2O_5/Nb (tip) STM point-contact devices demonstrating the operation of the resistive switching phenomenon at cryogenic temperatures. I applied superconducting subgap spectroscopy measurements to evaluate the τ_i transmission eigenvalues of the conducting nanofilaments in the active volume. For these measurements, I built a dedicated filtering circuitry to ensure the proper energy resolution of subgap spectra, and analyzed the τ_i transmission eigenvalues by a fitting procedure relying on the theory of multiple Andreev reflections. My studies give a direct experimental evidence that the Nb_2O_5 junctions operated near the quantum conductance unit exhibit a resistive switching phenomenon via the rearrangement of atoms in a truly single-atom diameter filament with a single highly transmitting conductance channel in the ON state. This finding clearly excludes alternative junction arrangements which would provide the same conductance in significantly wider filaments embedding a tunneling barrier [O6].

4. I investigated the quantum transmission properties of nanoscale Ta_2O_5 resistive switching filaments in STM point-contact devices. My studies concentrated on the $\approx 3 - 10\,\mathrm{G_0}$ conductance range, where the superconducting subgap $I(V)$ characteristics provide essential information on the transmission density function of the numerous open conduction channels via fitting with reasonable model transmission densities. This analysis revealed the formation of truly atomic-sized filaments composed of 3–8 Ta atoms at their narrowest cross-section, demonstrating that this diameter remains unchanged upon resistive switching. Instead, the switching is governed by the redistribution of oxygen vacancies or tantalum cations within the filamentary volume, and the reset process results in the formation of an extended barrier at the bottleneck of the filament, which reduces the transmission of the highly open conduction channels. These findings demonstrate a clear difference from the quantum transport properties of mechanically thinned pure Ta atomic wires, where the conductance decrease is related to decreasing junction diameter at preserved average transmission [O2].

5. I investigated application possibilities of the VO_2 oscillator circuit in an auditory sensing unit. I coupled the oscillator to a piezoelectric MEMS cantilever responsible for frequency selective sensing of mechanical vibrations. I performed measurements replicating some important aspects of real biological conditions, targeting the im-

plementation of the auditory sensing circuit in cochlear implants. My experiments demonstrate that the auditory sensing unit is capable of emitting a spiking current output due to biologically realistic, $\sim$ 10 nm excitation amplitudes (stimulus). I also demonstrated that the stimulus amplitude can be encoded in the frequency of spikes, and spike rates can be tuned to the domain required by the nervous system via proper selection of passive circuit elements of the VO_2 oscillator component. By adding further passive elements to the oscillator, I showed that unipolar current output spikes can be converted into a biologically motivated bipolar voltage waveform. My experiments demonstrate that the auditory sensing unit fulfills several important prerequisites to application in cochlear implants.

Acknowledgments

I would like to express my gratitude to my supervisor András Halbritter for his endless support in every aspect of my PhD studies, ranging from the smallest details of measurement setups to comprehensive scientific discussions. I am grateful for his guidance and I am fortunate to have had the opportunity to learn from him since the beginning of my MSc studies. I also highly appreciate the help of János Volk who took the role of industrial advisor and broadened the perspective of my studies, providing me an opportunity to learn nanofabrication techniques and seeking real-life applications of my findings.

I am thankful to László Pósa from whom I learned every important technological steps including the tiniest, yet vital details of device fabrication methods. I also thank László for sharing his ideas in thought-provoking discussions, and inspiring me to investigate neurodynamic VO_2 circuits. I am grateful to Péter Makk who provided valuable insights for my superconducting spectroscopy studies, and also provided data for pure tantalum and niobium junctions. I am thankful to Zoltán Balogh for teaching me the basics of MCBJ sample fabrication, for providing insights on $1/f$ noise spectroscopy, and also for supplying liquid helium whenever I needed it. I am grateful to Miklós Csontos for inviting me to study memristors during my BSc studies back in 2015, for his invaluable help with quantum transport studies, for providing Ta_2O_5 devices to our neural detector circuit, and also for the idea and opportunity to perform RF measurements on VO_2 memristors.

I am grateful to Gergely Zaránd for his insights on the theoretical background of my quantum transport studies, which also lead me to the work of Yu. V. Nazarov.

I am glad that I had the possibility to participate in supervising the work of some very talented and ambitious students during their BSc studies, Gergő Fehérvári, Roland Kövecs and Zsigmond Pollner. I am grateful to Gergő for his work on studying the set time statistics of SiO_x devices, to Roland for his work on the neural detector and the auditory sensing circuits, and to Zsigmond for his work on VO_2 oscillators. I am also thankful for their patience with me, at my first attempts of trying to be a good supervisor.

I am grateful to my colleagues Dániel Molnár, Sebastian Werner Schmid and Botond Sánta. I thank Dániel for his work on the realization of the neural detector circuit, Sebastian for his thorough work on noise spectroscopy measurements of VO_2 devices with different electrode materials, and Botond for his extensive noise spectroscopy measurements

on Nb_2O_5 devices. I am also grateful to György Lázár for his measurements investigating the precursor effect in the noise of Ta_2O_5 devices.

I am thankful to my colleagues at the Institute of Technical Physics and Materials Science, György Molnár, Nguyen Quoc Khánh, Zsófia Baji, Ferenc Braun, János Bozorádi, Attila Nagy, Levente Illés, Péter Neumann and Áron Vándorffy. All of them provided professional background vital for my studies. I am also thankful to Gábor Mészáros in this regard, for his design of the multiple output current to voltage converter.

I am grateful to former colleagues András Magyarkuti and Ágnes Gubicza for helping me in the laboratory when I started working at the Department. I also thank Anna Nyáry and Gréta Mezei their support.

I am thankful to colleagues at ETH Zurich, Nadia Jimenez Olalla and Jeurg Leuthold, for the Ta_2O_5 devices to the neural detector circuit. I am also thankful to Roland Hauert, Dávid Krisztián, Péter Hornung, Csaba Sinkó, Sadaf Arjmandabasi, Goran Dražić and Péter Balázs for their work related to our publications.

I am thankful to Gábor Takács for supporting my project within the Cooperative Doctoral Programme*, as head of the Doctoral School. I am also grateful to Ferenc Simon for his support in this matter.

I would like to thank all colleagues at the University and at the Institute as well, who helped me throughout the years, including the administrative and technical staffs.

I am grateful to my family, my parents Mária and Sándor, and my brothers Zoltán and Sándor who always aided me in every situation and kept me going. I am also grateful to my eternal partner in life, Tamás, who never gives up and always finds a way. Upon writing the last Chapter, I often remembered childhood memories of my dear grandfather, Sándor. Having a complete loss of hearing, he showed me an entirely different perspective on life. For these memories, I am grateful.

Funding

* Project 963575 has been implemented with the support provided by the Ministry of Culture and Innovation of Hungary from the National Research, Development and Innovation Fund, financed under the KDP-2020 funding scheme.

List of publications

[O1] B. Sánta, Z. Balogh, L. Pósa, D. Krisztián, T. N. Török, D. Molnár, C. Sinkó, R. Hauert, M. Csontos, and A. Halbritter. *Noise Tailoring in Memristive Filaments*. ACS Applied Materials & Interfaces, **13**, 7453 (2021).

[O2] T. N. Török, P. Makk, Z. Balogh, M. Csontos, and A. Halbritter. *Quantum Transport Properties of Nanosized Ta_2O_5 Resistive Switches: Variable Transmission Atomic Synapses for Neuromorphic Electronics*. ACS Applied Nano Materials, **6**, 21340–21349 (2023).

[O3] L. Pósa, P. Hornung, T. N. Török, S. W. Schmid, S. Arjmandabasi, G. Molnár, Z. Baji, G. Dražić, A. Halbritter, and J. Volk. *Interplay of Thermal and Electronic Effects in the Mott Transition of Nanosized VO_2 Phase Change Memory Devices*. ACS Applied Nano Materials, **6**, 9137 (2023).

[O4] D. Molnár, T. N. Török, R. Kövecs, L. Pósa, P. Balázs, G. Molnár, N. J. Olalla, J. Leuthold, J. Volk, M. Csontos, and A. Halbritter. *Autonomous neural information processing by a dynamical memristor circuit* (2023). Available at: `https://arxiv.org/abs/2307.13320`.

[O5] T. N. Török*, J. G. Fehérvári*, G. Mészáros, L. Pósa, and A. Halbritter. *Tunable, Nucleation-Driven Stochasticity in Nanoscale Silicon Oxide Resistive Switching Memory Devices*. ACS Applied Nano Materials, **5**, 6691 (2022).

[O6] T. N. Török, M. Csontos, P. Makk, and A. Halbritter. *Breaking the Quantum PIN Code of Atomic Synapses*. Nano Letters, **20**, 1192 (2020).

* Equal contributions.

References

[1] IEEE. *International Roadmap for Devices and Systems*. https://irds.ieee.org/editions/2020/beyond-cmos (2020).

[2] IEEE. *International Roadmap for Devices and Systems*. https://irds.ieee.org/editions/2021/beyond-cmos (2021).

[3] IEEE. *International Roadmap for Devices and Systems*. https://irds.ieee.org/editions/2022/irds%E2%84%A2-2022-beyond-cmos-and-emerging-research-materials (2022).

[4] J. J. Yang, D. B. Strukov, and D. R. Stewart. *Memristive devices for computing*. Nat. Nanotechnol., **8**, 13 (2013).

[5] M. A. Zidan, J. P. Strachan, and W. D. Lu. *The future of electronics based on memristive systems*. Nat. Electron., **1**, 22 (2018).

[6] Q. Xia and J. J. Yang. *Memristive crossbar arrays for brain-inspired computing*. Nature Materials, **18**, 309 (2019).

[7] S. Ambrogio, P. Narayanan, H. Tsai, R. Shelby, I. Boybat, C. Nolfo, S. Sidler, M. Giordano, M. Bodini, N. Farinha, B. Killeen, C. Cheng, Y. Jaoudi, and G. Burr. *Equivalent-accuracy accelerated neural-network training using analogue memory*. Nature, **558**, 60 (2018).

[8] C. Li, L. Han, H. Jiang, M. H. Jang, P. Lin, Q. Wu, M. Barnell, J. J. Yang, H. Xin, and Q. Xia. *Three-dimensional crossbar arrays of self-rectifying Si/SiO_2/Si memristors*. Nature Communications, **8**, 15666 (2017).

[9] W. Yi, K. Tsang, S. Lam, X. Bai, J. Crowell, and E. Flores. *Biological plausibility and stochasticity in scalable VO_2 active memristor neurons*. Nature Communications, **9**, 4661 (2018).

[10] P. Schofield, A. Bradicich, R. Gurrola, Y. Zhang, T. Brown, M. Pharr, P. Shamberger, and S. Banerjee. *Harnessing the Metal—Insulator Transition of VO_2 in Neuromorphic Computing*. Advanced Materials, 2205294 (2022).

[11] S. Kumar, X. Wang, J. P. Strachan, Y. Yang, and W. D. Lu. *Dynamical memristors for higher-complexity neuromorphic computing*. Nature Reviews Materials, **7**, 575 (2022).

[12] Z. Wang, H. Wu, G. W. Burr, C. S. Hwang, K. L. Wang, Q. Xia, and J. J. Yang. *Resistive switching materials for information processing*. Nature Reviews Materials, **5**, 173 (2020).

[13] X. Zhang, Y. Zhuo, Q. Luo, Z. Wu, R. Midya, Z. Wang, W. Song, R. Wang, N. K. Upadhyay, Y. Fang, F. Kiani, M. Rao, Y. Yang, Q. Xia, Q. Liu, M. Liu, and J. J. Yang. *An artificial spiking afferent nerve based on Mott memristors for neurorobotics*. Nature Communications, **11**, 51 (2020).

[14] R. Yuan, Q. Duan, P. J. Tiw, G. Li, Z. Xiao, Z. Jing, K. Yang, C. Liu, C. Ge, R. Huang, and Y. Yang. *A calibratable sensory neuron based on epitaxial VO2 for spike-based neuromorphic multisensory system*. Nature Communications, **13**, 3973 (2022).

[15] J. G. Fehérvári. *Nanoméretű fázisváltó memóriák időskáláinak kísérleti vizsgálata [Experimental study of time scales in nanoscale phase change memories]* (2020). TDK thesis.

[16] J. H. Shin, Y. J. Jeong, M. A. Zidan, Q. Wang, and W. D. Lu. *Hardware Acceleration of Simulated Annealing of Spin Glass by RRAM Crossbar Array*. In *2018 IEEE International Electron Devices Meeting (IEDM)*, 3.3.1–3.3.4 (2018).

[17] A. Sebastian, M. Gallo, R. Khaddam-Aljameh, and E. Eleftheriou. *Memory devices and applications for in-memory computing*. Nature Nanotechnology, **15**, 529–544 (2020).

[18] R. Kövecs. *Neurális dinamikával rendelkező memrisztor alapú detektoráramkör megvalósítása [Realization of a memristor based detector circuit with neurodynamical behavior]* (2022). TDK thesis.

[19] R. Kövecs. *Memrisztor-alapú jelfeldolgozó egység tervezése cochleáris implantátumokhoz [Designing a memristor-based signal processing unit for cochlear implants]* (2023). BSc thesis.

[20] L. Hoddeson and P. Garrett. *The discovery of Ovshinsky switching and phase-change memory*. Physics Today, **71**, 44 (2018).

[21] S. R. Ovshinsky. *Reversible Electrical Switching Phenomena in Disordered Structures*. Phys. Rev. Lett., **21**, 1450 (1968).

[22] M. Le Gallo and A. Sebastian. *An overview of phase-change memory device physics*. Journal of Physics D: Applied Physics, **53**, 213002 (2020).

[23] W. R. Hiatt and T. W. Hickmott. *Bistable switching in niobium oxide diodes*. Applied Physics Letters, **6**, 106 (1965).

[24] F. Argall. *Switching phenomena in titanium oxide thin films*. Solid-State Electronics, **11**, 535 (1968).

[25] J. Gibbons and W. Beadle. *Switching properties of thin NiO films*. Solid-State Electronics, **7**, 785 (1964).

[26] D. B. Strukov, G. S. Snider, D. R. Stewart, and R. S. Williams. *The missing memristor found*. Nature, **453**, 80 (2008).

[27] L. Chua. *Memristor-The missing circuit element*. IEEE Transactions on Circuit Theory, **18**, 507 (1971).

[28] W. Zhang, R. Mazzarello, M. Wuttig, and E. Ma. *Designing crystallization in phase-change materials for universal memory and neuro-inspired computing*. Nature Reviews Materials, **4**, 150 (2019).

[29] I. Boybat, M. Le Gallo, S. R. Nandakumar, T. Moraitis, T. Parnell, T. Tuma, B. Rajendran, Y. Leblebici, A. Sebastian, and E. Eleftheriou. *Neuromorphic computing with multi-memristive synapses*. Nature Communications, **9**, 2514 (2018).

[30] M. Salinga, E. Carria, A. Kaldenbach, M. Bornhöfft, J. Benke, J. Mayer, and M. Wuttig. *Measurement of crystal growth velocity in a melt-quenched phase-change material*. Nature Communications, **4**, 2371 (2013).

[31] J. Yao, L. Zhong, D. Natelson, and J. Tour. *In Situ Imaging of the Conducting Filament in a Silicon Oxide Resistive Switch*. Scientific reports, **2**, 242 (2012).

[32] L. Pósa. *Resistive switching in ultrasmall nanogap devices*. Ph.D. thesis, Budapest University of Technology and Economics (2019).

[33] J. Yao, Z. Sun, L. Zhong, D. Natelson, and J. Tour. *Resistive Switches and Memories from Silicon Oxide*. Nano Letters, **10**, 4105 (2010).

[34] C. He, J. Li, X. Wu, P. Chen, J. Zhao, K. Yin, M. Cheng, W. Yang, G. Xie, D. Wang, D. Liu, R. Yang, D. Shi, Z. Li, L. Sun, and G. Zhang. *Tunable Electroluminescence in Planar Graphene/SiO_2 Memristors*. Advanced Materials, **25**, 5593 (2013).

[35] F. Rao, K. Ding, Y. Zhou, Y. Zheng, M. Xia, S. Lv, Z. Song, S. Feng, I. Ronneberger, R. Mazzarello, W. Zhang, and E. Ma. *Reducing the stochasticity of crystal nucleation to enable subnanosecond memory writing*. Science, **358**, 1423 (2017).

[36] L. Posa, M. Abbassi, P. Makk, B. Santa, C. Nef, M. Csontos, M. Calame, and A. Halbritter. *Multiple physical timescales and dead time rule in few-nm sized graphene-SiO_x-graphene memristors*. Nano Letters, **17**, 6783 (2017).

[37] M. Kim, M. A. Rehman, D. Lee, Y. Wang, D.-H. Lim, M. F. Khan, H. Choi, Q. Y. Shao, J. Suh, H.-S. Lee, and H.-H. Park. *Filamentary and Interface-Type Memristors Based on Tantalum Oxide for Energy-Efficient Neuromorphic Hardware*. ACS Applied Materials & Interfaces, **14**, 44561 (2022).

[38] X. Lian, M. Wang, P. Yan, J. Yang, and F. Miao. *Reset switching statistics of TaOx-based Memristor*. Journal of Electroceramics, **39**, 132 (2017).

[39] C.-H. Yang, J. Seidel, S. Y. Kim, P. B. Rossen, P. Yu, M. Gajek, Y. H. Chu, L. W. Martin, M. B. Holcomb, Q. He, P. Maksymovych, N. Balke, S. V. Kalinin, A. P. Baddorf, S. R. Basu, M. L. Scullin, and R. Ramesh. *Electric modulation of conduction in multiferroic Ca-doped BiFeO3 films*. Nature Materials, **8**, 485 (2009).

[40] S. Bagdzevicius, K. Maas, M. Boudard, and M. Burriel. *Interface-type resistive switching in perovskite materials*. Journal of Electroceramics, **39**, 157 (2017).

[41] M.-J. Lee, C. B. Lee, D. Lee, S. Lee, M. Chang, J. Hur, Y.-B. Kim, C.-J. Kim, D. Seo, S. Seo, U.-I. Chung, I.-K. Yoo, and K. Kim. *A Fast, High-Endurance and Scalable Non-Volatile Memory Device Made from Asymmetric Ta2O5-X/TaO2-X Bilayer Structures*. Nat. Mater., **10**, 625 (2011).

[42] J. J. Yang, M.-X. Zhang, J. P. Strachan, F. Miao, M. D. Pickett, R. D. Kelley, G. Medeiros-Ribeiro, and R. S. Williams. *High switching endurance in TaOx memristive devices*. Appl. Phys. Lett., **97**, 232102 (2010).

[43] Y. Jeong, J. Lee, J. Moon, J. H. Shin, and W. D. Lu. *K-means Data Clustering with Memristor Networks*. Nano Lett., **18**, 4447 (2018).

[44] M. Csontos, Y. Horst, N. J. Olalla, U. Koch, I. Shorubalko, A. Halbritter, and J. Leuthold. *Picosecond Time-Scale Resistive Switching Monitored in Real-Time*. Advanced Electronic Materials, **9**, 2201104 (2023).

[45] X. Liu, S. M. Sadaf, M. Son, J. Park, J. Shin, W. Lee, K. Seo, D. Lee, and H. Hwang. *Co-Occurrence of Threshold Switching and Memory Switching in Pt/NbO_x/Pt Cells for Crosspoint Memory Applications*. IEEE Electron Device Letters, **33**, 236 (2012).

[46] M. D. Pickett and R. S. Williams. *Sub-100 fJ and sub-nanosecond thermally driven threshold switching in niobium oxide crosspoint nanodevices*. Nanotechnology, **23**, 215202 (2012).

[47] S. Kim, J. Park, J. Woo, C. Cho, W. Lee, J. Shin, G. Choi, S. Park, D. Lee, B. H. Lee, and H. Hwang. *Threshold-switching characteristics of a nanothin-NbO2-layer-based Pt/NbO2/Pt stack for use in cross-point-type resistive memories*. Microelectronic Engineering, **107**, 33 (2013).

[48] R. Winkler, A. Zintler, S. Petzold, E. Piros, N. Kaiser, T. Vogel, D. Nasiou, K. P. McKenna, L. Molina-Luna, and L. Alff. *Controlling the Formation of Conductive Pathways in Memristive Devices*. Advanced Science, **9**, 2201806 (2022).

[49] J.-W. Park, J.-W. Park, D.-Y. Kim, and J.-K. Lee. *Reproducible resistive switching in nonstoichiometric nickel oxide films grown by rf reactive sputtering for resistive random access memory applications*. Journal of Vacuum Science & Technology A, **23**, 1309 (2005).

[50] D.-H. Kwon, K. M. Kim, J. H. Jang, J. M. Jeon, M. H. Lee, G. H. Kim, X.-S. Li, G.-S. Park, B. Lee, S. Han, et al. *Atomic structure of conducting nanofilaments in TiO2 resistive switching memory*. Nature nanotechnology, **5**, 148 (2010).

[51] E. Piros, M. Lonsky, S. Petzold, A. Zintler, S. Sharath, T. Vogel, N. Kaiser, R. Eilhardt, L. Molina-Luna, C. Wenger, J. Müller, and L. Alff. *Role of Oxygen Defects in Conductive-Filament Formation in* Y_2O_3*-Based Analog RRAM Devices as Revealed by Fluctuation Spectroscopy*. Phys. Rev. Appl., **14**, 034029 (2020).

[52] A. Sawa. *Resistive switching in transition metal oxides*. Materials today, **11**, 28 (2008).

[53] Y. Yang, Y. Takahashi, A. Tsurumaki-Fukuchi, M. Arita, M. Moors, M. Buckwell, A. Mehonic, and A. J. Kenyon. *Probing electrochemistry at the nanoscale: in situ TEM and STM characterizations of conducting filaments in memristive devices*. Journal of Electroceramics, **39**, 73 (2017).

[54] J. P. Strachan, G. Medeiros-Ribeiro, J. J. Yang, M.-X. Zhang, F. Miao, I. Goldfarb, M. Holt, V. Rose, and R. S. Williams. *Spectromicroscopy of tantalum oxide memristors*. Applied Physics Letters, **98**, 242114 (2011).

[55] O. Gronenberg, G. Haberfehlner, F. Zahari, R. Marquardt, C. Kübel, G. Kothleitner, and L. Kienle. *Bio-Inspired Information Pathways: From Neuroscience to Neurotronics*, chapter Critical Discussion of Ex situ and In situ TEM Measurements on Memristive Devices, 129–157. Springer International Publishing (2024).

[56] S. Choi, T. Moon, G. Wang, and J. J. Yang. *Filament-free memristors for computing*. Nano Convergence, **10**, 58 (2023).

[57] G. Kim, S. Son, H. Song, J. B. Jeon, J. Lee, W. H. Cheong, S. Choi, and K. M. Kim. *Retention Secured Nonlinear and Self-Rectifying Analog Charge Trap Memristor for Energy-Efficient Neuromorphic Hardware*. Advanced Science, **10**, 2205654 (2023).

[58] W. Chen, S. Tappertzhofen, H. J. Barnaby, and M. N. Kozicki. *SiO2 based conductive bridging random access memory*. Journal of Electroceramics, **39**, 109 (2017).

[59] A. Gubicza, M. Csontos, A. Halbritter, and Gy. Mihály. *Non-exponential resistive switching in Ag_2S memristors: a key to nanometer-scale non-volatile memory devices*. Nanoscale, **7**, 4394 (2015).

[60] M. Aono and T. Hasegawa. *The Atomic Switch*. IEEE Proc., **98**, 2228 (2010).

[61] J. Sólyom. *Fundamentals of the Physics of Solids. Volume 3 - Normal, Broken-Symmetry, and Correlated Systems*. Springer Berlin, Heidelberg (2010).

[62] Y. Zhou and S. Ramanathan. *Mott Memory and Neuromorphic Devices*. Proceedings of the IEEE, **103**, 1289 (2015).

[63] K. Liu, S. Lee, S. Yang, O. Delaire, and J. Wu. *Recent progresses on physics and applications of vanadium dioxide*. Materials Today, **21**, 875 (2018).

[64] Z. Yang, C. Ko, and S. Ramanathan. *Oxide Electronics Utilizing Ultrafast Metal-Insulator Transitions*. Annual Review of Materials Research, **41**, 337 (2011).

[65] A. Cavalleri, T. Dekorsy, H. H. W. Chong, J. C. Kieffer, and R. W. Schoenlein. *Evidence for a structurally-driven insulator-to-metal transition in VO_2: A view from the ultrafast timescale*. Phys. Rev. B, **70**, 161102 (2004).

[66] A. Sood, X. Shen, Y. Shi, S. Kumar, S. J. Park, M. Zajac, Y. Sun, L.-Q. Chen, S. Ramanathan, X. Wang, et al. *Universal phase dynamics in VO2 switches revealed by ultrafast operando diffraction*. Science, **373**, 352 (2021).

[67] Y. Zhou, X. Chen, C. Ko, Z. Yang, C. Mouli, and S. Ramanathan. *Voltage-triggered ultrafast phase transition in vanadium dioxide switches*. IEEE Electron Device Letters, **34**, 220 (2013).

[68] C. Wan, Z. Zhang, D. Woolf, C. M. Hessel, J. Rensberg, J. M. Hensley, Y. Xiao, A. Shahsafi, J. Salman, S. Richter, Y. Sun, M. M. Qazilbash, R. Schmidt-Grund, C. Ronning, S. Ramanathan, and M. A. Kats. *On the Optical Properties of Thin-Film Vanadium Dioxide from the Visible to the Far Infrared*. Annalen der Physik, **531**, 1900188 (2019).

[69] J. Jeong, N. Aetukuri, T. Graf, T. D. Schladt, M. G. Samant, and S. S. Parkin. *Suppression of metal-insulator transition in VO2 by electric field–induced oxygen vacancy formation*. Science, **339**, 1402 (2013).

[70] M. Prezioso, F. Merrikh-Bayat, B. D. Hoskins, G. C. Adam, K. K. Likharev, and D. B. Strukov. *Training and operation of an integrated neuromorphic network based on metal-oxide memristors*. Nature, **521**, 61 (2015).

[71] E. Zamanidoost, F. M. Bayat, D. Strukov, and I. Kataeva. *Manhattan rule training for memristive crossbar circuit pattern classifiers*. In *2015 IEEE 9th International Symposium on Intelligent Signal Processing (WISP) Proceedings*, 1–6 (2015).

[72] C. Li, D. Belkin, Y. Li, P. Yan, M. Hu, N. Ge, H. Jiang, E. Montgomery, P. Lin, Z. Wang, W. Song, J. P. Strachan, M. Barnell, Q. Wu, R. S. Williams, J. J. Yang, and Q. Xia. *Efficient and self-adaptive in-situ learning in multilayer memristor neural networks*. Nature Communications, **9**, 2385 (2018).

[73] Y. Lecun, L. Bottou, Y. Bengio, and P. Haffner. *Gradient-based learning applied to document recognition*. Proceedings of the IEEE, **86**, 2278 (1998).

[74] J.-M. Hung, C.-X. Xue, H.-Y. Kao, Y.-H. Huang, F.-C. Chang, S.-P. Huang, T.-W. Liu, C.-J. Jhang, C.-I. Su, W.-S. Khwa, C.-C. Lo, R.-S. Liu, C.-C. Hsieh, K.-T. Tang, M.-S. Ho, C.-C. Chou, Y.-D. Chih, T.-Y. J. Chang, and M.-F. Chang. *A four-megabit compute-in-memory macro with eight-bit precision based on CMOS and resistive random-access memory for AI edge devices*. Nature Electronics, **4**, 921 (2021).

[75] W.-S. Khwa, Y.-C. Chiu, C.-J. Jhang, S.-P. Huang, C.-Y. Lee, T.-H. Wen, F.-C. Chang, S.-M. Yu, T.-Y. Lee, and M.-F. Chang. *A 40-nm, 2M-Cell, 8b-Precision, Hybrid SLC-MLC PCM Computing-in-Memory Macro with 20.5 - 65.0TOPS/W for Tiny-Al Edge Devices*. 1–3 (2022).

[76] W. Wan, R. Kubendran, C. Schaefer, S. B. Eryilmaz, W. Zhang, D. Wu, S. Deiss, P. Raina, H. Qian, B. Gao, S. Joshi, H. Wu, H.-S. P. Wong, and G. Cauwenberghs. *A compute-in-memory chip based on resistive random-access memory*. Nature, **608**, 504 (2022).

[77] M. Le Gallo, R. Khaddam-Aljameh, M. Stanisavljevic, A. Vasilopoulos, B. Kersting, M. Dazzi, G. Karunaratne, M. Brändli, A. Singh, S. M. Müller, J. Büchel, X. Timoneda, V. Joshi, M. J. Rasch, U. Egger, A. Garofalo, A. Petropoulos, T. Antonakopoulos, K. Brew, S. Choi, I. Ok, T. Philip, V. Chan, C. Silvestre, I. Ahsan, N. Saulnier, V. Narayanan, P. A. Francese, E. Eleftheriou, and A. Sebastian. *A 64-core mixed-signal in-memory compute chip based on phase-change memory for deep neural network inference*. Nature Electronics, **6**, 680 (2023).

[78] M.-K. Song, J.-H. Kang, X. Zhang, W. Ji, A. Ascoli, I. Messaris, A. S. Demirkol, B. Dong, S. Aggarwal, W. Wan, S.-M. Hong, S. G. Cardwell, I. Boybat, J.-s. Seo, J.-S. Lee, M. Lanza, H. Yeon, M. Onen, J. Li, B. Yildiz, J. A. del Alamo, S. Kim, S. Choi, G. Milano, C. Ricciardi, L. Alff, Y. Chai, Z. Wang, H. Bhaskaran, M. C. Hersam, D. Strukov, H.-S. P. Wong, I. Valov, B. Gao, H. Wu, R. Tetzlaff, A. Sebastian, W. Lu, L. Chua, J. J. Yang, and J. Kim. *Recent Advances and Future Prospects for Memristive Materials, Devices, and Systems*. ACS Nano, **17**, 11994 (2023).

[79] W. Wu, H. Wu, B. Gao, P. Yao, X. Zhang, X. Peng, S. Yu, and H. Qian. *A Methodology to Improve Linearity of Analog RRAM for Neuromorphic Computing*. In *2018 IEEE Symposium on VLSI Technology*, 103–104 (2018).

[80] A. Krizhevsky, G. Hinton, et al. *Learning multiple layers of features from tiny images* (2009).

[81] P. Warden. *Speech Commands: A Dataset for Limited-Vocabulary Speech Recognition* (2018).

[82] M. Rao, H. Tang, J. Wu, W. Song, M. Zhang, W. Yin, Y. Zhuo, F. Kiani, B. Chen, X. Jiang, H. Liu, H.-Y. Chen, R. Midya, F. Ye, H. Jiang, Z. Wang, M. Wu, M. Hu, H. Wang, Q. Xia, N. Ge, J. Li, and J. J. Yang. *Thousands of conductance levels in memristors integrated on CMOS*. Nature, **615**, 823 (2023).

[83] F. Cai, S. Kumar, T. Vaerenbergh, X. Sheng, R. Liu, C. Li, Z. Liu, M. Foltin, S. Yu, Q. Xia, J. J. Yang, R. Beausoleil, W. Lu, and J. W. Strachan. *Power-efficient combinatorial optimization using intrinsic noise in memristor Hopfield neural networks*. Nature Electronics, **3**, 1 (2020).

[84] J. G. Fehérvári, Z. Balogh, T. N. Török, and A. Halbritter. *Noise tailoring, noise annealing and external noise injection strategies in memristive Hopfield neural networks* (2023).

[85] J. G. Fehérvári. *Sztochasztikus jelenségek rezisztív kapcsoló memóriákban [Stochastic phenomena in resistive switching memories]* (2021). BSc thesis.

[86] B. Sánta, Z. Balogh, A. Gubicza, L. Pósa, D. Krisztián, G. Mihály, M. Csontos, and A. Halbritter. *Universal 1/f type current noise of Ag filaments in redox-based memristive nanojunctions*. Nanoscale, **11**, 4719 (2019).

[87] L. Pósa, Z. Balogh, D. Krisztián, P. Balázs, B. Sánta, R. Furrer, M. Csontos, and A. Halbritter. *Noise diagnostics of graphene interconnects for atomic-scale electronics*. npj 2D Materials and Applications, **5**, 57 (2021).

[88] Z. Balogh, G. Mezei, L. Pósa, B. Sánta, A. Magyarkuti, and A. Halbritter. *1/f noise spectroscopy and noise tailoring of nanoelectronic devices*. Nano Futures, **5**, 042002 (2021).

[89] H. Liu, Y. Qin, H.-Y. Chen, J. Wu, J. Ma, Z. Du, N. Wang, J. Zou, S. Lin, X. Zhang, Y. Zhang, and H. Wang. *Artificial Neuronal Devices Based on Emerging Materials: Neuronal Dynamics and Applications*. Advanced Materials, **35**, 2205047 (2023).

[90] A. A. Sharma, Y. Li, M. Skowronski, J. A. Bain, and J. A. Weldon. *High-Frequency TaOx-Based Compact Oscillators*. IEEE Transactions on Electron Devices, **62**, 3857 (2015).

[91] M. D. Pickett, G. Medeiros-Ribeiro, and R. S. Williams. *A scalable neuristor built with Mott memristors*. Nature materials, **12**, 114 (2013).

[92] L. Gao, P.-Y. Chen, and S. Yu. *NbOx based oscillation neuron for neuromorphic computing*. Applied Physics Letters, **111**, 103503 (2017).

[93] T. Tuma, A. Pantazi, M. Le Gallo, A. Sebastian, and E. Eleftheriou. *Stochastic phase-change neurons*. Nature nanotechnology, **11**, 693 (2016).

[94] C. D. Wright, P. Hosseini, and J. A. V. Diosdado. *Beyond von-Neumann Computing with Nanoscale Phase-Change Memory Devices*. Advanced Functional Materials, **23**, 2248 (2013).

[95] G. Csaba and W. Porod. *Coupled oscillators for computing: A review and perspective*. Applied Physics Reviews, **7**, 011302 (2020).

[96] E. M. Izhikevich. *Dynamical Systems in Neuroscience: The Geometry of Excitability and Bursting*. The MIT Press (2006).

[97] E. M. Izhikevich. *Which model to use for cortical spiking neurons?*. IEEE transactions on neural networks, **15**, 1063 (2004).

[98] A. Geresdi, M. Csontos, A. Gubicza, A. Halbritter, and G. Mihály. *A fast operation of nanometer-scale metallic memristors: highly transparent conductance channels in Ag_2S devices*. Nanoscale, **6**, 2613 (2014).

[99] A. Gubicza, M. Csontos, A. Halbritter, and Gy. Mihály. *Resistive switching in metallic Ag_2S memristors due to a local overheating induced phase transition*. Nanoscale, **7**, 11248 (2015).

[100] A. Gubicza, D. Z. Manrique, L. Pósa, C. J. Lambert, G. Mihály, M. Csontos, and A. Halbritter. *Asymmetry-induced resistive switching in Ag-Ag_2S-Ag memristors enabling a simplified atomic-scale memory design*. Sci. Rep., **6**, 30775 (2016).

[101] D. Molnár, T. N. Török, B. Sánta, A. Gubicza, A. Magyarkuti, R. Hauert, G. Kiss, A. Halbritter, and M. Csontos. *In situ impedance matching in Nb/Nb_2O_5/PtIr memristive nanojunctions for ultra-fast neuromorphic operation*. Nanoscale, **10**, 19290 (2018).

[102] B. Sánta, D. Molnár, P. Haiber, A. Gubicza, E. Szilágyi, Z. Zolnai, A. Halbritter, and M. Csontos. *Nanosecond resistive switching in Ag/AgI/PtIr nanojunctions*. Beilstein Journal of Nanotechnology, **11**, 92 (2020).

[103] J. P. Strachan, A. C. Torrezan, G. Medeiros-Ribeiro, and R. S. Williams. *Measuring the switching dynamics and energy efficiency of tantalum oxide memristors*. Nanotechnology, **22**, 505402 (2011).

[104] X. Lian, M. Wang, M. Rao, P. Yan, J. J. Yang, and F. Miao. *Characteristics and transport mechanisms of triple switching regimes of TaOx memristor*. Appl. Phys. Lett., **110**, 173504 (2017).

[105] C. E. Graves, N. Dávila, E. J. Merced-Grafals, S.-T. Lam, J. P. Strachan, and R. S. Williams. *Temperature and field-dependent transport measurements in continuously tunable tantalum oxide memristors expose the dominant state variable*. Appl. Phys. Lett., **110**, 123501 (2017).

[106] L. Pósa, G. Molnár, B. Kalas, Z. Baji, Z. Czigány, P. Petrik, and J. Volk. *A Rational Fabrication Method for Low Switching-Temperature VO2*. Nanomaterials, **11** (2021).

[107] J. del Valle, Y. Kalcheim, J. Trastoy, A. Charnukha, D. N. Basov, and I. K. Schuller. *Electrically Induced Multiple Metal-Insulator Transitions in Oxide Nanodevices*. Phys. Rev. Appl., **8**, 054041 (2017).

[108] J. del Valle, P. Salev, F. Tesler, N. M. Vargas, Y. Kalcheim, P. Wang, J. Trastoy, M.-H. Lee, G. Kassabian, J. G. Ramírez, M. J. Rozenberg, and I. K. Schuller. *Subthreshold firing in Mott nanodevices*. Nature, **569**, 388 (2019).

[109] Y. Li, Z. Wang, R. Midya, Q. Xia, and J. J. Yang. *Review of memristor devices in neuromorphic computing: materials sciences and device challenges*. Journal of Physics D: Applied Physics, **51**, 503002 (2018).

[110] H. Sim, D. Choi, D. Lee, S. Seo, M. Lee, I. Yoo, and H. Hwang. *Resistance-switching characteristics of polycrystalline Nb2O5 for nonvolatile memory application*. IEEE Electron Device Letters, **26**, 292 (2005).

[111] L. Chen, Q.-Q. Sun, J.-J. Gu, Y. Xu, S.-J. Ding, and D. W. Zhang. *Bipolar resistive switching characteristics of atomic layer deposited Nb2O5 thin films for nonvolatile memory application*. Current Applied Physics, **11**, 849 (2011).

[112] H. Mahne, H. Wylezich, S. Slesazeck, T. Mikolajick, J. Veselý, V. Klemm, and D. Rafaja. *Room temperature fabricated NbOx/Nb2O5 memory switching device with threshold switching effect*. 2013 5th IEEE International Memory Workshop, 174–177 (2013).

[113] H. Mähne, H. Wylezich, F. Hanzig, S. Slesazeck, D. Rafaja, and T. Mikolajick. *Analog resistive switching behavior of Al/Nb2O5/Al device*. Semiconductor Science and Technology, **29**, 104002 (2014).

[114] Y. Yang, S. Choi, and W. Lu. *Oxide Heterostructure Resistive Memory*. Nano Letters, **13**, 2908 (2013).

[115] S. Choi, J. Lee, S. Kim, and W. D. Lu. *Retention failure analysis of metal-oxide based resistive memory*. Applied Physics Letters, **105**, 113510 (2014).

[116] S. Kim, C. Du, P. Sheridan, W. Ma, S. Choi, and W. D. Lu. *Experimental Demonstration of a Second-Order Memristor and Its Ability to Biorealistically Implement Synaptic Plasticity*. Nano Letters, **15**, 2203 (2015).

[117] J. J. Yang, F. Miao, M. D. Pickett, D. A. A. Ohlberg, D. R. Stewart, C. N. Lau, and R. S. Williams. *The mechanism of electroforming of metal oxide memristive switches*. Nanotechnology, **20**, 215201 (2009).

[118] M. Lanza, H.-S. P. Wong, E. Pop, D. Ielmini, D. Strukov, B. C. Regan, L. Larcher, M. A. Villena, J. J. Yang, L. Goux, A. Belmonte, Y. Yang, F. M. Puglisi, J. Kang, B. Magyari-Köpe, E. Yalon, A. Kenyon, M. Buckwell, A. Mehonic, A. Shluger, H. Li, T.-H. Hou, B. Hudec, D. Akinwande, R. Ge, S. Ambrogio, J. B. Roldan, E. Miranda, J. Suñe, K. L. Pey, X. Wu, N. Raghavan, E. Wu, W. D. Lu, G. Navarro, W. Zhang, H. Wu, R. Li, A. Holleitner, U. Wurstbauer, M. C. Lemme, M. Liu, S. Long, Q. Liu, H. Lv, A. Padovani, P. Pavan, I. Valov, X. Jing, T. Han, K. Zhu, S. Chen, F. Hui, and Y. Shi. *Recommended Methods to Study Resistive Switching Devices*. Advanced Electronic Materials, **5**, 1800143 (2019).

[119] D. Molnár. *Implementation of tunable memory function in artificial synapses* (2020). Proceedings of the PhD Workshop of the Physics Doctoral School at the Faculty of Natural Science, Budapest University of Technology and Economics.

[120] A. Magyarkuti, O. Adak, A. Halbritter, and L. Venkataraman. *Electronic and mechanical characteristics of stacked dimer molecular junctions*. Nanoscale, **10**, 3362 (2018).

[121] Z. Balogh, G. Mezei, N. Tenk, A. Magyarkuti, and A. Halbritter. *Configuration-Specific Insight into Single-Molecule Conductance and Noise Data Revealed by the Principal Component Projection Method*. The Journal of Physical Chemistry Letters, **14**, 5109 (2023). PMID: 37249493.

[122] G. Lázár. *Filamentáris rezisztív kapcsoló memóriák zajjelenségeinek vizsgálata [Investigation of noise phenomena in filamentary resistive switching memories]* (2022). BSc thesis.

[123] H. Kim, N. S. Bingham, N. A. Charipar, and A. Piqué. *Strain effect in epitaxial VO2 thin films grown on sapphire substrates using SnO2 buffer layers*. AIP Advances, **7**, 105116 (2017).

[124] Z. Baji, L. Pósa, G. Molnár, Z. Szabó, M. Volom, A. K. Surca, G. Drazic, and J. Volk. *VO2 layers with high resistive switching ratio by atomic layer deposition*. Materials Science in Semiconductor Processing, **162**, 107483 (2023).

[125] A. Hendaoui. *Substrate Temperature-Dependent Structural, Optical, and Electrical Properties of Thermochromic VO¡sub¿2¡/sub¿(M) Nanostructured Films Grown by a One-Step Pulsed Laser Deposition Process on Smooth Quartz Substrates*. Advances in Condensed Matter Physics, **2021**, 7700676 (2021).

[126] L. Whittaker, C. J. Patridge, and S. Banerjee. *Microscopic and Nanoscale Perspective of the Metal-Insulator Phase Transitions of VO2: Some New Twists to an Old Tale*. The Journal of Physical Chemistry Letters, **2**, 745 (2011).

[127] S. W. Schmid. *Noise Analysis of Vanadium Dioxide Resistive Switches* (2022). Proceedings of the PhD Workshop of the Physics Doctoral School at the Faculty of Natural Science, Budapest University of Technology and Economics.

[128] M. Pan, H. Zhong, S. Wang, Z. Li, X. Chen, and W. Lu. *First-principle study on the chromium doping effect on the crystal structure of metallic VO2*. Chemical Physics Letters, **398**, 304 (2004).

[129] C. Ji, Z. Wu, X. Wu, J. Wang, X. Liu, J. Gou, H. Zhou, W. Yao, and Y. Jiang. *Terahertz transmittance and metal-insulator phase transition properties of M2 phase VO2 films induced by Cr doping*. Applied Surface Science, **455**, 622 (2018).

[130] F. Prins, T. Hayashi, B. J. A. de Vos van Steenwijk, B. Gao, E. A. Osorio, K. Muraki, and H. S. J. van der Zant. *Room-temperature stability of Pt nanogaps formed by self-breaking*. Applied Physics Letters, **94**, 123108 (2009).

[131] A. Mehonic, A. Shluger, D. Gao, I. Valov, E. Miranda, D. Ielmini, A. Bricalli, E. Ambrosi, C. Li, J. J. Yang, Q. Xia, and A. Kenyon. *Silicon Oxide (SiO_x): A Promising Material for Resistance Switching?*. Advanced Materials, **30**, 1801187 (2018).

[132] J. Yao, J. Lin, Y. Dai, G. Ruan, Z. Yan, L. Li, L. Zhong, D. Natelson, and J. M. Tour. *Highly transparent nonvolatile resistive memory devices from silicon oxide and graphene.*. Nature Communications, **3**, 1101 (2012).

[133] M. Mahmoodi, M. Prezioso, and D. B. Strukov. *Versatile stochastic dot product circuits based on nonvolatile memories for high performance neurocomputing and neurooptimization*. Nature Communications, **10**, 5113 (2019).

[134] W. A. Borders, A. Z. Pervaiz, S. Fukami, K. Y. Camsari, H. Ohno, and D. Supriyo. *Integer factorization using stochastic magnetic tunnel junctions*. Nature, **573**, 390 (2019).

[135] V. G. Karpov, Y. A. Kryukov, M. Mitra, and I. V. Karpov. *Crystal nucleation in glasses of phase change memory*. Journal of Applied Physics, **104**, 054507 (2008).

[136] V. Karpov, I. Karpov, and M. Mitra. *Field-induced nucleation in phase change memory*. Physical Review B, **78**, 052201 (2008).

[137] K. Kohary and C. D. Wright. *Electric field induced crystallization in phase-change materials for memory applications*. Applied Physics Letters, **98**, 223102 (2011).

[138] C. He, Z. Shi, L. Zhang, W. Yang, R. Yang, D. Shi, and G. Zhang. *Multilevel resistive switching in planar graphene/SiO_2 nanogap structures.*. ACS Nano, **6**, 4214 (2012).

[139] B. W. Fowler, Y.-F. Chang, F. Zhou, Y. Wang, P.-Y. Chen, F. Xue, Y.-T. Chen, B. Bringhurst, S. Pozder, and J. C. Lee. *Electroforming and resistive switching in silicon dioxide resistive memory devices*. RSC Adv., **5**, 21215 (2015).

[140] G. Mészáros, C. Li, I. Pobelov, and T. Wandlowski. *Current measurements in a wide dynamic range - Applications in electrochemical nanotechnology*. Nanotechnology, **18**, 424004 (2007).

[141] M. Le Gallo, A. Athmanathan, D. Krebs, and A. Sebastian. *Evidence for thermally assisted threshold switching behavior in nanoscale phase-change memory cells*. Journal of Applied Physics, **119**, 025704 (2016).

[142] J. A. Vázquez Diosdado, P. Ashwin, K. I. Kohary, and C. D. Wright. *Threshold switching via electric field induced crystallization in phase-change memory devices*. Applied Physics Letters, **100**, 253105 (2012).

[143] J. Nekola, A. Sizling, A. Boyer, and D. Storch. *Artifactions in the Log-Transformation of Species Abundance Distributions*. Folia Geobotanica, **43**, 259 (2008).

[144] E. Bibbona, G. Panfilo, and P. Tavella. *The Ornstein–Uhlenbeck process as a model of a low pass filtered white noise*. Metrologia, **45**, S117 (2008).

[145] S. Sharbati, I. Gharibshahian, T. Ebel, A. A. Orouji, and W.-T. Franke. *Analytical Model for Two-Dimensional Electron Gas Charge Density in Recessed-Gate GaN High-Electron-Mobility Transistors*. Journal of Electronic Materials, **50**, 3923 (2021).

[146] C. Kittel. *Introduction to Solid State Physics, 8^{th} edition*. John Wiley & Sons, Inc., New York (2005).

[147] B. J. van Wees, H. van Houten, C. W. J. Beenakker, J. G. Williamson, L. P. Kouwenhoven, D. van der Marel, and C. T. Foxon. *Quantized conductance of point contacts in a two-dimensional electron gas*. Phys. Rev. Lett., **60**, 848 (1988).

[148] N. Agrait, A. Yeyati, and J. van Ruitenbeek. *Quantum Properties of Atomic-Sized Conductors*. Physics Reports, **377**, 81 (2003).

[149] J. C. Cuevas and E. Scheer. *Molecular Electronics: An Introduction to Theory and Experiment*. World Scientific, Singapore (2010).

[150] E. Scheer, N. Agraït, J. C. Cuevas, A. L. Yeyati, B. Ludoph, A. Martín-Rodero, G. R. Bollinger, J. M. van Ruitenbeek, and C. Urbina. *The signature of chemical valence in the electrical conduction through a single-atom contact*. Nature, **394**, 154 (1998).

[151] C. Li, M. Hu, Y. Li, H. Jiang, N. Ge, E. Montgomery, J. Zhang, W. Song, N. Dávila, C. E. Graves, Z. Li, J. P. Strachan, P. Lin, Z. Wang, M. Barnell, Q. Wu, R. S. Williams, J. J. Yang, and Q. Xia. *Analogue signal and image processing with large memristor crossbars*. Nat. Elect., **1**, 52 (2018).

[152] H. Jiang, C. Li, R. Zhang, P. Yan, P. Lin, Y. Li, J. J. Yang, D. Holcomb, and Q. Xia. *A provable key destruction scheme based on memristive crossbar arrays*. Nature Electronics, **1**, 548 (2018).

[153] C. Li, Z. Wang, M. Rao, D. Belkin, W. Song, H. Jiang, P. Yan, Y. Li, P. Lin, M. Hu, N. Ge, J. W. Strachan, M. Barnell, Q. wu, S. Williams, J. J. Yang, and Q. Xia. *Long short-term memory networks in memristor crossbar arrays*. Nature Machine Intelligence, **1**, 49 (2019).

[154] Z. Wang, C. Li, W. Song, M. Rao, D. Belkin, Y. Li, P. Yan, H. Jiang, P. Lin, M. Hu, J. W. Strachan, N. Ge, M. Barnell, Q. wu, A. G. Barto, Q. Qiu, S. Williams, Q. Xia, and J. J. Yang. *Reinforcement learning with analogue memristor arrays*. Nature Electronics, **2**, 115–124 (2019).

[155] M. Hu, C. Graves, C. Li, Y. Li, N. Ge, E. Montgomery, N. Dávila, H. Jiang, S. Williams, J. J. Yang, Q. Xia, and J. W. Strachan. *Memristor-Based Analog Computation and Neural Network Classification with a Dot Product Engine*. Advanced Materials, **30**, 1705914 (2018).

[156] B. Ludoph, N. van der Post, E. N. Bratus', E. V. Bezuglyi, V. S. Shumeiko, G. Wendin, and J. M. van Ruitenbeek. *Multiple Andreev reflection in single-atom niobium junctions*. Phys. Rev. B, **61**, 8561 (2000).

[157] J. J. Riquelme, L. de la Vega, A. L. Yeyati, N. Agraït, A. Martin-Rodero, and G. Rubio-Bollinger. *Distribution of conduction channels in nanoscale contacts: Evolution towards the diffusive limit*. Europhysics Letters (EPL), **70**, 663 (2005).

[158] R. Cron, M. F. Goffman, D. Esteve, and C. Urbina. *Multiple-Charge-Quanta Shot Noise in Superconducting Atomic Contacts*. Phys. Rev. Lett., **86**, 4104 (2001).

[159] J. J. T. Wagenaar, M. Morales-Masis, and J. M. van Ruitenbeek. *Observing "quantized" conductance steps in silver sulfide: Two parallel resistive switching mechanisms*. J. Appl. Phys., **111**, 014302 (2012).

[160] B. Cheng, A. Emboras, Y. Salamin, F. Ducry, P. Ma, Y. Fedoryshyn, S. Andermatt, M. Luisier, and J. Leuthold. *Ultra compact electrochemical metallization cells offering reproducible atomic scale memristive switching*. Communications Physics, **2**, 28 (2019).

[161] P. Makk, S. Csonka, and A. Halbritter. *Effect of hydrogen molecules on the electronic transport through atomic-sized metallic junctions in the superconducting state*. Phys. Rev. B: Condens. Matter Mater. Phys., **78**, 045414 (2008).

[162] C. Schirm, M. Matt, F. Pauly, J. C. Cuevas, P. Nielaba, and E. Scheer. *A current-driven single-atom memory*. Nature Nanotechnology, **8**, 645 (2013).

[163] J. C. Cuevas, A. L. Yeyati, and A. Martín-Rodero. *Microscopic Origin of Conducting Channels in Metallic Atomic-Size Contacts*. Phys. Rev. Lett., **80**, 1066 (1998).

[164] Y. V. Nazarov. *Limits of universality in disordered conductors*. Phys. Rev. Lett., **73**, 134 (1994).

[165] C. W. J. Beenakker. *Random-matrix theory of quantum transport*. Rev. Mod. Phys., **69**, 731 (1997).

[166] R. Vardimon, M. Klionsky, and O. Tal. *Indication of complete spin filtering in atomic-scale nickel oxide*. Nano Letters, **15**, 3894 (2015).

[167] A. Geresdi. *Local probing of electronic transport with point contact Andreev reflection measurements*. Ph.D. thesis, Budapest University of Technology and Economics (2011).

[168] N. W. Ashcroft and N. D. Mermin. *Solid State Physics*. Saunders (1976).

[169] J. Halbritter. *On the oxidation and on the superconductivity of niobium*. Applied Physics A: Materials Science & Processing, **43**, 1 (1987).

[170] N. Pinto, S. J. Rezvani, A. Perali, L. Flammia, M. V. Milosevic, M. Fretto, C. Cassiago, and N. De Leo. *Dimensional crossover and incipient quantum size effects in superconducting niobium nanofilms*. Scientific Reports, **8**, 4710 (2018).

[171] N. Moussy, H. Courtois, and B. Pannetier. *Local spectroscopy of a proximity superconductor at very low temperature*. Europhysics Letters (EPL), **55**, 861 (2001).

[172] M. Vinet, C. Chapelier, and F. Leoch. *Spatially Resolved Spectroscopy on Superconducting Proximity Nanostructures*. Physical Review B, **63**, 165420 (2000).

[173] L. Y. L. Shen. *Superconductivity of Tantalum, Niobium and Lanthanum Studied by Electron Tunneling: Problems of Surface Contamination*. AIP Conference Proceedings, **4**, 31 (1972).

[174] H. le Sueur, P. Joyez, H. Pothier, C. Urbina, and D. Esteve. *Phase Controlled Superconducting Proximity Effect Probed by Tunneling Spectroscopy*. Physical Review Letters, **100**, 197002 (2008).

[175] E. Scheer, W. Belzig, Y. Naveh, M. H. Devoret, D. Esteve, and C. Urbina. *Proximity Effect and Multiple Andreev Reflections in Gold Atomic Contacts*. Phys. Rev. Lett., **86**, 284 (2001).

[176] W. Belzig, C. Bruder, and G. Schön. *Local density of states in a dirty normal metal connected to a superconductor*. Phys. Rev. B, **54**, 9443 (1996).

[177] W. Schulz, L. Forro, C. Kendziora, R. Wentzcovitch, D. Mandrus, L. Mihaly, and P. B. Allen. *Band structure and electronic transport properties of the superconductor NbO*. Physical Review B, **46**, 14001 (1992).

[178] A. Marchenkov, Z. Dai, C. Zhang, R. N. Barnett, and U. Landman. *Atomic Dimer Shuttling and Two-Level Conductance Fluctuations in Nb Nanowires*. Physical review letters, **98**, 046802 (2007).

[179] J. Senkpiel, R. Drost, J. C. Klöckner, M. Etzkorn, J. Ankerhold, J. C. Cuevas, F. Pauly, K. Kern, and C. R. Ast. *Extracting transport channel transmissions in scanning tunneling microscopy using superconducting excess current*. Phys. Rev. B: Condens. Matter Mater. Phys., **105**, 165401 (2022).

[180] I. Giaever and K. Megerle. *Study of Superconductors by Electron Tunneling*. Phys. Rev., **122**, 1101 (1961).

[181] H. Wylezich, H. Mähne, J. Rensberg, C. Ronning, P. Zahn, S. Slesazeck, and T. Mikolajick. *Local Ion Irradiation-Induced Resistive Threshold and Memory Switching in Nb_2O_5/NbO_x Films*. ACS Appl. Mater. Interfaces, **6**, 17474 (2014).

[182] H. Wylezich, H. Mähne, A. Heinrich, S. Slesazeck, J. Rensberg, C. Ronning, P. Zahn, and T. Mikolajick. *Adjusting the forming step for resistive switching in Nb_2O_5 by ion irradiation*. J. Vac. Sci. Technol. B, **33**, 01A105 (2015).

[183] J. M. van Ruitenbeek, M. Morales-Masis, and E. Miranda. *Resistive Switching: From Fundamentals of Nanoionic Redox Processes to Memristive Device Applications Ch. 7. Quantum Point Contact Conduction*, 197–224. Wiley-VCH, Weinheim (2016).

[184] M. Kaniselvan, M. Luisier, and M. Mladenović. *An Atomistic Model of Field-Induced Resistive Switching in Valence Change Memory*. ACS Nano, **17**, 8281 (2023).

[185] B. Xiao, X. Yu, and S. Watanabe. *A Comparative Study on the Diffusion Behaviors of Metal and Oxygen Ions in Metal-Oxide-Based Resistance Switches via ab Initio Molecular Dynamics Simulations*. ACS Applied Electronic Materials, **1**, 585 (2019).

[186] B. Xiao and S. Watanabe. *Oxygen vacancy effects on an amorphous-TaOx-based resistance switch: a first principles study*. Nanoscale, **6**, 10169 (2014).

[187] B. Xiao, T. Gu, T. Tada, and S. Watanabe. *Conduction paths in Cu/amorphous-Ta2O5/Pt atomic switch: First-principles studies*. Journal of Applied Physics, **115** (2014).

[188] A. Wedig, M. Luebben, D.-Y. Cho, M. Moors, K. Skaja, V. Rana, T. Hasegawa, K. K. Adepalli, B. Yildiz, R. Waser, and I. Valov. *Nanoscale cation motion in TaOx, HfOx and TiOx memristive systems*. Nature Nanotechnology, **11**, 67 (2016).

[189] M. Levy and I. Rudnick. *Ultrasonic Determination of the Superconducting Energy Gap in Tantalum*. Phys. Rev., **132**, 1073 (1963).

[190] R. Vardimon, M. Matt, P. Nielaba, J. C. Cuevas, and O. Tal. *Orbital origin of the electrical conduction in ferromagnetic atomic-size contacts: Insights from shot noise measurements and theoretical simulations*. Phys. Rev. B: Condens. Matter Mater. Phys., **93**, 085439 (2016).

[191] C. Lenk, K. Ved, S. Durstewitz, T. Ivanov, M. Ziegler, and P. Hövel. *Bio-Inspired Information Pathways: From Neuroscience to Neurotronics*, chapter Bio-inspired, Neuromorphic Acoustic Sensing, 287–315. Springer International Publishing (2023).

[192] M. F. Spiegel and C. S. Watson. *Performance on frequency-discrimination tasks by musicians and nonmusicians*. The Journal of the Acoustical Society of America, **76**, 1690 (1984).

[193] D. Pérez-González and M. S. Malmierca. *Adaptation in the auditory system: an overview*. Frontiers in Integrative Neuroscience, **8**, 19 (2014).

[194] I. C. Bruce, Y. Erfani, and M. S. Zilany. *A phenomenological model of the synapse between the inner hair cell and auditory nerve: Implications of limited neurotransmitter release sites*. Hearing Research, **360**, 40 (2018).

[195] L. A. Westerman and R. L. Smith. *Conservation of adapting components in auditory-nerve responses*. The Journal of the Acoustical Society of America, **81**, 680 (1987).

[196] M. Yip, R. Jin, H. H. Nakajima, K. M. Stankovic, and A. P. Chandrakasan. *A fully-implantable cochlear implant SoC with piezoelectric middle-ear sensor and arbitrary waveform neural stimulation*. IEEE journal of solid-state circuits, **50**, 214 (2014).

[197] J. Žák, Z. Hadaš, D. Dušek, J. Pekárek, V. Svatoš, L. Janák, and J. Prášek. *Model-based design of artificial zero power cochlear implant*. Mechatronics, **31**, 30 (2015).

[198] N. Mallegni, G. Molinari, C. Ricci, A. Lazzeri, D. La Rosa, A. Crivello, and M. Milazzo. *Sensing Devices for Detecting and Processing Acoustic Signals in Healthcare*. Biosensors, **12** (2022).

[199] E. Javel, I. L. Grant, and K. Kroll. *In Vivo Characterization of Piezoelectric Transducers for Implantable Hearing Aids*. Otology & Neurotology, **24** (2003).

[200] P. Udvardi, J. Radó, A. Straszner, J. Ferencz, Z. Hajnal, S. Soleimani, M. Schneider, U. Schmid, P. Révész, and J. Volk. *Spiral-Shaped Piezoelectric MEMS Cantilever Array for Fully Implantable Hearing Systems*. Micromachines, **8** (2017).

[201] N. Q. Khánh, Z. E. Horváth, Z. Zolnai, P. Petrik, L. Pósa, and J. Volk. *Effect of process parameters on co-sputtered Al(1-x)ScxN layer's properties: Morphology, crystal structure, strain, band gap, and piezoelectricity*. Materials Science in Semiconductor Processing, **169**, 107902 (2024).

[202] P. Maffezzoni, L. Daniel, N. Shukla, S. Datta, and A. Raychowdhury. *Modeling and simulation of vanadium dioxide relaxation oscillators*. IEEE Transactions on Circuits and Systems I: Regular Papers, **62**, 2207 (2015).